

# UNIVERSITÀ DEGLI STUDI DI NAPOLI “FEDERICO II”



Dottorato di Ricerca in Scienze della Terra  
XXVIII ciclo

## ANALYSIS AND INTERPRETATION OF AIRBORNE ELECTROMAGNETIC AND MAGNETIC DATA

*Domenico Di Massa*

**Tutor:** Prof. Giovanni Florio

**Co-Tutor:** Dr. Andrea Viezzoli

**Coordinatore:** Prof.ssa Maria Boni

*A mio padre e mia madre*

*"Nella vita non c'è nulla da temere, solo da capire."*

*Marie Curie*

# INDEX

|  |           |
|--|-----------|
| <b>INTRODUCTION .....</b>  | <b>6</b>  |
| <b>CHAPTER 1 – TIME DOMAIN ELECTROMAGNETIC METHOD,<br/>AIRBORNE EM SYSTEMS AND SAMPLING OPTIMIZATION OF AEM<br/>TRANSIENTS .....</b> | <b>10</b> |
| <b>1.1 Basic physics of EM .....</b>   | <b>10</b> |
| <b>1.2 Time domain electromagnetic method: principles and measuring<br/>procedures .....</b>   | <b>12</b> |
| 1.2.1 The transient response over a layered half-space .....   | 14        |
| <b>1.3 Airborne EM systems .....</b>   | <b>16</b> |
| <b>1.4 Types of noise in TEM data .....</b>  | <b>19</b> |
| <b>1.5 Geophysical data inversion .....</b>  | <b>22</b> |
| 1.5.1 Least squares solution for linear and non-linear inverse problems .....  | 23        |
| 1.5.2 Inversion of AEM data .....  | 25        |
| 1.5.3 Laterally Constrained Inversion (LCI) .....  | 28        |
| 1.5.4 Spatially Constrained Inversion (SCI) .....  | 30        |
| 1.5.5 Depth of investigation for 1D (EM-DC) model .....  | 31        |
| <b>1.6 Optimized sampling of AEM transients .....</b>  | <b>32</b> |
| <b>CHAPTER 2 – MAGNETIC METHOD AND INVERSION OF VERTICAL<br/>MAGNETIC SOUNDINGS .....</b>  | <b>54</b> |
| <b>2.1 Magnetic Field .....</b>  | <b>54</b> |
| <b>2.2 Magnetism of rocks and minerals .....</b>   | <b>56</b> |
| <b>2.3 The geomagnetic field and the magnetic anomalies .....</b>  | <b>58</b> |
| <b>2.4 Analysis of potential fields .....</b>  | <b>59</b> |
| 2.4.1 Upward and downward continuation .....   | 59        |
| 2.4.2 Vertical derivative .....  | 60        |
| 2.4.3 Horizontal derivative .....  | 61        |
| <b>2.5 Interpretation of potential field anomalies .....</b>   | <b>61</b> |
| 2.5.1 The forward model of Vertical Magnetic Sounding .....  | 63        |
| 2.5.2 The inversion method of Vertical Magnetic Sounding .....   | 64        |
| 2.5.3 Vertical Soundings inversion of synthetic magnetic data .....  | 66        |

|  |            |
|--|------------|
| <b>2.6 Vertical Soundings inversion of measured data</b> .....   | <b>69</b>  |
| 2.6.1 Effect of constraints ( $m_L < m < m_H$ ) on inversion process .....   | 73         |
| 2.6.2 Effect of constraints ( $d-\delta d < Gm < d+\delta d$ ) on inversion process .....  | 74         |
| 2.6.3 Effect of the errors on the estimation of the horizontal dimensions of the source .....  | 75         |
| <b>2.7 Vertical Soundings inversion of continued data</b> .....  | <b>77</b>  |
| 2.7.1 Effect of maximum altitude on inversion process .....  | 81         |
| 2.7.2 Vertical Soundings inversion of continued data in presence of a linear trend.....  | 82         |
| 2.7.3 Vertical Soundings inversion of continued data produced by an irregular shaped prism.....  | 84         |
| <br>   |            |
| <b>CHAPTER 3 – JOINT INVERSIONS OF TWO VTEM SURVEYS USING QUASI 3D TDEM AND VERTICAL MAGNETIC SOUNDINGS ALGORITHMS: THE CASE STUDY OF THE BROKEN EVIL PROSPECT, ONTARIO (CANADA)</b> ..... | <b>90</b>  |
| <b>3.1 Geological setting of the Superior Province, Ontario, Canada</b> .....  | <b>90</b>  |
| 3.1.1 The Abitibi Terrane in the Eastern Superior Province.....  | 91         |
| 3.1.2 The Broken Evil prospect in the Abitibi greenstone belt .....  | 92         |
| <b>3.2 Geophysical features of Volcanogenic Massive Sulfide Deposits</b> .....   | <b>93</b>  |
| <b>3.3 The 2013 Versatile Time Domain Electromagnetic (VTEM<sup>plus</sup>) survey over the Broken Evil prospect</b> .....   | <b>95</b>  |
| <b>3.4 The 2007 Versatile Time Domain Electromagnetic (VTEM) survey over the Broken Evil prospect</b> .....  | <b>98</b>  |
| <b>3.5 VTEM data processing</b> .....  | <b>99</b>  |
| 3.5.1 Navigation data processing.....  | 100        |
| 3.5.2 Voltage data processing .....  | 102        |
| 3.5.3 Fast smooth LCI inversion for post-processing of voltage data .....  | 105        |
| <b>3.6 Spatially Constrained Inversion of 2 VTEM datasets</b> .....  | <b>109</b> |
| 3.6.1 Joint SCI Inversion of 2 VTEM datasets .....   | 111        |
| <b>3.7 Interpretation of joint VTEM smooth inversion results</b> .....   | <b>115</b> |
| <b>3.8 Vertical Soundings Inversion of magnetic data over Broken Evil prospect</b> .....   | <b>119</b> |
| 3.8.1 Vertical Magnetic Soundings Inversion of Anomaly 1.....  | 122        |
| 3.8.2 Vertical Magnetic Soundings Inversion of Anomaly 2.....  | 127        |
| 3.8.3 Comparison of Vertical Magnetic Soundings inversion and 3D magnetic inversion for the Anomaly 1 and 2.....   | 131        |
| <b>3.9 Comparison of EM inversion and magnetic inversion at the magnetic Anomaly 1 and 2</b> .....   | <b>134</b> |

**CHAPTER 4 – SPATIALLY CONSTRAINED INVERSION OF IP PARAMETERS FROM AIRBORNE EM DATA AND INVERSION OF VERTICAL MAGNETIC SOUNDINGS FROM AEROMAGNETIC DATA: THE CASE STUDY OF DRYBONES KIMBERLITE, NORTHWEST TERRITORIES (CANADA) .....137**

**4.1 Induced-polarization effects in Airborne EM measurements ..... 137**

**4.2 Spatially Constrained Inversion for IP parameters ..... 140**

**4.3 Geological setting of the Slave Province in the Northwest Territories, Canada ..... 142**

**4.4 Geophysical methods for kimberlites detections ..... 144**

**4.5 The Drybones kimberlite in the Northwestern Territories, Canada 145**

4.5.1 AEM surveys over Drybones kimberlite ..... 147

**4.6 Processing VTEM data..... 149**

**4.7 SCI of VTEM data modelling IP effects ..... 153**

**4.8 Interpretation of constrained inversion of IP parameters results.. 155**

4.8.1 Resistivity and chargeability vertical cross-sections along the profile AA' ..... 158

4.8.2 Comparison of three resistivity models cross-sectioned at line 1210 (ZTEM) and line 70 (VTEM) ..... 159

**4.9 Vertical Soundings Inversion of magnetic data over Drybones kimberlite ..... 162**

4.9.1 Comparison of Vertical Magnetic Soundings inversion and 3D magnetic inversion along the AA' profile ..... 168

**4.10 Comparison of magnetic inversion and EM inversion along the AA' profile..... 170**

**CONCLUSIONS..... 172**

**REFERENCES ..... 178**

**ACKNOWLEDGEMENTS..... 196**

## **INTRODUCTION**

Electromagnetic and magnetic methods have been applied in mining exploration since at least the beginning of the 20th century. In the early 50s, the technological advances developed during the World War II move the interest from the ground to airborne systems. During the years a significant evolution has regarded the instrumentation, the acquisition phase and the processing techniques which was made possible thank to the parallel development of the electronic computers.

Nowadays airborne surveys often cover hundreds to thousands of square kilometers and contain thousands of line kilometers of data with measurement locations every few meters. Airborne systems are usually equipped with multiple sensors that allow to measure simultaneously different geophysical data as well as ancillary data (GPS position and radar altimetry).

In fact, time domain electromagnetic (TDEM) and magnetic surveys are often performed simultaneously, by a single airborne system carrying both the electromagnetic equipment and the magnetic sensor.

The opportunity of having two distinct datasets over the same area, obeying to different physical principles and thus investigating the distribution of different physical properties within the earth is, in principle, of great value. In fact, it makes possible an integrated study of the two types of data with a potentially strong improvement of the final interpretation model. The integration of different geophysical methodologies may allow a better definition and understanding of the studied geological problem but it is still not a very common used practice in exploration geophysics.

In this research, I focused on processing and modeling of TDEM and aeromagnetic data acquired during the same survey, with the aim of exploring the possibilities for a joint interpretation of these different datasets.

My research involved both methodological advances and applications to real dataset.

In particular, I will show two case studies, both located in Canada.

The first one, is related to Broken Evil prospect in Ontario. This region hosts some of the richest mineral deposits of Canada (especially volcanic massive

sulfide deposits). The second one is related to Drybones bay in Northwest Territories, where in 1994 a completely underwater kimberlite structure was discovered.

The inversion of TDEM data is usually performed by means of 1D inversion algorithms that use spatially constraints on model parameters in order to regularize the inversion process.

Two different electromagnetic (EM) surveys were flown over the Broken Evil prospect. The two TDEM systems used had different moment, waveform shapes and receiver times. From an instrumental point of view, they represent two completely distinct dataset. The TDEM data over this area were jointly inverted using the Spatially Constrained Inversion (SCI) approach (Viezzoli et al. 2008) providing a unique resistivity model that results more reliable in terms of overall robustness of the geophysical results and has greater spatial resolution. This joint inversion has required the addition of a calibration factor in the data space before the inversion in order to increase the consistence in the model space.

The analysis of the TDEM data acquired over the Drybones bay has shown clear effects of induced polarization (IP) phenomena. These phenomena are usually observed in the data derived from coincident-loop systems. In this case, the transient shows abnormal fast decay with the existence of negative values of the voltage data. Generally, these negative data are removed from the dataset before the inversion as, without considering a dispersive nature for the resistivity, no meaningful information can be derived from negative parts of transient. However, a polarizable earth may be described using an impedance model derived from the empirical Cole-Cole model (Cole and Cole, 1942). Thus, the TDEM data inversion was performed by using a 1D algorithm that permits to model the four Cole-Cole parameters in TDEM transient (Fiandaca et al., 2012).

The IP effects represent one of the phenomena that most affects the EM transient decay. However, even without considering IP effects, the shape of the EM transient decay depends on the distribution of the conductivity with depth. In the simplest case of layered earth model, I noticed that some information about the interface of different electro-layers could be derived, studying the first and the second order derivatives of the EM transient. In

particular, the transition from a conductive to a resistive layer results in a minimum of curvature of the transient while on the contrary the transition from a resistive to a conductive layer corresponds to a maximum of curvature. This confirms that there are some time intervals in the EM transient decay that contain more information on the structures in the subsurface.

Thus, I have proposed a new approach to sample the EM transient, called Adaptive-gating, that consists in a more detailed sampling of the time intervals at which the electromagnetic response shows slope variations.

I have proved that the use of such an alternative sampling scheme, compared to the classical Log-gating approach (Munkholm and Auken, 1996), which uses number of gates with a logarithmic increase of the width with time, aims to get more accurate inverse models by extracting the geological information from the measured data in an optimal way.

A 1D inversion algorithm applied on the collected soundings of the EM data provides vertical distributions of the investigated physical property at depth. The SCI approach, used in this work to invert the TDEM data, operates in this way. For the inversion of potential field data is not possible to define any 1D inversion algorithms. This is because the 1D algorithms assume a lateral homogeneity of layers with infinite horizontal dimensions that, producing a constant field in the space, are not able to explain any magnetic/gravimetric anomalies. In addition, the potential field data are usually collected at one altitude over the ground and not as vertical soundings.

However, the possibility of calculating the potential field data over an arbitrary surface if the field is known completely over another surface and no sources are located between the two surfaces, allows building vertical soundings. In this work, I have studied the inversion of the vertical magnetic soundings (Fedi and Rapolla, 1995) that can be considered as a 1D inversion method. Several synthetic tests were performed to set up the method, which was subsequently applied to magnetic data collected during the two examined case studies.

The interpretative results of the TDEM and magnetic data reveal that the sensitivity of the two methods may differ with respect to the investigated geological structures. This would imply a certain difficulty in setting up a true

joint inversion algorithm to interpret these two data types simultaneously that would be valid in all the studied cases.

However, results show how with different resolution and depth of investigation, in the studied areas the cooperation of the TDEM and aeromagnetic data can lead to a better understand of the structures at depth.

# CHAPTER 1 – Time Domain Electromagnetic Method, airborne EM systems and sampling optimization of AEM transients

## 1.1 Basic physics of EM

The fundamental electromagnetic phenomenon is that a varying magnetic field will result in a varying electric field which, again, will create another varying magnetic field and so on. This determines the propagation of the electromagnetic field.

An electromagnetic field is defined by five vector functions: **E** (electric field intensity, V/m), **B** (magnetic induction, Wb/m<sup>2</sup> or Tesla), **D** (dielectric displacement, C/m<sup>2</sup>), **H** (magnetic field intensity, A/m) and **J** (electric current density, A/m<sup>2</sup>).

Any electromagnetic phenomenon is described by the interaction of these elements that can be end up in the Maxwell's equations.

Maxwell's equations are uncoupled first order linear differential equations and in time domain are expressed by:

$$\nabla \times E = -\frac{\partial B}{\partial t} \quad (1.1)$$

$$\nabla \times H = J + \frac{\partial D}{\partial t} \quad (1.2)$$

$$\nabla \cdot B = 0 \quad (1.3)$$

$$\nabla \cdot D = \rho \quad (1.4)$$

where  $\rho$  is electric charge density (C/m<sup>3</sup>).

Moreover, there are three other equations, named constitutive equations, which establish the connections between the five vector functions and explain the response of a medium to an electromagnetic field. For an isotropic linear material they are:

$$J = \sigma E \quad (1.5)$$

$$D = \varepsilon E \quad (1.6)$$

$$B = \mu H \quad (1.7)$$

where  $\sigma$  is electric conductivity (S/m),  $\varepsilon$  dielectric permittivity (F/m) and  $\mu$  magnetic permeability (H/m) (Grant and West, 1965).

The equation 1.5 is the Ohm's law in microscopic context, while the equations 1.6 and 1.7 are two empirical relationships of electric and magnetic fields.

The equation 1.1, known as the first Maxwell equation or Faraday's law states that any magnetic field that varies through time will be accompanied by a spatially-varying, non-conservative electric field, and vice-versa. The electromotive force (*emf*) in a coil is equal to the negative of the rate of change of the magnetic flux.

The equation 1.2, known as the second Maxwell equation or Ampere's law, states that an electric current can generate an induced magnetic field. For an alternating current circulation, there will be an additional current in the medium, known as displacement current, that is proportional to the variation of the electric field, produced by the alternating current, through the dielectric permittivity (equation 1.6). This displacement current is added to the conductive current and both act to induce the magnetic field. The equations 1.3 and 1.4 are the Gauss' laws for magnetic and electric fields.

I refer to Ward and Hohmann (1988) and West and Macnae (1991) for a complete treatment of the EM theory.

The electromagnetic geophysical methods are based on the Maxwell's equations. An alternating current, flowing in a transmitter coil, produces a magnetic field that varies in time, i.e. the primary field. This field, according to Maxwell's equations, induces an electrical current in the conductive ground. These induced currents, with the associated electrical field, generate in turn a magnetic field, i.e. the secondary field, measurable with a receiver coil. At the receiver coil, a total field, that is the sum of the primary and the secondary is measured. This is valid for the electromagnetic method in the frequency domain (FDEM). As the information about the conductivity of the ground are contained in the secondary field, which is smaller than the primary field, the most challenge issue for these methods is to accurately measure the primary field in order to correctly compensate the measured data. Alternatively, the secondary field can be measured in the absence of a primary field as a

function of time (i.e. time domain methods, TEM). This chapter is focused on these latter methods.

## **1.2 Time domain electromagnetic method: principles and measuring procedures**

The time domain methods are relatively young if compared to the frequency domain and electric methods. Until the early 1960s, all the EM systems transmitted and received continuously on one frequency at a time. The first successful application to transmit transient pulses and measure the ground response during the off-time is dated to 1962 (Telford et al., 1990). These were the airborne Input (Barringer, 1962). Since the early 1970s, there has been a dramatic increase in the development of such time domain systems, i.e. the EMP pulse ground system of Newmont Exploration (Dolan, 1970). This inductive method was originally designed for mineral investigations. Only since the early 1990s, with the development of modern computers, that have made faster the processing and then the interpretations, these methods have been extensively applied in different fields: from mining exploration to hydrogeological purposes, from general geological mapping to environmental problems.

With time domain methods, as the name suggests, is measured the amplitude of a signal as a function of time.

The time domain systems usually consist of a receiver and transmitter unit attached to a receiver coil and a large transmitter loop, respectively. The receiving coil is connected to the receiver and the receiver, in turn, is connected to the transmitter allowing the synchronization between the transmitter and the receiver. The receiver coil can be placed in the middle of the transmitter loop, the center-loop configuration or can be placed outside with a characteristic offset, the offset-loop configuration.

Through the loop of the transmitter passes a constant current. This results in a static primary magnetic field. After few milliseconds, the current is quickly shut off, thereby interrupting the primary magnetic field. For the Faraday's law, an electromotive force (*emf*) is induced in the surroundings. In the ground, this *emf* will yield an electrical current, which runs below the transmitter and diffuses through the medium resembling smoke rings

(Nabighian, 1979). These eddy currents again will yield a magnetic field, the secondary magnetic field. The rate of change of the secondary magnetic fields is recorded using an induction coil and it is measured as a function of time (Fitterman and Stewart, 1986).

As time passes, the induced currents will attenuate (converting to heat) for the resistance of the ground and their maximum amplitude will diffuse downward and outward. In this phase, the current diffusion is controlled by the conductivity of the ground: high conductivity involves slow diffusion and decay of the current compared to poorly conductive ground, where currents diffuse and decay more quickly.

Just after the current in the transmitter loop is turned-off, the current will flow in the upper part of the ground and the amplitude of the measured signal will depend on the conductivity of the top layers. Later, the maximum current density will be at greater depths and the secondary magnetic field will contain information on the conductivity of the lower layers. The voltage measured at the receiver coil is called "transient" and gives information about the conductivity of the ground.

This transient has a large dynamic range as it is measured in a long time interval, showing a great variation of its amplitude. Typically, the variation is a factor  $10^6$ , and this field should be measured from  $10^{-5}$  s to  $10^{-3}$  s after the current in the transmitter loop is turned-off (Christiansen et al., 2009).

The data are recorded in time-windows, called "gates". The sampling of the secondary magnetic field is often performed following a standard approach, using the same number of gates per time-decade with a logarithmic increase of the width with time in order to improve the S/N ratio at late times. This is the classical log-gating configuration (Munkholm and Auken, 1996). Usually, the early time gates are very narrow to take into account the rapid changing of the transient voltage and they provide information about the shallower structures. The late time gates, that occur when the transient voltage is changing more slowly, are for this reason much longer and contain information on the deeper structures.

### 1.2.1 The transient response over a layered half-space

The time-domain EM method theory is based on solving Maxwell's equations given a set of conditions and assumptions. A detailed description of this theory is found in Ward and Hohmann (1988) and as a shorter version in Christiansen et al. (2009).

The vertical magnetic field  $H_z$  in the center of a circular loop, which is a good approximation for a square or otherwise segmented loop of the same area, with radius  $a$  and current  $I$ , is:

$$H_z = \frac{Ia}{2} \int_0^{\infty} [e^{-u_0|z+h|} + r_{TE}e^{u_0|z-h|}] \frac{\lambda^2}{u_0} J_1(\lambda a) d\lambda \quad (1.8)$$

with  $h$  and  $z$  are the transmitter and the receiver heights,  $J_1$  is the Bessel function of order one,  $\lambda = \sqrt{k_x^2 + k_y^2}$  where  $k_x$  and  $k_y$  are the spatial frequencies in the  $x$  and  $y$  direction and  $u_0$  is the propagation factor that in quasi-static approximation, when the displacement currents can be neglected, is equal to  $u_0 = \sqrt{\lambda^2 + i\omega\mu_0/\rho_0}$ .  $r_{TE}$  is the reflection coefficient and it expresses how the layered half-space modifies the source field.

The integral is called a Hankel integral and it is expressed in the frequency domain because  $r_{TE}$  is a function of frequency.

The transient response is obtained by inverse Laplace transform or inverse Fourier transform of the Hankel integral.

The expression above applies to the vertical magnetic field in the center of a circular loop. Any deviation from this setup (piecewise linear loops, off-set loops, x-component of the fields etc.) introduces other equations but, common to them all, only numerical solutions exist. In fact, generally, the integral in equation 1.8 cannot be easily solved analytically, because of the complexity of Bessel functions and has to be evaluated using numerical methods. However, for the model of a homogeneous half-space an analytic solution can be found, using this loop configuration. In this case  $r_{TE}$  becomes:

$$r_{TE} = \frac{\lambda - u}{\lambda + u} \quad (1.9)$$

assuming quasi-static conditions, i.e.  $u = \sqrt{\lambda^2 + i\omega\mu_0/\rho}$  where  $\rho$  is the half-space resistivity, and the vertical magnetic field simplifies to:

$$H_z = I_a \int_0^{\infty} \frac{\lambda^2}{\lambda - u} J_1(\lambda a) d\lambda \quad (1.10)$$

Using the relation between  $b_z$  and  $h_z$ , you can now solve for  $b_z$  by evaluating the integral and applying an inverse Laplace transform:

$$b_z = \frac{\mu_0 I}{2a} \left[ \frac{3}{\sqrt{\pi} \theta a} e^{-\theta^2 a^2} + \left( 1 - \frac{3}{2\theta^2 a^2} \right) \text{erf}(\theta a) \right] \quad (1.11)$$

with  $\theta = \sqrt{\frac{\mu_0 \sigma}{4t}}$ ,  $\sigma$  is the conductivity of the half-space,  $\text{erf}$  is the error function and  $t$  is the time window.

$b_z$  may be evaluated for  $t \rightarrow 0$  as  $b_z = \mu_0 I / 2a$ . This is the size of the primary field in free space or the magnetic intensity before the current is turned off.

As an induction coil is used for measurements in the field, the actual measurement is that of  $db/dt$  (the induced electromotive force is proportional to the time derivative of the magnetic flux passing the coil).

The time derivative, or the impulse response,  $db_z/dt$  is found through differentiation to be:

$$\frac{\partial b_z}{\partial t} = -\frac{1}{\sigma a^3} \left[ 3 \text{erf}(\theta a) - \frac{2}{\sqrt{\pi}} \theta a (3 + 2\theta^2 a^2) e^{-\theta^2 a^2} \right] \quad (1.12)$$

when  $\theta$  approaches zero, i.e. at late times, the time-derivative of the magnetic field can be approximated by:

$$\frac{\partial b_z}{\partial t} \approx \frac{M}{20} \left( \frac{\sigma}{\pi} \right)^{\frac{3}{2}} \left( \frac{\mu_0}{t} \right)^{\frac{5}{2}} \quad (1.13)$$

where  $M = I \pi a^2$  is the magnetic moment of the transmitter.

Thus, the time derivative of  $b$  exhibits a decay proportional to  $t^{-5/2}$ .

The decaying curve of the magnetic field is not very informative and usually it is preferred to display the apparent resistivity curve, instead. This curve is derived from equation 1.13 and is expressed as:

$$\rho_a = \frac{1}{\pi} \left( \frac{M}{20 \partial b_z / \partial t} \right)^{2/3} \left( \frac{\mu_0}{t} \right)^{5/3} \quad (1.14)$$

The apparent resistivity is not equal to the true resistivity for a layered earth, but it provides just a valuable normalization of the data with respect to the source and the measuring configuration.

These are the central equations for the TEM method, but they are applicable in this form only to the vertical field in the center of the transmitter loop at the Earth's surface.

### **1.3 Airborne EM systems**

Airborne electromagnetic systems (AEM) have been used for more than 60 years. The first applications were related to the exploration for minerals and justified by the need to cover large areas at reasonable costs.

AEM systems vary by their features, sizes and field of application, but they can be divided into two main categories: fixed-wing plane and helicopter based, implementing both frequency and time domain systems.

Starting from 1997, various reviews have been published regarding airborne electromagnetic surveying (Fountain, 1998; Witherly, 2000; Fountain and Smith, 2003; Nabighian and Macnae, 2005; Fountain et al., 2005; Sattel, 2006; Thomson et al., 2007; Allard, 2007; Macnae, 2008; Sattel 2009).

The birth of airborne electromagnetic surveying dates back to 1948, when Stanmac, a small exploration company, and McPhar Engineering tested the first airborne system in the Flin Flon area (Canada). The system consisted of a transmitter dipole axis, horizontal and transverse to the flight-line direction, mounted around the fuselage of a wooden Anson aircraft with the receiver towed in a bird behind.

In 1954, the discovery of the Heath Steele zinc-lead-copper-silver deposits (Canada) represents the first discovery obtained by an AEM survey, carried by Inco in joint venture with American Metal Corp. (Fountain, 1998).

In the first systems, the transmitter coils were mounted inside the aircraft. In 1954, the Hunting system established the system geometry of fixed-wing AEM systems with a transmitter loop installed on a metal aircraft as a horizontal triangular loop from the trailing edge of the wing to the leading edge of the tail fin.

In 1955 a new AEM system was introduced in Canada by Nucom that presented a first rigid-mounted-coil and represents the basic geometry of the modern helicopter systems with a rigid-beam, coaxial-coil-pair towed in a 6 m bird.

Until 1959 all the AEM systems, both fixed-wing and helicopter, worked on frequency domain. The first survey in time-domain was flown by Selco Exploration using the time-domain INPUT fixed-wing system with a transmitter loop slung from the nose, wings tip and tail of the aircraft establishing the

geometry of the modern time-domain fixed-wing AEM systems (Fountain, 1998).

In the 1970s, the 70% of all AEM survey were carried out by this system in order to discover base metal and uranium deposits (Palacky and West, 1991). In later years, many new systems have been developed and improved, following two different paths for the two types of systems, fixed-wing and helicopter. The fixed-wing systems, using large transmitter-receiver separation, focused on greater depth of penetration to the detriment of the near surface resolution in order to identify metal deposits for mining explorations, while the helicopter systems sacrificed the depth of penetration for higher resolution and were applied especially for near surface mapping. Moreover, by the end of 1970s, the fixed-wing systems are nearly all time-domain, leaving the frequency-domain for the helicopter systems that become multi-frequency and multi-component.

In the past decade, one of the most important developments in acquisition capability is the rise to prominence of helicopter time-domain electromagnetic systems (HTEM) (Thomson et al., 2007). These new systems have the objective to get the best of the two world by combining the high transmitter power of fixed wing systems for depth penetration, with the slower speed and flying altitude of the helicopter frequency-domain electromagnetic systems (HFEM) for higher spatial resolution and surveys over more rugged topography (Allard, 2007). Certainly, the development of these new systems is related to the simultaneous technological advancements in data quality, signal to noise ratio, investigation depth and spatial resolution. A major development is driven also by the development of the accessory technologies like accurate GPS location, fast A/D converter, data storage capacity, data processing speed.

At date, two transmitter loop – receiver coils configurations exist and are adopted by all the HTEM systems: the first one, named central loop configuration, presents the receiver coils in the center of the transmitter loop. This configuration is adopted by the SkyTEM of SkyTEM ApS (Sørensen and Auken, 2004), the VTEM by Geotech Ltd (Whiterly et al., 2004 and 2005), the AeroTEM by Aeroquesto Ltd (Boyko et al., 2001; Balch et al., 2003), and the HoisTEM of Normandy Exploration Ltd (Boyd, 2001 and 2004). The second

configuration has a vertical separation between the receiver coils and the transmitter loop with the receiver coils located above on the towed cable. This configuration is used by the HeliGEOTEM of Fugro Airborne Survey (Fountain et al., 2005), the NewTEM of Newmont Mining Corp. (Eaton et al., 2002 and 2004), and the THEM by THEM Geophysics Inc. (Bodger et al., 2005). Moreover, some systems (AeroTEM, SkyTem, HeliGEOTEM) have two receiver coils with different orientations to measure the vertical and the horizontal EM components.

Concentric coil systems suffer from the strong primary field induced during on-time which can persist into off-time as a high system transient, overpowering the weaker secondary field. This problem is overcome using a bucking coil to reduce the primary field amplitude by over four orders of magnitude at the Z-axis receiver coil (Walker et al., 2008). The VTEM system has a 3 m radius bucking coil located in the center of the transmitter loop and around the receiver Z coil to reduce the primary field strength.

To remove the primary field, first the response of the bucking-coil is subtracted from receiver coil Z response and then a post-processing algorithm including a deconvolution of the system's current waveform reduces further the primary field signal.

In addition, every system selected a specific waveform at one or more base frequencies, which, as studied by many authors (Smith 1998, Lui 1998, Stolz and Macnae, 1998), have an important role on the intensity of the induced EM response. Each transmitter waveform meets precise objectives and strategies: in general a fast transmitter current shut-off is used when near surface resistivity mapping is needed, generating early off-time responses in weakly conductive zones, while a long shut off transmitter current, penetrating deeper, induces secondary currents in good conductors.

Another important characteristic of the HTEM systems is the dipole moment. Over the years, this has been the main factor of development of the HTEM systems. The increasing in loop sizes, number of loop turns and transmitter current resulted in a spectacular mutation of the systems. However, the necessity of smaller and less heavy equipment, compared to fixed-wing systems, will set a limit to transmitter power and, as a consequence, a limit on depth penetration. The useful dipole moment with the transmitter current shut

off depend on the survey objective: for example, if the purpose of the survey is to map the near surface conductivity, then a lower dipole moment with a faster turn off current is more suitable.

One of the most important limitations of the AEM system is related to the difficulty of obtaining unbiased early-time data, where the bias is the self-response of the system, which is usually measured by flying the system at very high altitudes where the response of the ground is negligible. This can prevent a correct primary field removal and a precise definition of the time shift between the Tx and Rx system (timing) (Macnae and Baron-Hay, 2010).

Another problem is related to the definition of the absolute time-zero of the systems (Christiansen et al., 2011). It must be considered that an instantaneously shutting down of a current in a loop is highly problematic, because a plethora of self-inductance, back currents and other phenomena occur, with the result that the current is effectively not off. However, fortunately, most modern systems are able to accurately measure the turn-off time even for each recorded sounding.

In the last decade, the success of the HTEM systems has been driven by several advantages associated with these systems, as the excellent horizontal accuracy (especially with the coincident transmitter-receiver configuration), good near surface resolution (in large part due to wide high frequency contents), cost-effective implementation and significant depth of exploration. This opened the possibility of using such systems in a wide range of applications, as mining exploration, groundwater mapping and environmental problems. In their evolutionary process, the HTEM systems have evolved to meet the need to deal with the discovery of those targets that previous systems failed to detect because they were too deep, too conductive or had complex geometry.

## **1.4 Types of noise in TEM data**

The quality of AEM data can be compromised by a variety of noise sources from both inside and outside the system.

The sources of noise related to the system include the coil motion and the secondary response of the system. The receiver coil movement in the earth's magnetic field produces a large amplitude, low frequency and parasitic signal

(Annan, 1983). This can be easily removed by high-pass filtering. However, rapid oscillations of the receiver coil can add some noise at higher frequency, very difficult to filter out and this explains why a mechanically stable receiver coil mounting is necessary during data acquisition. Another source of noise is due to the response of the system. In the HTEM systems, the transmitter and the receiver are far enough from the helicopter, so these effects can be considered weak and constant. However, the standard compensation procedure consists in measuring the system response at high altitude, before and after each flight, and deconvolving these responses from the measured off-time response (Allard, 2007).

The noise affecting the measured signal, and not related to the system, can be produced by natural sources or derived from cultural sources. The natural noise presents several peaks in the EM noise spectrum. The natural noise at frequency below 1 Hz derives from fluctuations in the Earth's magnetic field. This noise, because of its low frequency, does not influence the transient measurements. On the contrary, the noise at frequency higher than 1 Hz can compromise the TEM data quality. This type of noise originates from flashes of lightning from thunderstorms. This noise has a random character and it varies during the day, being less powerful during the night than during the day, and during the year, being stronger during the summer compared to winter. The amplitudes are generally 5 to 10 times greater than the vertical field, and when numerous spherical events are present, it is difficult to filter them out because their amplitude and time distribution are essentially random.

A complete discussion on the minimization and process techniques of noise for TEM systems can be found in Macnae et al. (1984), McCracken et al. (1986), Spies and Frischknecht (1991), Effersø et al. (1999), and Nyboe and Sørensen (2012).

The most intuitive way to improve the signal quality, considering the random nature of the noise, is a stacking procedure.

The stacking may concern a single transient with the definition of time windows or the stacking of many transients at the same position. Considering the stack in time windows, a small number of stacks allows for a good near surface resolution, but low signal to noise at late times. On the contrary, a large number of stacks reduces the resolution at early times, but increase the

signal to noise at late times. A correct trade-off between these two aspects must be considered when collecting the data. Usually, the followed approach provides the measurement of the secondary field using time windows with a logarithmical increase of their width in time. This is the classical log-gating approach (Munkholm and Auken, 1996). Even using the log-gating configuration a single transient can be affected significantly by noise. By repeating the measurement at the same position the noise is decreased and the signal is enhanced. Assuming that the noise has a Gaussian distribution and using a log-gating configuration the S/N ratio is proportional to  $\sqrt{N}$  where  $N$  is the number of measurement in the stack. This means that the log-gating strategy has the effect of increasing the stack size for progressively later time gates and thus reducing the standard deviation of the noise through time by a factor of the square root of the gate length. The ground surveys have a definite advantage on the AEM systems coming from the stacking of measurements at fixed position for a long time. The AEM systems, being moving systems, derive less benefit from this procedure. However, the lesser flight speed of the HTEM systems, compared with the fixed wing systems, allows to collect and to stack 2 to 3 times more data per km.

Regarding the noise produced by cultural sources, it assumes greater importance in the populated areas. It must be considered the noise originating from the supply of electricity and the related electrical installations, resulting in spectral peaks at 50 and 60 Hz and the relative odd harmonics. In addition, all the electromagnetic fields from communication equipment act as source of noise. The most important cultural noise affecting a measured signal is the so-called coupling noise. It is due to the induced currents in the man-made electrical conductors as buried pipelines, cables, fences, power lines, road networks, and others features included in the volume where the primary field propagates (Nekut and Eaton, 1990). The secondary field arising from these currents is superimposed to the ground response. Obviously, this disturbance cannot be reduced by stacking. The data affected by coupling effects should be removed in order to get reliable interpretations. To minimize these effects the distance of the transmitter-receiver system from the man-made conductors should be more than 100 m.

Sørensen et al. (2000), and later Danielsen et al., (2003), differentiate two types of coupling: galvanic and capacitive. The capacitive coupling is easily recognized also in a single EM transient for its oscillating character, while the galvanic coupling, involving a simple shift of the EM transient can be more difficult to identify when considering a single transient. The only way to identify and then remove the data affected by coupling and at same time have enough data for meaningful interpretation is related to a sampling that is spatially dense. This is certainly achieved by the AEM systems.

## **1.5 Geophysical data inversion**

The method of predicting data for given sources with some physical properties is referred to the forward problem solution. Knowledge of the subsoil properties by the observed data acquired on earth's surface is a typical case of the inverse problem's geophysical applications. A typical inverse problem solution consists in using the data to reconstruct the internal structure of the earth. Inversion of geophysical data is complicated by the fact that data are usually contaminated by noise and are acquired at a limited number of observation points. At same time, the mathematical relations between data and model parameters are usually complicated and in most cases some simplifications of the geophysical phenomena are considered in the inversion processes (for example, representing 3D ground with 1D or 2D approximations). All these features represent a source of error and lead to solutions that are ambiguous.

Moreover, all geophysical inverse problems are ill-posed, that means that the solution is not unique or it is not a continuous function of the data, in other words, small variations of the data correspond to large perturbation of the solution. When the solution is not unique, equivalence problems can exist. For a finite number of data, there are, in many cases, infinite models that have a predicted response that is in agreement with the measured data. The most important way to obtain reasonable results from the inversion process of ill-posed problems deals with the application of different types of regularization algorithms, allowing an automatic selection of the useful solutions using a-priori information (Tikhonov and Arsenin, 1977). A-priori information can be introduced from geological constraints, from the interpretation of the inversion

of other geophysical surveys, from drill logs or from a mathematical statement of complete ignorance, such as the model smoothness (Ellis, 1998).

Many techniques have been developed to solve linear, linearized and non-linear inverse problems and include different approaches such as least-square, conjugate-gradient and others. The underlying theory of the inverse problem is well described in the geophysical literature from several authors: Jackson (1972 and 1979), Tarantola and Valette (1982), Menke (1984), Tarantola (1987 and 2005), Constable et al., (1987), Meju (1994a and 1994b), Parker (1994), Newman and Alumbaugh (1997), Scales et al. (2001), Zhdanov (2002), Aster et al. (2005).

### 1.5.1 Least squares solution for linear and non-linear inverse problems

The simplest and best-understood inverse problems are those that can be represented with the integral linear equation:

$$\int_V f(m) dv \approx \sum_{j=1}^M f(m_j) = d \quad (1.15)$$

where  $f(m)$  is the functional relating model parameters ( $m$ ) to model response ( $d$ ) over the volume  $V$ .

The corresponding matrix equation is:

$$Am = d \quad (1.16)$$

where  $\mathbf{A}$  is the forward modeling operator, incorporating the physical equations and the details of survey design, relating the vector of measurement  $\mathbf{d}$  and the vector of the model parameters  $\mathbf{m}$ .

When the number of the data ( $N$ ) is greater than the number of model parameters ( $M$ ) the problem in equation 1.16 is called overdetermined problem.

The simplest of methods for solving this kind of problem is based on measures of the size, or length, of the estimated model parameters  $\mathbf{m}_{est}$  and of the predicted data  $\mathbf{d}_{PR} = \mathbf{A}\mathbf{m}_{est}$ .

One of the most common measures of length is the least squares method.

For each observation one defines a prediction error, or misfit,  $\mathbf{e}_i = \mathbf{d}_i^{obs} - \mathbf{d}_i^{pre}$ .

The least square solution is then the one with model parameters that leads to the smallest overall error  $\mathbf{E}$ , defined as:

$$E = (d - Am_{est})^T(d - Am_{est}) = e^T e = \sum_{i=1}^N e_i^2 \quad (1.17)$$

The total error  $\mathbf{E}$  (the sum of the squares of the individual errors) is exactly the squared Euclidean length of the vector  $\mathbf{e}$ .

Extending the least squares to general linear inverse problem we obtain the least square solution of the problem 1.16 (Menke, 1984):

$$m = [A^T A]^{-1} A^T d \quad (1.18)$$

where  $[A^T A]^{-1} A^T$  is the known generalized inverse matrix operator, which apply to the data vector to recover the vector of parameters.

In EM methods, the relation between the data and the model parameters is non-linear. In this case, the problem 1.16 is still valid if a conversion to a linear approximation is found. The usual way is to expand the model response by Taylor's series, around a starting initial model ( $\mathbf{m}_0$ ), approximating the expansion by the first term:

$$f(m) = f(m_0) + \left( \sum_{j=1}^M \frac{\partial f_i(m)}{\partial m_j} \Big|_{m=m_0} \delta m_j \right) \quad (1.19)$$

The true model has to be sufficiently close to the starting model for the linear approximation to be good that means  $\delta m_j$  must be small for all  $j$  indexes. The summation in equation 1.19, that contains all the partial derivatives of the data against the parameters, is called Jacobian ( $\mathbf{G}$ ).

The problem 1.15 is expressed by:

$$d = [f(m_0) + G\delta m] \rightarrow \delta d = G\delta m \quad (1.20)$$

Again, by least square method, a similar expression to equation 1.18 is found:

$$\delta m = (G^T G)^{-1} G^T \delta d \quad (1.21)$$

$\delta m$  represent the small change of the  $\mathbf{m}$  parameters of the starting model to get a better fit between the observed and the predicted data:

$$m_1 = m_0 + \delta m \quad (1.22)$$

If the new model  $\mathbf{m}_1$  is still far from the "true model", i.e., if the model response does not fit to a certain degree the observed data, the process is repeated, but now taking  $\mathbf{m}_1$  as the new starting model. These operations are repeated iteratively until a reasonable solution with a good fit is found. The iterative process scheme is given by the next expression:

$$m_{k+1} = m_k + (G^T G)^{-1} G^T \delta d \quad (1.23)$$

and to each iterative step a new Jacobian matrix  $\mathbf{G}$  must be calculated. New model is always found from previous one. This iterative method is known as Gauss-Newton method (Menke, 1984).

The method is simple and powerful, but can be tricky, producing solutions with no physical meaning when the  $\mathbf{G}^T\mathbf{G}$  matrix is singular (or almost singular) that is, when its eigenvalues are near zero. When the  $\mathbf{G}^T\mathbf{G}$  matrix is not singular, very slow convergence can take place or even diverging situations, due to a wrong chosen starting model. To overcome this problem, a priori information can be incorporated to define a better starting model.

### **1.5.2 Inversion of AEM data**

The inversion of AEM data refers to a mathematical methodology that consists in estimating a conductivity model from the EM measured data. However, it must be considered that the EM response is also sensitive to other properties of the earth, as the magnetic susceptibility, the dielectric permittivity and the chargeability.

The main purpose of an inverse problem solved following a deterministic approach consists in the minimization of an objective function (in a process of a global optimization). The model that is solution of the inverse problem should minimize the model objective function and also has a predicted response in satisfactory agreement with the measured data (within the noise level).

As for all the inverse problems, also the AEM inversion problem is an ill-posed problem. In order to obtain a unique and stable solution, a procedure of regularization, by using a-priori information, is necessary. Another difficulty in the EM inversion is the non-linear relation between the observed data and the geoelectric properties of the geological structures. This makes the inversion problem non-linear and the solution is usually obtained by a numerically-intensive iterative method.

At the same time, the calculation of the forward response, that plays an important role in the inversion process, is itself difficult and very time consuming for 2.5D or 3D models. Moreover, it must be considered that an AEM survey may contain a great amount of data collected on tens of

thousands of line kilometers of multi-channel data sampled every tens of meters, which can be very time consuming to process and invert.

All these issues, joint with the limitation of the computer technology, help to explain why the inversion of the AEM data, in the last decades, was performed assumed 1D earth models.

The increase of the computer power and the fact that the geological structures cannot always be approximated by a 1D model, have brought to more realistic inversions, turning the interest to higher dimensional models and to improvements of the existing 1D inversion algorithms.

Various 3D modeling algorithms have been proposed (Aarnason, 1995; Best et al., 1995; Sugeng, 1998; Zhdanov and Tartaras, 2002; Zhang, 2003). However, the routine use of full 3D modeling and inversion methods has yet to be realized. The problem with this type of inversion is related to the necessity to solve large systems of equations for all the transmitter positions and for all the points in the subsurface. This require a huge computation power that is, despite the technological advancements, still very time consuming. Recent developments have focused on fine-tuning of fast 2D or 3D inversion schemes (Cox et al., 2010; Guillemoteau et al., 2012). However, in contexts where the 3D lateral variations are gradual and the conductivity contrasts are not so strong, it was sometimes shown that the differences in the inverse models obtained by 3D and 1D inversion are not so obvious (Viezzoli et al., 2010).

For all these reasons, a lot of emphasis has been placed on improving 1D methods over the development of 3D inversion.

In some cases, the resulting 1D models are stitched together (Macnae and Lamontagne, 1987; Auken et al., 2003; Huang and Fraser, 2003), involving abrupt variations in neighboring models for the presence of inherently noisy data and model equivalence. This approach can lead to results that are not useful for sedimentary environments where the lateral variations are expected to be smooth. In these situations, a gradual lateral variation can be achieved by using lateral constraints on model parameters of adjacent soundings during the inversion process (Newman et al., 1987, Sengpiel and Siemon 2000, Auken et al. 2005). Normally, AEM inversion codes based on 1D forward modeling apply lateral/spatial constraints to regularize the inversions so as to achieve solutions compliant with the predicted geological variations (Vallée

and Smith 2009, Christensen and Tølbøll 2009, Brodie 2010, Auken et al., 2014, Kirkegaard and Auken 2015).

Laterally Constrained Inversion (LCI, Auken and Christiansen 2004) and Spatially Constrained Inversion (SCI, Viezzoli et al., 2008) are based on this approach. These algorithms are able to produce quasi-2D and quasi-3D images of the subsurface using a 1D forward solution and their use is justified where lateral changes in conductivity are gradual.

This type of algorithms normally offer support for two modeling approaches: “layered/discrete models or the L1 norm optimization method” inversions, which invert for a limited number of layers with variable layer boundaries; or “smooth models or the L2 norm based least-squares optimization method” inversions, which are based on a large number of stacked layers in a fixed vertical discretization.

The smooth approach produces sections with formation boundaries smeared out by regularization. Vertical constraints are applied in the smooth models to generally stabilize the inversion (Constable et al., 1987).

Smooth models are discretized with a number of layers up to 30, with a maximum depth that is consistent with the penetration capability of the system. The thickness of the layers increases logarithmically with depth, starting from few meters thickness for the shallower layer.

One of the advantages of smooth inversions is the greater independence from the starting model. The gradual resistivity transitions allow defining more accurately complex geological structures.

In the layered or “blocky” approach, the inversion can operate without additional regularization, due to the much smaller number of free model parameters.

The blocky inversions are used to determine layer interfaces, resistivity, and depth of penetration. Blocky models consist of small number of layers, representative of the existing geological context, with lateral and vertical constraints applied for resistivity and layer thickness.

In this approach, the inversion is more sensitive to the specific choice of the starting model and it can introduce artifacts if the geology is particularly complex.

In environments with pronounced 3D model characteristics, 1D inversion is strongly influenced by 3D effects and will in many cases provide unreliable models with artifacts known as “pantlegs” (Christiansen et al., 2009).

Goldman and Stoyer (1983) showed that the resistivity of a buried axially symmetrical body is significantly overestimated while its depth and thickness are obtained fairly accurately using 1D inversion.

The effect of 3D structures on 1D interpretation of TEM data has been dealt with in a number of papers, e.g., Auken (1995), Hördt and Scholl (2004), Newman et al. (1987) and Goldman et al. (1994).

### 1.5.3 Laterally Constrained Inversion (LCI)

This inversion algorithm is described in detail in Auken and Christiansen (2004). It allows performing the inversion of large data set, where the parameters of the earth model (resistivity and thickness or depth of the electro-layers) for each sounding are connected laterally by means of lateral constraints, defining a specified variance of the model parameters. The lateral constraints can be considered as a-priori information on the geological variability in the area of measurements. In LCI, the connection of the soundings occurs along a profile, producing quasi-2D images of the subsurface with smooth lateral transitions. The constraints allow the migration of information from one model to neighboring models, helping to resolve areas with poorly constrained parameters or soundings particularly noisy. The strength of the constraints controls the allowed variation in the adjacent soundings. Roughly speaking, a constraint value of 1.1 means that the model parameters are allowed to vary up to the 10% between neighboring models (figure 1.1).

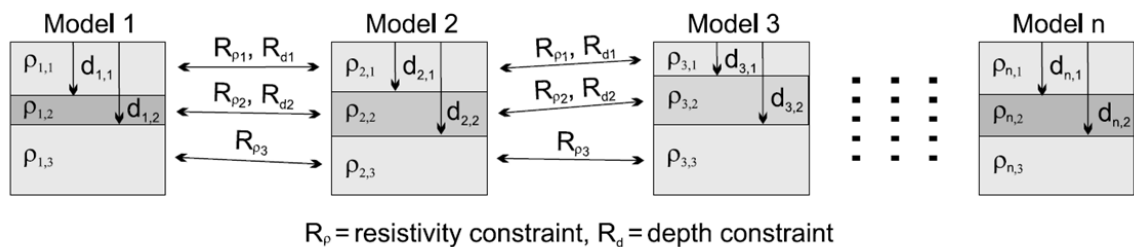


Figure 1.1: Model parameters with vertical and lateral constraints (adapted from Auken and Christiansen, 2004).

The LCI is a full non-linear damped least squares inversion based on an exact forward solution, modeling the instrumentation's system transfer function (STF). The solutions developed by Ward and Hohmann (1988) are used as the basis for the forward modeling algorithm. Modeling the STF also includes the low-pass filters (Effersø et al., 1999), and turn-on/turn-off ramps (Fitterman and Anderson, 1987).

The dependence of apparent resistivity on subsurface parameters is in general described as a non-linear differentiable forward mapping. The linearization of the problem is established by the approximation with the first term of the Taylor expansion:

$$d_{obs} + e_{obs} \cong G(m_{true} - m_{ref}) + g(m_{ref}) \quad (1.24)$$

where  $\mathbf{d}_{obs}$  denotes the observed data,  $\mathbf{e}_{obs}$  is the error on the observed data and  $\mathbf{g}$  is the non-linear mapping of the model to the data space. The true model,  $\mathbf{m}_{true}$  has to be sufficiently close to some arbitrary reference model,  $\mathbf{m}_{ref}$ , for the linear approximation to be valid.  $\mathbf{G}$  is the Jacobian and contains all partial derivatives of the mapping. The covariance matrix for the observation errors is  $\mathbf{C}_{obs}$ , which we assume to be a diagonal matrix. In short, equation 1.24 is expressed by:

$$G\delta m_{true} = \delta d_{obs} + e_{obs} \quad (1.25)$$

The constraints are connected to the true model as:

$$R\delta m_{true} = \delta r + e_r \quad (1.26)$$

where  $\mathbf{e}_r$  is the error on the constraints with 0 as expected value and  $\mathbf{R}$  is the roughening matrix, containing 1's and -1's for the constrained parameters, and 0 in all other places. The variance, or strength of the constraints, is described in the covariance matrix  $\mathbf{C}_R$ .

Combining equations 1.25 and 1.26, the inversion problem can be written:

$$\begin{bmatrix} \mathbf{G} \\ \mathbf{R} \end{bmatrix} \delta m_{true} = \begin{bmatrix} \delta d_{obs} \\ \delta r \end{bmatrix} + \begin{bmatrix} e_{obs} \\ e_r \end{bmatrix} \quad (1.27)$$

The covariance matrix for the joint observation error becomes:

$$C' = \begin{bmatrix} \mathbf{C}_{obs} & 0 \\ 0 & \mathbf{C}_R \end{bmatrix} \quad (1.28)$$

if any a-priori information on model parameters, allowing to reduce the ambiguity on the inverse models, are available, they can be added, following Jackson (1979), as an extra row ( $\mathbf{m}_{prior}$ ) to the system 1.27 and the a-priori model variance ( $\mathbf{C}_{prior}$ ) is described in covariance matrix.

In a compact form, the equation 1.25 is rewritten as:

$$G'\delta m_{\text{true}} = \delta d' + e' \quad (1.29)$$

the model estimate is (Menke, 1984):

$$\delta m_{\text{est}} = (G'^T C'^{-1} G')^{-1} G'^T C'^{-1} \delta d' \quad (1.30)$$

that minimizes the objective function:

$$Q = \left( \frac{1}{N + A} [\delta d'^T C'^{-1} \delta d'] \right)^{\frac{1}{2}} \quad (1.31)$$

The algorithm inverts all the soundings simultaneously, considering all the data and the lateral constraints. A common objective function is thus minimized. The output model, including all the 1D soundings, is balanced between the constraints, the physics and the data.

#### 1.5.4 Spatially Constrained Inversion (SCI)

In LCI algorithm, the connections between the soundings are established along the flight lines, providing inverse models that are profile oriented. The spatial maps produced, following this approach, result in some lineation in the direction of flight. Between the soundings of two adjacent lines no connections is created. This involves that any features perpendicular to the flight lines benefits only partially from inline constraints as no information on model parameters is passed line to line. Spatially Constrained Inversion, or SCI, described in Viezzoli et al., (2008), overcomes these limitations, extending the idea of constraints not only along the lines, but also across the lines. SCI is similar the quasi-3D layered inversion methodology proposed by Brodie and Sambridge (2006), with their algorithm specially designed for helicopter survey electromagnetic TEM data and allowing for the inversion of large data sets.

The mathematical formulation of SCI algorithm is similar to LCI. It consists in a least-squares inversion of 1D earth, regularized with spatial constraints, producing smooth lateral transitions. The forward 1D calculation is based on the solutions of Ward and Hohmann (1988). The system geometry is accurately modeled including frame geometry, frame position (altitude, angle), accurate shape of the transmitted current waveform, timing, bandwidths of the receiver system and low-pass filter.

The main difference between SCI and LCI is in the elements of the **R** matrix. In LCI case, this matrix contains only 1's and -1's for the constrained parameters of adjacent soundings along the lines. In SCI case, each sounding is connected to more than one sounding along and across the lines. Each row of the R matrix, related to an individual sounding, contains many -1's as the number of connections for this sounding, while its entry in the **R** matrix is the absolute value summation of all the -1's. This structure of **R** matrix ensures the connection between the soundings. The connection between the soundings is the first step in SCI algorithm and it is performed through the Delaunay triangulation (Aurenhammer, 1991). There are number of different algorithms for calculating the Delaunay triangulation, SCI uses the Quickhull algorithm described in Barber et al. (1996). The number of connections to each sounding depends on the data density and distribution, so there are small and numerous connections in high-density areas while in low-density area, they are large and few. The constraints are set between the soundings connected by Delaunay triangles. This ensures a continuum interconnection between the soundings and allows the migration of the information in the model space.

### **1.5.5 Depth of investigation for 1D (EM-DC) model**

For the diffusive method, such as Airborne EM, there is no specific depth limit for information on the resistivity structures of the ground.

It is thus of great importance to establish to what depth the model can be considered reliable. Any method for the determination of the depth of investigation (DOI) needs to assign a depth limit for the information. In most cases this value is relative and might be, for example, 5% of total sensitivity, being the sensitivity defined by the Jacobian matrix.

The simplest formula to calculate DOI is based on the diffusion depth of a planar wave in a full-space with conductivity  $\sigma$ . In this case, the diffusion depth, for time domain method, is related to the time  $t$  of last gate and to the conductivity (Ward and Hohmann, 1988). Various other approaches for calculating DOI have been developed over the years. Some methods are based on empirical formulas or tables based on model studies or thin sheet calculations (Banerjee and Pal, 1986; Huang, 2005; Szalai et al., 2009). These methods are fast and simple, but their limitations reside in the assumptions on

which are formulated: they don't consider the system geometry, the noise on the data, the actual number of data points, and the model is usually a half-space.

Christiansen and Auken (2012) proposed a method, valid for any 1D EM and DC geophysical models, based on a recalculated Jacobian matrix of the final 1D model. The Jacobian is used to calculate the cumulated sensitivity from which the DOI can be deduced, by defining an absolute global threshold value that indicates the minimum amount of sensitivity needed for indicative information. It resembles the approach of Oldenburg and Li (1999) in the use of the full system transfer function and system geometry, the entire data set, and the data noise handling. Contrarily to their approach, the constraints are not included in the DOI calculation; only the portion of the Jacobian regarding observed data is included in the DOI calculations. The obtained value is a measure of the capability of the measured data, with their associated errors, to resolve the model, without considering the model parts defined by constraints and a-priori information.

## **1.6 Optimized sampling of AEM transients**

In my work, I have investigated the Airborne TEM gating schemes. Basically the idea is that it might be advantageous to change the transients' gating across the survey, depending on different issues that affect the signal. This would be possible for those AEM systems with digital receivers recording the full decay at high sampling rate.

The material presented in this section was included in a recently published scientific paper (Di Massa et al., 2016).

Focusing on the binning of the streamed transients, I demonstrated, using synthetic models, how different sampling schemes can influence the results of the inversion. My new sampling method consists in adapting the gating on the base of the slope variations in the EM transient sampled at the highest possible frequency. As the EM transient decay depends on the distribution of the conductivity at depth in the sensitive area (footprint), there are some time intervals in the EM transient that contain more information on the subsurface structures. My idea has been to extract this information from measured data with an optimized sampling, in order to get more accurate inverse models.

On a related note, another reason for not applying the same log-gating throughout a given AEM survey is given by the fact that the overall S/N ratio might, and usually does, vary across the survey area. Reasons vary from the presence of noisier background areas (natural or man-made activities) to varying geology (varying secondary signal), to varying AEM system altitude (e.g., higher flying height due to forested areas). It would be worth considering customized gating for each one of these areas, based on the local S/N conditions, with the aim of using best the gates. For example, in places where the signal drops into noise early in the transient, it would be beneficial to move most of the gates above the noise level (albeit narrowing them).

Time-domain airborne electromagnetic data are regularly acquired over wide areas for various applications such as groundwater, environmental and mining exploration (e.g. Fitterman, 1987; Auken et al., 2003; Reid and Viezzoli, 2007; Viezzoli et al., 2010; Podgorsky et al., 2013). The modeling of these data is often aimed at obtaining a quantitative estimate of the 3D spatial distribution of the conductivity of the earth, through an inversion process. The obtained model may be used for further geological or hydrogeological interpretations.

The EM secondary field is measured as a function of time using an induction coil. Its decay is measured as average response over time windows of finite width (gates).

The width of the gates is a crucial factor in the acquisition of electromagnetic data. In fact, it controls two signal features strongly influencing the inversion results: the data signal to noise (S/N) ratio and the capacity of resolving the structure in the subsurface (resolution).

In general, the S/N ratio increases with the gates width in contrast the resolution capability is better for smaller gates that provide more details on specific parts of EM decay and will be necessarily noisier than larger gates (Nabighian and Macnae, 1991). A correct sampling must take into account the trade-off between these two components.

The "gating", i.e., the sampling in time of the secondary field, is often chosen following a standard approach, using the same number of gates per time decade with a logarithmic increase of the width with time in order to improve S/N ratio (log-gating) (Munkholm and Auken, 1996).

The log-gating has two main benefits: improving the S/N ratio at late times, when the electromagnetic signal has amplitudes equal or lower than the natural background noise, and at same time ensuring a good resolution at the early times.

Nowadays, thanks to technological advancements and recent developments in mass storage capacity, new airborne systems are able, to measure and record the secondary field at high sampling rate, yielding a virtually continuous stream of data. As the processing of small width gates, affected significantly by noise, can be difficult and the inversion of large amount of gates is very time consuming, an average of measurements (binning) over windows of finite width is necessary.

Customers will commonly only see the processed data after filtering, binning and stacking of the full stream data which is normally done in real time.

Having recorded the fully streamed data, data can be reprocessed post flight to improve spherics and power line noise rejection that are often only smoothed out in the standard processing phase. At same time it is possible to define different gating schemes in the binning phase, adapting the gates width across the transient. This means that, instead of defining a priori the type of gating (such as log-gating) and the characteristics of the gating of the different channels (center times, width), it may be advantageous to define a-priori only the maximum number of channels to use, and place them adaptively across the transient.

As shown in the equation 1.13 in Section 1.2.1, the time variation of the secondary magnetic field, measured as  $db/dt$  at an induction receiver coil, exhibits, at late times, a decay proportional to  $t^{-5/2}$  in a log-log plot for a homogeneous half-space (Christiansen et al., 2009).

$$\frac{\partial b_z}{\partial t} \approx \left(\frac{M}{20}\right) \left(\frac{\sigma}{\pi}\right)^{\frac{3}{2}} \left(\frac{\mu_0}{t}\right)^{\frac{5}{2}} \quad (1.13)$$

where  $M$  is the magnetic moment of the transmitter ( $\text{Am}^2$ ),  $\sigma$  is the conductivity (S/m) and  $\mu_0$  is the magnetic permeability of the free-space (H/m).

At the interface of two layers with different conductivity, the value of the secondary field changes according to the variation of the conductivity as shown in equation 1.13. This means that for a horizontally layered model, the

transient decay,  $\partial b_z/\partial t$ , shows a slope variation in correspondence of the transition between two layers with different conductivity.

Figure 1.2 (from Christiansen et al., 2009) shows the EM transient for a homogeneous half-space with varying resistivities. The response of a two-layers earth having a resistivity of 100  $\Omega\text{m}$  in layer 1 and 10  $\Omega\text{m}$  in layer 2, and with the thickness of layer 1 of 40 m, is also shown.

The slope variations are related to the conductivity contrast between two electro-layers.

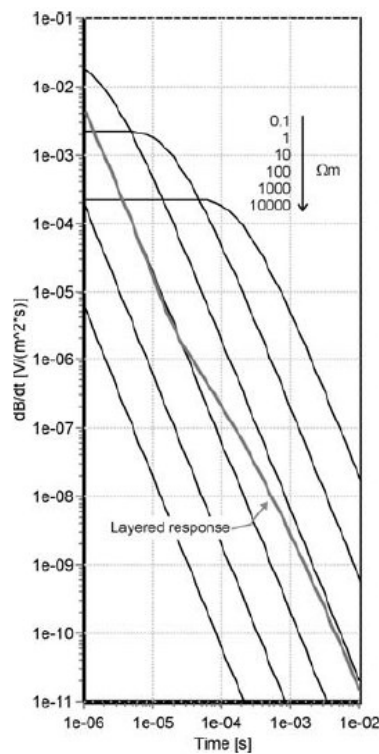


Figure 1.2: Transient responses for a homogeneous half-space with varying resistivities and for a layered half-space (adapted from Christiansen et al., 2009).

The conductivity controls also the diffusion speed of the current in the ground:

$$v = 2(\pi\sigma\mu t)^{-1/2} \quad (1.32)$$

where  $\sigma$  and  $\mu$  are the conductivity (S/m) and the relative magnetic permeability (H/m) of the medium and  $t$  is the time (s).

The diffusion speed decreases when going through conductive layers. Equations 1.13 and 1.32 explain why the TDEM method is highly sensitive to conductivity layers (Telford et al., 1990).

The analysis of noise-free data produced by simple two-layer models and calculated from the solution of 1D forward model (Ward and Hohmann, 1988)

shows that the transition from a conductive layer to a resistive one corresponds to a minimum in the second time derivative of the transient. On the contrary, the transition from a resistive layer to a conductive one shows a maximum of curvature. In figure 1.3a the EM transient (blue curve) and the curvature (green curve) for two-layer earth with  $50 \Omega\text{m}$  in layer 1 and  $10 \Omega\text{m}$  in layer 2, with the thickness of layer 1 of 50 m, are shown. In figure 1.3b, I plotted the same quantities when the conductive layer is the shallowest.

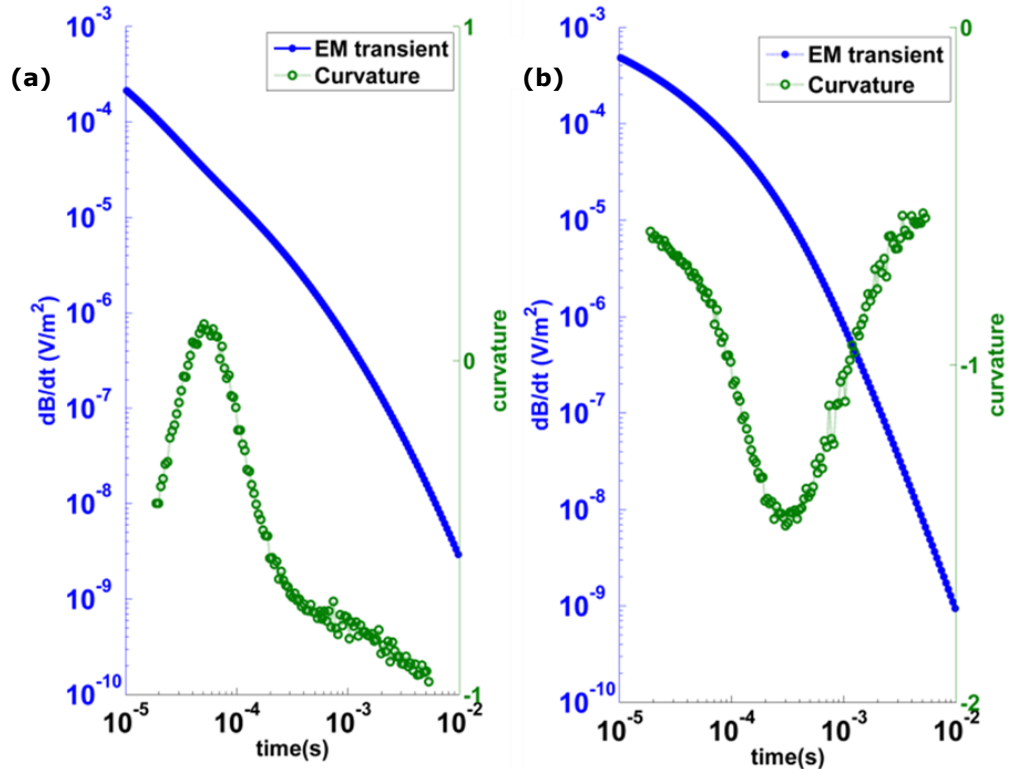


Figure 1.3: EM transient (blue curve) and its curvature (green curve) for two-layers model earth with a resistive layer of  $50 \Omega\text{m}$  and a conductive one of  $10 \Omega\text{m}$ , the thickness of shallowest layer being 50 m. (a) The resistive layer is the shallowest. (b) The conductive is the shallowest.

It is clear that in order to obtain correct models a good sampling of the EM transient is needed. I demonstrate the previous statement by illustrating how changes the inversion result when EM transient is undersampled in various ways (figure 1.4). In these tests, I used noise-free data, calculated from the solution of the 1D forward problem (Ward and Hohmann, 1988) for a four layer model. I used 21 gates in log-gating configuration and inverted the data using AarhusInv inversion code that offers support for a layered model inversion, inverting for a limited number of layers (Kirkegaard and Auken, 2015), removing a group of three adjacent gates. The starting model is a

layered half-space with a resistivity of 90  $\Omega\text{m}$ . Being noise-free data, the inversion should (or rather could, depending on the sampling scheme) recover a useful model.

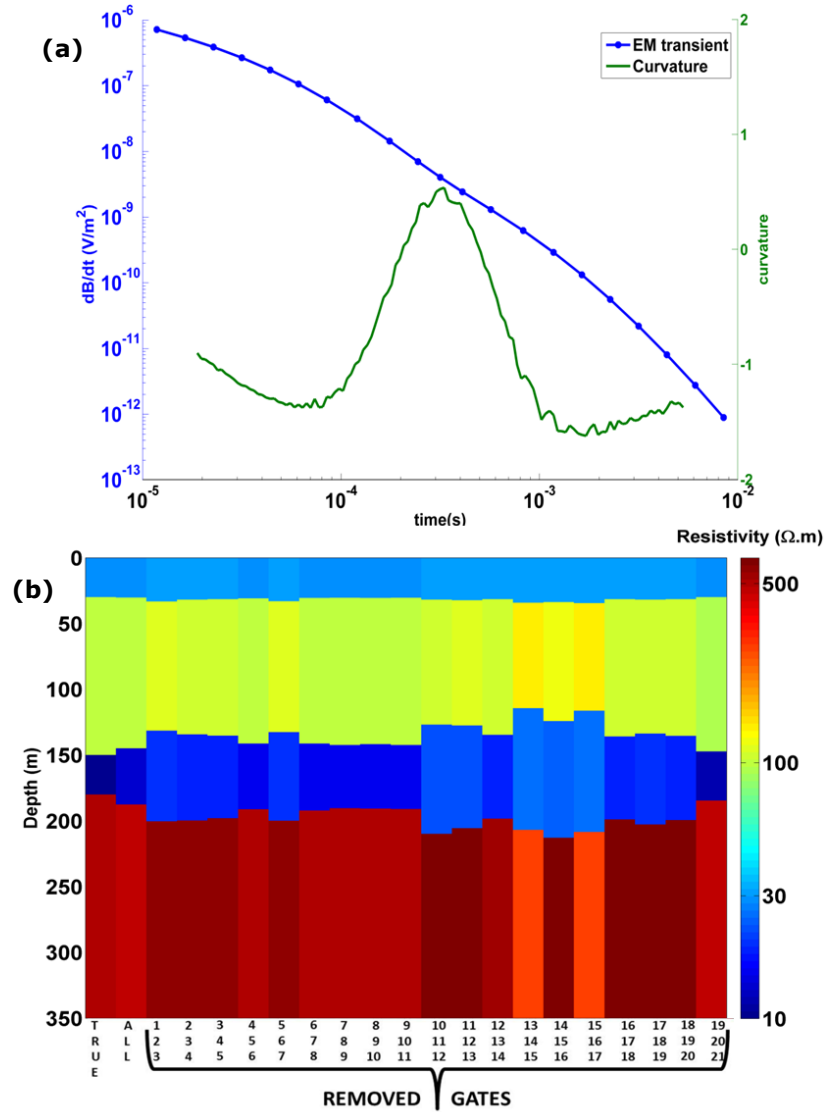


Figure 1.4: (a) The EM transient (blue curve) sampled with 21 gates in log-gating configuration and its curvature (green curve). (b) The inverse models, obtained by removing different groups of three adjacent gates, are compared with the true model ("TRUE" column) and with that obtained using all the available gates ("ALL" column).

The analysis of the results illustrated in figure 1.4 shows that removing the information carried by even a small number of data (gates) causes a loss of resolution, with inaccuracies on both conductivity and thickness in the computed inverse models. However, the worst models are obtained when the removed gates are in correspondence with the maxima and the minima of curvature that, as shown in figure 1.3, mark the transition between two

layers. In fact, from the curvature of the EM transient in figure 1.4a, I note the presence of two minima in the first and the third decade and one maximum in the second decade. Undersampling the transient in correspondence of the minimum of the first decade does not affect the inversion results more than removing other gates of this decade. However, by removing the gates that are in correspondence with the maximum and the minimum of curvature in the second and third decade (from 11th to 17th), the recovered models are less accurate in the definition of the thickness and resistivity of the electro-layers. This confirms that there are some time-intervals in the EM transient decay that contain more information on the structures in the subsurface.

Basing on this study, I proposed a new approach to sample the EM transient that I call "adaptive-gating".

My method simply consists in a more detailed sampling of the time intervals at which the electromagnetic response shows the greater sensitivity to the changes of resistivity of the subsurface. The second derivative of the EM transient is the base for my adaptive-gating.

I extensively tested my adaptive-gating procedure for the maxima and for the minima of curvature arising from four-layer models. I noticed that the most correct inversion results are those obtained adapting the gating only for maxima of curvature.

This is hardly surprising, as it is in this case that the EM methods have most resolution power, as opposed to a transition towards higher resistivities. I conclude that the crucial parts of the transient that require customized gating are those in correspondence to the maxima of curvature, which marks the transition from a resistive layer to a conductive one. According to this strategy, the gate-width at the maximum of curvature is reduced, while I progressively increase the widths of the gates at the sides of the identified maximum.

This scheme should guarantee a better resolution for the most informative part of the signal that, according to the velocity propagation and the density of the currents, is in correspondence of the conductive layers.

To demonstrate the benefits of such a sampling scheme of the EM transient, I present now a series of tests on synthetic data where I compare the inversion

models obtained with the “classical” log-gating and my adaptive-gating approaches.

To perform these tests, I have:

- simulated a continuous acquisition of the EM transient decay. The parameters of the electromagnetic airborne system are listed in table 1.1;

|                        |  |
|------------------------|--|
| <i>Secondary field</i> | <i>dB/dt (V/m<sup>2</sup>), vertical component Z</i> |
| <i>Flying height</i>   | <i>30 m</i>  |
| <i>Magnetic moment</i> | <i>160000 Am<sup>2</sup></i>                         |
| <i>On-time</i>         | <i>7000 μs, trapezoidal waveform</i>                 |
| <i>Off-time</i>        | <i>13000 μs</i>                                      |
| <i>Ramp-on</i>         | <i>4000 μs</i>                                       |
| <i>Ramp-off</i>        | <i>100 μs</i>  |
| <i>Low pass filter</i> | <i>100 kHz</i>                                       |

Table 1.1: Parameters of the electromagnetic airborne system used in the simulation.

- defined a 1D model of electro-layers, defined by thicknesses and conductivities;
- added a noise to the data based on the model by Munkholm and Auken (1996);
- applied a denoising filter through the Discrete Wavelet Transform (DWT; Fedi and Quarta, 1998);
- computed the second derivatives of the EM transient to identify the most sensitive time intervals;
- sampled the continuous acquisition data using both log-gating and adaptive-gating schemes;
- inverted the two data sets and compared the results.

I simulated a continuous acquisition by using 147 gates having a width increasing logarithmically in the range between  $10^{-5}$  and  $10^{-2}$  s.

Then, the solution of the 1D forward problem was computed (Ward and Hohmann, 1988) for each considered model.

The forward response was perturbed with a random noise. I used the model noise proposed by Munkholm and Auken (1996). Following this approach, the noise is approximated to a straight line with slope equal to  $-1/2$  in a log-log plot, with a value of 3 nV/m<sup>2</sup> at 1 ms.

The second derivative is computed in the time domain by simple finite differences relations.

Then, to find the most sensitive time intervals needed to implement the sampling with my adaptive-gating scheme, the maxima of the curvature of the EM transient were investigated. However, the noise on the data prevents the reliable identification of these time intervals. Thus, data must be first denoised. Among various techniques, I chose to low-pass filter using the Discrete Wavelet Transform (DWT; Fedi and Quarta, 1998). In the wavelet domain, the scales may be associated with the frequency: small scales are in connection with high-frequency components of the signal and large scales with those at low frequency. Thanks to the characteristics of the DWT to provide a time-scale approximation of the analyzed signal, it is possible to perform a localized denoising that is filtering certain frequencies only at some times leaving intact the rest of the signal.

Figure 1.5 shows the effect of the DWT on one of the transients (figure 1.5a). The DWT filtering includes a multiresolution analysis of the signal (figure 1.5b). In this case the EM transient is decomposed in 7 details at different scale and a low-resolution approximation of the signal (black line on the upper part of the multiresolution graph, figure 1.5b).

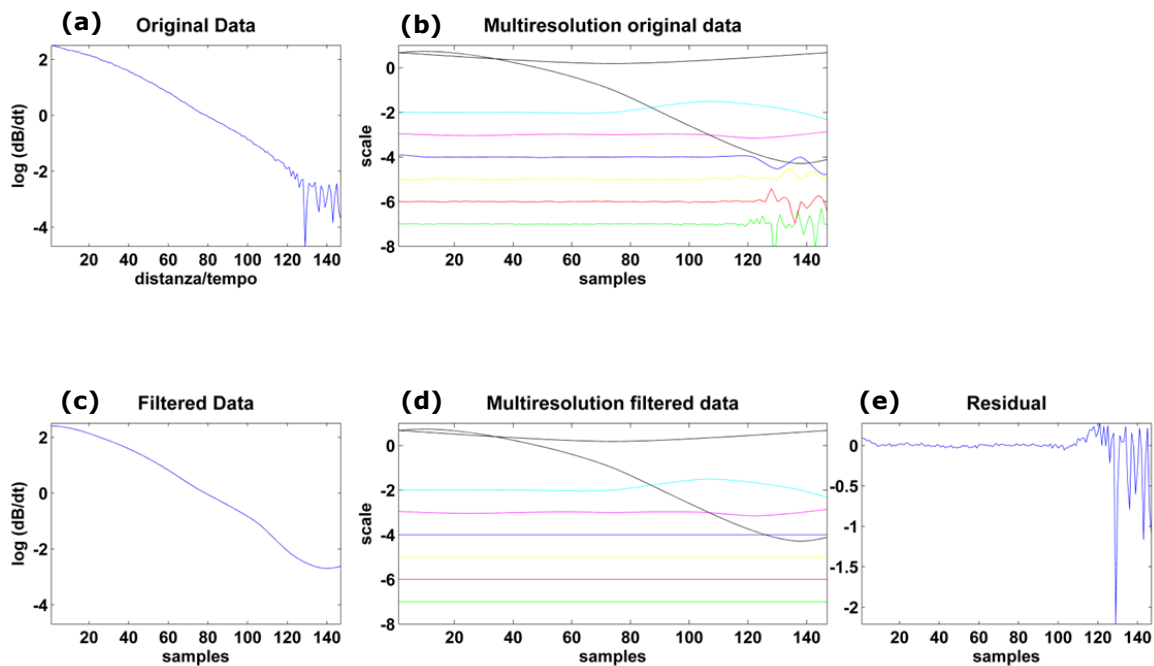


Figure 1.5: DWT filtering on EM transient. (a) Original EM transient. (b) Multiresolution of the original data. (c) Filtered EM transient. (d) Multiresolution of the filtered data. (e) Residual filtering.

The noise gives evidence on different scales, and especially on the scales with number -4, -5, -6 and -7 and from 110th sample that represents the point when the EM transient drops into the noise. To remove it, I set to zero the coefficients of the DWT corresponding to these scales (figure 1.5d), and the filtered signal (figure 1.5c) was then reconstructed using the details from -1 to -3. The residual signal (figure 1.5e) shows that the filtering acts for the entire transient and especially where the effects of noise become dominant on the secondary field.

After the filtering of the EM transient, I identified the most sensitive time intervals and I sampled the data of the continuous acquisition using 21 gates by both the adaptive-gating and log-gating schemes.

The last step was the 1D inversion with AarhusInv inversion code (Kirkegaard and Auken, 2015) of these data and the comparison of the resulting models.

I first tested my approach on synthetic TDEM data obtained from two different individual four-layer models. The first four-layer model has a third conductive layer between two resistive layers (figure 1.6a).

The second four-layer model has a third resistive layer between two conductive layers (figure 1.6b).

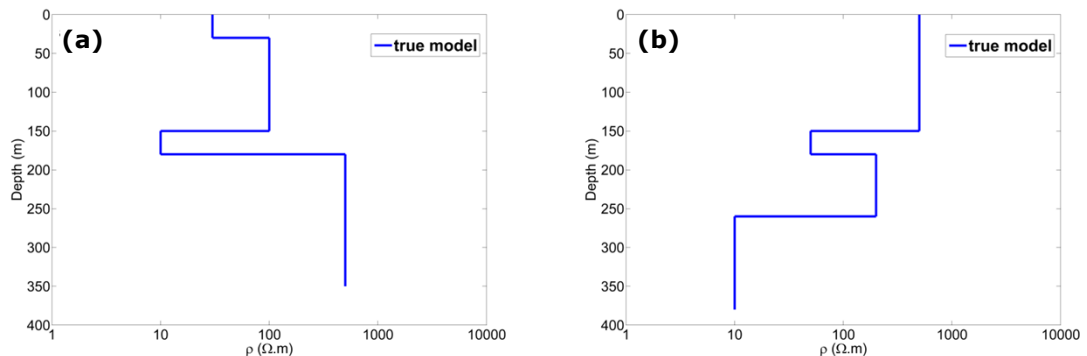


Figure 1.6: (a) Four-layer model with a third conductive layer between two resistive layers; (b) four-layer model with a third resistive layer between two conductive layers.

Then I moved to a more complex structure that could be representative of a buried valley model.

The buried valley model consists in a series of 52 four-layer models, with a thickness variation of the second resistive layer (figure 1.13a).

Below I will show all the steps of the application of my approach for the two four-layer models. The same steps were followed also for every sounding of the buried valley model, even if I will show only the final results.

First, I calculated the forward response for the considered model using 147 logarithmically spaced gates in time interval between  $10^{-5}$  and  $10^{-2}$  s. The center time of the first gate is  $1.2 \times 10^{-5}$  s and the center time of the last gate is  $9.8 \times 10^{-3}$  s. The data were perturbed with a random noise and I calculated the curvature of the EM transient (figure 1.7).

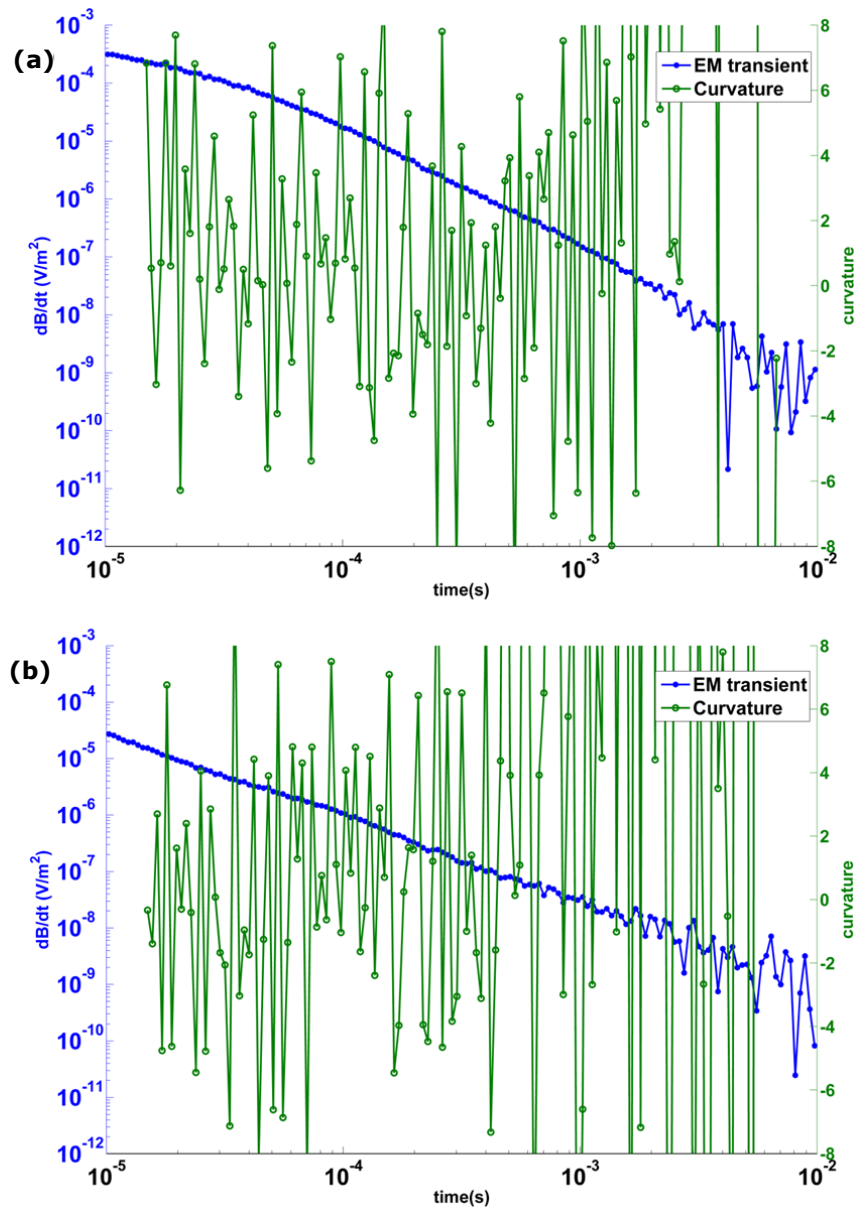


Figure 1.7: (a) EM transient (blue curve) and its curvature (green curve) for the first four-layer model earth; (b) EM transient (blue curve) and its curvature (green curve) for the second four-layer model earth.

The noise in the data is strongly enhanced in the second derivative of the EM transient and makes it impossible any reliable identification of the most representative maxima of the curvature. A denoising filter is then applied to

emphasize those time intervals at which reduce or enlarge the gate widths following the adaptive-gating scheme. The DWT proved to be a suitable low-pass filtering technique. As I am dealing with synthetic data, I could compare the filtering results with those achieved with noise-free data and I verified that the positions in time of the maxima of curvature in the filtered data were the same of noise-free data (figure 1.8).

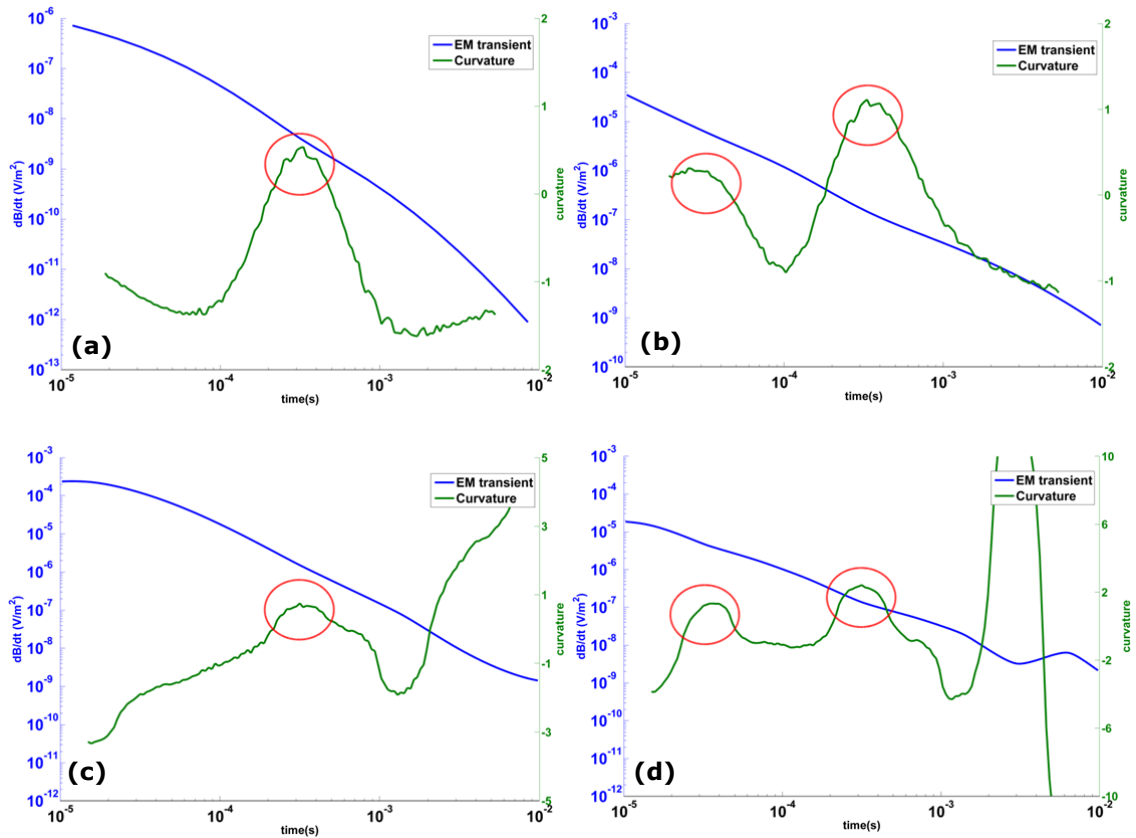


Figure 1.8: Comparison, for the first and the second four-layer model earth, between the identified maxima of curvature for free-noise data (a and b) and filtered data through DWT (c and d).

I computed the second derivative of the filtered EM transient and could easily identify the time intervals corresponding to the maxima (figure 1.9), marking the transition from data mostly influenced by the upper resistive layer to those mostly influenced by the below conductive one. The identification of the maxima was performed by considering only those having a great amplitude (at  $3 \times 10^{-4}$  s in figure 1.9a; at  $3 \times 10^{-5}$  and at  $3 \times 10^{-4}$  s in figure 1.9b) and discarding minor oscillations of the second derivative (at  $6.7 \times 10^{-4}$  s in figure 1.9a; at  $7.7 \times 10^{-5}$  s and  $7 \times 10^{-4}$  s in figure 1.9b). Moreover, I excluded maxima at the late times, when the S/N ratio is evidently low.

Then I sampled the data according to the adaptive-gating and log-gating schemes, by defining the center and the width of 21 gates. The adaptive-gating approach was different from the “classical” log-gating scheme in that I sampled the EM transient by reducing the gate-width at the time corresponding to the maximum of the curvature, with a progressive increase of the gates widths at the sides of the identified maximum.

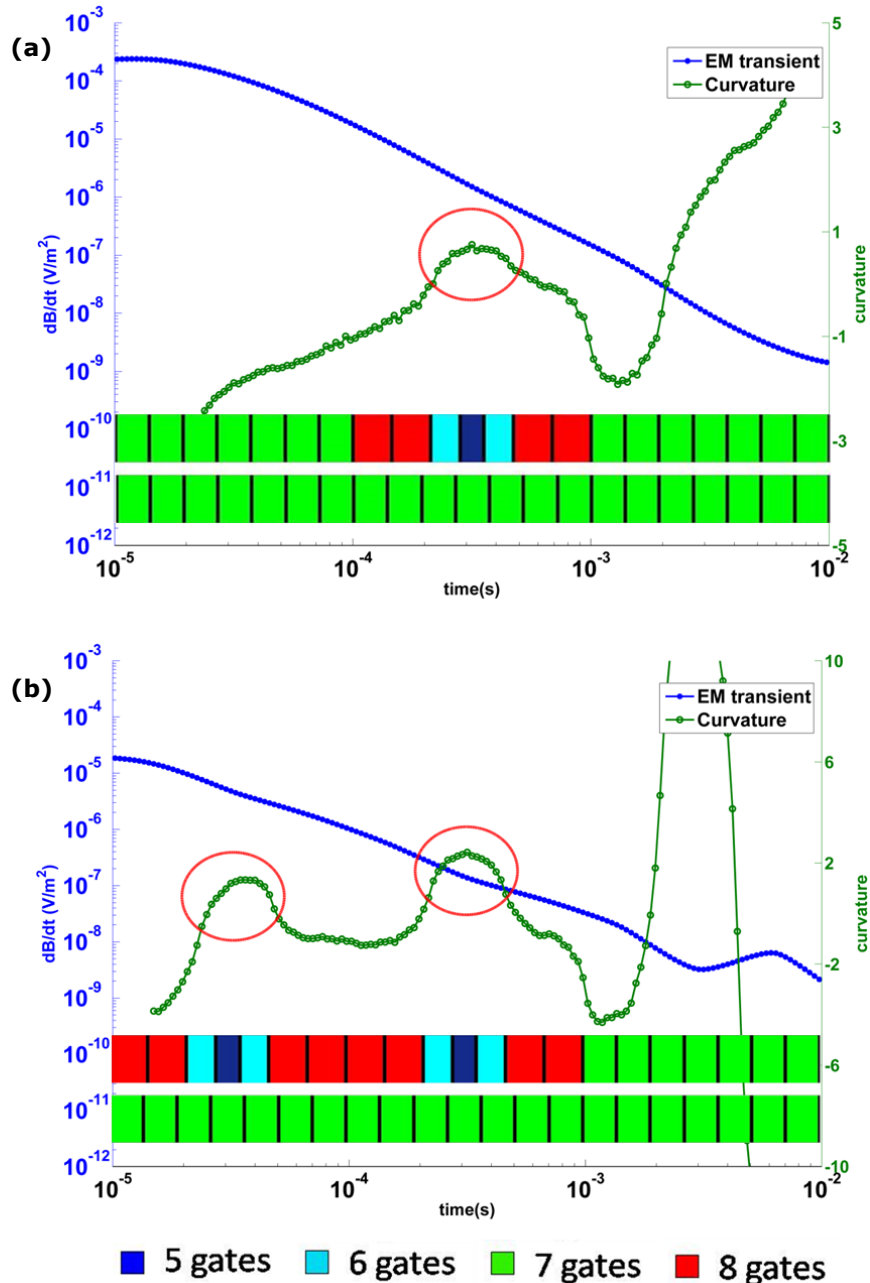


Figure 1.9: (a) EM filtered transient (blue curve) and its curvature (green curve) for the first four-layer model earth; (b) EM filtered transient (blue curve) and its curvature (green curve) for the second four-layer model earth. The dashed circles mark the maxima of curvature. The lower and the upper colored bars indicate the width of the gates for log-gating and adaptive-gating schemes, respectively. The colors correspond to the gate-width.

The upper colored bar in figure 1.9 shows the gate widths determined by my adaptive-gating scheme while the lower bar shows those defined in the log-gating scheme. The colors correspond to the gate-width. My adaptive scheme departs from the previous log-gating only near the maxima of the transient curvature. The gate-width is smaller with respect to the log-gating scheme in correspondence to blue or light-blue colors, while is slightly greater at their sides (red bars in figure 1.9).

In my cases, this implies a decrease of the 20-30% of the gate widths at the maximum of curvature, compared with those in log-gating scheme. These values may vary depending on some dataset characteristics (e.g., sampling rate, etc.), but I expect that the optimum value should not depart significantly from this figure.

The data sampled with both the adaptive-gating and log-gating schemes were inverted with AarhusInv inversion code (Kirkegaard and Auken, 2015).

The results of individual inversions depend significantly on the random noise present in the data and this can overprint the effect of the type of sampling used, preventing us from getting a unique conclusion on the validity of my new approach to sampling the EM transient.

To overcome this problem I decided to conduct my study with a probabilistic approach. I carried out 1000 inversions with adaptive-gating configuration and 1000 inversions with log-gating configuration, considering 1000 different random noise realizations.

In this way, my results are independent from a specific random noise, but depend only on the gating scheme that I used.

The figure 1.10 synthesizes all the steps that I conducted for the considered four-layer models.

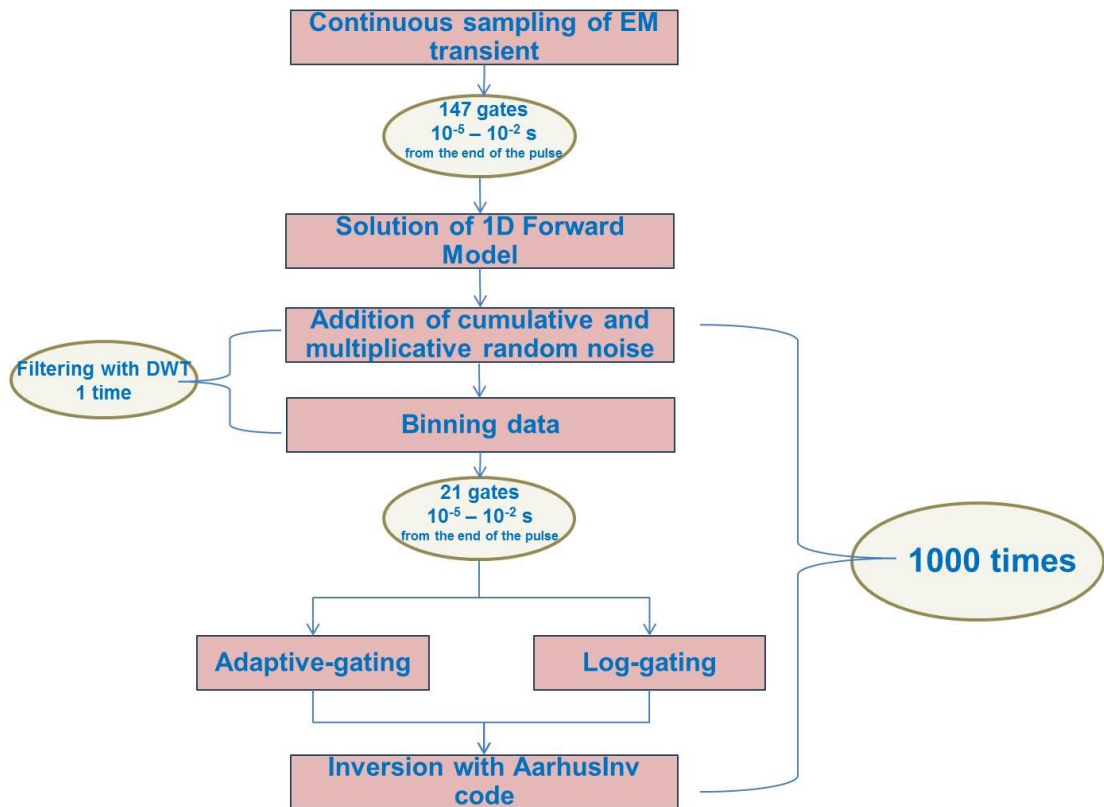


Figure 1.10: All the steps of my workflow to make comparison between adaptive-gating and log-gating.

From the 1000 inversion models for both sampling schemes, I calculated an average inverse model and compared the results with the true models. The results for the two four-layers models are shown in figures 1.11 and 1.12, where the true model (blue curve), the average model (black curve) and the 1000 inverse models (red curves) are plotted in the depth/resistivity space. As it can clearly see from figure 1.11, the adaptive gating, detailing the sampling at the maximum of the curvature (figure 1.9a), allows the inversion to recover more accurate information on the resistivity and the thickness of the third layer, with respect to the log-gating.

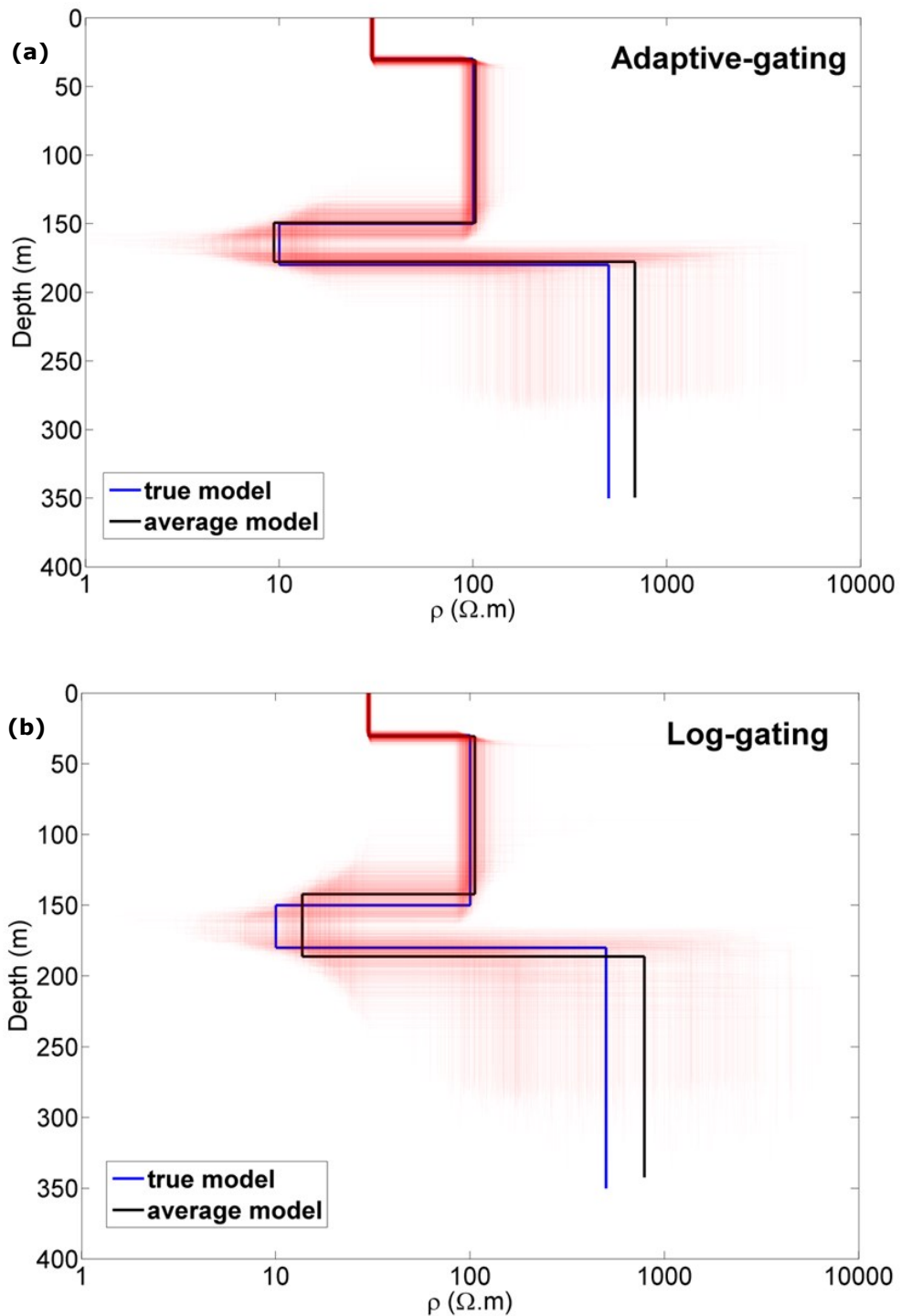


Figure 1.11: True model (blue curve), average model (black curve), 1000 inverse models (red curves) for the first four-layer model obtained with adaptive-gating (a) and log-gating (b) schemes.

The results are similar also for the second four-layer model. In this case, the second derivative showed two maxima of curvature (figure 1.9b), marking the transition, respectively, between the first and the second layer, and the third and the fourth layer (figure 1.12).

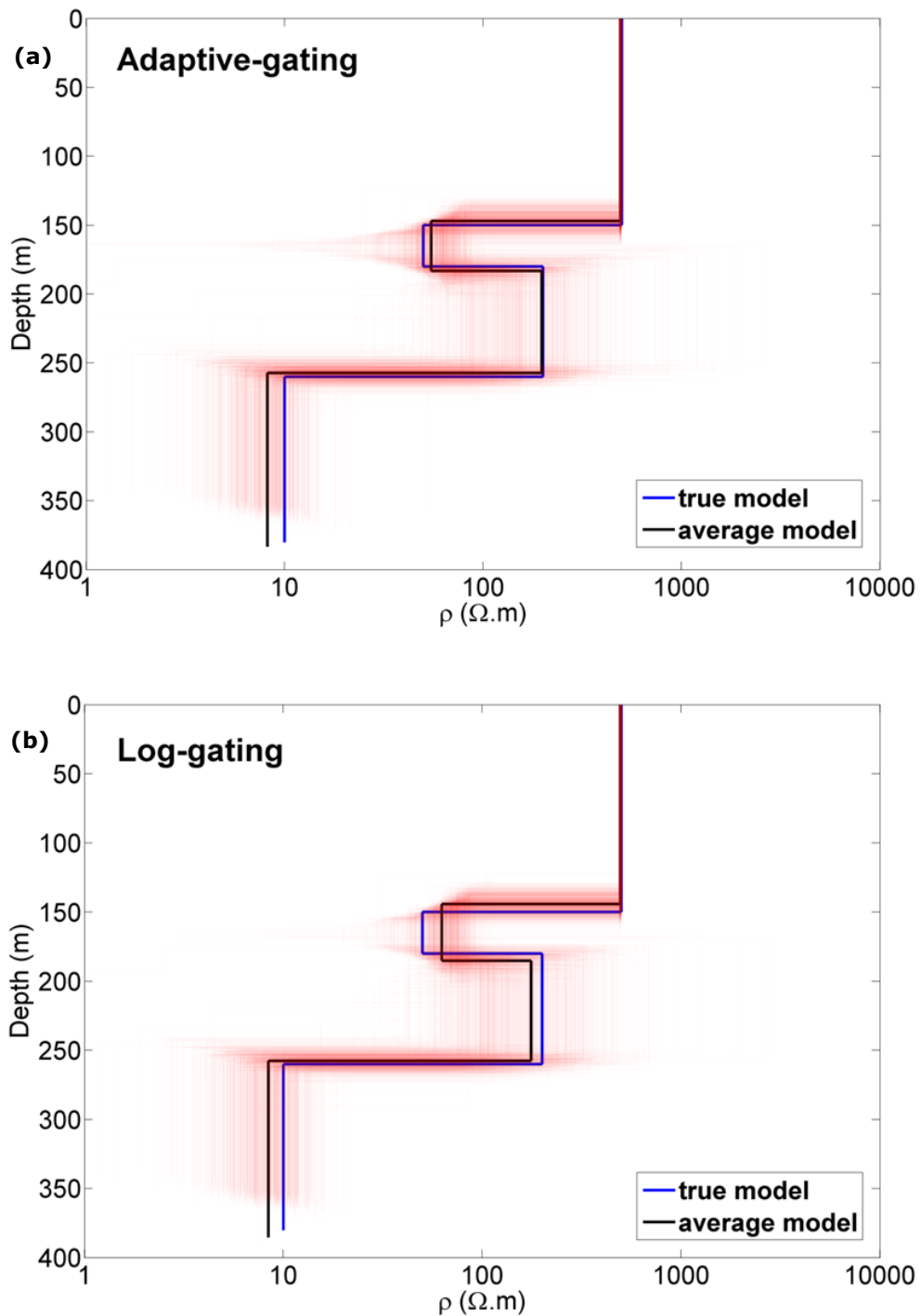


Figure 1.12: True model (blue curve), average model (black curve), 1000 inverse models (red curves) for the second four-layer model obtained with adaptive-gating (a) and log-gating (b) schemes.

A closer inspection of the scattering of the individual models also reveals that the adaptive-gating provides, in general, more precise results (i.e., closer to true model, smaller dispersion and standard deviation) across all layers. In fact, based on the 1000 inversion models, for both four-layer models, I also

carried out a study on the precision of the model parameters recovered. In particular, I calculated the standard deviation, as percentage, associated with the resistivities and the thicknesses of the average models. The results are listed in table 1.2:

|          | First four-layer model |               |                 |               | Second four-layer model |               |                 |               |
|----------|------------------------|---------------|-----------------|---------------|-------------------------|---------------|-----------------|---------------|
|          | Adaptive-Gating        |               | Log-gating      |               | Adaptive-Gating         |               | Log-gating      |               |
|          | Resistivity (%)        | Thickness (%) | Resistivity (%) | Thickness (%) | Resistivity (%)         | Thickness (%) | Resistivity (%) | Thickness (%) |
| 1° layer | 1                      | 6             | 1               | 7             | 1                       | 5             | 1               | 5             |
| 2° layer | 11                     | 8             | 48              | 11            | 25                      | 17            | 28              | 18            |
| 3° layer | 28                     | 15            | 40              | 30            | 78                      | 8             | 90              | 9             |
| 4° layer | 93                     |               | 122             |               | 36                      |               | 38              |               |

Table 1.2: Standard deviation as percentage of the value of the model parameters obtained with adaptive-gating and log-gating schemes for both four-layer models used in this simulation.

As you can see, the parameters obtained using the adaptive-gating scheme are more precise than those in log-gating scheme.

The next experiment is related to a simulation of field data from a buried valley structure. All the steps in the previous section were independently applied for each of the 52 soundings in this simulation. That is, the time of the gates varies across the 2D model. For each sounding, I calculated an average model from the 1000 inversions in both adaptive-gating and log-gating scheme. The plotted results refer to the 52 average models obtained with the two tested sampling schemes (figure 1.13). The adaptive-gating allowed us to recover with more accuracy the geometry of the buried valley (figure 1.13b). The thicknesses of the second and the third layer are better defined than in the log-gating case, especially when the depth of the third layer is greater than 120 m. At the sides of the section, where the third conductive layer is located at shallow depth, both configurations give correct results and its geometry is correctly retrieved. Conversely, when the depth to the third layer increases, the classical log-gating of the EM transient can lead to considerable errors on both resistivity and thickness of the third layer (figure 1.13d). For each average model, I calculated also the data residual defined as (Auken and Christiansen, 2004): from the figure 1.13c and 1.13e it can see that the values are similar for both gating schemes and every model fits the data within the noise level.

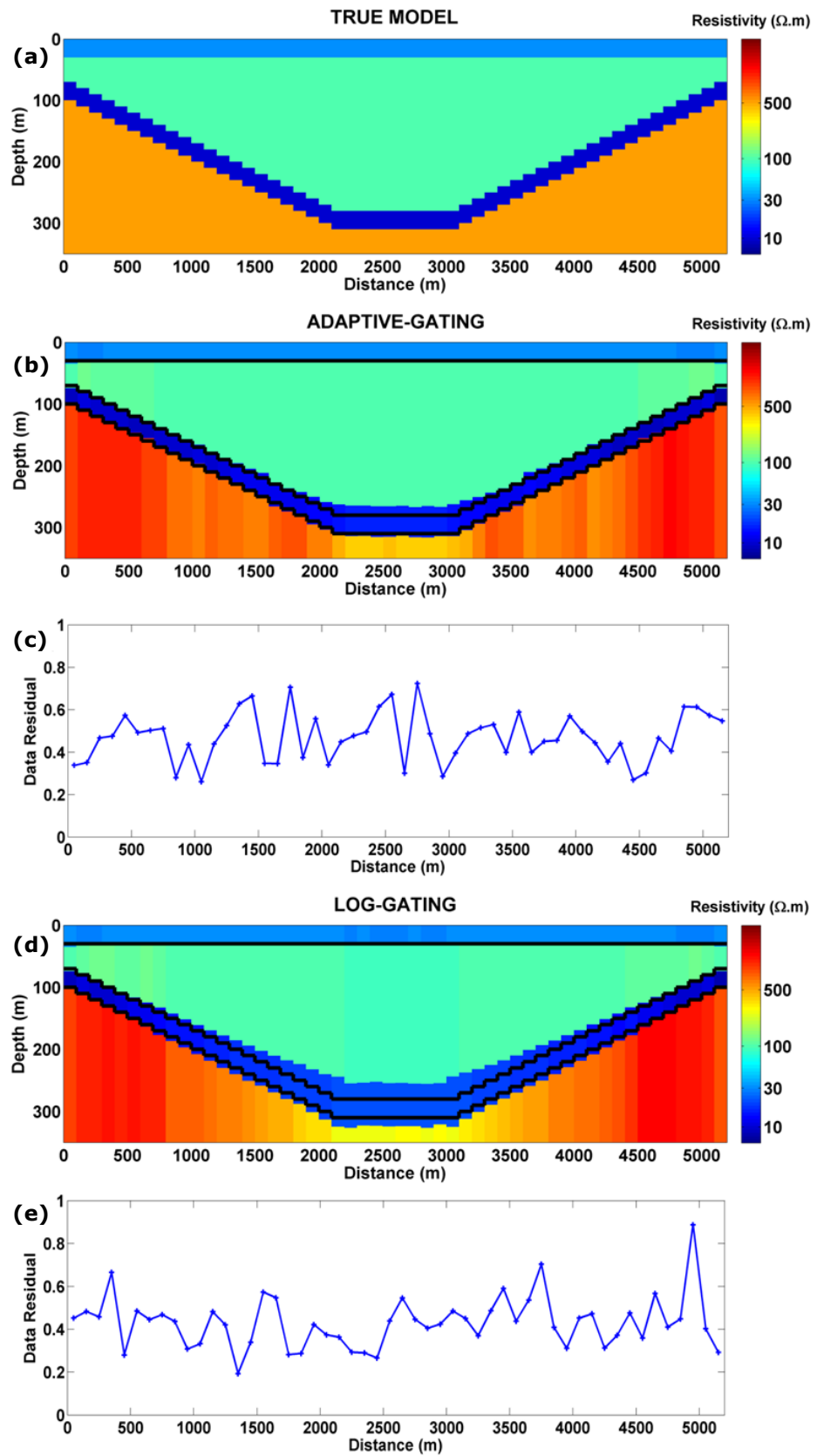


Figure 1.13: (a) True buried valley model. Buried valley model obtained with adaptive-gating (b) and log-gating (d) schemes. Data residual for each average model using adaptive-gating (c) and log-gating (e) configuration.

Based on the 1000 performed inversions I also carried out a study on the precision of the model parameters recovered. In particular, I calculated the standard deviation associated with the resistivity (figure 1.14) and the thickness (figure 1.15) of average models.

In general, the standard deviation of the resistivity decreases in the central soundings, while for the same sounding the standard deviation of the thickness increases. However, for both parameters, the standard deviation is lower for the models obtained by using the adaptive-gating scheme.

In conclusion, by sampling the EM transient with the adaptive-gating scheme I obtain inverse models that are more accurate (figure 1.13), more precise (figures 1.14 and 1.15) than standard sampling scheme. These results yield overall more reliable information on the resistivity structures of the subsurface.

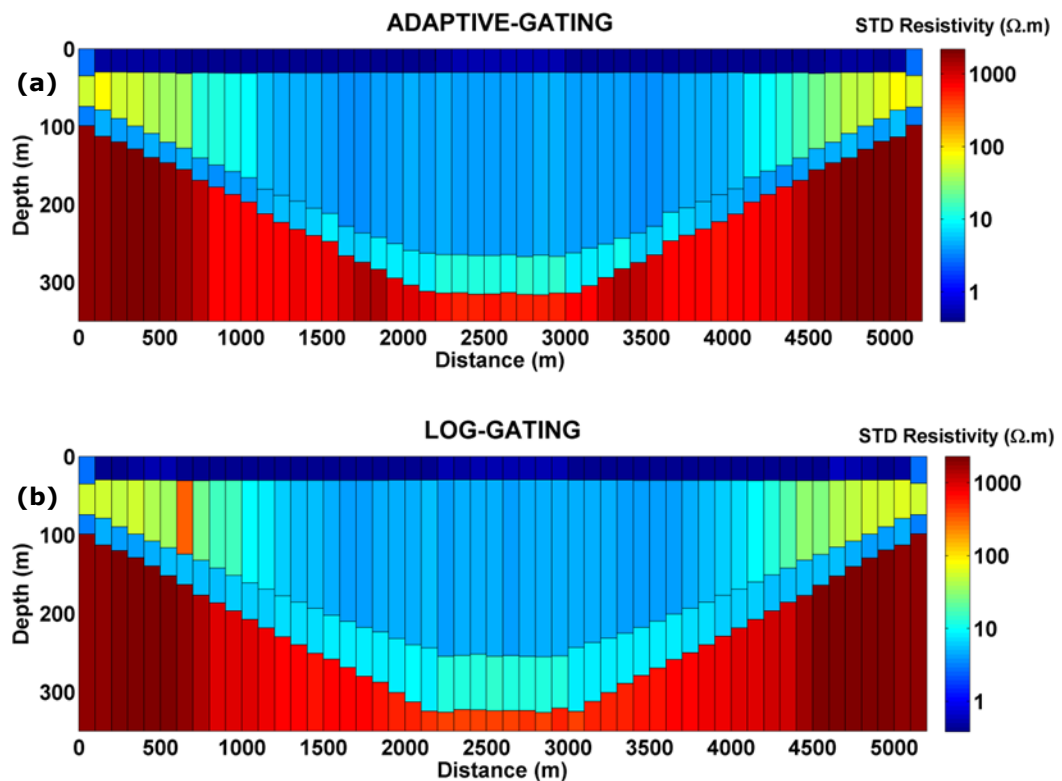


Figure 1.14: Standard deviation associated with the resistivity of the average inverse models for adaptive-gating (a) and log-gating (b) schemes.

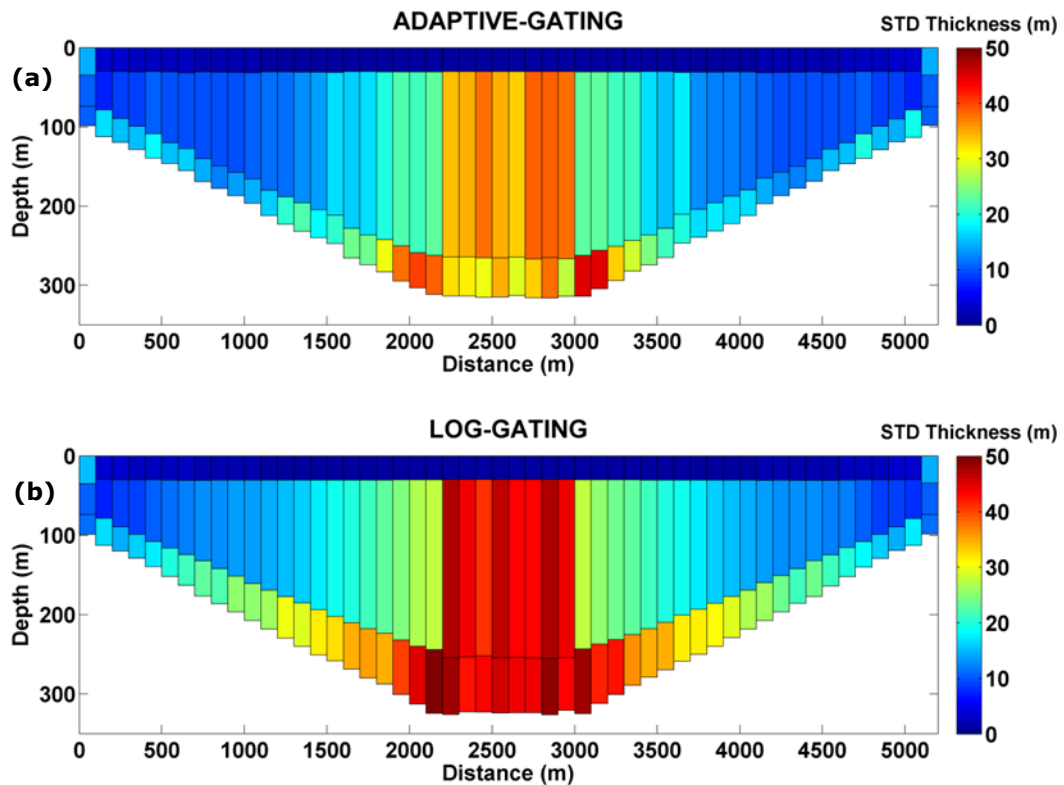


Figure 1.15: Standard deviation associated with the thickness of the average inverse models for adaptive-gating (a) and log-gating (b) schemes.

From the shown examples, it is evident that the adaptive-gating technique allows to accurately solve the geometry of the subsurface structures. Considering the example of a buried 2D valley, the depth and the thickness of the electro-layers are better determined by this technique than by standard methods. Although this structure can be considered a rather common one in hydrogeological applications, I expect good results also in the case of structures typical of other areas of exploration (e.g.: oiltrap structures).

The results shown were obtained by considering the changes of slope in transient electromagnetic related to resistivity contrasts between the layers in the subsurface and defining a detailed sampling in correspondence of the maximum of curvature which marks the transition between resistive layers to conductive layers. However, similar variations of shape, and then variation of slope, within an electromagnetic transient, may also be due to other effects, not taken into account in this study, such as the effects of the low-pass filter at the receivers or the presence of highly polarizable bodies that can lead to induced polarization phenomena. It is expected that applying the adaptive gating also to these effects would be beneficial to a more accurate sampling

and modeling of these effects. This in turn will provide better recovery of the resistivity distribution in the subsurface.

I do however realize that in real AEM data, some post-processing filtering procedures are often applied to the acquired data (e.g., leveling or bias removal). Such procedures usually require constant sampling scheme of the transients, and are therefore probably unsuitable for completely unconstrained adaptive gating. This may imply that the right compromise might be found in slowly varying adaptive gate times.

## CHAPTER 2 – Magnetic Method and Inversion of vertical magnetic soundings

### 2.1 Magnetic Field

Within the vicinity of a bar magnet, the iron filings is arranged in directions which represent the lines of force of the magnet. If the bar magnet is freely-suspended, it aligns in the flux of the Earth's magnetic field. The pole of the magnet, which tends to point in the direction of the Earth's north pole is called the north-seeking or positive pole, and this is balanced by a south-seeking, or negative pole, of identical strength at the opposite end of the magnet (Kearey et al, 2002).

The magnets consist in 2 poles. The force  $F$  between two magnetic poles of strengths  $P_1$  and  $P_2$  separated by a distance  $r$  is given by:

$$F = \frac{\mu_0 P_1 P_2}{4\pi\mu_R r^2} \quad (2.1)$$

where  $\mu_0$  ( $4\pi \times 10^{-7}$  Henry/m) is the magnetic permeability of the vacuum and  $\mu_R$  (dimensionless) corresponds to the relative magnetic permeability of the medium separating the poles. For air and water  $\mu_R$  is close to unity.

The force is attractive if the poles are of different sign and repulsive if they are of same sign.

The magnetic field  $H$  due to a pole of strength  $P$  at a distance  $r$  from the pole is defined as the force exerted on a unit positive pole at that point:

$$H = \frac{\mu_0 P}{4\pi\mu_R r^2} \quad (2.2)$$

Magnetic fields can be defined in terms of magnetic potentials in a similar manner to gravitational fields. For a single pole of strength  $P$ , the magnetic potential  $V$  at a distance  $r$  from the pole is given by:

$$V = \frac{\mu_0 P}{4\pi\mu_R r} \quad (2.3)$$

The magnetic field component in any direction is then given by the partial derivative of the potential in that direction. The magnetic potential obeys Laplace's equation, which states that the sum of the rates of change of the

field gradient in three orthogonal directions is zero (Kearey et al, 2002). In Cartesian coordinates, Laplace's equation is:

$$\frac{\partial^2 \phi}{\partial x^2} + \frac{\partial^2 \phi}{\partial y^2} + \frac{\partial^2 \phi}{\partial z^2} = 0 \quad (2.4)$$

where  $\phi$  refers to a gravitational or magnetic field and is a function of  $(x, y, z)$ . Magnetic field can also be defined in terms of a force field which is produced by electric currents. This magnetizing field strength  $H$  is defined as being the field strength at the center of a loop of wire of radius  $r$  through which a current  $I$  is flowing such that  $H=I/2r$  and it is expressed in A/m (Kearey et al, 2002).

The density of the magnetic flux, measured over an area perpendicular to the direction of flow, is known as the magnetic induction ( $B$ ) of the coil. The magnetic induction ( $B$ ) is related to magnetic field ( $H$ ) through the magnetic permeability ( $\mu_0$ ):

$$B = \mu_0 H \quad (2.5)$$

The unit of measure of  $B$  is the tesla (T). However, the tesla is a too large as a unit to express the small magnetic anomalies caused by rocks. For this reason, usually it is used a subunit, the nanoTesla (nT, 1 nT=10<sup>-9</sup> T).

A material placed in a magnetic field acquires an induced magnetization in the direction of the field that is lost when the material is removed from the field. The induced intensity of magnetization is proportional to the strength of the magnetizing force  $H$  of the inducing field:

$$J_i = kH \quad (2.6)$$

The proportionality constant  $k$  is called the magnetic susceptibility (Blakely, 1996).

Susceptibility is in essence a measure of how susceptible a material is to becoming magnetized (Reynolds, 1997) and is dimensionless.

The induced magnetization produces in turn an induced field that is proportional to  $J$ . This means that in a magnetic body the total magnetic induction  $B$  is given by:

$$B = \mu_0 H + \mu_0 J_i \quad (2.7)$$

And replacing  $J_i$  with the equation (2.6)

$$B = \mu_0 H + \mu_0 kH = (1 + k)\mu_0 H = \mu_R \mu_0 H \quad (2.8)$$

where  $\mu = \mu_R \mu_0$  is the magnetic permeability of the medium and has the same dimensions as  $\mu_0$ .

The relationship between  $J_i$  and  $H$  is not necessarily linear as implied by equation (2.6);  $k$  may vary with field intensity, may be negative, and may be represented more accurately in some materials as a tensor.

## 2.2 Magnetism of rocks and minerals

Substances can be divided on the basis of their behavior when placed in an external field (Kearey et al, 2002).

In diamagnetic materials all electron shells are full and no unpaired electrons exist. When placed in a magnetic field, the orbital paths of the electrons rotate so as to produce a magnetic field in opposition to the applied field.

Consequently, the susceptibility of diamagnetic substances is weak and negative. The most common diamagnetic earth materials are graphite, marble, quartz and salt.

In paramagnetic substances the electron shells are incomplete so that a magnetic field results from the spin of their unpaired electrons. When placed in an external magnetic field, the dipoles corresponding to the unpaired electron spins rotate to produce a field in the same sense as the applied field so that the susceptibility is positive. This is still, however, a relatively weak effect.

In small grains of certain paramagnetic substances whose atoms contain several unpaired electrons, the dipoles associated with the spins of the unpaired electrons are magnetically coupled between adjacent atoms. This phenomenon creates the magnetic domains. Depending on the degree of overlap of the electron orbits, this coupling may be either parallel or antiparallel.

In ferromagnetic materials the dipoles are parallel, giving rise to a very strong spontaneous magnetization which can exist even in the absence of an external magnetic field, and a very high susceptibility. Ferromagnetic substances include iron, cobalt and nickel, and rarely occur naturally in the Earth's crust.

In antiferromagnetic materials such as hematite, the dipole coupling is antiparallel with equal numbers of dipoles in each direction. The magnetic

fields of the dipoles cancel each other, so that there is no external magnetic effect.

In ferrimagnetic materials, the dipole coupling is similarly antiparallel, but the strength of dipoles in each direction are unequal. Consequently ferrimagnetic materials can exhibit a strong spontaneous magnetization and a high susceptibility. Examples of the ferrimagnetic substances are magnetite, titanomagnetite, pyrrhotite, oxides of iron and of iron and titanium (Telford et al., 1990).

The strength of the magnetization of ferromagnetic and ferrimagnetic substances decreases with temperature and disappears at the Curie temperature (500-600° C). Above this temperature interatomic distances are increased to separations, which preclude electron coupling, and the material behaves as an ordinary paramagnetic substance.

The magnetization of rocks depends on the present geomagnetic field and the magnetic mineral content. This is the induced magnetization that I have defined in equation (2.6), and has the same direction of the applied field  $H$ . If this field is removed the induced magnetization falls to zero. However, ferromagnetic materials have the ability to retain a magnetization even in the absence of external magnetic fields.

This permanent magnetization is called remanent magnetization, which I denote here by  $J_r$ . In crustal materials, remanent magnetization is a function not only of the atomic, crystallographic, and chemical make-up of the rocks, but also of their geologic, tectonic, and thermal history. In geophysical studies, it is customary to consider the total magnetization  $J$  of a rock as the vector sum of its induced and remanent magnetizations, that is:

$$J = J_i + J_r = kH + J_r \quad (2.9)$$

These may be oriented in different direction and may differ significantly in magnitude. The magnetic effects of a rock arise from the resultant  $J$  of the two magnetization vectors. Magnetic anomalies caused by rocks are localized effects superimposed on the normal magnetic field of the Earth. Consequently, knowledge of the behavior of the magnetic field is necessary in the interpretation of the resulting anomalies.

## 2.3 The geomagnetic field and the magnetic anomalies

On the Earth's surface a freely suspended magnetic needle assumes a position that indicates the direction of the geomagnetic total field  $B$  at that point. This direction may be described by two angles: an horizontal angle, named Declination ( $D$ ), between the geographic and the magnetic north; a vertical angle, named Inclination ( $I$ ), that represent the dip of  $B$ . The strength of  $B$  varies from about 25000 nT in equatorial areas to about 70000 nT at the poles (Kearey et al, 2002).

The strength of  $B$  is measured through the total-field magnetometers that are the instruments used in airborne magnetic survey.

The total field  $T$  is given by:

$$T = F + \Delta F \quad (2.10)$$

where  $F$  is the geomagnetic field and  $\Delta F$  represents the perturbation of  $F$  due to some crustal magnetic source.

The total-field anomaly is calculated from total-field measurements by subtracting the magnitude of a suitable regional field, usually the IGRF model appropriate for the date of the survey. If  $T$  represents the total field at any point, and  $F$  is the regional field at the same point, then the total-field anomaly is given by (Blakely, 1996):

$$\Delta T = |T| - |F| \quad (2.11)$$

If  $|F| \gg |\Delta F|$  the total field  $\Delta T$  can be considered as the component of the anomalous field  $\Delta F$  in the direction of  $F$  and thus it can be considered a harmonic function (e.g., Blakely, 1996). This condition is verified in crustal magnetic studies presented in this work where the magnetic anomalies are one or two orders of magnitude smaller than the value of the total field and have local variations of several hundred nT (sometimes several thousand nT).

The interpretation of the magnetic anomalies is more complex than the gravity case. The dipolar nature of the magnetic phenomenon, in fact, implies that the anomaly of finite body consists in a positive and a negative part. Moreover, the geomagnetic field varies not only in amplitude, but also in direction, so that the direction of magnetization controls the shape of magnetic anomaly. Usually, during the processing of the magnetic anomaly map, an operation of conversion of the shape of anomalies into their equivalent form at the north

magnetic pole is applied. At the north magnetic pole, where the inclination of the total field is vertical, the shape of the magnetic anomaly is axisymmetric. This operation, known as reduction to pole (Baranov & Naudy, 1964), simplifies the total field maps. However, it must be considered that when remanent magnetization is present and for magnetic anomalies at low latitude, the reduction to the pole cannot be safely used as a mean to produce the desired simplification.

## **2.4 Analysis of potential fields**

The measured magnetic field is a superposition of anomalies resulting from magnetization changes at various depths. The horizontal extent and smoothness of an anomaly is a measure of the depth of anomalous bodies. The effects of shallow bodies are of short wavelength while for a deeper source, the anomaly becomes more horizontally extended and its amplitude decreases (Telford et al., 1990). In this section I describe some numerical transformation used in the analysis of the potential fields that will be useful in the inversion process of magnetic data shown afterwards: upward and downward continuations, vertical and horizontal derivatives.

These analysis methods, dealing with the measured potential field data as the sum of effect with different spatial extension, allow a separation of contributions with a detailed analysis.

### **2.4.1 Upward and downward continuation**

The fact that the magnetic fields obey to Laplace's equation allows calculating the field over an arbitrary surface, if the field is known completely over another surface and no masses are located between the two surfaces (Telford et al., 1990). This process is called "analytical continuation". The field can be both continued upward and downward, yielding to a processed field with different characteristics.

In the first case, as the continuation altitude is higher than the measured altitude, high-frequency anomalies, associated to shallow sources, are attenuated while the anomalies of the deep seated sources are enhanced. The upward continuation can be described as a particular low-pass filter without phase distortions.

In space domain, the upward continuation is expressed as a convolution integral between the measured field and a continuation function:

$$G(x, y, z) = \frac{1}{2\pi} \iint_S G(\xi, \eta, z_m) \times \frac{z - z_m}{[(x - \xi)^2 + (y - \eta)^2 + (z - z_m)^2]^{3/2}} d\xi d\eta \quad (2.12)$$

which derives from Green theorem (Baranov, 1976), where  $G(x, y, z)$  is the continued field at height  $z$  and  $G(\xi, \eta, z_m)$  is the measured field at height  $z_m$ .

In the frequency domain, for the convolution theorem, the above convolution is equivalent to the product between the Fourier transforms of the measured field and that of the continuation function, called continuation filter:

$$F[U_{cont}] = F[U]F[upcont] = F[U]e^{-\Delta z|k|} \quad (2.13)$$

where  $F[...]$  is the Fourier transform operator and  $|k|$  is the module of the frequencies:

$$|k| = \sqrt{u^2 + v^2} \quad (2.14)$$

( $u$  and  $v$  are the spatial wavenumber in the two orthogonal horizontal directions).

The downward continuation allows obtaining a representation of the field at an altitude lower than the measured one. It may be used to try to separate anomalies caused by adjacent structures whose effects overlap at the level of observation. Using the downward continuation, the high-frequency contributions are greatly enhanced, but inevitably it will be amplified even the high-frequency noise present in signal. Moreover, the downward continuation is valid as long as the continuation altitude is greater than the minimum depth of the causative sources of anomaly, in other words until you operate in the harmonic region (Baranov, 1976). If the field is continued in the region occupied by the sources the anomalies show extreme fluctuations.

In Fourier domain the downward continuation is expressed by:

$$F[U_{cont}] = F[U]F[downcont] = F[U]e^{+\Delta z|k|} \quad (2.15)$$

### 2.4.2 Vertical derivative

The vertical derivative is used to enhance the high frequency components of anomalies and to increase the signal resolution separating the effects of the adjacent structures that interfere at the level of observation. Enhancing the high frequencies, the vertical derivative presents the limitation to amplify also the high-frequency noise in the data.

In Fourier domain, the vertical derivative operator for the potential field  $\Phi(x,y)$  is given by:

$$F\left[\frac{\partial^n \Phi}{\partial z^n}\right] = |k|^n F[\Phi] \quad (2.16)$$

where  $F[\Phi]$  is the Fourier transform of the potential field  $\Phi$ ,  $|k|$  is the module of frequencies, as in equation 2.14, and  $n$  is the derivation order.

### 2.4.3 Horizontal derivative

Also the horizontal derivatives may be calculated in the frequency domain. However, they are most commonly calculated in the space domain by approximating them with finite differences relations.

The derivative along the x-direction is expressed by:

$$h(x) = \left[ \frac{U(x) - U(x + dx)}{dx} \right] \quad (2.17)$$

where  $dx$  is the measurement sampling step along the x direction.

The combination of the two horizontal derivatives in the module of the horizontal gradient is used to define the horizontal positions of the density/magnetization contrasts. Cordell and Grauch (1985) showed that the maxima of the horizontal derivative of gravity or pseudogravity anomalies are located above abrupt changes of density or magnetization. This technique, coupled with an automated method to locate maxima (Blakely and Simpson 1986), proved to be an effective tool for the boundary analysis.

## 2.5 Interpretation of potential field anomalies

The interpretation of potential field anomalies is inherently ambiguous. The ambiguity arises because any given anomaly could be caused by an infinite number of possible sources. This ambiguity represents the inverse problem of potential field interpretation, which states that, although the anomaly of a given body may be calculated uniquely, there are an infinite number of bodies that could give rise to any specified anomaly (Kearey et al, 2002).

The inverse problem is solved by determining a set of parameters that describes the sources of the measured field.

If the unknown parameters are the density or the magnetization, this type of problem is linear and in most cases it is an indeterminate problem, since the data are less than the number of unknown parameters.

An important task in interpretation is to decrease this ambiguity by using all available external constraints on the nature and shape of the anomalous sources. Such constraints include geological information derived from surface outcrops, boreholes and mines, and from other geophysical techniques.

With the inversion of the potential fields you would like to obtain satisfactory information about the characteristics of the sources of interest, as the top and the bottom of the structures that generate anomalies and estimates and trends of density values (or intensity of magnetization, in the case of magnetic fields) relating to them.

The scientific literature is extraordinarily rich in both 2D and 3D gravity and magnetic data inversion algorithms.

All these methods provide density/magnetization distributions at depth having certain properties.

Green (1975) searched for a density model that minimizes its weighted norm to some reference model. Safon et al. (1977) used the method of linear programming to compute moments of the density distribution. Fisher and Howard (1980) solved a linear least-squares problem constrained for upper and lower density bounds. Last and Kubik (1983) introduced a "compact" inversion minimizing the body volume. Guillen and Menichetti (1984) assumed as a constraint the minimum momentum of inertia. Barbosa and Silva (1994) suggested allowing compactness along given directions using a priori information. Li and Oldenburg (1996, 1998) introduced model weighting as a function of depth using a subspace algorithm. Pilkington (1997) used preconditioned Conjugate Gradients (CG) method to solve the system of linear equations. Portniaguine and Zhdanov (1999, 2002) introduced regularized CG method and focusing using a reweighted least squares algorithm with different focusing functional. Li and Oldenburg (2003) use wavelet compression of the kernel with logarithmic barrier and conjugate gradient iteration. Barbosa and Silva (2006) proposed a 2D method to invert potential field data by a procedure incorporating a priori knowledge. Wijns and Kowalczyk (2007) propose a semi-automatic procedure that allows defining solutions geologically reasonable. Pilkington (2009) used data space inversion in Fourier domain. Barnes and Barraud (2012) have developed instead an inversion algorithm to

solve geometrical interfaces between different geological bodies, through the introduction of information concerning the depth and regularizing the solution. However, there are no 1D algorithms, since the forward problem in this case should be referred to horizontally infinite layers, which would produce a constant field in space and, therefore, could not explain any gravity or magnetic anomaly.

Fedi and Rapolla (1995) explored for the first time the possibility to perform the inversion of "vertical gravity/magnetic soundings", that is a 1D inversion method. The forward problem consisted in assuming a volume of layers of different densities/magnetizations. The volume is however finite vertically and horizontally, this last condition is necessary to avoid the above-mentioned "Bouguer-slab effect", which would make impossible the inversion of field anomalies. The vertical sounding is central with respect to the layers volume, so yielding a 1D density/magnetization distribution at depth.

In this thesis, I will develop and use on real datasets a 1D inversion method for magnetic fields based on the above Fedi and Rapolla (1995) paper. In the following sections the method will be set up and then analyzed in detail before of its application on real data, in Chapter 3 and 4.

### 2.5.1 The forward model of Vertical Magnetic Sounding

The basic idea is that the vertical density or magnetic distribution can be deduced from the gravity or magnetic field known at different altitudes (Fedi and Rapolla, 1995).

I start from the relation defining the magnetic field at a point  $P(x_k, y_k, z_k)$  generated by a distribution of magnetization  $J$  in a volume  $V$ .

$$B(P) = \frac{\mu_0}{4\pi} \int_V \nabla \nabla \frac{1}{|\vec{r} - \vec{r}_k|} \cdot J(\vec{r}) dv \quad (2.18)$$

where  $\mu_0$  is the magnetic permeability of the vacuum and

$$|\vec{r} - \vec{r}_k| = \sqrt{(x - x_k)^2 + (y - y_k)^2 + (z - z_k)^2} \quad (2.19)$$

If the magnetization varies only along the vertical direction:

$$J(\vec{r}) = J(z) \quad (2.20)$$

and if considering a set of  $N$  magnetic data along a vertical direction (vertical sounding)  $[P_{k1}, \dots, P_{kj}, \dots, P_{kN}]$ , then equation 2.18 becomes:

$$B(P_{kj}) = \frac{\mu_0}{4\pi} \int_V \nabla \nabla \frac{1}{|\vec{r} - \vec{r}_{kj}|} \cdot J(z) dv \quad (2.21)$$

This equation describes the 1D forward problem of a continuous unknown function  $J(z)$  linearly related to the measured magnetic data. Diversely from 1D electrical or seismic problems, the horizontal extension of the volume in equation 2.21 is finite and has to be fixed before inverting. To set up this parameter many methods can be used. For example, Fedi and Florio (2001) shows a technique to estimate with high resolution the source volume horizontal dimensions based on the computation of the module of the horizontal derivative of a summation the vertical derivatives of various order of the field data.

If we assume a discrete number  $M$  of homogeneously magnetized layers, I have:

$$B(P_{kj}) = \sum_{i=1}^M J_i G_{ij}(P_{kj}) \quad (2.22)$$

where:

$$G_{ij}(P_{kj}) = \frac{\mu_0}{4\pi} \int_{V_i} \nabla \nabla \frac{1}{|\vec{r} - \vec{r}_{kj}|} dv \quad (2.23)$$

is the unit-magnetization contribute due to  $i^{th}$  prismatic layer.  $[J_1, \dots, J_i, \dots, J_M]$  and  $[V_1, \dots, V_i, \dots, V_M]$  are respectively the magnetizations and the volumes of the  $M$  layers.

Equation 2.22 defines the forward problem of a vertical magnetic sounding in matrix notation.

There are two possible ways to obtain a vertical sounding of magnetic data. The first, and the most obvious, is measuring the magnetic field at fixed altitudes. However, it is quite unlikely to collect data at different altitudes; in this case the vertical sounding is built by upward continuation.

## 2.5.2 The inversion method of Vertical Magnetic Sounding

The estimate of the magnetization from vertical magnetic soundings is obtained using a technique, that Fedi and Rapolla 1995 called "Minimum Length with Inequality Constrains" or IML, which produces stable solutions without losing high-frequency solution components. It is used to solve indeterminate linear problems such as:

$$d = Gm \quad (2.24)$$

where  $\mathbf{d}$  represents the data vector (with dimensions  $N \times 1$ ) referred to the vertical sounding,  $\mathbf{m}$  represents the parameters vector (with dimension  $M \times 1$ ) referred to the source volume and  $\mathbf{G}$  represents the matrix of the theoretical kernel (with dimension  $N \times M$ ), defined by the equation 2.23.

For these problems, the estimated model parameters are given by the solution having the minimum Euclidean length:

$$m^T m = \sum_{i=1}^M m_i^2 = \|\mathbf{m}\|_2^2 \quad (2.25)$$

and which also satisfies some set of linear inequality constraints:

$$d - \delta d \leq Gm \leq d + \delta d \quad (2.26)$$

$$m_L \leq m \leq m_U \quad (2.27)$$

where  $\delta d$  is the experimental data error,  $m_L$  and  $m_U$  are the lower and the upper bounds of the model parameters.

The inequality constraints are based essentially on two points:

1. The unknown parameters vector must satisfy the forward model, taking into account experimental data errors  $\delta d$ ;
2. The parameters vector is bounded to avoid unrealistic estimates.

The lower and the upper bounds can be chosen considering available a-priori information.

In matrix notation, an indeterminate problem with inequality constraints may be expressed as:

$$Fm \geq h \quad (2.28)$$

where:

$$F = \begin{bmatrix} I \\ -I \\ G \\ -G \end{bmatrix} \quad h = \begin{bmatrix} m_L \\ -m_U \\ d - \delta d \\ -(d + \delta d) \end{bmatrix} \quad (2.29)$$

The  $F$  matrix, containing the identity matrix  $\mathbf{I}$  ( $M \times M$ ) and the kernel  $\mathbf{G}$  ( $N \times M$ ), has dimension  $(2M+2N) \times M$ ; the vector  $\mathbf{h}$ , containing the lower and the upper bounds of model parameters and the data with the experimental errors, has dimension  $(2M+2N) \times 1$ .

A way to solve the IML problem is based on the Kuhn-Tucker theorem (Fiacco and Mc Cormick, 1968) which indicates the conditions that should be satisfied by the solution. According to this theorem, the constraints of equations 2.28 define a volume in the model-space of feasible solutions. If constraints are consistent, this volume is non-zero and there is at least one solution satisfying both conditions of equations 2.26 and 2.27.

According to a technique described in Menke (1984, pag.130), the minimum-length is first transformed into the non-negative least squares problem:

$$\text{minimize: } e = \|f - Eu\|_2 \quad \text{subject to: } u \geq 0 \quad (2.30)$$

where  $\mathbf{u}$  is an  $N$  vector, while the  $\mathbf{E}$  matrix and the  $\mathbf{f}$  vector are given by:

$$E = \begin{bmatrix} F^T \\ h^T \end{bmatrix}, \quad f = \begin{bmatrix} 0 \\ 1 \end{bmatrix} \quad (2.31)$$

$$F^T u = 0, \quad h^T u = 1 \quad (2.32)$$

It can be shown that if the prediction error,  $e = \|f - Eu\|_2$ , is null then the constraints are inconsistent, but if  $e \neq 0$ , the constraints are consistent and the solution of the problem 2.28 is:

$$m_i = -\frac{e_i}{e_{M+1}} \quad \text{with } i = (1, \dots, M) \quad (2.33)$$

So, inequalities constraints allow managing the overall tolerance of this particular technique. The problem thus posed is the resolution of a single sounding.

### 2.5.3 Vertical Soundings inversion of synthetic magnetic data

The major change that I made to the existing 1D method of Fedi and Rapolla (1995) consists in extracting the vertical soundings at different horizontal positions, and no more just at the center of the volume. I performed the inversion of multiple one-dimensional vertical magnetic soundings. In this case, each sounding is inverted independently of each other. The main feature of this approach is that a multiscale dataset is inverted. In the following sections, I tested this method by analyzing both synthetic perfect data, to simulate data measured at different levels, and synthetic upward continued data.

According to numerous tests that I performed and that will be described in the next sections, I noticed that the inverse models that I am able to estimate with the inversion of the vertical magnetic soundings depend on three variables:

1. the experimental data errors;
2. the upper and lower bounds of model parameters;
3. the horizontal dimensions of the source, that can be estimated by boundary analysis techniques.

A better resolution of the model is obtained when the vector components  $\delta d$  are as small as possible, preserving the compatibility with the other constraints. However, I noticed that, for the same sources the inversion of continued data needs more tolerance on  $\delta d$  than the inversion of measured data.

The constraints on model parameters should be chosen according to the expected minimum and the maximum magnetization contrast of the anomaly source. However, as it will be shown, an overestimation of the maximum contrast of magnetization does not prevent the computation of a meaningful result.

The correct estimation of the horizontal dimensions of an anomaly source, that are used to define the horizontal dimensions of the volume in the kernel calculation, represents the most challenging parameter to set up. I used, as boundary analysis technique, the simple horizontal derivative method (Cordell and Grauch, 1985).

As I have already said, by calculating the module of horizontal derivative field along the two horizontal directions and selecting the distance between the identified maxima, it can be obtained an estimation of the source limits.

In some cases, the horizontal dimensions obtained with the horizontal derivative method may be overestimated.

The overestimation depends on the ratio between the horizontal dimensions of the source and the distance of observation. As an example, the horizontal derivative of small sided sources at remarkable depth identifies a source that is bigger than the real one. The estimated dimensions may be less accurate even for non-vertical sided sources. In order to calculate the correct positions of boundaries in the magnetic case, it is also necessary to perform a

preliminary reduction to pole, to eliminate the dipolar shape of magnetic anomalies. Finally yet importantly, also a data-sampling step too coarse can prevent a correct estimation of the source dimensions.

However, as it will be shown in the next sections, it is possible to perform some transformations of the field data in order to obtain more accurate estimation of the source dimensions. For example, in some cases, it will be advantageous applying the horizontal derivative method on the vertical derivative of the field, which, as I have already said, is an appropriate tool to increase the signal resolution.

The increase of resolution can also be achieved downward continuing the data within the harmonic region, i.e. free-source region. This is possible, as I will show in Chapter 3, when you are dealing with aeromagnetic data that are usually collected at average height of 50-60 m above the ground.

However, these operations, enhancing the high frequency, tend to amplify also the high-frequency noise in the data and in real cases, they should be used very carefully. In most cases it is impossible to achieve an increase in resolution without enhancing the noise.

Moreover, an average useful dimension for a prism with irregular shape can always be found and allows recovering a useful estimated inverse model.

I define an estimated model as “useful” when the inversion process allows to recover a model with feasible values for the parameters, not forced to the upper magnetization bound for all the vertical discretized volume.

To complete the discussion about the variables that can be controlled during the inversion process, I need to mention the number of the layers in which the theoretical volume is discretized (i.e. the number of unknowns of the inverse problem), the maximum altitude and the number of altitudes where the field is measured or continued.

In order to obtain a better inversion result, I noticed that the number of the layers, for both measured and continued data, is not crucial as long as it stays above a certain threshold (about 70 layers). Same considerations apply to the number of altitudes where the field is measured or continued if it stays within a certain range (from 8 to 75) assuming the same maximum altitude. The analysis of synthetic tests, shows that the maximum altitude of sampling, with a fixed sampling step in  $z$  direction, does not have a strong influence on the

recovered inverse models, when measured data are concerned. When the data are obtained by upward continuation, it is necessary to increase the tolerance on the variable  $\delta d$  to recover the same model with a vertical sounding having a higher maximum altitude.

If the maximum altitude is relatively low, the inversion model shows low resolution. The notion of “relatively low” depends on the depth and on the horizontal dimensions of the anomaly source.

In real cases, this issue is complicated because of the presence of adjacent sources causing separate anomalies whose effects can interfere at the level of observation. In this case, it is recommended to choose an optimal maximum altitude, which ensures no interference effects with the neighboring anomalies and, at same time, an appreciable variation of the field with the height in order to avoid the “slab effect”.

In the following sections, I will show the Vertical Soundings inversions related to synthetic tests. In particular I will use computed (“measured”) and continued data generated by a prismatic buried body and I will evaluate the effects of the variables that are used in the inversion process and control the final results.

## **2.6 Vertical Soundings inversion of measured data**

The inversion method, described in the previous section, was tested on synthetic magnetic data obtained from the calculation of the magnetic effect of a single source in the investigated volume. The data at different heights were generated thanks to an algorithm that calculates the magnetic response, at a fixed altitude, of a prismatic source for defined physical (magnetization or susceptibility) and geometrical properties. In this frame, I consider these data, not obtained through upward continuation, as “measured” data, i.e., data free from errors linked to the continuation process.

For this test, I used a single source with horizontal dimensions equal to 250×150 m at depths from 100 m to 300 m. The magnetization contrast with the surrounding volume is 3 A/m and its direction is vertical. The magnetic anomaly generated by this source and calculated at an altitude of 0.001 m above the ground surface is shown in figure 2.1. The vertical soundings consist of magnetic data calculated at 20 different altitudes from the first level at 5 m

up to the last level at 100 m with a 5 m constant step above the ground. The positions of the vertical soundings are those shown in figure 2.1 by the green points, while the magnetic anomaly, along the profile and at different heights, is shown in figure 2.2.

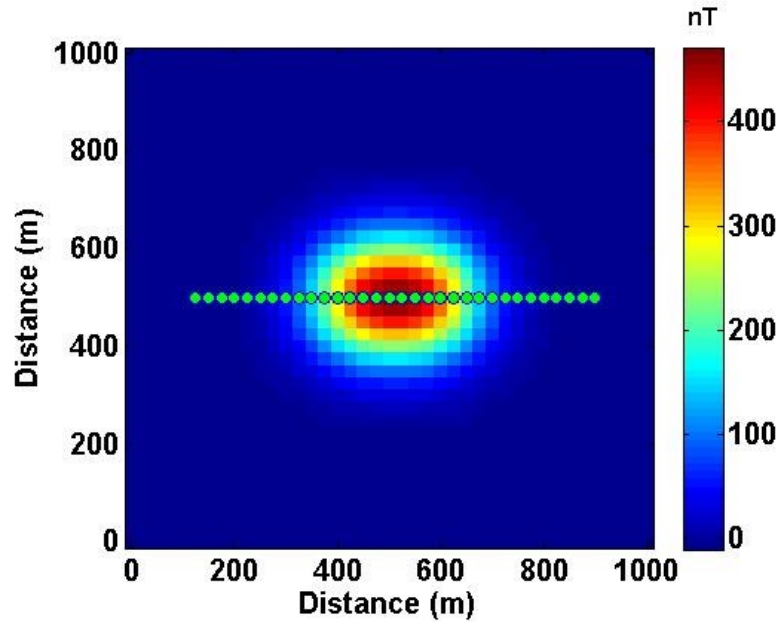


Figure 2.1: Map of magnetic data generated by a single buried prismatic source. The green dots represent the horizontal positions of the measuring stations and then the individual vertical soundings.

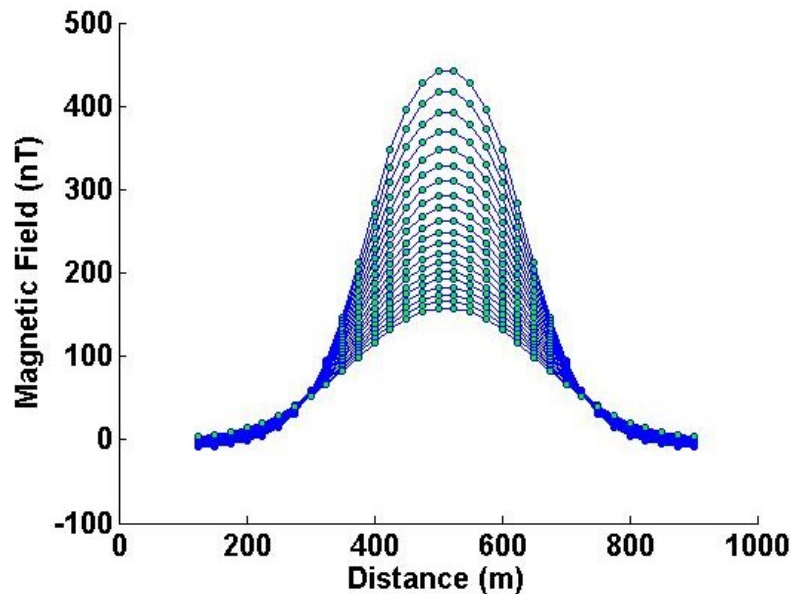


Figure 2.2: Profiles of the magnetic data at different altitudes of measure. The green dots represent, for each altitude, the horizontal positions of the measuring stations and then the individual vertical soundings.

For the calculation of the kernel, a theoretical volume has been defined with horizontal dimensions that are in agreement with those of the true source (this

will remain valid also in later tests, until the contrary will be clearly expressed). The vertical dimension of the theoretical volume is defined so as to completely contain the source of anomaly and it is discretized from 0 to 1000 m, with 100 layers with an equal thickness of 10 m (figure 2.3).

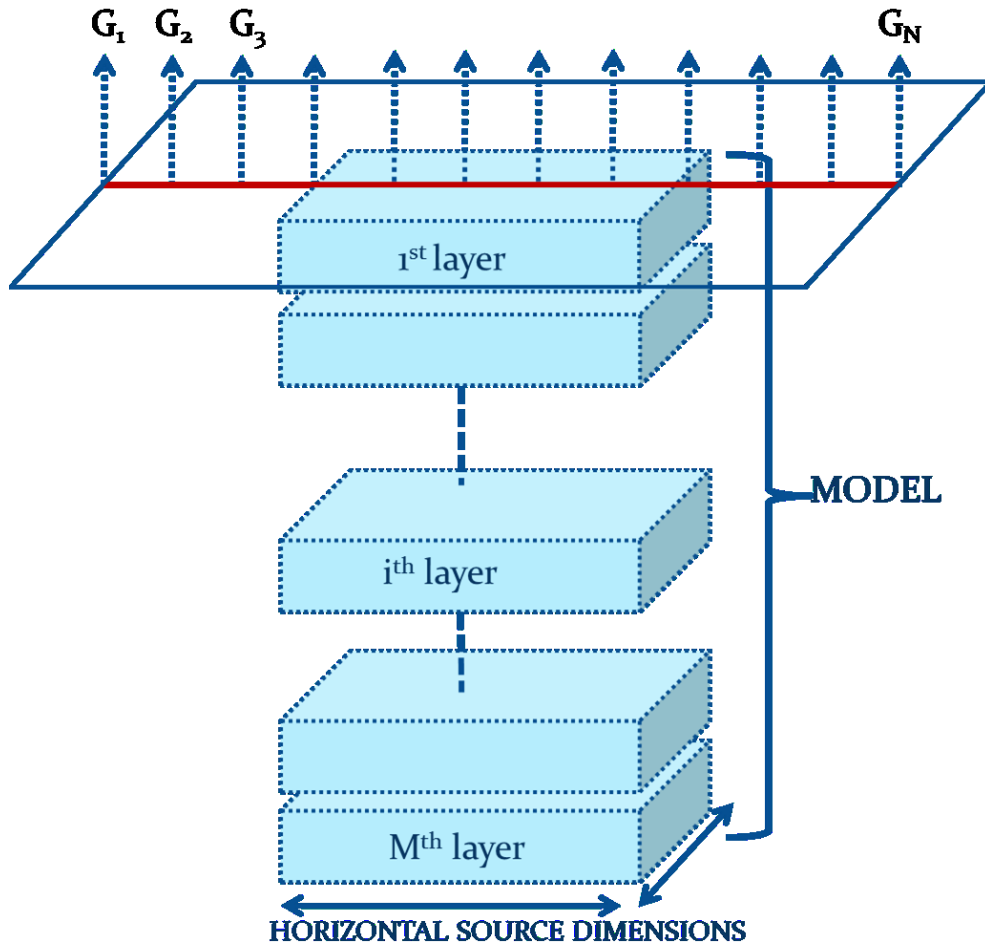


Figure 2.3: Schematic picture of the of the finite layers forming the source volume. The dashed arrows indicate the horizontal positions of the vertical soundings. The single kernels,  $G_i$ , are computed according to the spatial coordinates of the soundings that are related to.

As shown in figure 2.3, for each vertical sounding, I computed, at its position, the kernel  $G_N$  to perform the inversion. In this way, each vertical sounding is inverted independently of each other.

For this preliminary test, I used the correct magnetization contrasts for the lower and the upper bounds, setting the lower bound equal to 0 and the upper bound equal to 3 A/m. The experimental error is set to a very low value, equal to  $10^{-6}$  nT. In this case, the inversion of the vertical soundings provides excellent results in estimating the position and the magnetization contrast of

the source (figure 2.4). The black rectangle in figure 2.4 identifies the exact location of the buried body.

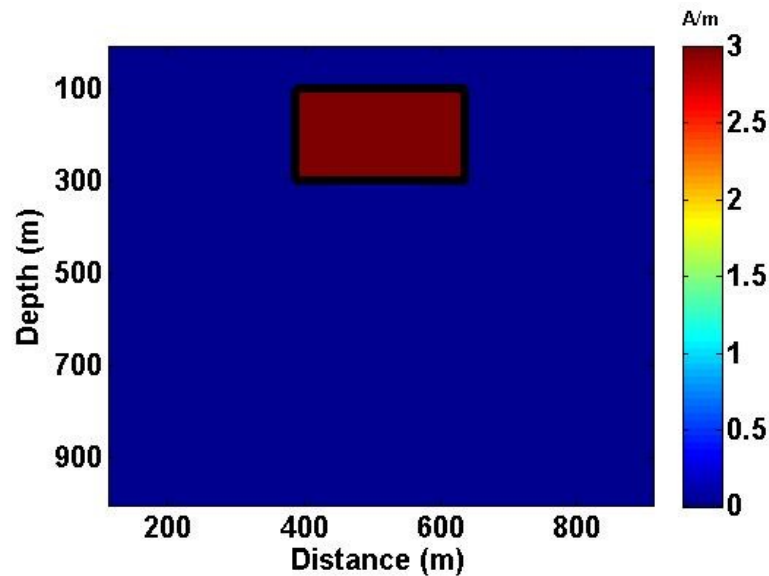


Figure 2.4: Vertical Soundings inversion of the magnetic data produced by a single buried prismatic source and calculated at 20 different altitudes. The black rectangle identifies the horizontal and vertical positions of the anomaly source.

From the estimated parameters, I calculated also the estimated data along the considered profile, at a fixed altitude (in this case the first height, 5 m), and I compared them with the initial data related to the same profile (figure 2.5). I noticed that the data are very well reproduced, as the fitting is very good, along all the profile with a Root Mean Square Deviation (RMSD) of  $5.8 \times 10^{-4}$  nT.

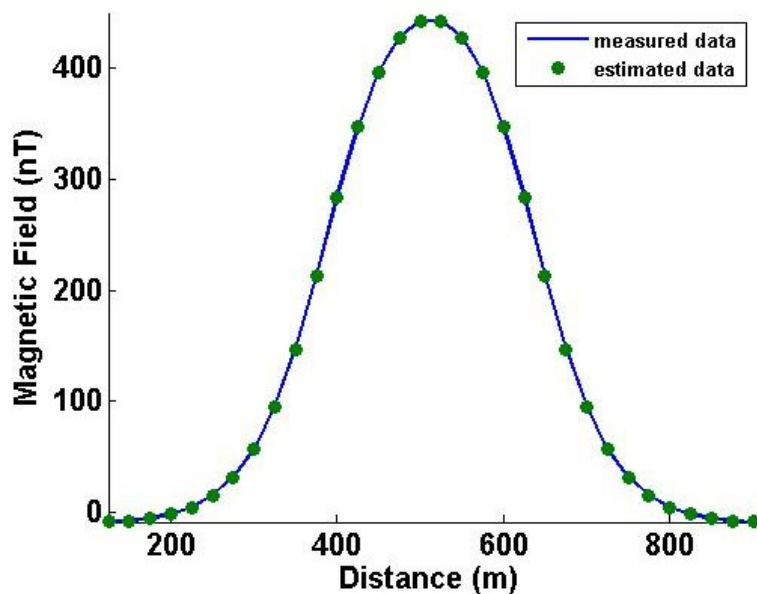


Figure 2.5: Comparison between the measured and the estimated data.

These results are not trivial if you consider that the inversion method is applied independently on each vertical sounding. So even building a section by joining independent models related to several 1D inversions, I get a good data fitting along the entire profile. This means that the results obtained from a single 1D inversion are validated also along a profile.

### 2.6.1 Effect of constraints ( $m_L < m < m_H$ ) on inversion process

The constraints on model parameters allow taking into account any a-priori geological information in the inversion process. As I shown in the previous section, these constraints should reflect the minimum and the maximum magnetization contrasts of the source that produces the magnetic anomaly. In general, for magnetized bodies, I noticed that lower bounds must be set to zero in order to avoid slight shallow instabilities in the inverse model. To illustrate this effect, in figure 2.6 I show the Vertical Soundings inversion carried out as in the previous section, but changing the lower bound value to a negative value, equal to -3 A/m.

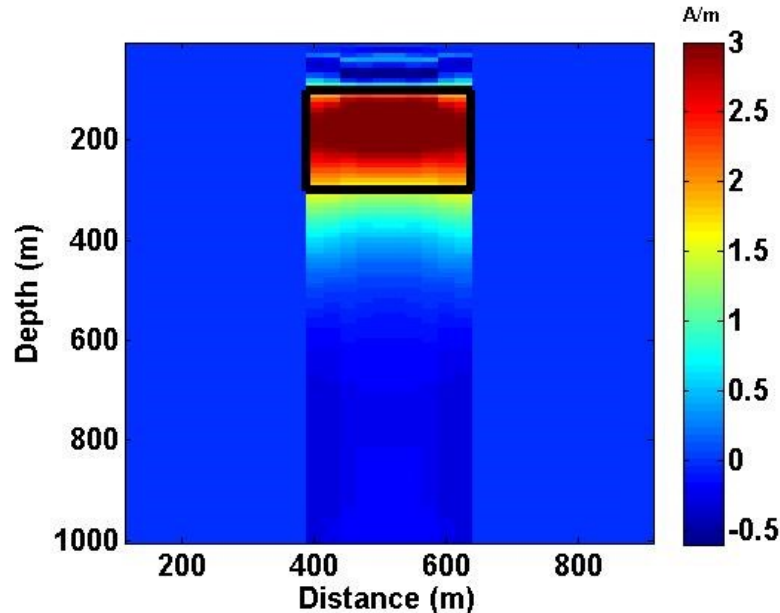


Figure 2.6: Vertical Soundings inversion of the calculated magnetic data produced by a single buried prismatic source obtained using a negative value for the lower bound. The black rectangle identifies the horizontal and vertical positions of the anomaly source.

As regards the upper bound, I performed another Vertical Soundings inversion using a higher upper bound (equal to 5 A/m). Figure 2.7 shows that a good result is obtained also in this case. The depth of the top is very precisely

estimated, while the bottom is less defined. The main observation is that even using such a large upper bound, the estimated magnetizations are very close to the true values.

This represents an important simplification in real cases where usually you do not have accurate information on the magnetization contrasts between the anomaly source and the host rocks.

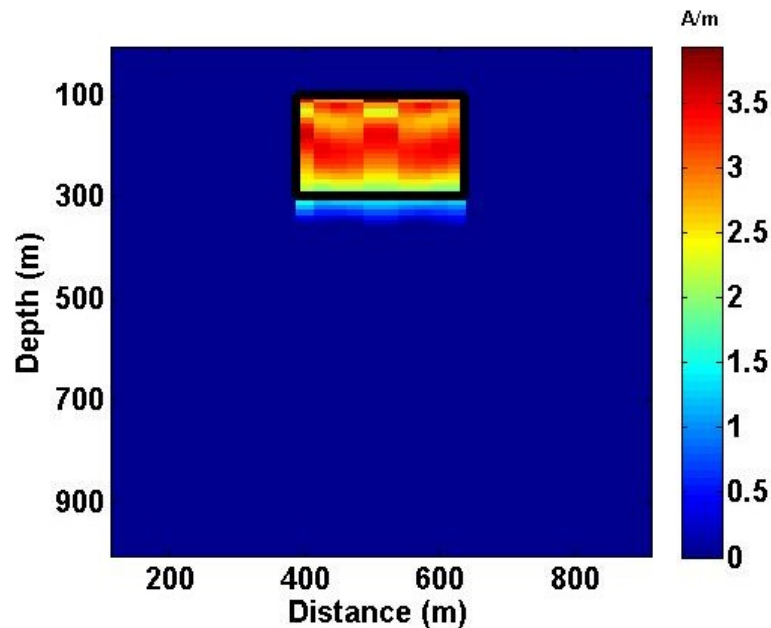


Figure 2.7: Vertical Soundings inversion of the calculated magnetic data produced by a single buried prismatic source obtained using an upper bound value greater than the true value. The black rectangle identifies the horizontal and vertical positions of the anomaly source.

### 2.6.2 Effect of constraints ( $d - \delta d < Gm < d + \delta d$ ) on inversion process

These constraints take into account experimental data errors. In order to obtain a better resolution of the recovered model, the components of  $\delta d$  vector should be as small as possible, while maintaining compatibility with the other constraints. In figure 2.8, I show the inverse model obtained from the Vertical Soundings inversion related to the data of the buried body, as in the previous sections, evaluating the effects of the constraints on data errors. Figure 2.8a is related to a Vertical Soundings inversion with  $\delta d = 10^{-4}$  nT, while figure 2.8b using  $\delta d = 10^{-2}$  nT.

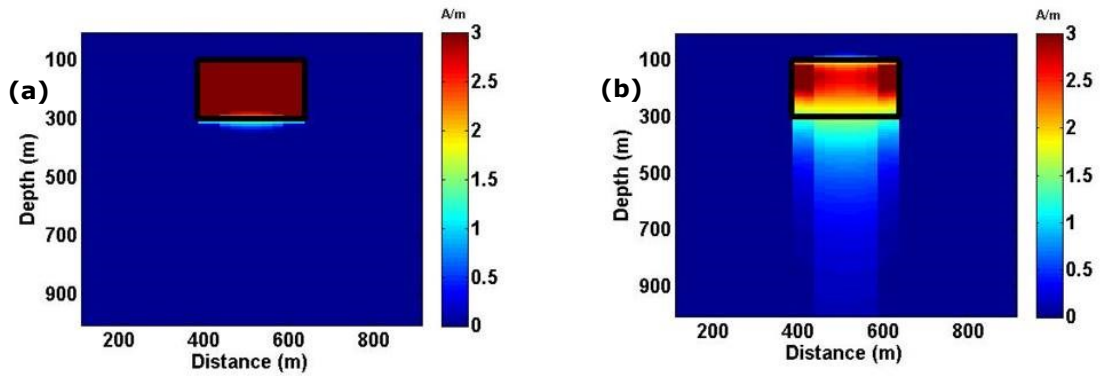


Figure 2.8: Vertical Soundings inversion of the calculated magnetic data produced by a single buried prismatic source obtained using for the data error a value of  $10^{-4}$  nT (a) and  $10^{-2}$  nT (b). The black rectangles identify the horizontal and vertical positions of the anomaly source.

As can be observed, increasing the value of the experimental data error causes a loss of resolution of the inverse models, which is mainly reflected in a loss of information about the correct location of the bottom of the anomaly source, while the top and the magnetization contrast are still successfully recovered.

### 2.6.3 Effect of the errors on the estimation of the horizontal dimensions of the source

The horizontal dimensions of an anomaly source are used to define the horizontal dimensions of the volume in the kernel calculation. In this work, the estimation of these horizontal dimensions was performed using a boundary analysis technique through the horizontal derivative method (Cordell and Grauch, 1985).

As I have already said, the horizontal dimensions obtained by the horizontal derivative method may be overestimated and should be considered as an upper bound to the true dimensions.

For the source used in the previous section, the horizontal derivative method allows to estimate the horizontal dimensions as 250×200 m (the right dimensions, as stated in Section 2.6, are 250×150 m) (figure 2.9).

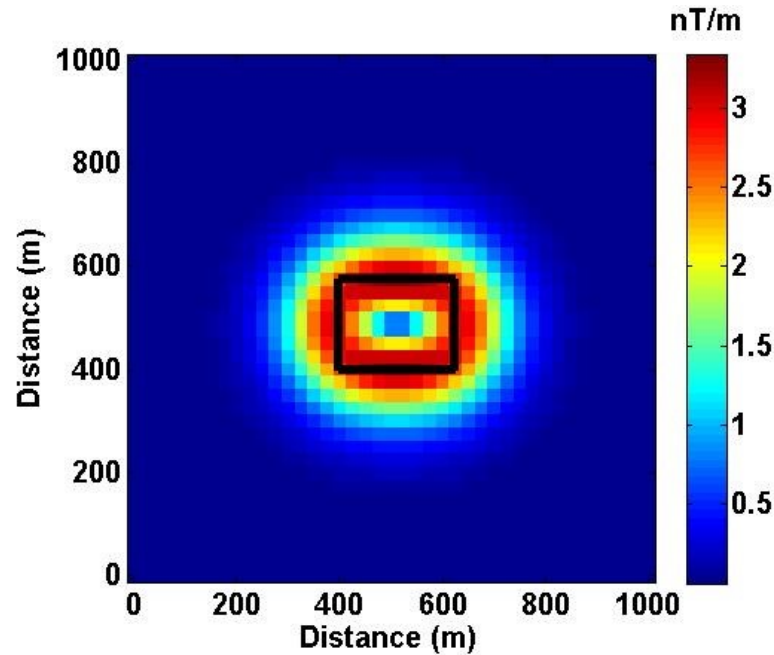


Figure 2.9: Total horizontal derivative of magnetic data generated by a single buried prismatic source. The maxima of this map are local estimations of the edges of the source. The black rectangle represents an estimation of the horizontal dimensions of the buried source, i.e. the position of the maxima of the horizontal derivative.

If I assume these horizontal dimensions in the kernel calculation, it is possible to obtain a useful inverse model only by increasing the value of the experimental data error. Figure 2.10 shows the inverse model recovered by using the horizontal dimensions obtained from the horizontal derivative method and using for  $\delta d = 2$  nT.

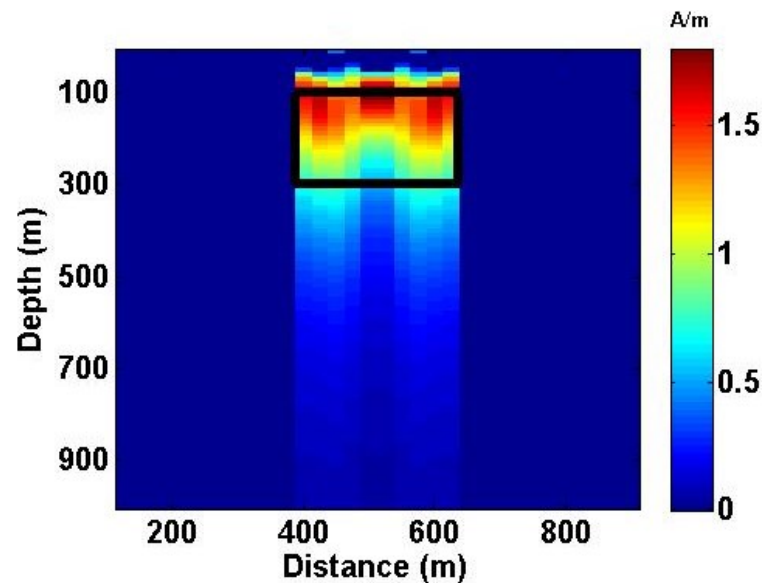


Figure 2.10: Vertical Soundings inversion of the calculated magnetic data obtained using for the kernel calculation a prismatic source with horizontal dimensions estimated from the horizontal derivative map. The black rectangle identifies the horizontal and vertical positions of the anomaly source.

The magnetization results underestimated, the position of the top is less accurate and for the bottom, there is a loss of resolution as consequence of the high value of  $\delta d$  constraints. However, it should be noted that in this case I overestimated one of the horizontal dimensions more than 30% of the real dimension, which is an error quite remarkable and depends mainly on the true dimensions and the position at depth of the source. For this type of source may be advantageous performing some transformations on the field data in order to obtain a more accurate estimation of the source dimensions. In fact, when the method of the horizontal derivative is applied on the vertical derivative of the field, the correct horizontal dimensions of the source are estimated (figure 2.11).

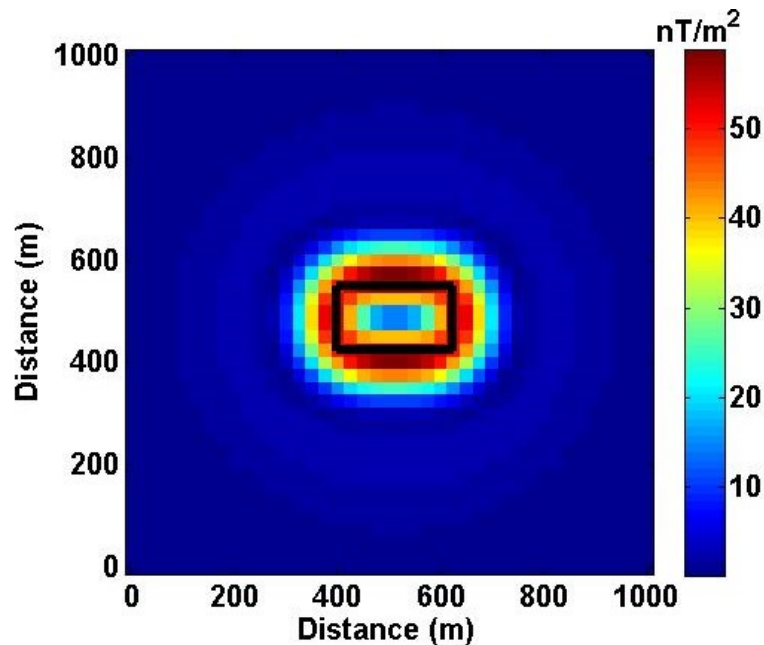


Figure 2.11: Total horizontal derivative of the vertical derivative of magnetic data generated by a single buried prismatic source. The black rectangle represents an estimation of the horizontal dimensions of the buried source, i.e. the position of the maxima of the horizontal derivative.

## 2.7 Vertical Soundings inversion of continued data

For the synthetic examples shown in the previous sections, the data were calculated thanks to an algorithm that allowed to evaluate the magnetic response at different altitudes. In a real case, it is quite unlikely to measure the magnetic field more than at one height over the ground. In the best case, with the gradiometric configuration, using two magnetic sensors, it might be possible have two different measurements at different altitude. As I am dealing with the inversion of vertical magnetic sounding, I need a way to

calculate the magnetic field at different altitudes, starting from the field measured at one altitude. It is well known that the magnetic field, as a potential field, obeys to Laplace's equation. This property allows the computation of a magnetic field over an arbitrary surface in the harmonic region. This procedure is called continuation. In order to build the vertical soundings, I have to upward continue the data taken at a single altitude, thus in this case the continuation altitudes are higher than the measurements altitude.

However the upward continuation operator introduces some errors in the calculated data at different altitudes. This because I approximate the convolution integral with a finite and discrete set of magnetic data, known on finite region. Anyway, the most severe errors commonly arise when using conventional circular convolution Fast Fourier Transform (FFT) algorithms, because frequency aliasing errors can affect the low-frequency content of the upward-continued data at high altitudes (Fedi et al., 2012). Fortunately, these errors can be kept low by performing the circular convolution on a larger area than that of interest (Oppenheim & Schaffer, 1975).

Therefore, the input data sequences can be extended to a greater length by using other surveys in nearby areas, if available, or, alternatively, by mathematical extrapolation algorithms, such as smooth extension, zero-padding, maximum entropy prediction, symmetrization and others. In my cases I used smooth extension of order 0 algorithm, simply consisting in extrapolating using the values of the anomaly field at its edges.

Such extrapolation will surely reduce the circular convolution error although introducing by itself a new error (since the continuation is performed using also the extrapolated data and not only the true data; Castaldo et al., 2014). However, such error, if the analyzed profile is chosen far from the boundaries of the measurement area and the continuation altitude is not too high with respect to the measurement area size, should be rather low (Fedi et al., 2012).

The effects of this error can be mitigated by approximating it by a first-order polynomial (I tested that a higher degree of the polynomial order does not produce an improvement in the recovered model).

$$P(z) = C_1 + C_2z \tag{2.34}$$

where  $C_1$ ,  $C_2$  are the unknown coefficients of the first-order polynomial. Using this polynomial I modify the dimensions of matrix  $F$  and vector  $h$  (equation 2.29).

The unknown coefficients are estimated automatically during the inversion process. Now the matrix  $I$  has dimension  $(M+2) \times (M+2)$  and the kernel  $G$  ( $N \times (M+2)$ ), while for the vector  $h$ , the bounds related to polynomial coefficients are completely unconstrained and its dimension becomes  $(2(M+2)+2N) \times 1$ .

In order to perform a Vertical Soundings inversion, I used the same source as for the calculated data. The horizontal dimensions are  $250 \times 150$  m and it is located at depth from 100 m to 300 m. The magnetization contrast with the surrounding volume is 3 A/m and its direction is vertical.

In this case, the vertical soundings consist of magnetic data continued at 20 different altitudes from the first level at 5 m up to the last level at 100 m with a 5 m constant step. The positions of the vertical soundings are the same as shown in figure 2.1 by the green points.

Even for this test, the calculation of the kernel considers a source volume with horizontal dimensions that are in agreement with those of the source that generates the anomaly while its vertical dimension contains the source of anomaly and it is discretized with 100 layers from 0 to 1000 m.

For this test, I set the correct magnetization contrasts for the lower and the upper bounds, the lower bound is equal to 0 and the upper bound is equal to 3 A/m.

I noticed that in order to recover a useful inverse model, the experimental error must be set to a value that is several order of magnitude greater than for calculated data. In this case I used a value equal to  $2 \times 10^{-2}$  nT. Its value takes into account the existence of the continuation errors but at same time it introduces a loss of resolution, especially at the bottom of the inverse model where some widenings appears and make more difficult a precise estimation of the depth of the bottom.

However, as shown in figure 2.12, the Vertical Soundings inversion is able to correctly recover the depth of the top of the source, the magnetization contrast is correctly estimated.

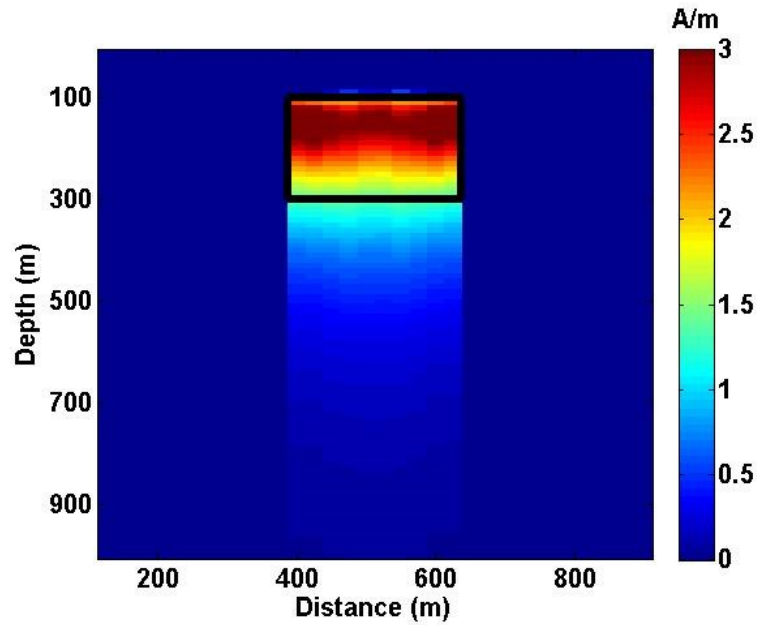


Figure 2.12: Vertical Soundings inversion of the magnetic data produced by a single buried prismatic source and continued at 20 different altitudes. The black rectangle identifies the horizontal and vertical positions of the anomaly source.

Even in this case I evaluated how the continued data along the profile at a fixed altitude (in this case the first height, 5m) are reproduced, calculating the estimated data from the estimated parameters. As shown in figure 2.13, the misfit is still very good along all the profile with a RMSD of 3.3 nT.

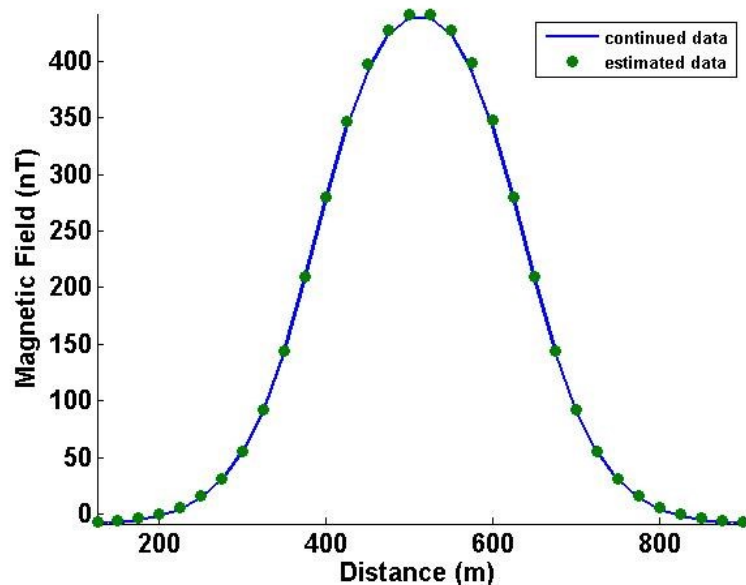


Figure 2.13: Comparison between the continued and the estimated data.

### 2.7.1 Effect of maximum altitude on inversion process

As I said in the Section 2.7, the continuation error increases with the altitude. This error has been approximated by a first-order polynomial and has requested more tolerance on the value of the experimental data error in order to obtain a useful inverse model. In this section, I analyze the effect of the choice of different maximum altitude of data continuation on the inversion process. In these tests I changed only the set of continuation altitudes, leaving unchanged all the others variables in the inversion process. In particular, I performed some Vertical Soundings inversions using the following continuation altitudes:

- from 3 m to 60 m with a constant step of 3 m (figure 2.14a);
- from 7 m to 140 m with a constant step of 7 m (figure 2.14b).

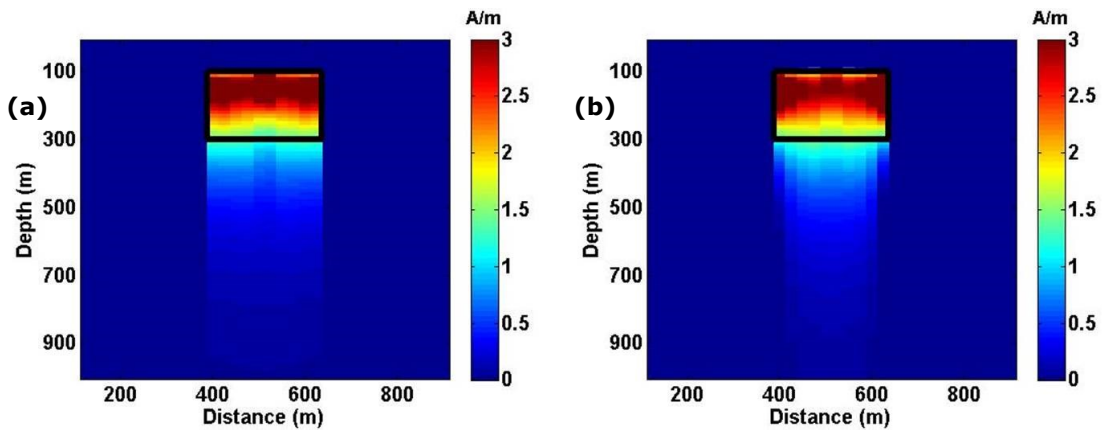


Figure 2.14: Vertical Soundings inversion of the magnetic data produced by a single buried prismatic source and continued at 20 different altitudes. The maximum continuation altitudes are 60 m (a) and 140 m (b). The black rectangles identify the horizontal and vertical positions of the anomaly source.

In order to obtain these inverse models I used different values for the components of the experimental data error vector. In particular for the first case, with a maximum altitude of sampling equal to 60 m, I used  $\delta d = 8 \times 10^{-3}$  nT, while for the second case, with a maximum altitude of sampling equal to 140 m I used  $\delta d = 5 \times 10^{-2}$  nT. As it can be seen the recovered inverse models are quite similar each other and at same time they are similar to the test in the previous section (figure 2.12), when the maximum altitude of sampling was equal to 100 m and where I have set  $\delta d = 2 \times 10^{-2}$  nT. In conclusion the Vertical Soundings inversion of continued data seems to be little sensitive to the maximum altitude of sampling if more tolerance on  $\delta d$  value with the increasing of the altitude is allowed.

### 2.7.2 Vertical Soundings inversion of continued data in presence of a linear trend

The synthetic tests described in the previous sections, both for calculated and continued data, refer to a simplified case, as it is really unlikely to find in nature completely isolated magnetic anomaly sources. In most cases, a map of magnetic data is the result of superposition of the magnetic anomalies generated by many sources, having different shapes and sizes, different depths and with different magnetization contrasts.

In order to build a test being closer to a real case, in this section, I describe a Vertical Soundings inversion performed on continued data related to the same source used so far with the addition of a linear trend. This trend is the magnetic anomaly produced by a very deep and large horizontal source. In particular, the prism created to generate this type of linear trend is placed at depth between 2 and 3 km, has a vertical magnetization of 7 A/m and both horizontal dimensions of 7.5 km.

The magnetic anomaly generated by the addition of these 2 sources and calculated at an altitude of 0.001 m above the ground is shown in figure 2.15a. The positions of the vertical soundings are those shown by the green points and they consist of magnetic data continued from the base level at 20 different altitudes from the first height at 5 m up to the last height at 100 m with a 5 m constant step (figure 2.15b).

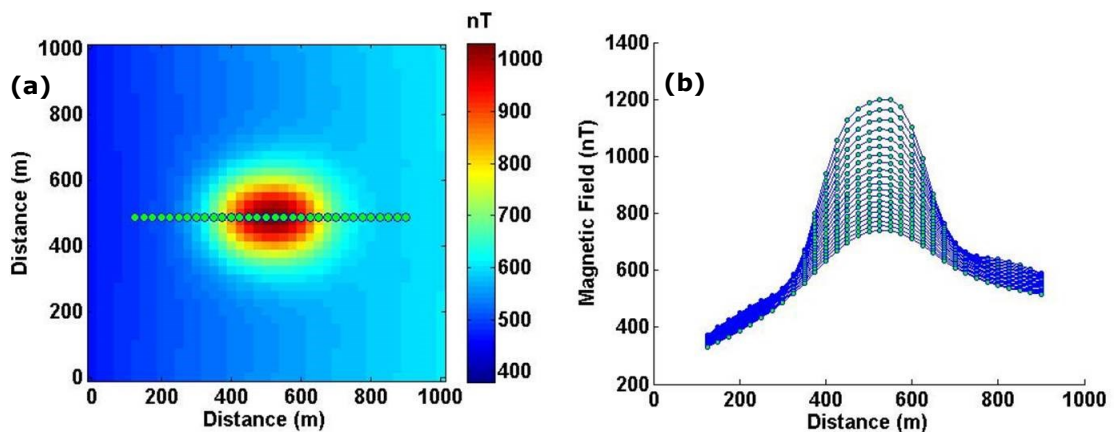


Figure 2.15: (a) Map of magnetic data generated by a single buried prismatic source and a deeper and larger horizontal source, that results in a E-W linear trend at observation level. The green dots represent the horizontal positions of the vertical soundings. (b) Profiles of magnetic data at different altitudes of continuation.

The presence of a linear trend involves a necessary modification to the procedure of the inversion technique. The linear trend may be seen like an error in the signal that should be mitigated.

A simple, yet effective way to remove a linear trend is the calculation of the vertical derivative of the field. This operator is able to increase the signal resolution, enhancing the high frequency components of anomalies map. For derivative field, the linear trend, which corresponds to a low frequency component of the signal, is greatly reduced. In figure 2.16a is shown the vertical derivative of the magnetic map and in figure 2.16b the profile of the vertical soundings that will be inverted.

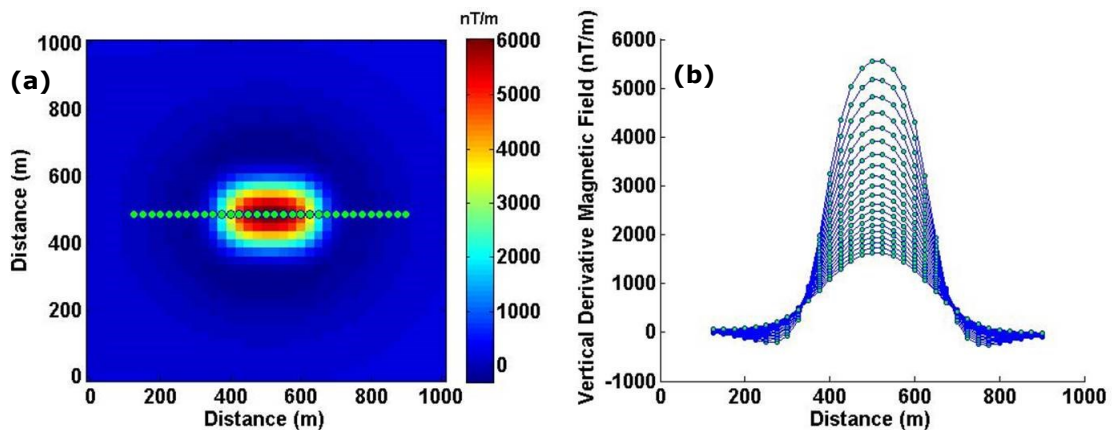


Figure 2.16: (a) Map of the vertical derivative of magnetic data generated by a single buried prismatic source and a deeper and larger horizontal source, resulting in a linear trend at observation level. The green dots represent the horizontal positions of the vertical sounding. (b) Profiles of vertical derivative of magnetic data at different altitudes of continuation.

As the Vertical Soundings inversion is performed on the data of the vertical derivative of the field, in order to obtain a correct dimension of the estimated parameters, I need to calculate the vertical derivative of the kernel. The source volume has, in this case, horizontal dimensions in agreement with those of the true source.

For this test, I used the correct magnetization contrasts for the lower and the upper bounds, setting the lower bound equal to 0 and the upper bound equal to 3 A/m. I noticed that to recover a useful inverse model, the experimental error must set to a very high value, if compared with previous tests, equal to 2 nT. The Vertical Soundings inversion provides good results in estimating the position of the top of the source and a correct magnetization contrast is also retrieved. It is instead more difficult to correctly define the position of the bottom (figure 2.17a). However, even in this case the magnetic anomaly along

a profile at a fixed altitude is very well reproduced with a RMSD of 5.2 nT (figure 2.17b).

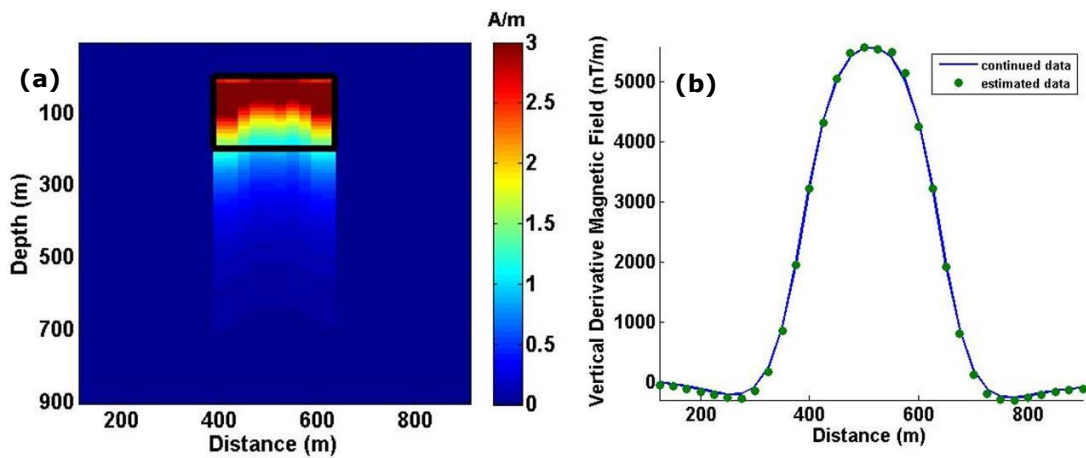


Figure 2.17: (a) Vertical Soundings inversion of the vertical derivative of magnetic data produced by a single buried prismatic source and continued at 20 different altitudes. The black rectangle identifies the horizontal and vertical positions of the anomaly source. (b) Comparison between the continued and the estimated data.

### 2.7.3 Vertical Soundings inversion of continued data produced by an irregular shaped prism

Until now I have considered calculated and continued data generated by sources with regular prismatic shape and I have seen that in order to recover a useful inverse model a correct estimation of the horizontal dimensions of the source of anomaly is needed. The real cases might involve several complications that have not been considered in the performed tests. One of these is related to the shape of the anomaly source that, in most cases, is not a regular prism. In this case, it might be difficult obtaining an accurate estimation of the horizontal dimensions, especially when the source is located at a considerable depth and its horizontal dimensions are not much larger than this depth. For this type of source I will show in this section that it is possible to define an equivalent prism with average horizontal dimensions allowing to recover a useful inverse model that still fits the data. These average dimensions are found with a trial and error approach.

The Vertical Soundings inversion was performed on continued data generated by a prismatic source of irregular shape as shown in figure 2.18a. A plan sketch of the synthetic source with its dimensions is shown in figure 2.18b.

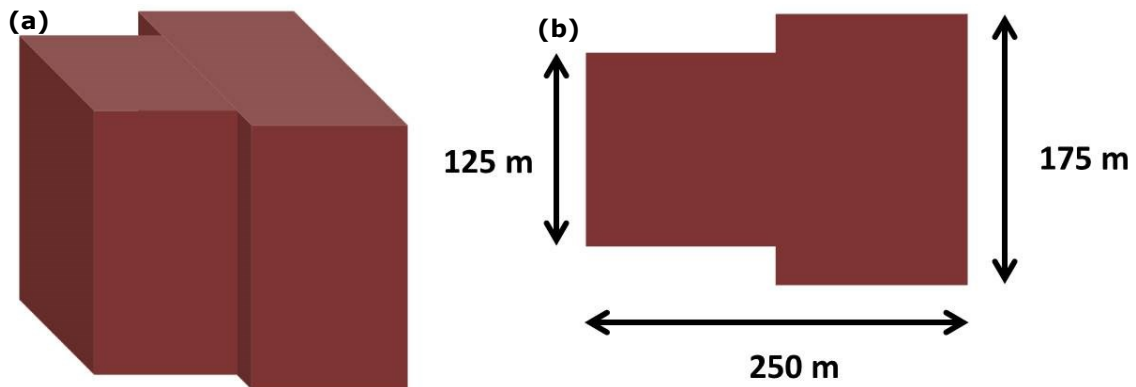


Figure 2.18: (a) 3D sketch of irregular prismatic source used to generate synthetic magnetic data. (b) Horizontal plan sketch of the same source.

The source is located at depths from 100 m to 300 m. The magnetization contrast with the surrounding volume is 3 A/m and its direction is vertical. The magnetic anomaly generated by this source, and calculated at an altitude of 0.001 m above the ground, is shown in figure 2.19a. The vertical soundings, as in the previous sections, are obtained by continuing the magnetic map from the base level at 20 different altitudes, from 5 to 100 m. If I try to estimate the horizontal dimensions of this source, by applying the horizontal derivative method on the vertical derivative of the field, I obtain, as shown in figure 2.19b, the following values: 250×175m. In this case the irregular geometry of the anomaly source (figure 2.18b) is not correctly recovered.

In order to increase the resolution, I applied the horizontal derivative method on the second vertical derivative of the field (figure 2.19c). In this case the dimensions of the anomaly source are retrieved accurately.

This means that it might be useful using higher order derivatives in order to characterize the horizontal dimensions of the source. However, the applicability of the vertical derivative in the real cases, especially of order greater than one, is closely related to the quality of the collected data. The noise at high-frequency in the data, enhanced by the vertical derivatives, can prevent a correct estimation of the horizontal dimensions. For this reason, the Vertical Soundings inversions performed for this type of source and shown below, have considered, for the kernel calculation, both the estimations of the source horizontal dimensions, i.e. those coming from analysis of the first and the second vertical derivative.

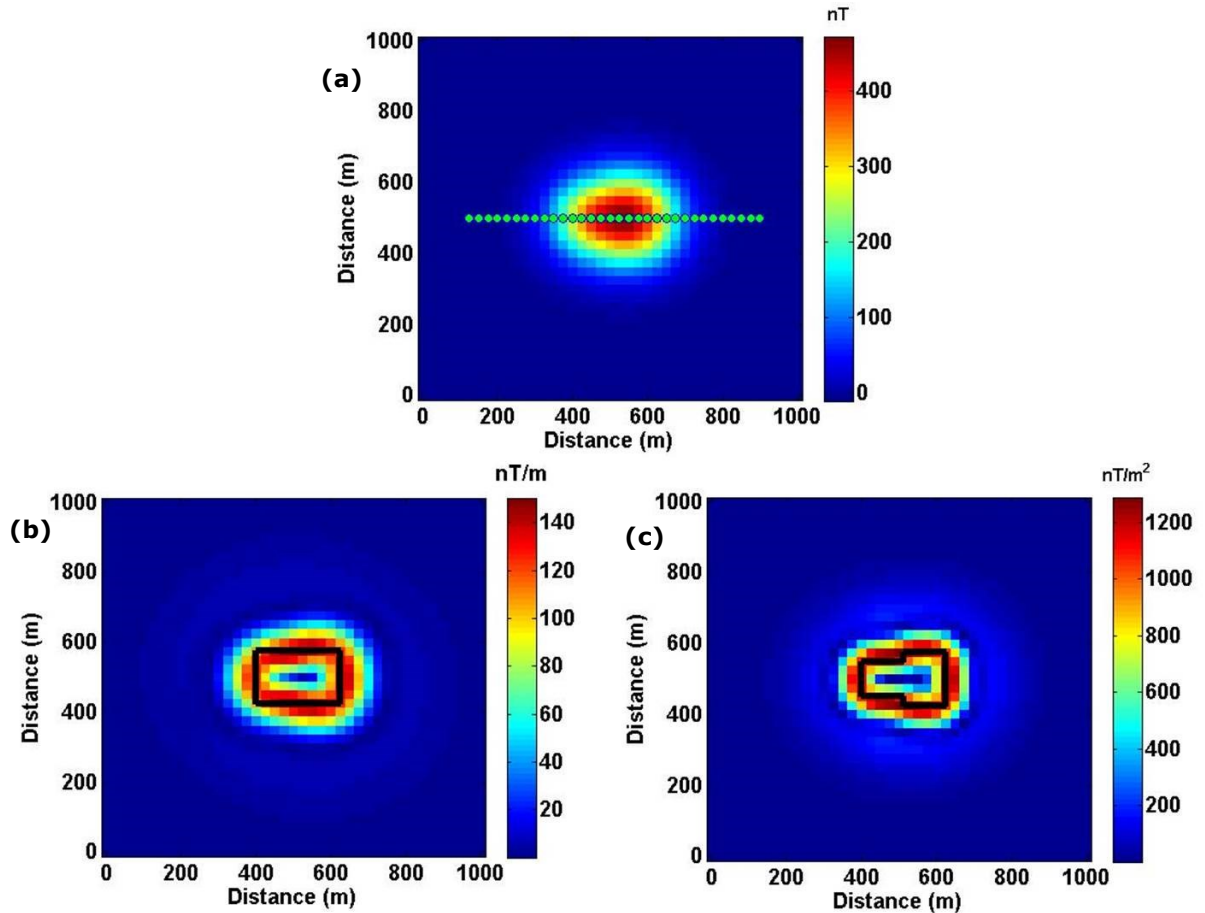


Figure 2.19: (a) Map of magnetic data generated by a single buried irregular prismatic source. The green dots represent the horizontal positions of the vertical soundings. (b) Total horizontal derivative of the vertical derivative of magnetic data. (c) Total horizontal derivative of the second vertical derivative of magnetic data. The black rectangles represent an estimation of the horizontal dimensions of the buried source, i.e. the position of the maxima of the horizontal derivative.

In the inversion process the magnetization lower and the upper bound have been set to the real values (0 and 3 A/m, respectively), while the components of the experimental data error are equal to  $\delta d = 2 \times 10^{-2}$  nT when using, in the kernel calculation, the correct shape and horizontal dimension of the anomaly source, while it is equal to  $2 \times 10^{-1}$  nT using the horizontal dimensions estimated from the horizontal derivative of the first vertical derivative of the field. The model obtained using the correct source dimensions (figure 2.20a) is in agreement with the previous results: the top of the source and the magnetization contrast are correctly estimated while the bottom of the source is described with less resolution. The model obtained using the overestimated source dimensions (figure 2.20b), shows a greater loss of resolution for each sounding, with an underestimation of the magnetization contrast that results

correct only for the central soundings. However, the depth to the bottom for these soundings is completely incorrect.

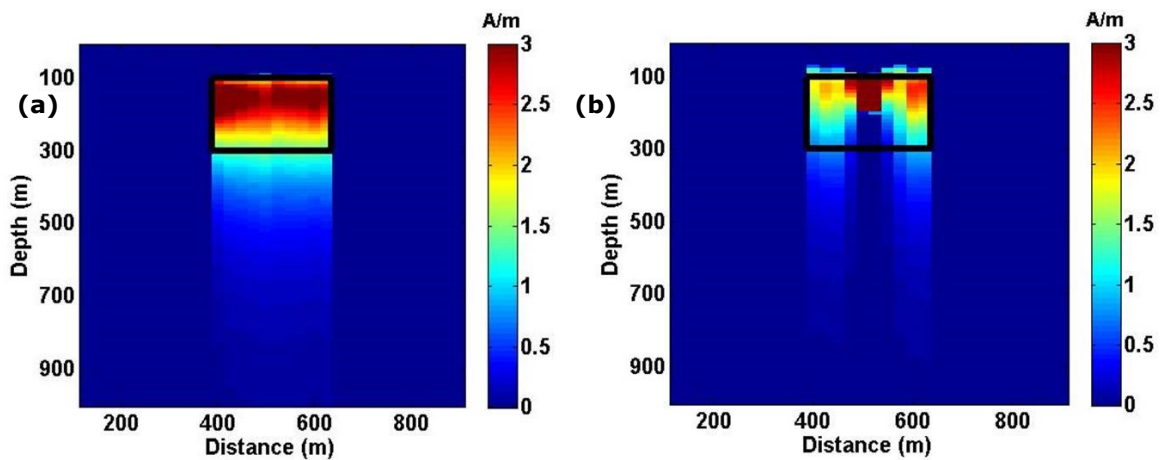


Figure 2.20: (a) Vertical Soundings inversion of the continued magnetic data obtained using for the kernel calculation a prismatic source with horizontal dimensions estimated from the horizontal derivative of the second vertical derivative of magnetic data. (b) Vertical Soundings inversion of the continued magnetic data obtained using for the kernel calculation a prismatic source with horizontal dimensions estimated from the horizontal derivative of the first vertical derivative of magnetic. The black rectangles identify the horizontal and vertical positions of the true anomaly source.

Fedi and Rapolla (1995) have shown a case of source with irregular vertical shape. In particular, in order to simulate the anomaly of a sedimentary basin, they inverted the gravity anomaly produced by a layered source with a depth-increasing density and with a decreasing horizontal width for each layer. In this case the horizontal derivative provided the dimensions of the shallow layer. These authors have demonstrated that these dimensions are not useful as the source doesn't have vertical sides. In this case, they used a prism that is smaller than the real one at shallow depth. The dimensions of this prism are obtained by a trial and error approach. In other words they have shown that it is possible to find an equivalent prismatic source to calculate the kernel in the inversion process in order to recover a useful inverse model.

Starting from this result I performed two other Vertical Soundings inversions, using as the theoretical volume in the kernel calculation, two prisms with lower dimensions than those estimated in figure 2.19b:

- 250×150 m;
- 250×125 m.

In the inversion process I set the lower and the upper bound equal to the real

values and the components of the experimental data error are equal to  $\delta d = 2 \times 10^{-2}$  nT.

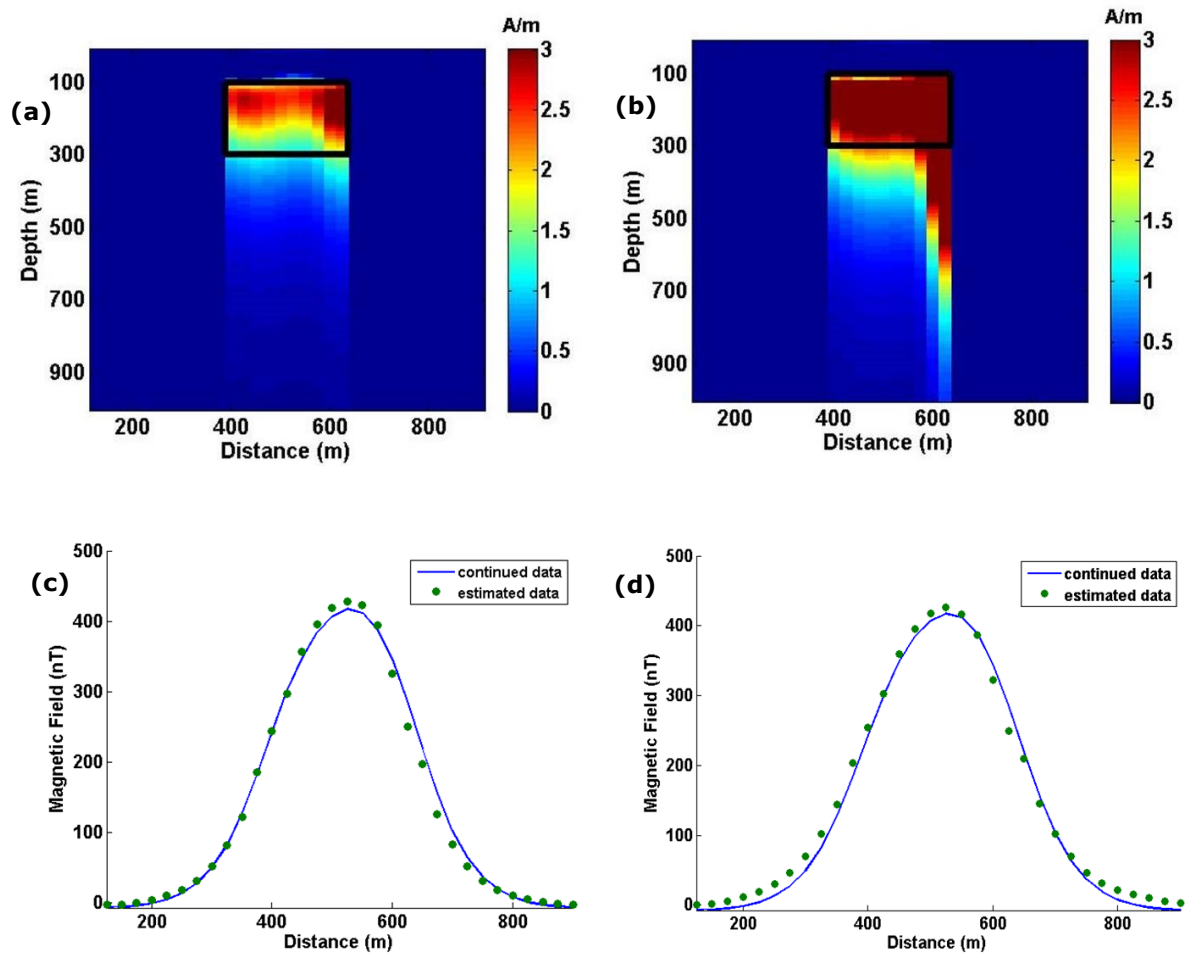


Figure 2.21: Vertical Soundings inversions of the continued magnetic data obtained using for the kernel calculation an equivalent prismatic source prismatic source with horizontal dimensions of  $250 \times 150$  m (a) and  $250 \times 125$  m (b). The black rectangles identify the horizontal and vertical positions of the anomaly source. Plot (c) and plot (d) show the comparisons between the continued and the estimated data related to the inverse models (a) and (b) respectively.

The inversion model obtained using an equivalent prism with horizontal dimensions of  $250 \times 150$  m (figure 2.21a) allows to recover an inverse model that is quite similar to that obtained using the real horizontal dimensions for the kernel calculation (the horizontal dimension in x direction is 250 m, while in y direction are 125 and 175 m; see figure 2.20a) and with a really acceptable data misfit with a RMSD of 11.9 nT (figure 2.21c). In the other case, when the equivalent prism has dimensions  $250 \times 125$  m (figure 2.21b), the depth to the top and the magnetization contrast are correctly retrieved, while the depth of the bottom is now overestimated. This involves a

deterioration of the data misfit with a RMSD of 14.6 nT as shown in figure 2.21d.

In conclusion, the possibility to find an equivalent prism that can approximate the real horizontal dimensions of anomaly source represents an important simplification when you are dealing with the real data, where the anomaly sources are of different irregular shapes, both horizontally and vertically.

## **CHAPTER 3 – Joint inversions of two VTEM surveys using quasi 3d TDEM and Vertical Magnetic Soundings algorithms: the case study of the Broken Evil prospect, Ontario (CANADA)**

### **3.1 Geological setting of the Superior Province, Ontario, Canada**

The Canadian Shield is subdivided into geological provinces (Percival, 2007). The Superior Province consists of east-west trending alternating belts of predominantly volcanic, sedimentary and gneissic rocks, representing the accreted remains of ancient continents and ocean basins. The Superior Province is accordingly further subdivided into a number of sub-provinces, described according to their lithologies, structures, and metamorphic grade character.

The Superior Province, which is the oldest, largest and consists of rocks of Achaean age (i.e. greater than 2.5 billion years old), with autochthonous cover sequences underlie approximately 80% of the province of Ontario.

Current views regard the Superior Province as a collage made up of small continental fragments of Mesoarchean age and Neoproterozoic oceanic plates with a complex history of aggregation between 2.72 and 2.68 Ga (Percival 2007) and subsequent post-orogenic effects.

Tectonic stability has prevailed since ca. 2.6 Ga in large parts of the Superior Province (e.g., Percival, 2007). Proterozoic and younger activity is limited to rifting of the margins, emplacement of numerous mafic dyke swarms (Buchan and Ernst, 2004), compressional reactivation, large-scale rotation at ca. 1.9 Ga, and failed rifting at ca. 1.1 Ga. With the exception of the NW and NE Superior margins that were pervasively deformed and metamorphosed at 1.9 to 1.8 Ga, the Craton has escaped ductile deformation.

Sedimentary rocks as old 2.48 Ga unconformably overlie Superior Province granites, indicating that most erosion had occurred prior to ca. 2.5 Ga.

A first-order feature of the Superior Province is its linear subprovinces of distinctive lithological and structural character, accentuated by subparallel

boundary faults (Card and Ciesielski, 1986, Percival, 2007). Trends are generally East-West.

Several domains of Mesoarchean age are recognized in spite of pervasive Neoproterozoic magmatism, metamorphism, and deformation. The term “terrane” is used in the sense of a geological domain with a distinct geological history prior to its amalgamation into the Superior Province during 2.72 to 2.68 Ga assembly events. “Superterrane” show evidence for internal amalgamation of terranes prior to the Neoproterozoic assembly. “Domains” are defined as distinct regions within a terrane or superterrane.

Domains of oceanic ancestry, identified by juvenile isotopic signatures, separate most of the continental fragments. These dominantly greenstone-granite terranes generally have long strike lengths and record geodynamic environments including oceanic floor, plateaux, island arc, and back-arc settings (Thurston, 1994). Rocks formed in these environments host some of the largest massive sulfide deposits (VMS) of the Province, particularly in the Abitibi greenstone belt (southeastern part of the Superior Province).

Still younger features, the metasedimentary terranes (Breaks, 1991; Williams, 1991; Davis, 2002), separate some of the continental and oceanic domains. Extending across the entire Province, these 50 to 100 km wide belts of metagreywacke, migmatite, and derived granite appear to represent thick synorogenic sequences that were deposited, deformed, and metamorphosed during collisional orogeny. Faults, developed in association with several distinct tectonic events, host a variety of orogenic gold deposits across the Province.

### **3.1.1 The Abitibi Terrane in the Eastern Superior Province**

Large parts of the Abitibi terrane in Ontario are poorly exposed as a result of subdued topography and extensive glacial lake clay deposits. The Abitibi terrane has been subdivided into three domains with overlapping tectonostratigraphic histories. In the northern Abitibi, volcanic assemblages are mainly 2.74 to 2.72 Ga old (Ludden et al., 1986; Chown et al., 1992; Legault et al., 2002) and associated with layered intrusions. The central zone is dominated by plutonic rocks (Chown et al. 2002). Volcanic rocks of 2.71 to 2.695 Ga and their associated mineral deposits are restricted to the southern

Abitibi of Ontario and Quebec (Dimroth et al. 1984; Daigneault et al. 2002). In addition, the southern Abitibi has relatively young sedimentary volcanic deposits including greywackes (ca. 2.69 Ga) of the Porcupine Group (Bleeker and Parrish 1996) and conglomeratic and alkaline volcanic rocks (2.677 to 2.673 Ga) of the Timiskaming Group (Davis 2002).

### 3.1.2 The Broken Evil prospect in the Abitibi greenstone belt

The Broken Evil prospect lies in the Abitibi greenstone belt, in the eastern part of Superior Province.

The region hosts some of the richest mineral deposits of the Superior Province, including the giant Kidd Creek massive sulfide deposit (Hannington et al. 1999) and the large gold camps of Ontario and Quebec (Robert and Poulsen 1997).

The area is underlain by intermediate and mafic metavolcanics, pyroclastics and metasediments. These early Precambrian units have been intruded by several metamorphosed mafic and ultramafic bodies. Figure 3.1 shows the general bedrock types present in the area.

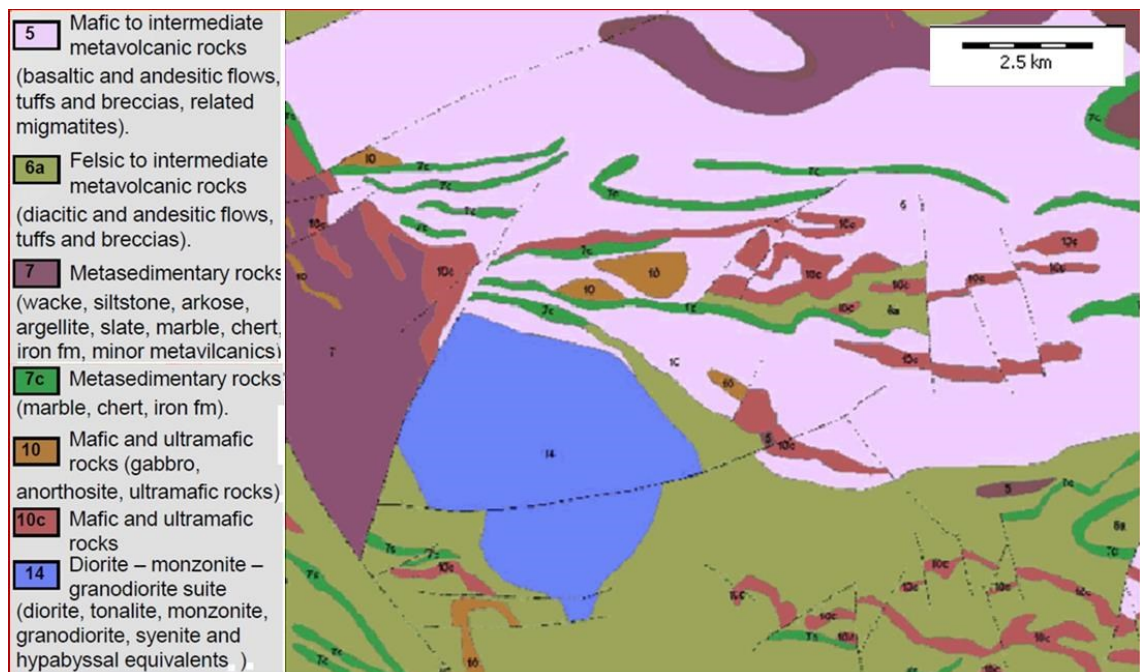


Figure 3.1: Bedrock geology of the area under study.

Bedrock outcrops in the area of interest are very rare; thick Quaternary overburden is widely spread. The overburden thickness may reach 30-50 meters.

The property was extensively covered by drill holes. There is historic and new drilling data available. The most recent drilling program took place in 2011 initialized by Promiseland Exploration, Ltd of Vancouver, following the information provided by a ground geophysical survey of the area using ERA low frequency EM profiling (Kaminski et al., 2011). Based on the interpretation of the geophysical data, anomalous conductive zone was delineated and interpreted as potential Volcanic Massive Sulfide (VMS) mineralization target. The drilling program, carried out in 2011, has revealed a 21 m thick zone with disseminated to massive mineralized interval starting at 82 m depth.

Exploration is currently under way. This area is undergoing active mineral exploration, including VMS and VMS-Au targets.

It is expected that VMS deposits in the area will generate strong conductive and chargeable anomalies, which may or may not be magnetic (Kidd Creek deposit is non-magnetic).

### **3.2 Geophysical features of Volcanogenic Massive Sulfide Deposits**

Volcanogenic massive sulfide deposits are major sources of Zn, Cu, Pb, Ag, and Au and significant sources for Co, Sn, Se, Mn, Cd, In, Bi, Te, Ga and Ge.

The most common feature among all types of VMS deposits is that they are formed in extensional tectonic settings, including both oceanic seafloor spreading and arc environments.

They typically occur as lenses of polymetallic massive sulphide that form at or near the seafloor in submarine volcanic environments. They form from metal-enriched fluids associated with seafloor hydrothermal convection. Their immediate host rocks can be either volcanic or sedimentary.

Most VMS deposits have two components. There is typically a mound-shaped to tabular, stratabound body composed principally of massive (>40%) sulfide. These stratabound bodies are typically underlain by a discordant stockwork or stringer zone with vein-type sulfide mineralization.

The mineralization results in precipitation of pyrite, pyrrhotite, chalcopyrite, sphalerite and galena. Other possible nonsulfide minerals associated in VMS deposits include magnetite, hematite and cassiterite (Galley et al., 2007).

Volcanogenic Massive Sulfide (VMS) deposits have typically strong geophysical contrasts with their host rocks, due to substantial differences in physical properties between the deposits and the rock in which they form (Thomas et al., 2000). These properties are mainly susceptibility, density, and resistivity.

Mining geophysics has long played a major role in VMS exploration. It is well known that numerous discoveries have been directly due to geophysics, commonly detected by magnetic or electromagnetic surveys (Boivin, 2007).

Many sulfide minerals have high values of magnetic susceptibility resulting in prominent magnetic anomalies associated with VMS ore bodies. In some cases, the strong magnetic signature of a VMS deposit is associated with noneconomic mineralization. For example, a Cu-rich, chalcopyrite-bearing VMS deposit may have a strong magnetic anomaly due to its association with pyrrhotite, a highly magnetic but noneconomic mineral. Pyrrhotite and pyrite are the most common mineral associated with VMS deposits and are characterized by high values of magnetic susceptibility ( $3200 \times 10^{-3}$  SI for pyrrhotite and  $5 \times 10^{-3}$  SI for pyrite (Thomas et al., 2000)).

These high values, compared to the lower values measured in most sedimentary and volcanic host rocks, produce strong positive magnetic anomalies.

Other common sulfide minerals in VMS deposits, such as chalcopyrite, sphalerite and galena, have lower values of magnetic susceptibility that are similar to those found for their sedimentary and volcanic host rocks and thus do not contribute to any magnetic anomaly associated with the VMS ore body. However, these minerals rarely form as an isolated sulfide and their association with noneconomic sulfide, with high values of magnetic susceptibility, allow their identification (Bishop and Emerson, 1999).

In addition, nonsulfide metallic mineral with high susceptibility values, such as magnetite ( $5500 \times 10^{-3}$  SI) and hematite ( $40 \times 10^{-3}$  SI) also are common in some massive sulfide deposits and contribute to the strong positive magnetic anomalies found associated with these ore bodies (Thomas et al., 2000). The metallic minerals can occur in the core of the stockwork and central base part

of the overlying sulfide lens (Ford et al., 2007). Alternatively, iron formation deposits rich in magnetite and hematite can be temporally and spatially associated with VMS deposits (Peter et al., 2003), amplifying the associated magnetic anomalies.

In some cases, VMS deposits can be associated to small localized magnetic anomalies for the hydrothermal alteration of footwall rocks beneath massive sulfide deposits that may lead to the destruction, through oxidation, of the magnetic phase (Tivey et al., 1993, 1996).

In order to identify VMS deposits also conductivity represents a useful physical property. The physical contrast between VMS deposits and its host rock may be significant. In fact, these deposits have high conductivities exceeding 500 mS/m and are similar in magnitude to graphite and saltwater, compared to igneous and metamorphic rocks with typical conductivities of <1 mS/m and sedimentary rocks with conductivities from 1 to 500 mS/m (Ford and others, 2007).

A complicating factor, however, may be the presence of a water-rich unit overlying the VMS ore body, this unit may be highly conductive and can mask the signal from the ore body. Saturated overburden may produce conductivity values that effectively mask the EM response of the VMS mineralization (Thomas and others, 2000). Also anoxic sedimentary horizons that contain graphite are also highly conductive and are difficult to distinguish from massive sulfide deposits.

In addition airborne electromagnetic techniques are effective in detecting massive sulfide mineralization, only if the sulfide grains in the deposit are electrically connected (Dubé et al., 2007). In cases where sulfide grains are not electrically connected, such as in the disseminated sulfide stockwork below the main massive sulfide ore body, induced polarization can be successfully employed to detect these and other disseminated sulfides.

### **3.3 The 2013 Versatile Time Domain Electromagnetic (VTEM<sup>plus</sup>) survey over the Broken Evil prospect**

During June 4<sup>th</sup> to 8<sup>th</sup> 2013, Aeroquest Airborne performed a helicopter-borne geophysical survey over the Broken Evil Block located approximately 11 km southwest of Cochrane, Ontario (figure 3.2a).

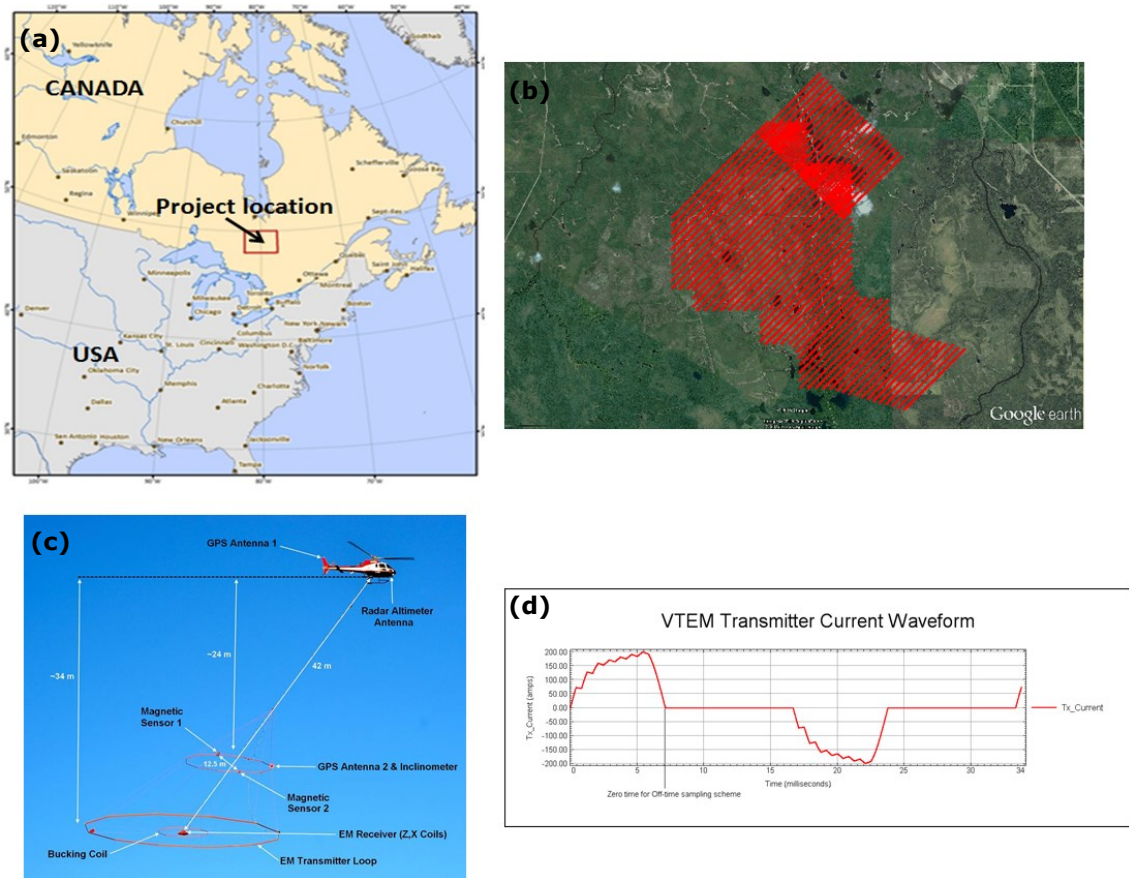


Figure 3.2: (a) The location of the Broken Evil prospect in northern Ontario (Canada); (b) the area of 2013 VTEM survey on Google Earth; (c) the VTEM<sup>plus</sup> system configuration; (d) VTEM waveform (adapted from Aeroquest Broken Evil survey report, 2013).

The geophysical surveys consisted of helicopter borne EM using the Geotech “Versatile time-domain electromagnetic” (VTEM<sup>plus</sup>) system with Z and X component measurements and horizontal magnetic gradiometer using two cesium magnetometers. The system included a GPS navigation system and a radar altimeter (figure 3.2c) (Legault et al., 2012).

A total of 323 line-kilometers of geophysical data were acquired during the survey over an area of 61 square kilometers (figure 3.2b).

The block was flown in a southwest to northeast direction with traverse line spacing of 100 and 200 m.

Topographically, the blocks exhibit a shallow relief with an elevation ranging from 258 to 296 m above mean sea level.

There are various rivers and streams running through the survey area which connect various lakes and wetlands. There are visible signs of culture such as roads, buildings and trails throughout the survey area.

During the survey the helicopter was maintained at a mean altitude of 68 m above the ground with an average survey speed of 80 km/hour. This allowed for an actual average EM bird terrain clearance of 36 m and a magnetic sensor clearance of 44 m.

The electromagnetic system consists of receiver and transmitter coils that were in concentric-coplanar and Z-direction oriented configuration. The receiver system also included a coincident-coaxial X-direction coil. In table 3.1 are listed the transmitter and the Z-receiver specifications:

| <b>Transmitter</b>                |   |
|-----------------------------------|---|
| <i>Coil diameter</i>              | <i>26 m</i>                             |
| <i>Number of turns</i>            | <i>4</i>                                |
| <i>Effective transmitter area</i> | <i>2123.7 m<sup>2</sup></i>             |
| <i>Base frequency</i>             | <i>30 Hz</i>                            |
| <i>Peak current</i>               | <i>187 A</i>                            |
| <i>Pulse width</i>                | <i>7.12 ms</i>                          |
| <i>Waveform shape</i>             | <i>Bi-polar trapezoid (figure 3.2d)</i> |
| <i>Peak dipole moment</i>         | <i>397131 nIA</i>                       |
| <b>Z-Receiver</b>                 |   |
| <i>Coil diameter</i>              | <i>1.2 m</i>                            |
| <i>Number of turns</i>            | <i>100</i>                              |
| <i>Effective receiver area</i>    | <i>113.04 m<sup>2</sup></i>             |

Table 3.1: VTEM<sup>plus</sup> system specifications.

The VTEM decay was sampled using 32 time measurement gates in the range from 0.096 to 7.036 ms after the time-off.

Zero time for off-time sampling scheme is equal to current pulse width and defined as the time near the end of the turn-off ramp where the dI/dt waveform falls to 1/2 of its peak value.

Some processing procedures, through a digital filtering process, were used to reject major spherical events and to reduce the system noise. Then, the raw collected data are stacked and recorded at 0.1 s.

The horizontal gradients data from the VTEM<sup>plus</sup> system are measured by two magnetometers 12.5 m apart on an independent bird mounted 10 m above the VTEM loop. A GPS and an inclinometer help to determine the positions and orientations of the magnetometers. The data from the two magnetometers are

corrected for position and orientation variations, as well as for the diurnal variations using a base station data.

The position of the center of the horizontal magnetic gradiometer bird is calculated from the GPS positions of the 2 magnetometers and at that position the total magnetic intensity is obtained by calculating the mean values from both sensors. The magnetic data are recorded at a sampling interval equal to 0.1 s.

### 3.4 The 2007 Versatile Time Domain Electromagnetic (VTEM) survey over the Broken Evil prospect

Previously, in 2007, another geophysical survey was carried out over the same area along traverse line spacing of 200 m (figure 3.3b).

The geophysical survey consisted of helicopter borne EM using the VTEM systems and aeromagnetics using a caesium magnetometer. The system included also a GPS navigation system and a radar altimeter.

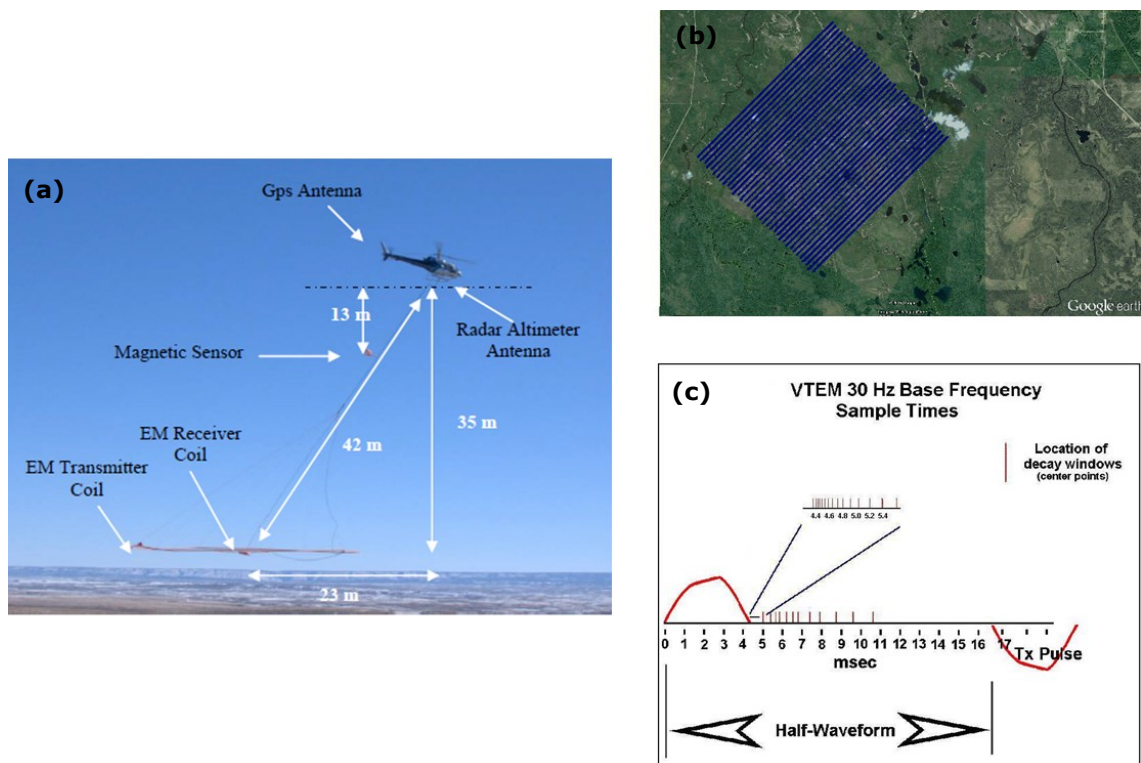


Figure 3.3: (a) the VTEM system configuration; (b) the area of 2007 VTEM survey on Google Earth; (c) VTEM waveform (adapted from Aeroquest Broken Evil survey report, 2007).

Receiver and transmitter coils of the EM system are concentric and Z-direction oriented. The coils were towed at a mean distance of 35 m below the aircraft (figure 3.3a).

Transmitter and Z-receiver specifications are listed in table 3.2:

| <b>Transmitter</b>                |                         |
|-----------------------------------|-------------------------|
| <i>Coil diameter</i>              | 26 m                    |
| <i>Number of turns</i>            | 4                       |
| <i>Effective transmitter area</i> | 2123.7 m <sup>2</sup>   |
| <i>Base frequency</i>             | 30 Hz                   |
| <i>Peak current</i>               | 262 A                   |
| <i>Pulse width</i>                | 4.2 ms                  |
| <i>Waveform shape</i>             | Trapezoid (figure 3.3c) |
| <i>Peak dipole moment</i>         | 556400 nIA              |
| <b>Z-Receiver</b>                 |                         |
| <i>Coil diameter</i>              | 1.2 m                   |
| <i>Number of turns</i>            | 100                     |
| <i>Effective receiver area</i>    | 113.04 m <sup>2</sup>   |

Table 3.2: VTEM system specifications.

The 2007 VTEM decay was sampling using 26 time measurement gates in the range from 0.120 to 9.245 ms after the time-off.

The strength of magnetic field is measured by a magnetic sensor mounted in a separate bird, 13 m below the helicopter. The magnetic data are corrected for diurnal variation using the digitally recorded ground base station magnetic values. The EM and magnetic data are sampled at 0.1 s.

The VTEM system used in 2007 had different moment, waveform shape and receiver times from the 2013 VTEM system. From an instrumental point of view, they represent two completely distinct datasets.

### **3.5 VTEM data processing**

The AEM data handling represents a logistical challenge for every AEM survey. The main steps of the data handling, which lead to the presentation of the results and the following geophysical and geological interpretations, involve the processing and the inversion.

The 2 dataset, related to the 2 VTEM systems, consist of navigation data, voltage data and magnetic data.

The aim of data processing is to prepare data before an inversion is run.

The processing of magnetic data including diurnal correction, IGRF removal and leveling, is usually done by the contractors.

The processing procedures of navigation and voltage data include importing the data, altitude corrections, filtering and discarding the data contaminated by cultural noise. A spatial average is then applied on the data in order to improve the S/N ratio without compromising the lateral resolution.

The AEM data were processed using the Aarhus Workbench software package (Auken et al., 2009). The Aarhus Workbench is a common platform for working with geophysical, geological, and GIS data. It includes fully integrated modules for generating geophysical thematic maps, geo-statistic modeling, and visualizations on GIS maps. This is extremely important when working in densely inhabited areas where long data sequences often have to be culled because data are severely biased by coupling to man-made conductors (Danielsen et al. 2003).

In general the AEM data processing is realized in a four-step process (Auken et al., 2009):

1. automatic filtering and averaging of navigation data; any manual corrections may also have to applied to the altitude data;
2. automatic filtering and averaging of voltage data, in order to minimize high frequency noise;
3. further refinement of voltage data through manually processing, especially in areas with cultural responses;
4. a fast inversion, using a smooth model to fine-tune the processing done in the previous steps.

### **3.5.1 Navigation data processing**

The 2013 VTEM system includes 2 GPS antennas: the first is mounted on the helicopter tail; the second is installed on the additional magnetic loop together with an inclinometer. The GPS receiver is mounted on the instrument panel, in front of the pilot to direct the flight. As many as 11 GPS and 2 WAAS (Wide Area Augmentation System) may be monitored at one time. The positional accuracy is 1 m. The differentially corrected GPS positional survey data are recorded in real-time as 0.2 s interval geodetic coordinates. In addition a radar altimeter was used to record the terrain clearance, with a sampling rate

of 0.2 s. The antenna was mounted beneath the bubble of the helicopter cockpit. The 2007 VTEM system comprises a GPS receiver with an antenna mounted on the helicopter tail. The data measured every 0.2 s have an accuracy of 1 m. Even in this case, a radar altimeter is mounted beneath the bubble of the helicopter to measure, every 0.2 s, the terrain clearance.

The position of the transmitter, receiver and magnetometer (when the GPS is not present) are calculated by using the nominal distances of the system.

As mentioned above, navigation data are automatically filtered and averaged.

In general, the results of the automatic processing are checked using profile plots of flight time versus data value (altitude, voltage data, etc). These plots can include also other quality control parameters as flight speed, topography, etc or system parameters as transmitter current, transmitter temperature, etc. (figure 3.4a).

An integrated interactive GIS map allows defining the location of the helicopter (figure 3.4b).

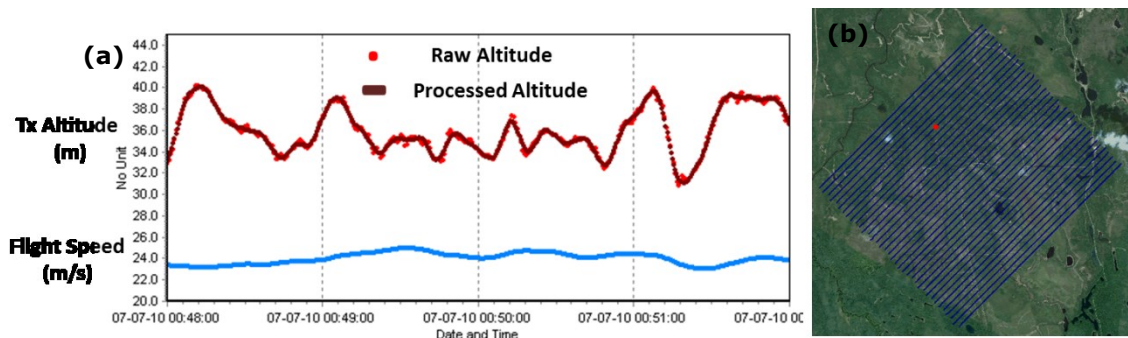


Figure 3.4: (a) Integrated plot of navigation data. Raw altitude data from the altimeter are shown in red, the processed and transmitter altitude in brown. The helicopter speed is light-blue; (b) the area of 2007 VTEM survey on Google Earth, with a red dot defining the position of the helicopter.

When combined with proper GIS themes, this generally enables explanation of the majority of data features, for example a sudden increase in altitude and relatively coherent noise is caused by the helicopter crossing a power line, road, or railway, and poor reflections can be caused by the helicopter traveling over a forest.

A correct estimation of the altitude of the EM system is necessary, especially, in highly resistive areas to distinguish the ground from air and to prevent shallow false resistive artifacts in the inverse models. At the same time, the flight altitude is included as an inversion parameter with a priori value and an

accurate measurement helps to stabilize and speed up the inversion (Auken et al., 2009).

### **3.5.2 Voltage data processing**

There are 3 categories of voltage data according to their processing stage:

1. instrument data that consist in stream un-stacked transients from the receiver (both VTEM systems, operating at 30 Hz, measured 30 transients every second);
2. raw data that consist in stacks of transients and their binning according to decay sampling scheme specific of each system (both VTEM systems record the data at a sampling rate of 0.1 s, this means that every transient of raw data is obtained from the stacking of 3 transients of instrument data);
3. average data that consist in averages of raw data stacks.

Some processing procedure are applied over the first 2 categories of data using some proprietary software algorithms developed by Geotech Ltd. Mainly, they consist in the compensation of the data for the primary field, in digital filtering processes to reduce noise level and in data leveling.

Other corrections, applied by the contractor using proprietary software, concern the variations in the transmitter current and the drift in the transmitter and receiver electronics that result from changes in temperature, humidity, and pressure. Both effects may significantly influence the measured data.

Transmitter current can be monitored and system drift can be estimated from measurements made at high elevations not influenced by the earth.

The average data are obtained using the Aarhus Workbench software package. The voltage data required a lot of manual processing, even though filters have been designed to help cull disturbed data. This occurs especially in areas with a significant amount of man-made structures, such as pipes, power lines and metal fences. In these areas capacitive and galvanic phenomena affect the data, which have to be removed entirely from the raw stacks. Danielsen et al. (2003) describe the physics of these phenomena in detail. The detection of galvanic coupling is not considered viable through a designed filter as the signal level is simply raised and does not shows oscillation. The capacitive

coupling, instead, shows oscillations and sign changes in the EM transient and for this reason is simple to detect and is easy to design an appropriate filter. This filter search the oscillations and the sign changes within the time interval where a useful signal is to be expected, this means starting from the first gate until the signal reaches the noise floor.

The data averaging of raw data stacks, performed by the Aarhus Workbench, responds to two different issues. The first is related to S/N ratio: the averaging allows, in fact, an improvement of data quality. The second considers the spatial distance between the soundings. Both VTEM systems fly at a speed equal to 22 m/s and the data are recorded every 0.1 s. This means that the average distance among two soundings is 2.2 m. This short sounding distance does not produce an increase of lateral resolution, but it results in a high level of information redundancy.

The standard approach for AEM data uses the same distance at early and late times in which the data are averaged. The limitations of this approach are that it is not possible to maintain a high resolution at early times (corresponding to the near surface), where the S/N ratio is usually high and, at same time, a reasonable S/N ratio at late times (corresponding to a large penetration depth). These limitations can be overcome using a trapezoidal window to average the data in order to average less the data at early times than those at late times.

Using a trapezoidal window is justified by the nature of the electrical fields itself in the ground. At early times the current is in the upper layers of the ground and according to the "smoke rings" described by Nabighian (1979) its footprint is smaller than that at late times. Based on this observation it makes sense using different average windows. In this way, is maintained an optimal resolution for the shallowest resistivity structures, where the current system in the ground is relatively small and the S/N ratio is high, and is obtained a reasonable S/N ratio at late times, preserving a good depth penetration (figure 3.5).

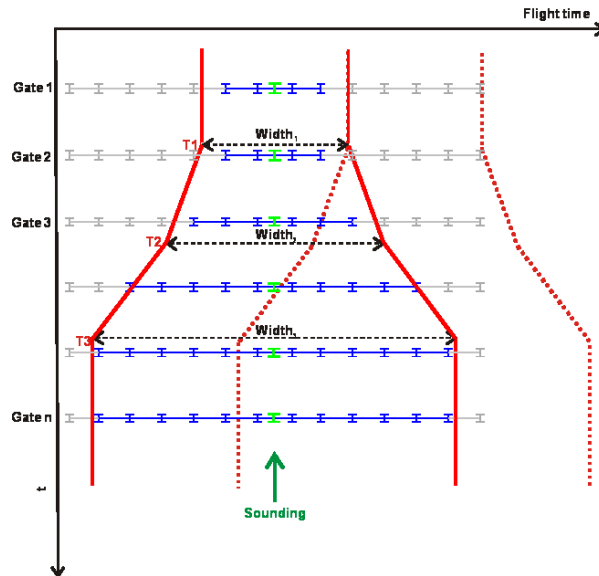


Figure 3.5: The principle behind the trapezoid shaped averaging core, in which data are averaged over larger time spans at later times to maintain as much lateral resolution as possible at early times while maintaining a high penetration depth (Auken et al. 2009).

The width of the trapezoidal filter is chosen as narrow as possible for the early times in order to get the highest possible unsmoothed resolution for the shallowest structures, while it is enlarged at late times to improve the S/N ratio and achieve the desired depth of penetration without losing lateral resolution. This involves that a unique scheme, useful for all the systems and all the data, is difficult to define.

Usually, the user proceeds by attempts. It sets out an outline for the filter, then the data are processed and the user, comparing raw data and average ones, decide if the results are acceptable. In this case, for the two VTEM systems, I have defined 2 trapezoidal filters with different widths.

I set the trapeze sounding distance at 1.5 s and considering the helicopter speed, that is 22 m/s, this means that the averaging produces a sounding every 30-35 m (figures 3.6a, 3.6b).

| (a) | Trapez Filter                | ON   |
|-----|------------------------------|------|
|     | Trapez Sounding Distance [s] | 1.5  |
|     | Trapez Gate Time 1 [s]       | 1e-4 |
|     | Trapez Gate Time 2 [s]       | 1e-3 |
|     | Trapez Gate Time 3 [s]       | 1e-2 |
|     | Trapez Width 1 [s]           | 1    |
|     | Trapez Width 2 [s]           | 2    |
|     | Trapez Width 3 [s]           | 3    |

| (b) | Trapez Filter                | ON   |
|-----|------------------------------|------|
|     | Trapez Sounding Distance [s] | 1.5  |
|     | Trapez Gate Time 1 [s]       | 1e-4 |
|     | Trapez Gate Time 2 [s]       | 1e-3 |
|     | Trapez Gate Time 3 [s]       | 1e-2 |
|     | Trapez Width 1 [s]           | 2    |
|     | Trapez Width 2 [s]           | 3    |
|     | Trapez Width 3 [s]           | 4    |

Figure 3.6: Trapezoidal filter settings employed for 2013 survey (a) and for 2007 survey (b). 1.5 s is the time distance of the averaged soundings (corresponding to 30-35 m distance per sounding) with the time widths of the trapezoidal filter.

Another output of the average process is the calculation of the standard deviation associated at each gates. In the import phase at all the raw data is assigned a uniform standard deviation of 3%.

Subsequently, the automatic stacking soundings were displayed in a number of different data plots. The main aim of this phase is assessing the late time data points and deciding if higher uncertainty should be ascribed to these data or if they should be removed entirely from the dataset. These decisions are up to the user through the evaluation of the decay curves, noise measurements (if available) and spatial distance from potential noise sources. Generally is normal to cull data when the Earth response reaches the background noise level. Random noise, after stacking, falls proportional to  $t^{-1/2}$  and its effective values normally varies between 0.1 and 10 nV/m<sup>2</sup>. Clearly, the early measurements are many times higher than the noise level (Christiansen et al., 2009).

### 3.5.3 Fast smooth LCI inversion for post-processing of voltage data

A fast inversion represents the last step of the data processing. The aim of this inversion is to check if further manual processing is required. This operation can be useful both in situations where a large part of the data are culled

because of coupling and in situation where the main noise source is the natural background noise. In this work, I used the Laterally Constrained Inversion (LCI) algorithm (Auken et al., 2005) to find and remove any outlier data that, for some reasons, have not been eliminated during the automatic and manual previous processing. Such data usually occur at late times, where the S/N ratio is low. As I will show later, some effects can be found also at early times. Both can produce some artifacts in the resistivity models with the presence of unrealistic conductive/resistive layers and at same time they compromise the misfit between the forward response and the measured data. In this study, all the processing steps, as well as the fast LCI inversion, were performed on the two datasets from the two VTEM systems separately. Figure 3.7a shows an average sounding from 2007 VTEM system, also transformed into late time apparent resistivity (Rhoa) (figure 3.7b) with different time gates, each with the associated error-bar. The solid line represents the forward response. As it can be seen, the forward response matches the data within the noise level.

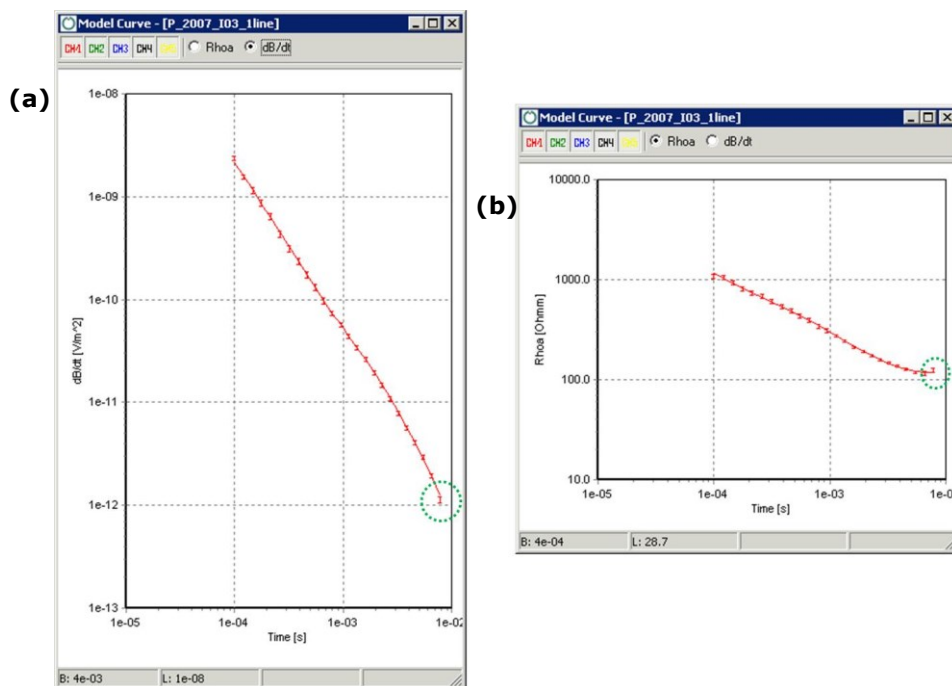


Figure 3.7: (a) Averaged sounding from 2007 VTEM system with different time gates and the associated error-bars. The solid line represents the forward response. (b) averaged sounding transformed into late time apparent resistivity. As seen, the data are generally well fitted, but an evident discrepancy between the forward model and measured data is observable at a late time (the green dashed circles highlight the last gate that is not correctly fitted).

Only the last gate, highlighted by the green dashed circles is not correctly fitted. For this gate, you can act in two different ways: the first consists in removing completely the data; this operation can involve a loss of resolution and a reduction of the investigation depth. The second approach considers an increase of the standard deviation associated with the data. In fact, the standard deviation enters in the inversion scheme and is used to weight the individual data. This means that data with high standard deviation does not provide much information on the subsurface structure recovered by inversion. The geophysicist, processing the data, decides which gates are kept or discarded and if greater standard deviation could be associated to them.

At early times, the main problem is related to the presence of the residual primary field. The primary field present during the on-time can extend into off-time, overpowering the weaker secondary field.

In this case the current in the transmitter loop is not completely extinct and the earliest time gate will be contaminated if current continues to flow in the transmitter loop while they are being recorded. Because currents take longer to decay in big loops, this problem is exacerbated with larger moment systems. Moreover, this problem is typical of concentric coil system (systems that are not null-coupled).

This effect, known as bias effect (Macnae et al., 1984), results in high signal level for this gate, signal that cannot be associated to the earth response. The consequence of bias effect is that the early time gates are not fitted by the forward response and the model can show a thin shallow conductive layer.

This phenomenon can be present during all the survey and can affect the early time gates. The evidence of this effect, which can be considered constant, depends on the conductivity of the ground.

Conductive earth, producing a strong secondary field, tend to mask this effect (figures 3.8a, 3.8b) while it becomes predominant for resistive earth and can affect several gates, producing a significant change in curve inclination during the early times (figures 3.8c, 3.8d).

I noticed this effect especially for the 2013 VTEM system.

Both figures, in fact, show two average sounding from 2013 VTEM system and their forward model, expressed as dB/dt (figures 3.8a, 3.8c) and  $\rho_{ho}$  (figures 3.8b, 3.8d). The apparent resistivity plot of figure 3.8d shows very clearly the

fictitious shallow conductive layer. The forward response also over-fits other gates, in order to fit the biased gates.

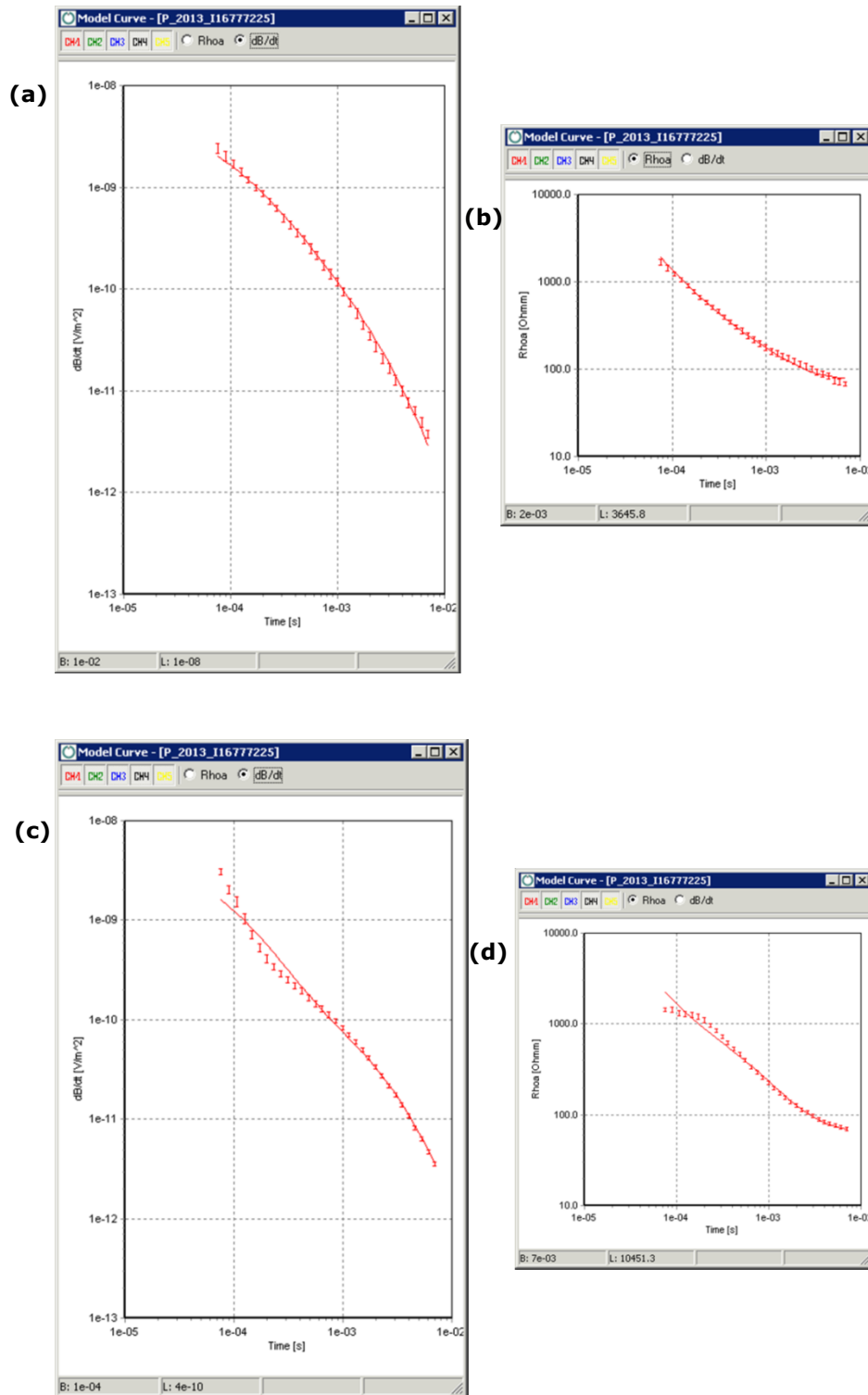


Figure 3.8: (a-c) Two averaged soundings from 2013 VTEM system with different time gates and the associated error-bars; the solid line represents the forward model. (b-d) Averaged soundings transformed into late time apparent resistivity. As seen, the early time gates are not well fitted by the forward response.

Usually a bucking coil on the frame is used for primary field compensation, however no other procedures of filtering and pre-leveling of the raw data allow recovering biases gates. The practice involves removing these early time gates from the subsequent inversions in order to eliminate this shallower conductive artifact from the output resistivity models at cost of losing near-surface resolution. This can easily be done in the inversion setting window.

In general, a compromise between the number of removed early time gates and the desired shallow resolution is needed.

### **3.6 Spatially Constrained Inversion of 2 VTEM datasets**

After the fast LCI inversions to post-process the data, both datasets of the two VTEM systems were inverted separately using the quasi 3-D Spatially Constrained Inversion algorithm (SCI; Viezzoli et al. 2008). SCI is a full non-linear damped least squares solution, in which the transfer function of the instrumentation is modeled. The system transfer function includes transmitter current, waveform with turn-on and turn-off ramps, repetition frequency, loop area, gate times, low pass filters and system altitude.

In the SCI scheme the model parameters for different soundings are tied together spatially with a partially dependent covariance, which is scaled according to distance (Viezzoli et al. 2008). Model parameters are constrained spatially to reflect the lateral homogeneity expected from the geology (vertical and horizontal layer resistivity, boundary thickness, or depth). Constraints set boundary conditions and delimit the allowed variation of the parameter values within a defined deviation. The flight altitude is also treated as an inversion parameter. The measured value is set as a-priori information and an uncertainty is associated to it. Usually this uncertainty is not greater than 10% of the a-priori value. This allows the inversion to move the altitude around its correct value, not compromising the validity of the model. It can happen, in fact, that a good misfit is found moving considerably the flight altitude, obtaining an unreliable inverse model.

Another output that can be calculated during the inversion is the depth of investigation (DOI). The DOI represents the maximum depth at which there is sensitivity to the model parameters (Christiansen et al. 2012), in other words

each model parameter lying significantly below the DOI should be disregarded because its value is poorly determined. Considering a simple model with a conductive overburden over a resistive basement, the DOI lies at the interface between these two layers discerning the upper well-resolved parameters from the lower poorly ones.

The DOI is superimposed to the resistivity models to crop the average resistivity horizontal maps, and as fading colors below the DOI on the vertical cross sections.

The SCI inversions of the two datasets were performed using a layered homogeneous half-space with a starting resistivity of 100  $\Omega\text{m}$ . Following a smooth approach the models are discretized by 25 layers with fixed thickness. The maximum depth of the model (from 0 to 500 m) is chosen according to the penetration capability of the system and the thickness of the layers increases logarithmically with depth, starting from few meters in the shallow part of the model. Vertical constraints (equal to 3, it means that the resistivity is allowed to vary by 200% between two adjacent layers) are added on resistivity values to stabilize the inversion, for example to remove fictitious layers especially in models based on a small number of data points. Moreover, the smooth inversion allows the use of lateral constraints, applied to the resistivity values to take into account the lateral variability in layer resistivity. In this case I used a value equal to 2 (allowed variation of 100%) with a reference distance of 30 m, to take into account the soundings distance ( $\sim 30$  m) and a power-law dependence of 1 (linear).

The choice of using a smooth approach, that has advantages and disadvantages as described in Section 1.5.2, to discretize the model is related to the geological complexity of the study area. In this case, the delineation of layer interfaces with associated resistivities and thicknesses can be misleading while gradual transitions in resistivities can facilitate the delineation of complex geological structures.

The two SCI inversions carried out on the two datasets from the VTEM systems have provided a total data residual less than 3 for both datasets.

The data residual, that is dimensionless, is defined as a Root Mean Square Deviation between the measured and the calculated data normalized to the noise for each data (Auken and Christiansen, 2004).

Values lower than 1 indicate that the modeled data fit the measured data within noise level. Values higher than one can be due either to strong 3D effects, or to noisier or less accurate data.

In particular, the data residual for the 2007 system is lower than that obtained for the 2013 system.

In both cases, the obtained misfit is considered acceptable for various reasons. First of all, the existence of 3D effects that have been treated with 1D approach. Secondly, the existence of bias effects at early times data, even if I have decided to omit the first five gates for the 2013 VTEM system.

### 3.6.1 Joint SCI Inversion of 2 VTEM datasets

The 2 VTEM surveys over the Broken Evil prospect were flown in 2007 and in 2013, both at 200 m spacing. Together, the surveys create an area of 100 m spacing (figure 3.9).

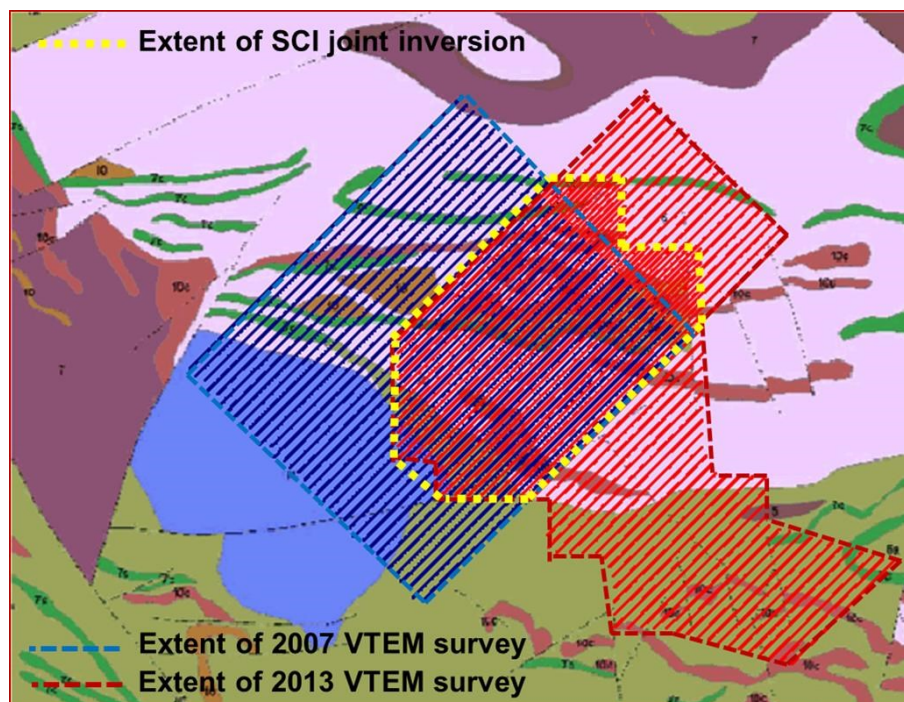


Figure 3.9: The extents of 2007 and 2013 VTEM survey and SCI joint inversion plotted over bedrock geology of the area under study.

The EM data inversion of the two dataset over the dashed yellow area was carried out in a joint approach using SCI algorithm (Viezzoli et al., 2008). The data misfit is still satisfactory (average below 3 (dimensionless)), but all maps and resultant conductivity models contain linear artifacts parallel to the flight

lines in correspondence to the different surveys. These effects are evident although I have set tighter spatially constraints, with a value of 1.7 (70% allowed variation), with a higher reference distance (60 m) and nonlinear power-law dependence (0.75), to ensure a greater homogeneity between two adjacent lines.

These artifacts are indicative of imperfect calibration between the 2 VTEM datasets.

Christiansen et al. (2011) shown the effects in the inverse model of inaccurate system description in the 1D forward modeling of AEM data.

They described the most important processes that need to be applied to obtain accurate TEM data ready for modeling and inversion. These include, in addition to those previously described, any processes related to a correct calibration of the airborne system: the correction of any timing errors between the transmitter and the receiver electronics and calibrating data amplitudes.

The time between the current extinction and the first time gate may only be poorly determined (zero-time is usually defined at the beginning, at the end of the current turn-off ramp or at the end of the linear part of the ramp). An airborne system that is not correctly calibrated can produce a systematic error on the amplitude of the measured data.

Following Christiansen et al. (2009), an EM system may be calibrated in a relative or in absolute sense.

A system is calibrated in a relative sense when the measured data are compensated for the primary field through high altitude measurements and when the data between adjacent lines are leveled, performing some measurements along tie-lines perpendicular to the flight lines.

The absolute calibration can be performed in the laboratory, at a well-understood test site (Foged et al., 2013) before the equipment is used in surveys or its performance may be compared to that of a well-calibrated instrument at the investigation site. Calibrating an EM system means applying a time-shift to the center time of the gates and a data level shift to the  $db/dt$  measured data for the individual TEM systems.

After calibration, the different systems could reproduce the reference response within a low range of error at all time-gates.

The different time-shifts come from variations in transmitter-receiver delays and minor variations in waveforms and low-pass filter cut-off frequencies. The factor shift is assumed to come from inaccurate current measurements by the transmitter.

The calibration of the VTEM systems is usually relative rather than absolute (Christiansen et al., 2011).

The imperfect calibration of the two VTEM systems, studied in this work, results in an amplitude shift between soundings, measured at same position. To show that, I have selected one sounding of 2007 VTEM system and one sounding of 2013 system, over an area of overlapping of the flight lines (figure 3.10a) and I have plotted the two extract soundings on the same graph (figure 3.10b).

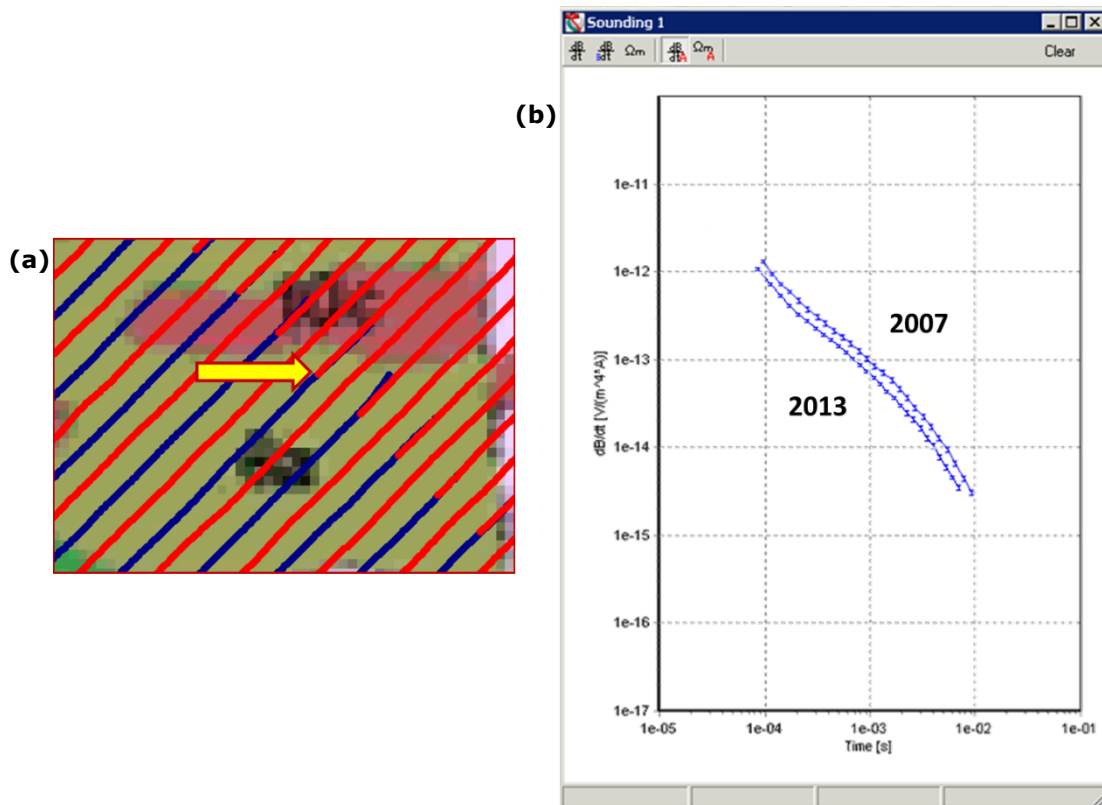


Figure 3.10: (a) Area of overlapping of the flight lines (red for 2013 survey and blue for 2007 survey). The yellow arrow indicates the position of the two extract soundings that have been plotted on the same graph (b).

In this phase, it is impossible to obtain an absolute calibration of the two VTEM systems. I have therefore decided, in order to reduce the stripping effects in correspondence to the different surveys, to calibrate the two systems each other.

In particular I have applied a shift factor to 2013 voltage data, prior the inversion, to make these data comparable with the 2007 data. This operation has been driven by several observations derived from the information on the systems specifications and from the results obtained by the 2 singular SCI inversions.

The 2007 VTEM system has, in fact, a higher magnetic moment than the 2013 system, and the average data residual obtained by the SCI inversion on 2007 data is lower than that obtained from the SCI inversion on the 2013 data. The application of the shift factor to the 2013 data produced the result shown in figure 3.11. The two soundings of two different systems at the same position are now better overlapping.

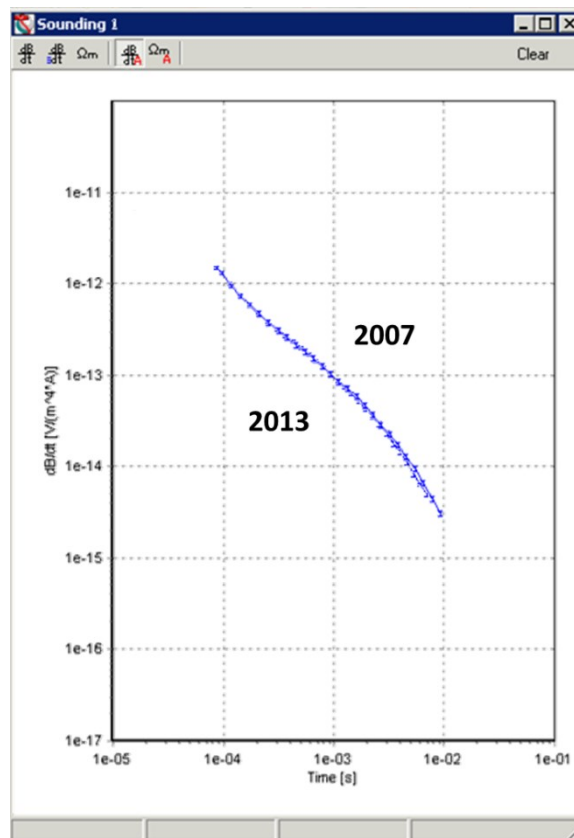


Figure 3.11: Comparison between the two soundings of the two VTEM systems after the application of a constant amplitude shift factor on the 2013 data. As seen, a better overlapping is now achieved.

This procedure provides improved model output reducing the striping artifacts significantly and, without increasing the data misfit (that on average remains lower than 3 (dimensionless)). Figure 3.12 shows a comparison between the same depth slice obtained from the joint SCI inversions with (figure 3.12a) and without (figure 3.12b) the shift factor.

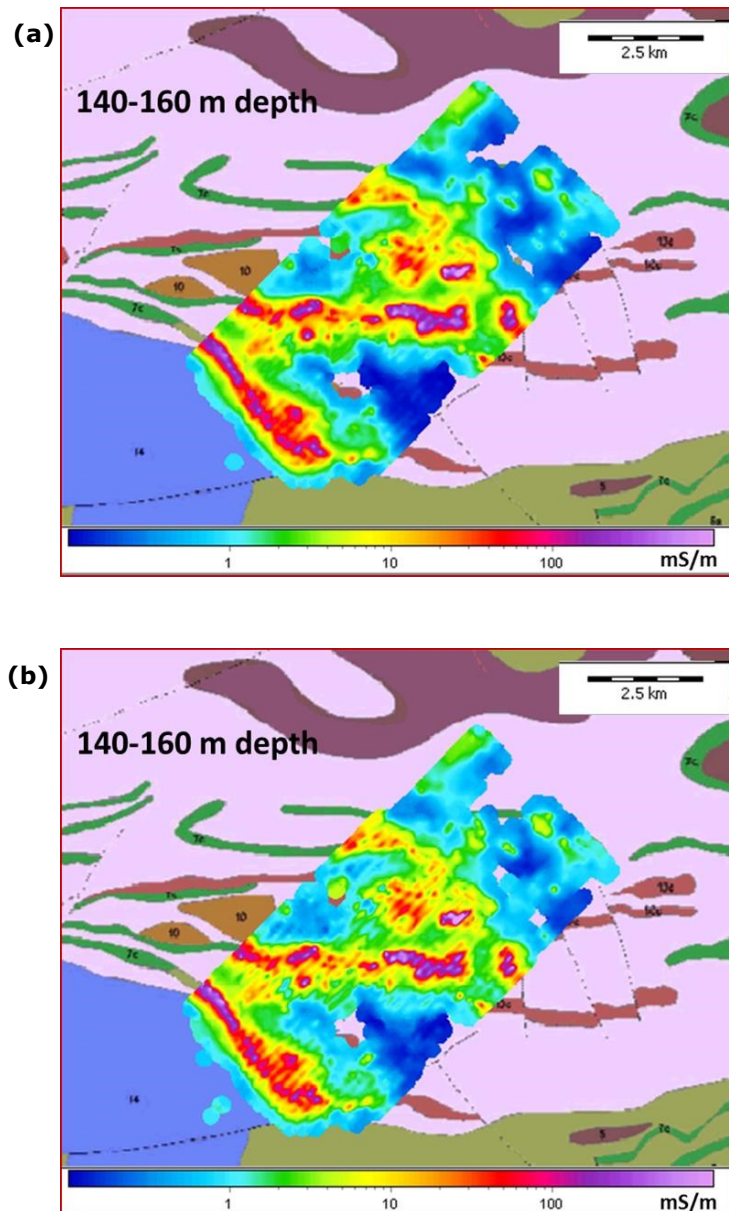


Figure 3.12: Reduction of striping effects by applying a constant amplitude shift factor. (a) SCI joint inversion with the amplitude shift; (b) SCI joint inversion without the amplitude shift.

### 3.7 Interpretation of joint VTEM smooth inversion results

In order to visualize the conductivity structures of the Broken Evil area, a number of horizontal geophysical maps and vertical sections are presented. The maps show an average conductivity at different depth intervals below the ground surface. This representation is valid in a setting like the survey area, which is characterized by little topographic relief.

The average conductivity maps plotted over the bedrock geology, in figure 3.13, shows a clear connection between the geological facies and the conductivity structures.

There are both long linear conductive zones and isolated local conductors. The most significant conductive zones formed a letter “Z” similar shape with up direction NE in the survey area.

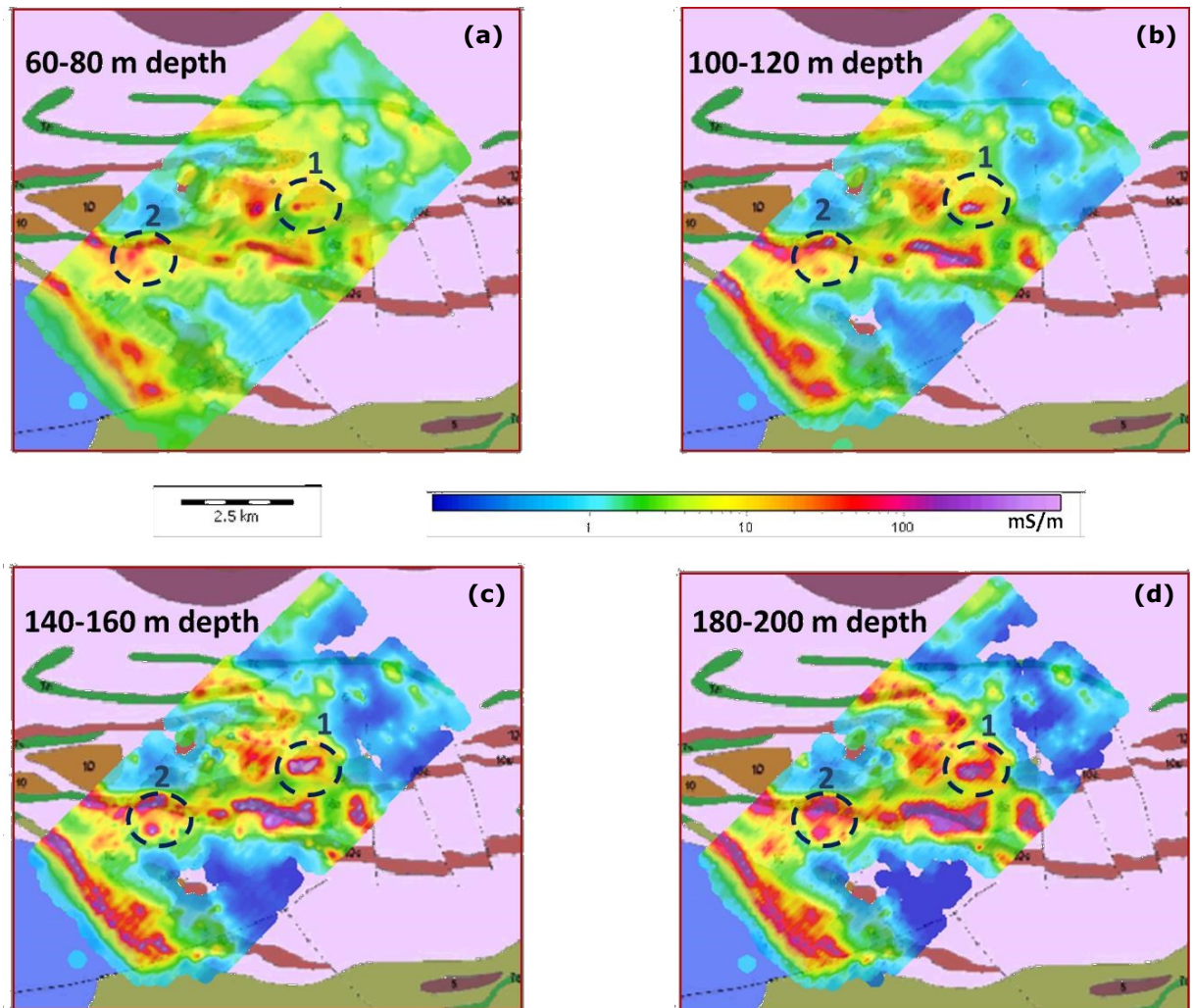


Figure 3.13: SCI joint inversion result: (a) 60-80 m depth; (b) 100-120 m depth; (c) 140-160 m depth; (d) 180-200 m depth. Dashed circles highlight some areas of particular interest, classified as priority drill targets.

The conductivity anomalies are associated to metasedimentary rocks, to felsic and intermediate metavolcanic rocks, as well as to ultramafic rocks. These kinds of rocks may host massive sulfide mineralizations that usually produce a strong conductive anomaly with conductivity values greater than 500 mS/m.

Two areas were of particular interest, which have been highlighted on the conductivity maps by means of dashed circles (1 and 2), as they are subject to current mineral exploration and are classified as priority drill targets (Galkine, 2012). I plotted two profiles crossing these areas as W-E cross-sections in figures 3.14 and 3.15. The cross-sections are related to parts of two flight lines of 2013 VTEM survey (line 1260 and line 1080).

As expected, as it is common in mining exploration, where the anomaly sources have usually finite horizontal dimensions, these interesting anomalies are related to sources with pronounced 3D characteristics. Using a 1D inversion algorithm, the obtained models are influenced by 3D effects that result in artifacts, known as “pantlegs” (Christiansen et al., 2009), in the inverse models (at 600 m and at 1100 m horizontal distance in figure 3.14; at 800 m and at 1400 m horizontal distance in figure 3.15).

However, these evident 3D effects are interpreted to be representative of thin steeply dipping conductors.

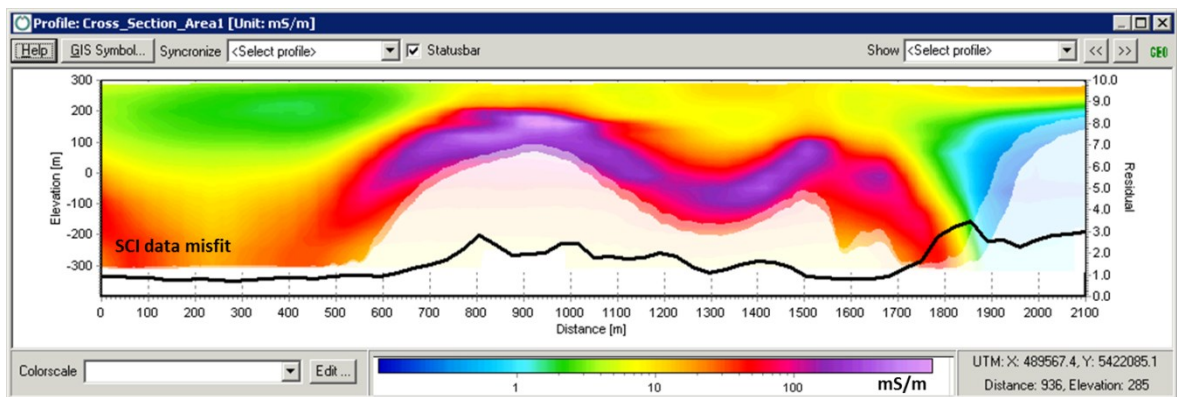


Figure 3.14: Results of SCI joint inversion for VTEM line 1260 (2013 survey).

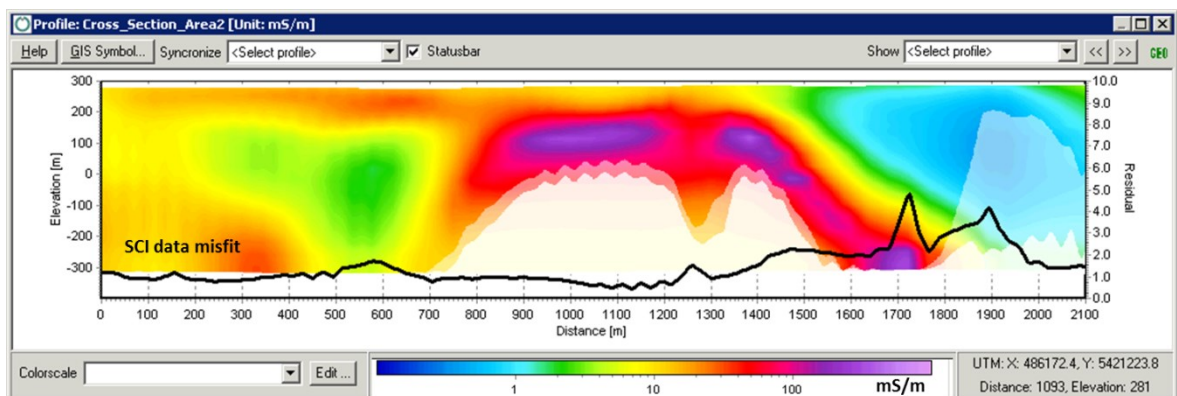


Figure 3.15: Results of SCI joint inversion for VTEM line 1080 (2013 survey).

Figure 3.16a shows an interpolated cross-section crossing both exploration targets from SW to NE. The cross-section is drawn across both VTEM surveys (2007 and 2013). The cross-section shows also on average a good data fit for both surveys in correspondence of the two exploration targets, as shown for two distinct transients (figures 3.16b and 3.16c).

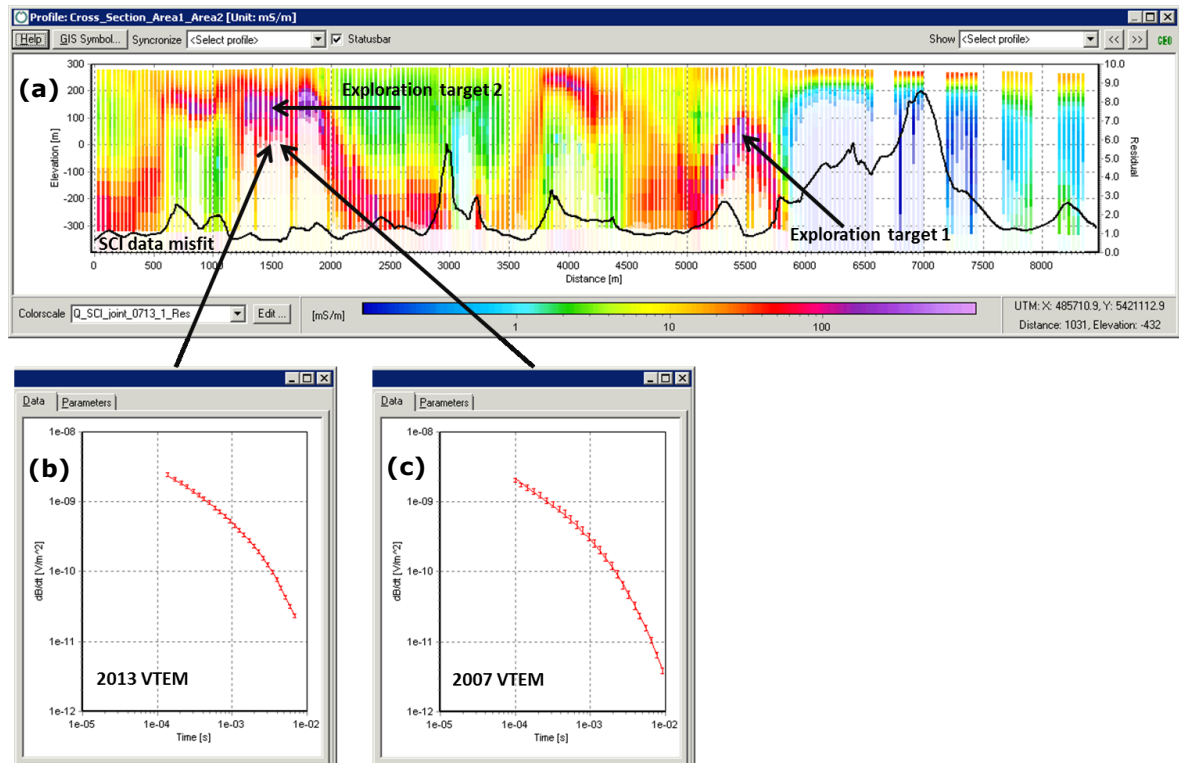


Figure 3.16: (a) Conductivity cross-section based on SCI joint inversion results over the two priority exploration targets; (b) data fit for a selected 2013 transient; (c) data fit for a selected 2007 transient.

The joint inversion of the electromagnetic data sets, collected by two VTEM systems, that can be considered for their features (different waveform, magnetic moment and time gates) as two completely different systems, has provided a unique resistivity model which fits both data sets to an acceptable misfit. The advantage of obtaining one single model fitting all data at once, rather than 2 models one fitting each dataset, is obvious, in terms of overall robustness of the geophysical results and of any subsequent modeling.

This result has been obtained by applying a calibration factor to the 2013 data set in order to ensure higher spatial consistence in the model space.

Despite the existence of 3D effects, arising from the use of a 1D inversion algorithm to modeling 3D sources, the results appear to be quite interpretable geologically and consistent with previous interpretations of these data sets

(Galkine, 2012) and the geological knowledge of the study area. In addition the joint SCI inversion produced an enhancement of spatial resolution due to the closer line spacing (100 m in combined data set as opposed to 200 m in each of the individual sets).

### **3.8 Vertical Soundings Inversion of magnetic data over Broken Evil prospect**

Both VTEM systems are equipped with caesium magnetometers that allow measuring the total magnetic field. The sampling rate is 0.1 s.

The 2013 VTEM system mounts 2 magnetometers on independent birds located 10 m above the VTEM loop. The horizontal distance between the two magnetometers is 12.5 m. On the birds is mounted also a GPS and an inclinometer that controls the position and the orientation of the sensors.

In addition, a value of total magnetic field and its position is calculated at the center of the magnetic bird from the measured magnetic field and measured position at two sensors.

The 2007 VTEM system mounts 1 magnetometer on a separate bird, 13 m below the helicopter. Its position is calculated indirectly from the position of the helicopter, using the nominal distance of the magnetic bird.

After the acquisition, the contractor corrected the data for diurnal variation using the digitally recorded ground base station magnetic values. Also the IGRF removal and a leveling procedure between adjacent lines are performed in this phase.

The inversion of magnetic data was performed building a single dataset from the two measured ones over an area of overlapping between the two surveys with spacing line of 100 m, approximately corresponding to the selected area for which I have performed the joint SCI inversion of the EM data (figure 3.17).

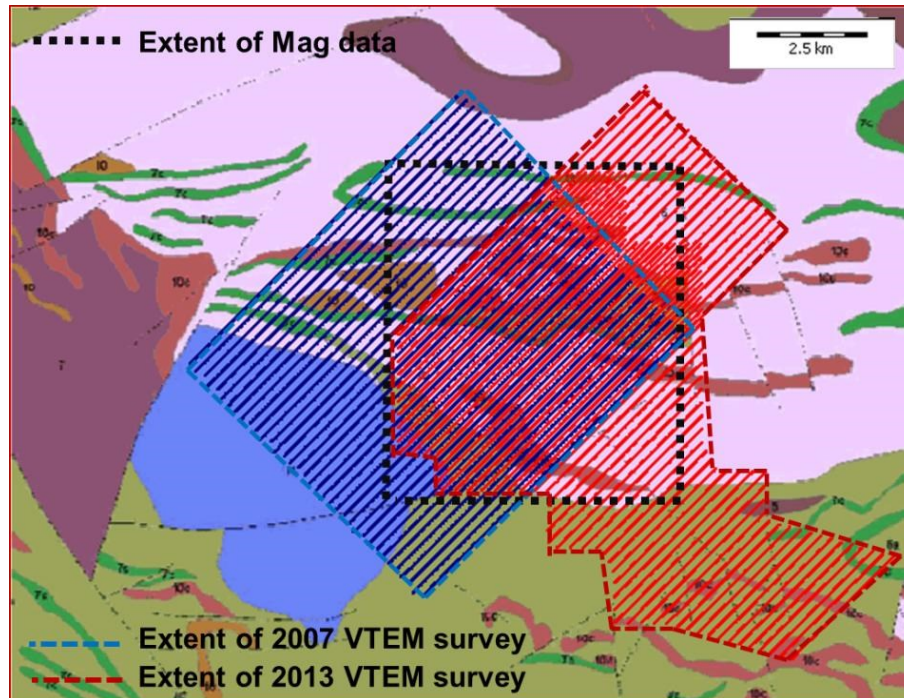


Figure 3.17: The extents of 2007 and 2013 VTEM survey and the extent of magnetic dataset plotted over bedrock geology of the area under study.

The combined data are further micro-levelled in order to adjust the different levels after the IGRF corrections.

The 3D magnetic inversion was carried out and presented in Di Massa et al. (2015), using Mag3D, the inversion code developed at UBC-GIF (Li and Oldenburg, 1996).

In this work, I have selected two anomalies, for which I have performed the inversion of vertical soundings, as explained in Chapter 2. These two anomalies occur in correspondence of outcropping metasedimentary rocks and are caused by the presence in this unit of highly magnetic pyrrhotite as confirmed by the information derived from a drill hole that intersects these rocks. This noneconomic mineral can be associated to economic sulphide mineralizations, which are usually non-magnetic.

I will refer to them as “Anomaly 1” and “Anomaly 2”.

In particular the Anomaly 2 (figure 3.18) is related to the Area 2 in conductivity maps (figure 3.13), classified as priority drill target (Galkine, 2012).

Before calculating the vertical magnetic soundings, I needed to apply further transformations to the magnetic data.

The first transformation was a differential upward continuation of the magnetic data to obtain a magnetic map related to the same horizontal surface. In fact, the height of the magnetic sensor varies between 310 and 355 m above the sea level. Thus, the data were upward continued to the maximum altitude (355 m). After this operation, the clearance (distance between magnetic sensor and ground) for the two areas where are located the two magnetic anomalies is about 70 m, being the topography for these areas almost flat, at an altitude of 285 m above the sea level.

The clearance is information that I need to consider in the inversion process, in order to avoid the generation of inverse models not in agreement with the measurement system geometry.

The second transformation applied to the magnetic data is the reduction to pole (Baranov and Naudy, 1964). This transformation of the shape of anomalies into their equivalent form at the north magnetic pole is usually applied to simplify the total field map. As stated in Chapter 2, to perform the inversion of vertical soundings, I need to estimate the horizontal dimensions of the anomaly source. This estimation is performed through the horizontal derivative method (Cordell and Grauch, 1985), and this method operates correctly only for monopolar magnetic anomalies.

The reduction to pole works well if the anomaly is measured at a high magnetic latitude (this is our case, in fact the IGRF in the area of the Broken Evil Prospect has a magnetic inclination of  $74^\circ$ ) and if any effects of remanent magnetization are not appreciable (both selected anomalies seem to have monopolar shape after the reduction to pole). The figure 3.18 shows the total magnetic field map after the reduction to pole. On the map, I have highlighted the two anomalies. I have also located the positions of the drill hole by means of the red point.

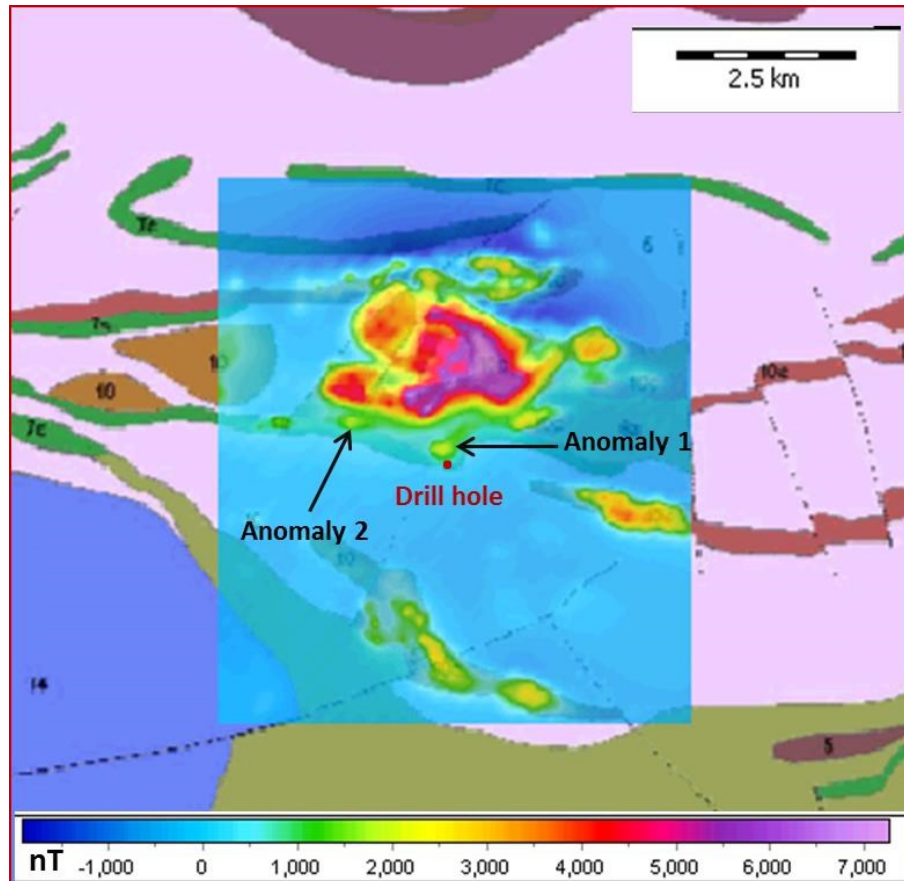


Figure 3.18: Total magnetic field after the reduction to pole over bedrock geology of the area under study. Two magnetic anomalies and the location of a drill hole are shown on the map.

### 3.8.1 Vertical Magnetic Soundings Inversion of Anomaly 1

There is a hole close to the Anomaly 1, completed in 2006 in order to test a magnetic and electromagnetic anomaly detected by ground surveys. This hole, identified by R06-01 tag, was performed by Norex Drilling Company.

The hole was drilled with an azimuth of  $360^\circ$  and with a dip of  $-50^\circ$ , and was stopped in serpentinized ultramafic rocks at 251 m depth.

Drill testing of the target anomaly revealed the causative body to be graphitic sediments (at a starting depth of 55 m) with seams and heavy disseminations of pyrrhotite and pyrite within felsic tuffs.

In order to perform the inversion of the vertical soundings, the first step is the calculation of the vertical soundings.

Their positions are shown in figure 3.19 by the green points. Each consists of magnetic data upward continued to 20 different altitudes from the first level at 71 m above the ground up to the last level at 90 m above the ground with a 1 m constant step.

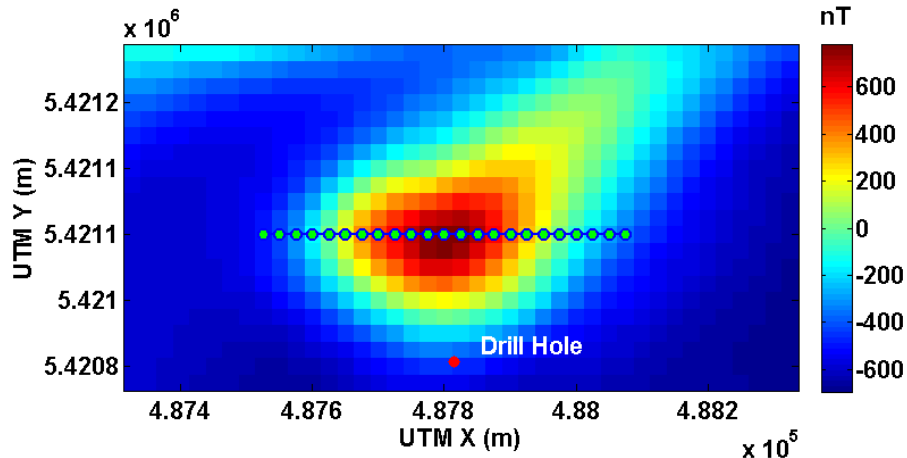


Figure 3.19: Magnetic Anomaly 1. The green dots represent the horizontal positions of the measuring stations and then the individual vertical soundings. The red dot indicates the location of the drill hole.

The choice of the maximum altitude of continuation and consequently the step between two altitudes takes into account two issues: it minimizes the interference with adjacent anomalies (in this case there is a strong magnetic anomaly flanking to the north, caused by a magnetic serpentinized ultramafic intrusive) and at same time these altitudes produce an appreciable variation of the field with the height to avoid the slab effect (as explained in Section 2.5.3). The magnetic anomaly along the chosen profile and at different altitudes is shown in figure 3.20:

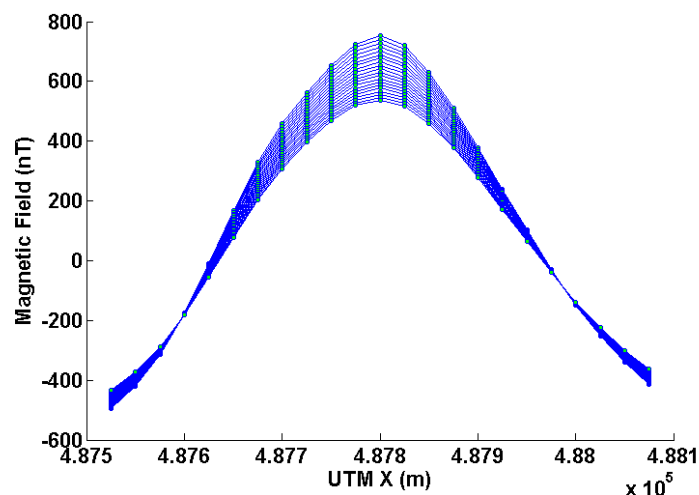


Figure 3.20: Profiles of the magnetic data at different altitudes of measure for the Anomaly 1. The green dots represent, for each altitude, the horizontal positions of the measuring stations and then the individual vertical soundings.

The next step deals with the estimation of the horizontal dimensions of the anomaly source in order to calculate the kernel to perform the inversion.

This operation is accomplished by applying the horizontal derivative method to the map of the magnetic data (figure 3.21) and, in order to improve the resolution, to the map of the vertical derivative of magnetic data (figure 3.22). Higher order derivatives have not been used for the excessive enhancement of high frequency noise.

The estimation of the horizontal dimensions of the anomaly source was performed using all the information derived from the horizontal derivative maps and also from the anomaly along the profile at different altitudes.

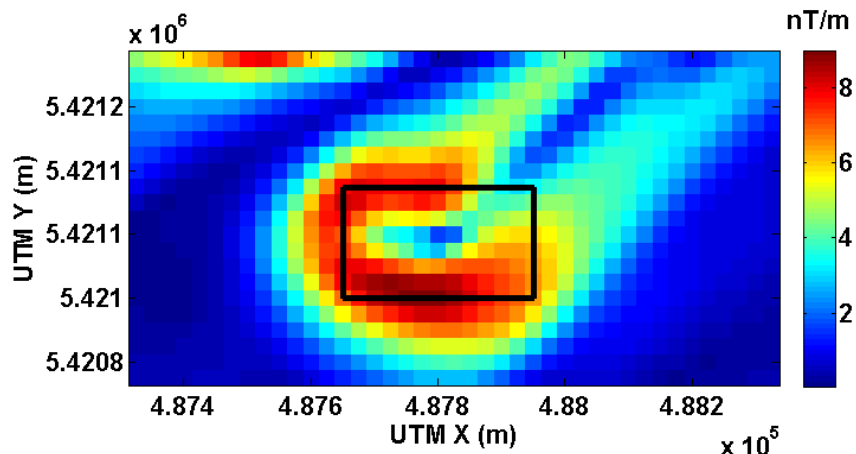


Figure 3.21: Total horizontal derivative of magnetic data related to the Anomaly 1. The black rectangle represents an estimation of the magnetic source horizontal dimensions.

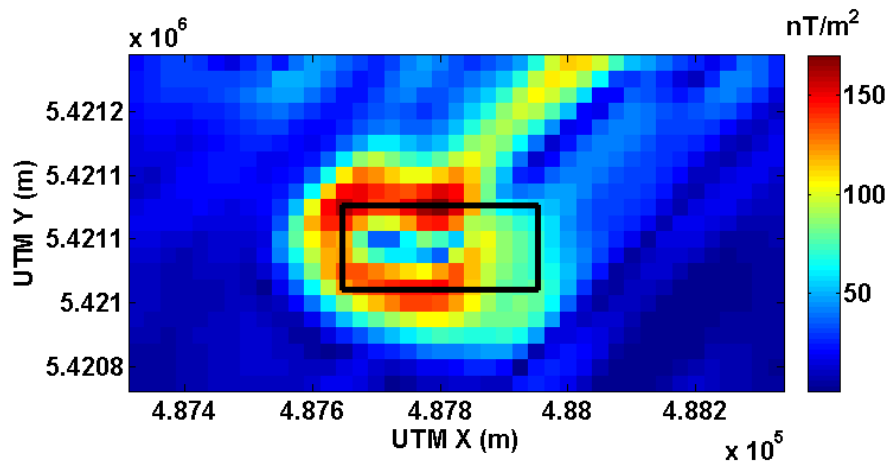


Figure 3.22: Total horizontal derivative of the vertical derivative of magnetic data related to the Anomaly 1. The black rectangle represents an estimation of magnetic source horizontal dimensions.

The horizontal derivative method applied on the magnetic data shows that the source could be approximated by a prismatic shape whose dimensions are 325×175 m (figure 3.21). The map of the horizontal derivative applied on

vertical derivative of magnetic data provides a smaller dimension in the N-S direction (125 m). For the E-W direction, the horizontal derivative provides a clear estimate only on the western part of the source that is probably shallower than the eastern part. This is confirmed by the anomaly profiles (figure 3.20) that show a clear asymmetry between East and West sides. In particular, the vertical soundings of eastern part (right side in figure 3.20) show a slower decay of the magnetic field with the altitude than the vertical soundings of western part (left side in figure 3.20). This evidence in the data is compatible with the existence of an eastward dipping source. The map of the horizontal derivative on the vertical derivative of the magnetic data, enhancing the higher frequencies, highlights the shallowest part of the source. Following these observations, I defined, for the kernel calculation, a prism of dimensions 325×125 m. However, these dimensions did not allow recovering a useful model. For this reason, I decided to reduce these horizontal dimensions further, to 325×100 m.

To perform the inversion, the vertical dimension of the source volume is discretized from 0 to 1000 m, with 100 layers, 10 m thick.

In order to approximate the continuation error, the unknowns to be estimated through inversion included the coefficients of a first-order polynomial, following the approach described in Section 2.7. Then, I set the constraints on the model parameters, i.e. the susceptibility, varying from 0 to 0.25. This upper limit may be justified by the presence of pyrrhotite that is a very magnetic mineral, with high values of susceptibility (e.g., Thomas et al., 2000). The experimental error on the measured data has been set as low as possible, to recover a useful model; I used a value of  $2 \times 10^{-2}$  nT.

The Vertical Soundings inversion is able to recover a complex source with nonhomogeneous susceptibility (figure 3.23). As anticipated by analyzing the data, the inverse model represents a source dipping eastward. The estimated depths (expressed in Figure 3.23 as elevation above sea level) are consistent with the information derived by the drill hole.

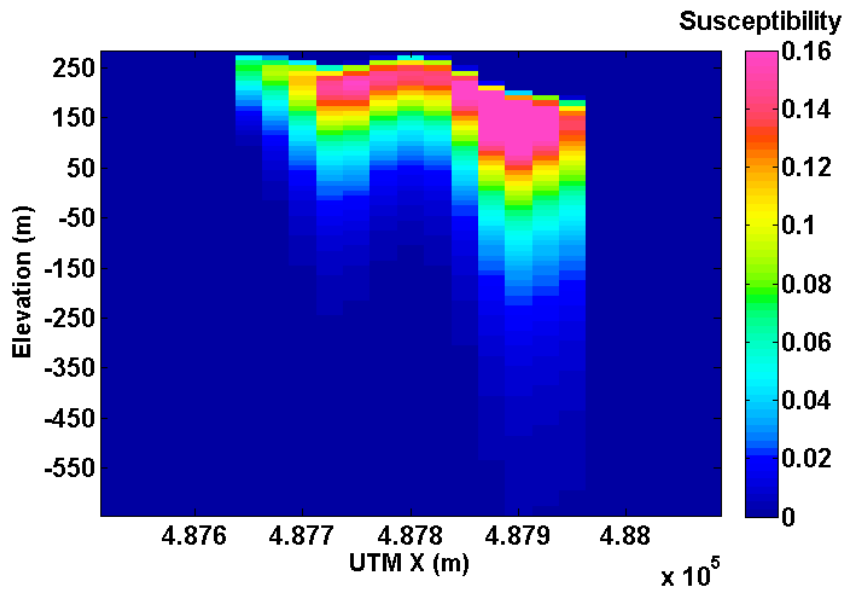


Figure 3.23: Vertical Soundings inversion of the magnetic data related to the Anomaly 1.

From the estimated parameters I calculated the data along the considered profile (in this case at the first continuation height, i.e. 71 m above the ground), and I compared them with the measured data related to the same profile (figure 3.24).

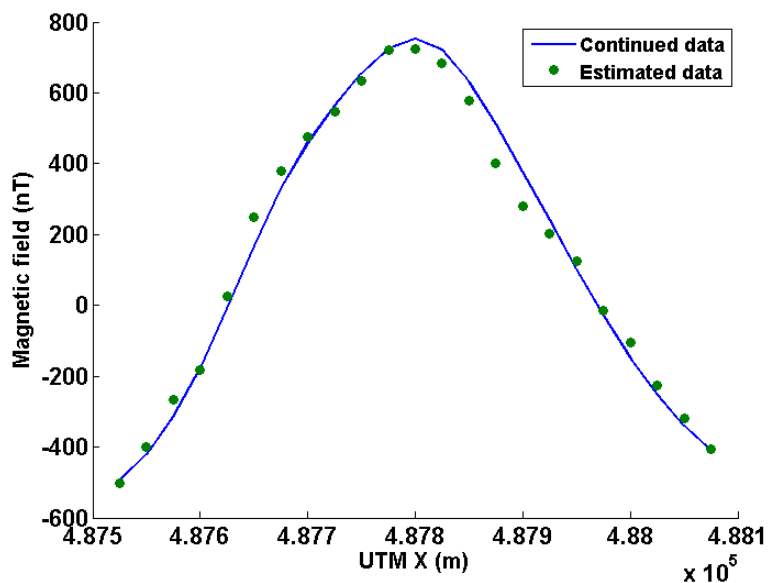


Figure 3.24: Comparison between the continued and the estimated data related to the Anomaly 1 at 71 m height above the ground.

The comparison provides a RMSD of 45.5 nT, that is an acceptable value, considering that a regular prismatic source for the kernel calculation was used. A more accurate estimation of the horizontal dimensions that might allow an improvement of the matching between the continued and the estimated data is, in this case, problematic. In fact, a major limit to the accuracy of the

horizontal dimensions is given in this case by the sampling step. Considering that the distance between the flight lines was 100 m all the magnetic data have been gridded with a sampling step of 25 m.

### 3.8.2 Vertical Magnetic Soundings Inversion of Anomaly 2

Also for the Anomaly 2, I calculated the vertical soundings starting from the measured data (at 70 m height) by upward continuation at 20 different heights with a constant step of 1 m. The vertical soundings positions are highlighted in figure 3.25 by the green points.

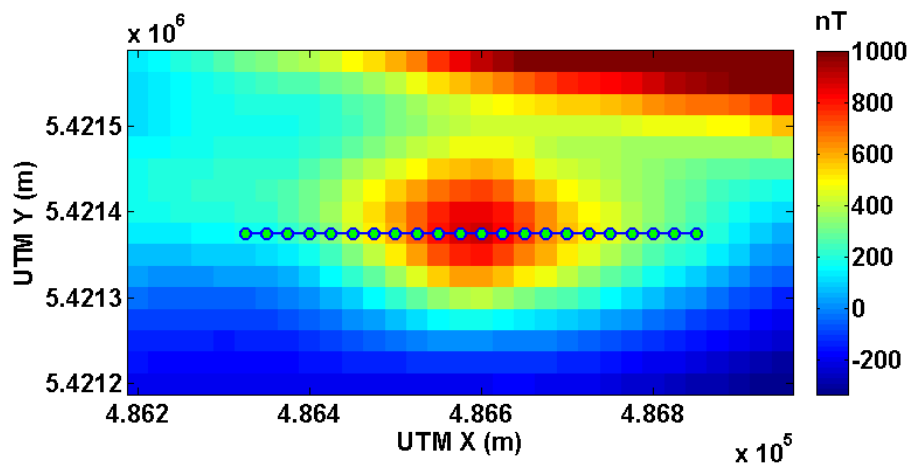


Figure 3.25: Magnetic Anomaly 2. The green dots represent the horizontal positions of the measuring stations and then the individual vertical soundings.

The magnetic anomaly along the profile and at 20 different altitudes is shown in figure 3.26:

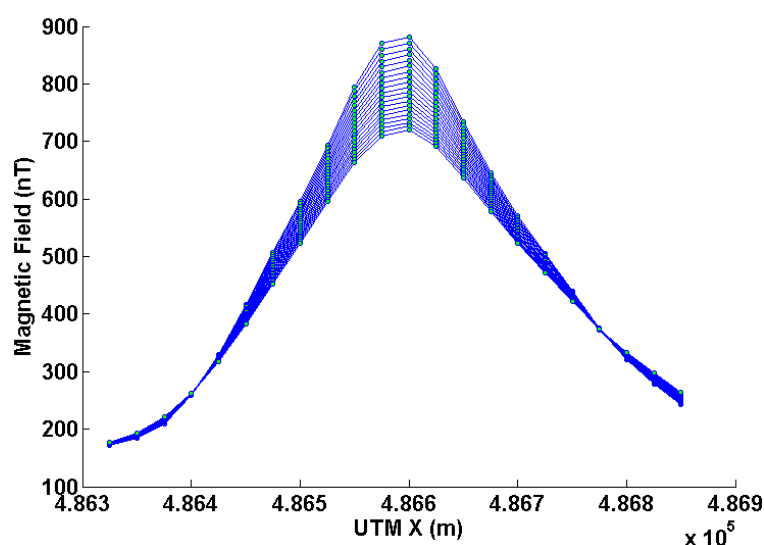


Figure 3.26: Profiles of the magnetic data at different altitudes of measure for the Anomaly 2. The green dots represent, for each altitude, the horizontal positions of the measuring stations and then the individual vertical soundings.

For the estimation of the horizontal dimensions of the anomaly source, I used the maps of the total horizontal derivative calculated from the magnetic data (figure 3.27) and from the vertical derivative of the magnetic data (figure 3.28).

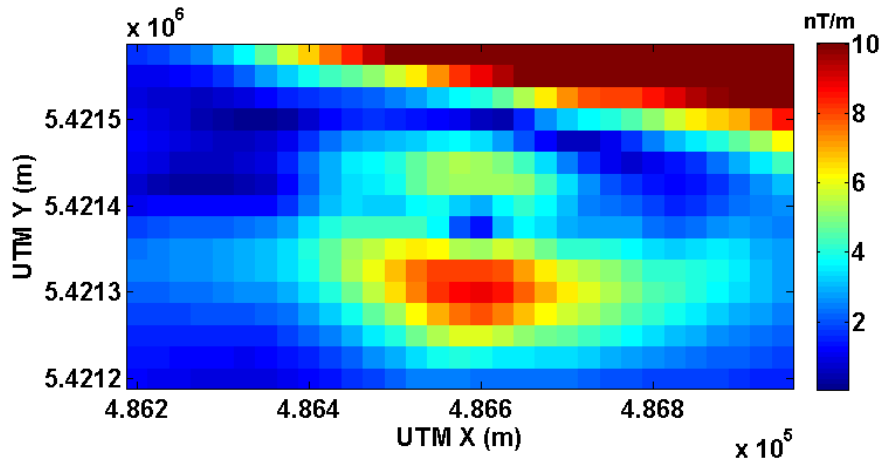


Figure 3.27: Total horizontal derivative of magnetic data related to the Anomaly 2.

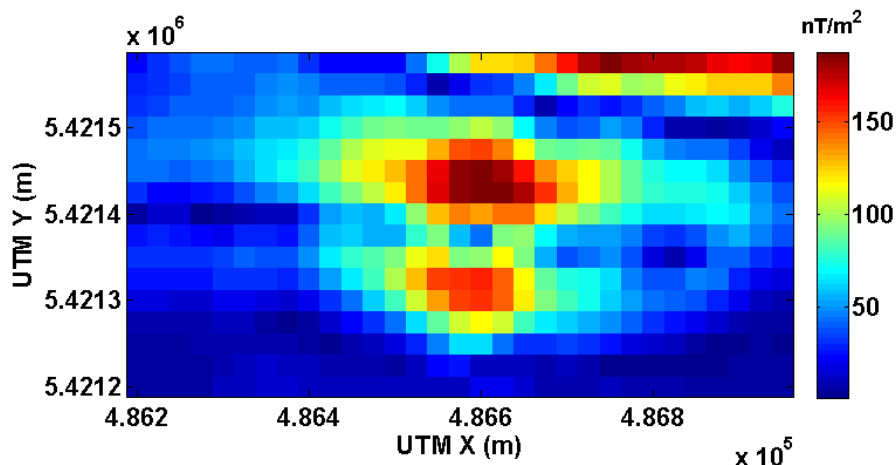


Figure 3.28: Total horizontal derivative of the vertical derivative of magnetic data related to the Anomaly 2.

Both maps provide a clear estimate of the N-S dimension. Even in this case the method applied on the vertical derivative of magnetic data, increasing the resolution, indicates a smaller dimension (100 m) than that estimated from the magnetic data (150 m).

In the W-E direction the position of the boundaries is not obvious. The vertical derivative highlights the central part of the anomaly providing an estimation of 125 m. This part is probably related to the shallowest and most magnetized part of the anomaly source. However, as clearly appears in both maps, the source extends well beyond of 125 m.

In order to retrieve more information on the W-E dimension of the anomaly source, I downward continued the magnetic data. One of the advantages of the downward continuation is the improvement of the lateral resolution. As described in Section 3.8, the first transformation applied on magnetic data has been an upward continuation for referring them to a unique horizontal surface. The height of this surface was the maximum altitude of magnetic sensor above the sea level (355 m). Starting from the collected data, I performed a downward continuation and I referred the data to the same horizontal surface with a height that is equal to the minimum altitude of the magnetic sensor above the sea level (310 m). Then, I calculated the horizontal derivative (figure 3.29):

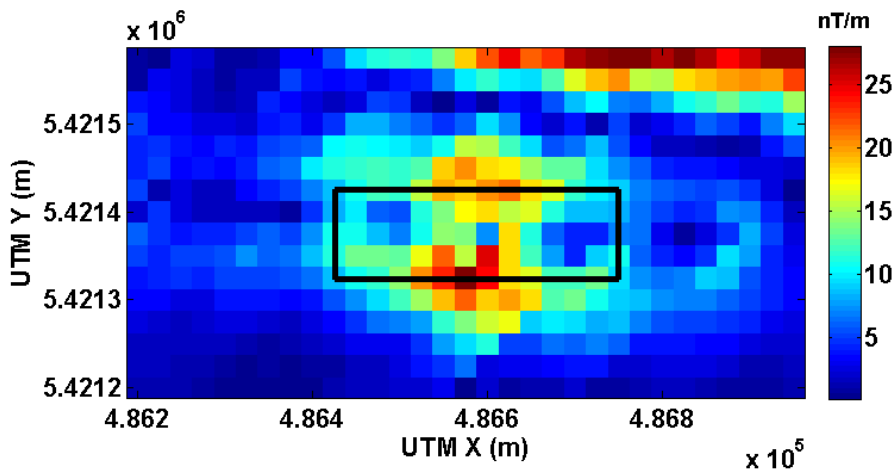


Figure 3.29: Horizontal derivative of magnetic data related to the Anomaly 2 after downward continuation.

The downward continuation allowed obtaining a more reliable estimation of the dimension along the X direction (black rectangle in figure 3.29). Using the information retrieved from this map, I calculated the kernel by using a prismatic source with horizontal dimensions equal to 350×100 m.

In the inversion process, I discretized the model in the same way as done for Anomaly 1. A first-order polynomial is added to approximate the continuation error. The constraints on susceptibility consider the existence of magnetic minerals (especially pyrrhotite) in the rocks and are set varying from 0 to 0.25 as in the previous case.

For the experimental error on the measured data, I needed to use a higher value to recover a useful model (2 nT).

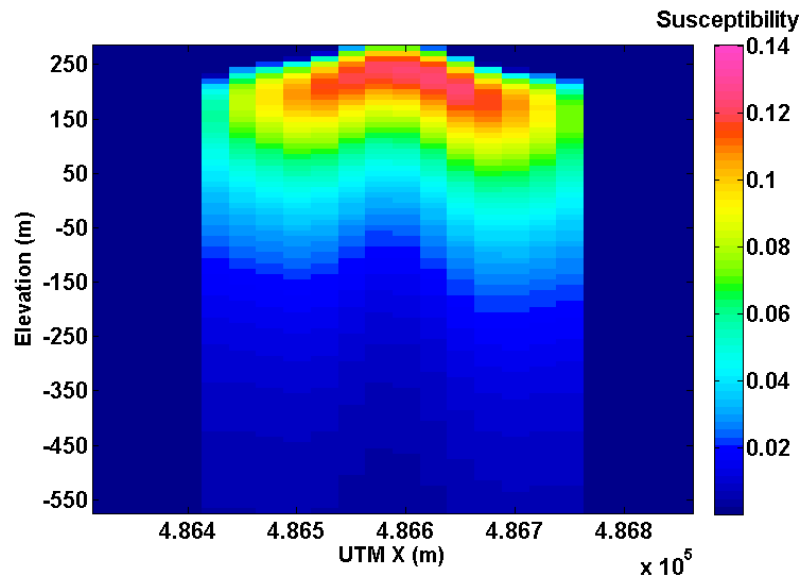


Figure 3.30: Vertical Soundings inversion of the magnetic data related to the Anomaly 2.

Even in this case, the Vertical Soundings inversion allow to recover a complex source (figure 3.30), with a more shallow and magnetized central part, while both sides, the source shows a west and eastward dip with a decrease of the magnetic susceptibility, that is more pronounced in western part.

The comparison between the estimated data and the measured data is shown in figure 3.31. In this case, the fitting is really good with a RMSD value of 27.5 nT.

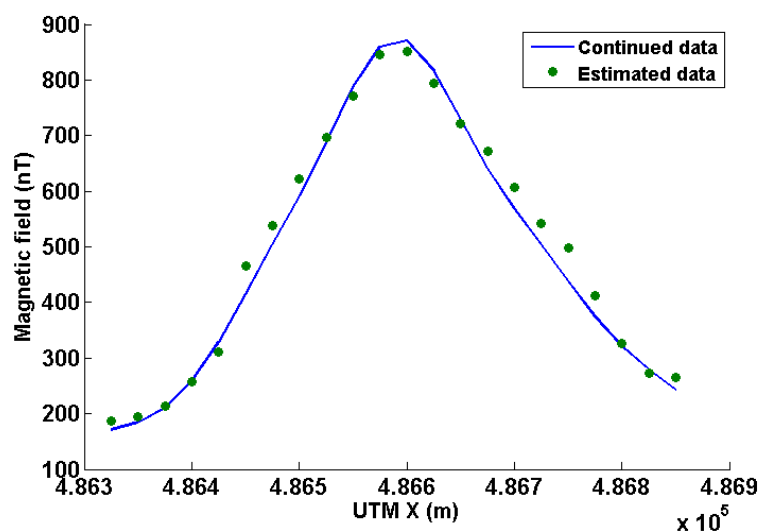


Figure 3.31: Comparison between the continued and the estimated data related to the Anomaly 2 at 71 m height above the ground.

### 3.8.3 Comparison of Vertical Magnetic Soundings inversion and 3D magnetic inversion for the Anomaly 1 and 2

A single magnetic dataset was built from the two measured ones over an area of overlapping between the two VTEM survey (figure 3.17). The 3D magnetic inversion of these data was performed by using the inversion code Mag3D, developed at UBC-GIF (Li and Oldenburg, 1996). The main characteristic of this algorithm is the introduction in the inversion process of a depth-weighting function. This depth-weighting function overcomes the intrinsic limitation of the minimum length solution that is characterized by model parameter values as close as possible to zero. This leads to a distribution of the unknown susceptibility or density, which is very shallow and not representative of the true source distribution. The depth-weighting function defined by Li and Oldenburg (1996) is expressed as:

$$w(z) = \frac{1}{(z + z_0)^{\beta/2}} \quad (3.1)$$

where  $z$  is the depth of the layers and  $z_0$  is related to the height of survey. For the exponent  $\beta$ , Li and Oldenburg (1996) suggested to use a value of 3 for the magnetic case and a value of 2 for the gravity case. These values correspond to the fall-off rates of the field produced by a small cubic cell in the magnetic and gravity cases. The depth-weighting function, opposing to the natural decay of the kernel, allows to obtain more realistic inversion models.

Cella and Fedi (2012) shown instead that the appropriate value of  $\beta$  should not be associated to the field decay of a single cell but to the field decay of the studied field. For these authors the value of  $\beta$  exponent must be related to  $N$ , the structural index of the source, that is related to the fall-off decay of the field and reflects the type of source, rather than to the power-law decay of the field generated by a single cell. The structural index may be, in turn, estimated with standard methods such as Euler Deconvolution or the study of the scaling function (Fedi, 2007; Florio et al., 2009). As shown by Cella and Fedi (2012), using a unique value for the exponent of the depth-weighting function (equal to 3 for magnetic case) can lead to recover sources at greater depths than the real ones, in case of sources for which the structural index is lower than 3.

The inverse models recovered by the Vertical Soundings inversions applied to the two selected magnetic anomaly (Anomaly 1 and 2) and presented in Section 3.8.1 and 3.8.2 were compared to the inverse models for the same vertical cross-sections obtained from Mag3D inversion (figures 3.32 and 3.33). These latest results have been obtained, using a depth-weighting function with a unique exponent ( $\beta = 3$ ) for the entire dataset during the inversion process. Figure 3.32 shows the inverse models, obtained by using the Vertical Soundings inversion algorithm (figure 3.32a) and Mag3D inversion code (figure 3.32b) on the magnetic Anomaly 1.

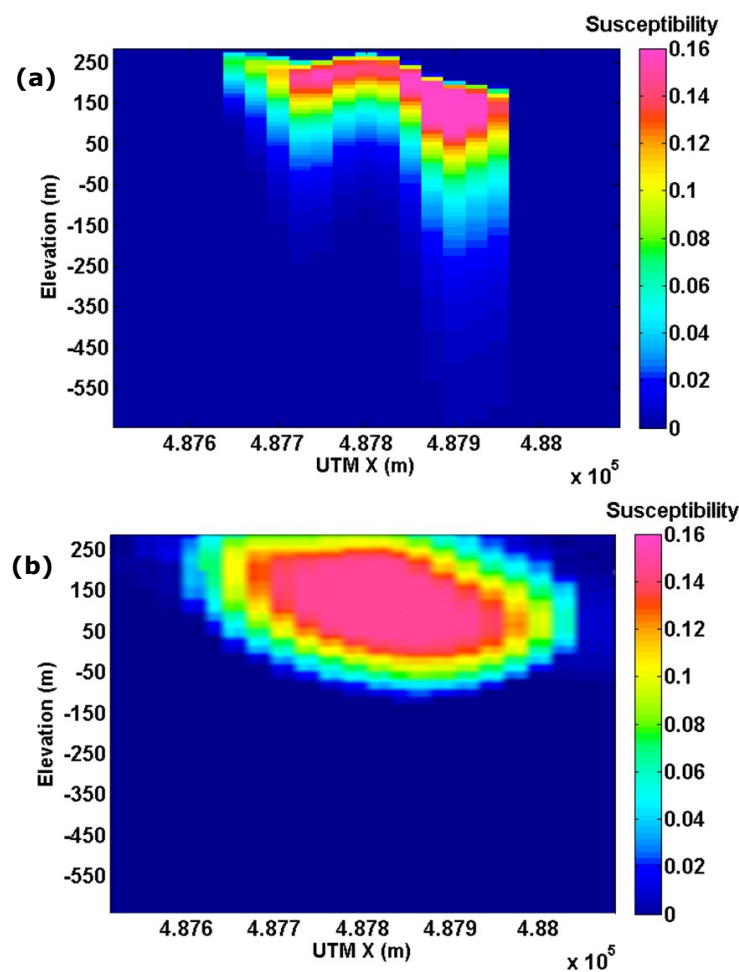


Figure 3.32: Vertical Soundings inversion (a) and Mag3D inversion (b) of the magnetic Anomaly 1.

The results are quite comparable. Both are able to identify a source dipping eastward with susceptibility values varying over the same range. The Vertical Soundings inversion, as shown in Chapter 2 on synthetic case, is very accurate in the definition of the depth to the top of the structures, while some loss of resolution at depth makes more problematic the definition of the bottom.

Conversely, the Mag3D inversion, using for the depth-weighting function an exponent  $\beta$  equal to 3, gives information mainly about the position of the center of the anomaly source.

Also for the Anomaly 2, the inverse models obtained by using the Vertical Soundings inversion algorithm (figure 3.33a) and the Mag3D inversion code (figure 3.33b) show a remarkable level of consistency both in geometry of the source and in susceptibility values.

Both the inversions allow recovering a complex source with a shallower and more magnetized central part. A west and eastward dip, with lower value of susceptibility, is shown at sides of the source for both models. Again, the estimated depths of the source are more representative of the top of the source for the Vertical Soundings inversion, while the Mag3D inversion is more focused on the center of the anomaly source.

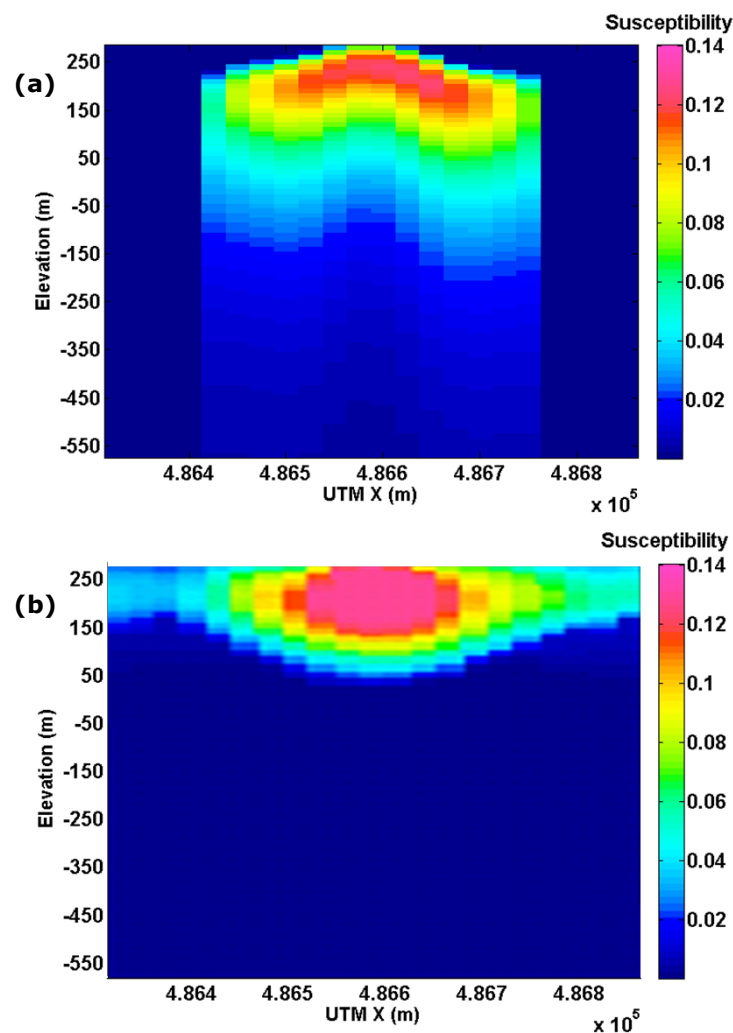


Figure 3.33: Vertical Soundings inversion (a) and Mag3D inversion (b) of the magnetic Anomaly 2.

### **3.9 Comparison of EM inversion and magnetic inversion at the magnetic Anomaly 1 and 2**

In order to investigate the potentiality of a joint, or cooperative, inversion of TEM and aeromagnetic data, it is interesting to compare the inverse models obtained by inverting independently these two dataset along the profiles over the Anomaly 1 and 2.

The integration of the inversion results obtained from the electromagnetic and magnetic data, which obey to different physical principles and investigating the distribution of different physical properties within the earth, may help to validate the single interpretation models and could finally provide a better understanding of the geological setting at Broken Evil prospects.

The figure 3.34 shows the conductivity and the susceptibility vertical sections over the Anomaly 1, while the same sections over the Anomaly 2 are shown in figure 3.35.

In both cases, the joint SCI inversion and the Vertical Soundings inversion are able to recover a source presenting high values of conductivity and susceptibility. For the comparison related to the vertical cross-sections at the Anomaly 1 (figure 3.34), the inverse models are in agreement with the information derived from the drill hole located close to the magnetic anomaly. As already mentioned, these well data showed that the causative body should be related to a source characterized by high values of conductivity and susceptibility (graphitic sediments with seams and heavy disseminations of pyrrhotite within felsic tuffs). Both models reproduce an eastward dipping source, with the susceptibility source slightly shallower than the conductivity model. However, synthetic cases in Chapter 2 showed that the Vertical Soundings inversion provides its most accurate results in the definition of the depth to the top of the magnetic anomaly source, where the model shows the susceptibility maxima. In the case of the conductivity model, the maximum observed value are deeper than the top and tend to coincide with the center of the source.

For the comparison related to the vertical cross-sections at the Anomaly 2 (figure 3.35), there are no drill hole information. However, as stated in Section 3.8, the magnetic anomaly occurs in correspondence of metasedimentary rocks and could be caused by the presence in this unit of highly magnetic and

conductive pyrrhotite, which may be associated to sulfide mineralization. The Magnetic Anomaly 2 occurs, in fact, in the Area 2, shown in the conductivity maps (figure 3.13), classified as priority drill target (Galkine, 2012). Both models reproduce a source with a shallower conductive and magnetized central part, while the source tends to be deeper going east or west from there. Also in this case, the source depths estimated from the susceptibility section are in good agreement with those estimated by the conductivity model. Again it is confirmed that the maximum of the investigated physical property is localized at the top of the source for the magnetic inversion, while it is deeper for the conductivity model.

The comparison between the inversion of the two dataset demonstrates that, in this case, the TEM and magnetic methods are sensitive to the same sources, showing a positive correlation between the two investigated physical properties, i.e. high values of conductivity and high values of susceptibility, although with some slight differences in the estimated depth. This suggests, in this case, the possibility to set up a method of joint inversion of the two dataset. However, it must be considered that a simple petrophysical relationship between susceptibility and resistivity is not known. A joint inversion approach could be applied by building an empirical relationship between the two parameters by using, for example, borehole measurements of resistivity and susceptibility (Dell'Aversana, 2014).

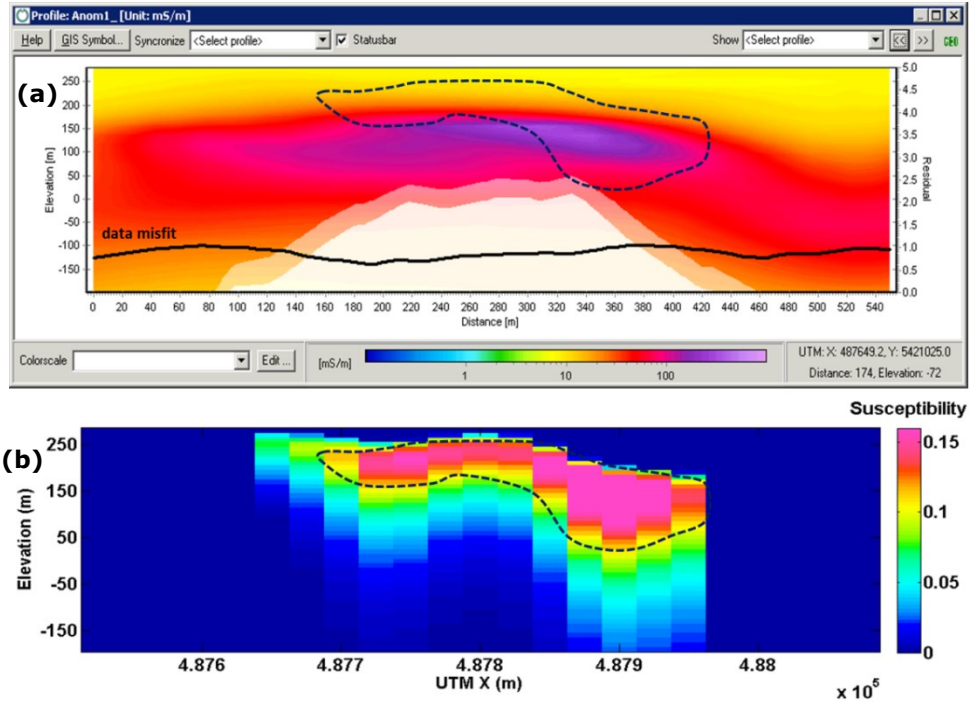


Figure 3.34: Conductivity section (a) recovered by joint SCI inversion and susceptibility section (b) recovered by Vertical Soundings inversion along a profile at the magnetic Anomaly 1. The dashed line approximates the outline of the magnetic source and is plotted on the conductivity model for comparison. Depths are expressed as elevation above sea level.

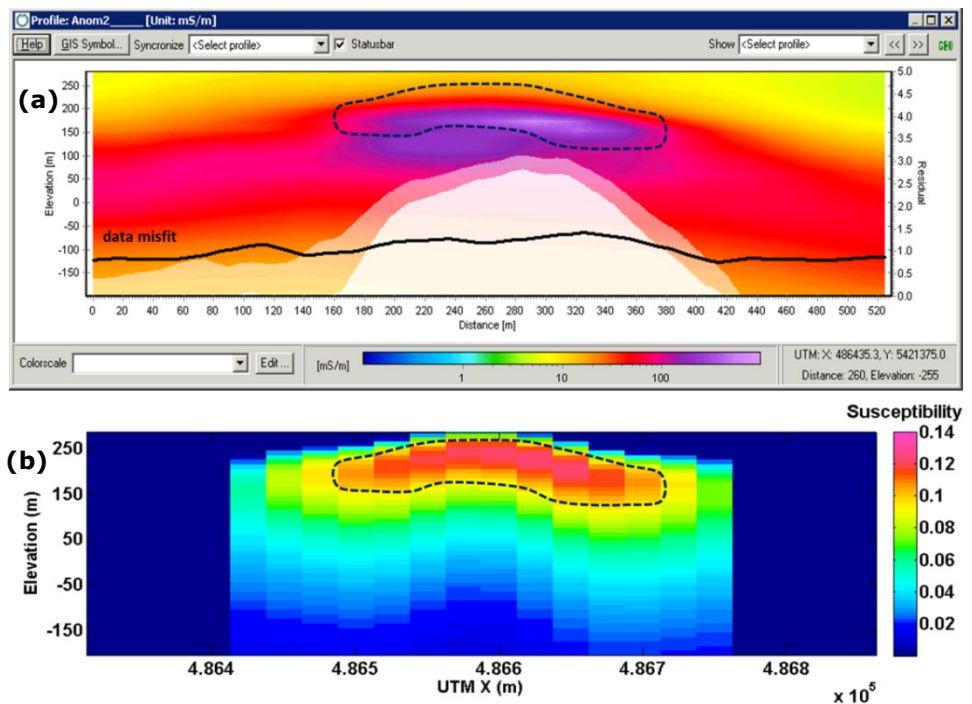


Figure 3.35: Conductivity section (a) recovered by joint SCI inversion and susceptibility section (b) recovered by Vertical Soundings inversion along a profile at the magnetic Anomaly 2. The dashed line approximates the outline of the magnetic source and is plotted on the conductivity model for comparison. Depths are expressed as elevation above sea level.

## **CHAPTER 4 – Spatially Constrained Inversion of IP parameters from airborne EM data and inversion of Vertical Magnetic Soundings from aeromagnetic data: the case study of Drybones kimberlite, Northwest Territories (CANADA)**

### **4.1 Induced-polarization effects in Airborne EM measurements**

In Chapter 1, I stated that the EM transient decay depends on the distribution of the conductivity with depth. I have also shown that slope variations are related to the transition between electro-layers with different conductivity.

There is another phenomenon that can significantly alter the shape of the transient and, if not considered, may lead to recover false structure, with incorrect conductivity-thickness parameters (Viezzoli et al., 2015). It is usually observed in the data derived from coincident-loop systems, showing abnormal fast EM decay with the existence of negative values of the voltage data. This phenomenon can be explained by induced polarization (IP) effects in TDEM data.

The first studies of IP effects in TDEM data date back to Morrison et al. (1969), Spies (1980) and Weidelt (1982). For these authors the appearance of negative transient in coincident-loop systems could be explained using dispersive resistivities. Subsequent workers (Lee, 1981; Raiche, 1983; Wait and Debroux, 1984; Lewis and Lee, 1984) investigated the possibility of extracting IP effects, using numerical modeling, from transient EM data.

Flis et al., (1989) explain the shape of the EM transient, for a polarizable half-space, describing the behavior of the induced current and of the polarization current.

When the transmitter current is turn-off, vortex currents are induced in the earth below the transmitter loop. These currents flow in a direction such as to support the rapidly decaying magnetic field.

An additional current, flowing in the same direction, is created by the movement, driven by the induced current, of the ions in fluid-filled pore

spaces within the rock. This additional current is termed the polarization current and can be thought of as being caused by the additional charge carriers supplied by the pore-space electrolyte.

The polarizable conductor is completely charged when the ionic movement has finished and the ions are piling up at boundaries between regions of varying ion mobility.

When the vortex current decays sufficiently, the ions return to the equilibrium position that existed prior to the induction of the vortex current. This ion movement again constitutes a polarization current, but this current flows in the opposite direction to that of the decaying vortex current with a slower decay. If the earth is sufficiently polarizable, the polarization current may be large enough to dominate the vortex current, causing the *emf* to decay faster than normal and possibly reverse completely.

Although polarization and vortex currents are coupled, their separation is justified considering the different sources generating these currents: a collapsing magnetic field for the vortex current and the capacitive nature of the IP phenomenon (membrane and electrode polarization) for the polarization currents.

This concept is illustrated in figure 4.1 (adapted from Flis et al., 1989), which shows a small volume of polarizable rock under the influence of a vortex current.

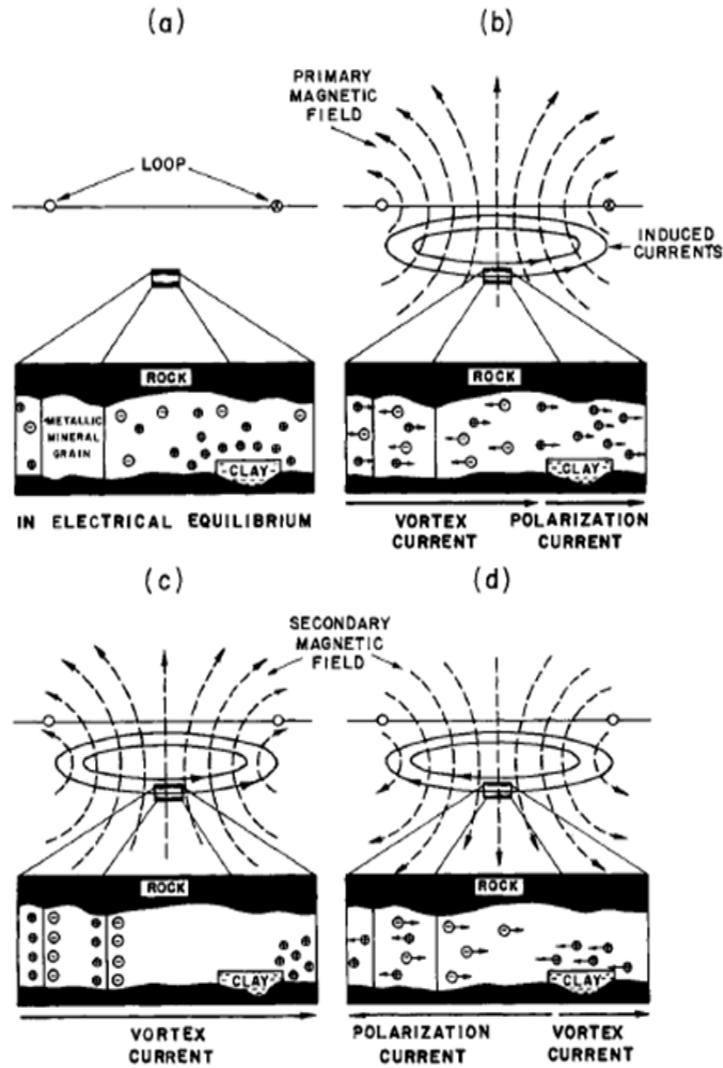


Figure 4.1: Schematic diagram of ionic movement in a volume of polarizable rock beneath a TEM transmitter loop (adapted from Flis et al., 1989).

A polarizable earth may be described using an impedance model derived from the empirical Cole-Cole model (Cole and Cole, 1942):

$$Z(\omega) = \rho \left[ 1 - \frac{m_0}{10^3} \left( 1 - \frac{1}{1 + (i\omega\tau)^c} \right) \right] \quad (4.1)$$

The equation 4.1 introduces a complex impedance relationship, as a function of four parameters:  $\rho$  ( $\Omega\text{m}$ ) is the electrical resistivity,  $m_0$  (mV/V) is the chargeability,  $C$  (dimensionless) is the frequency parameter, describing the variation of phase with frequency and  $\tau$  (s) is the relaxation time. The Cole-Cole parameters determine the amplitude of the polarization current and establish when the *emf* reverses. In general, the amplitude of the polarization current depends mostly on the chargeability and resistivity. In fact, the increase of resistivity decreases the strength of the induced current, allowing

the polarization current to dominate at early times, while an increase of chargeability involves an increase of the amplitude of the polarization current. As mentioned above, there are two evidences in the coincident-loop data that are explained by the existence of IP effects: a sign reversal of voltage data and an anomalously fast decay rate. A sign reversal is obvious. Anomalous decay rates may be a little more ambiguous, especially when the earth is not strictly layered. In this case, an IP effect may be confused with the effect due to a 3D structure. In general, an increasing decay rate with time may be one criterion for identifying an approaching sign reversal in the transient, but it is not sufficient.

In addition, the presence of IP effects can mask the response of deeper layer if its conductivity is not so high that the vortex current dominates over the polarization current (Raiche et al., 1985).

Without considering a dispersive nature for the resistivity, no meaningful information can be derived from a negative transient (Spies and Eggers, 1986), in fact it is a common practice, prior the inversion, to remove any negative values from the data. At the same time the inversion of the data affected by IP effects, without considering them, can lead to significant errors in the estimation of the resistivity. In fact, the early-time enhancement in the *emf* causes the early-time resistivities to be underestimated, while the late-time attenuation causes the late-time resistivities to be overestimated.

## **4.2 Spatially Constrained Inversion for IP parameters**

Over the years, the handling of the IP effects in TDEM data has kept its relevance with a further interest from ground to airborne data (Smith and Klein, 1996; Kratzer and Macnae, 2012). For the airborne data the appearance of IP effects is closely related to the flight height and to the waveform shape (Viezzoli et al., 2013). The increase of flight height causes a delay in the appearance of the IP effects, which can also disappear if the transition occurs below the noise level. The duration of turn-off controls the injection time of the induced currents in the ground that in turn controls its effective charging. Therefore, a slower turn-off current causes the IP effects to dominate over the induced currents at earlier times.

Viezzoli et al., 2013 have also investigated the dependence of the IP effects in the AEM systems, varying the Cole-Cole parameters and they concluded that the values of resistivity and chargeability are positively correlated with an increase of IP effects, i.e. the IP effects appear at earlier times, while for  $C$  and  $\tau$  they didn't observe a similar behavior. The increase of their values is not always followed by an appearance of the IP effects at earlier times.

The possibility of extracting chargeability information from transient EM data, that can have a significant impact to mineral exploration, has provided several suggestions to handle the IP effect with Cole-Cole model. It has been demonstrated how the Cole-Cole model can be modeled in TDEM transients.

Fiandaca et al., (2012) have introduced a 1D algorithm allowing to solve for complex impedance model, where the Cole-Cole model (equation 4.1) represents the forward mapping kernel. The four Cole-Cole parameters are the unknowns of the inverse problem. As we are dealing with a non-linear inversion problem, we need to use a half-space with different starting Cole-Cole values in the inversion process.

Following this approach, some experiments on synthetic AEM data were presented by Viezzoli et al. (2013), showing how 1D inversion is able to recover the unknown parameters and which is their standard deviation, for a chargeable half-space. These tests have highlighted that, in general, the resistivity and chargeability parameters are well-resolved, displaying also some degree of coupling. Low standard deviations are usually associated to frequency parameter  $C$ , for which a low value of starting model is preferable to obtain better convergence and sensitivity.  $\tau$  parameter is the worst resolved and in addition it has been noted that a starting value close to real value is needed to avoid a negative influence to all the other parameters.

In real cases, the inversion of AEM data with the combined estimation of the Cole-Cole parameters is performed following the same approach described for LCI (Auken and Christiansen, 2004) and SCI (Viezzoli et al., 2008) algorithms. A set of vertical and lateral constraints, tied together the parameters of the neighboring soundings along the flight lines for LCI, and along and across the flight lines for SCI.

### **4.3 Geological setting of the Slave Province in the Northwest Territories, Canada**

The Slave Structural Province, 400 km x 750 km in size, is an Archean segment of the North American Craton that is composed of granites, gneisses and supracrustal rocks. Sialic basement remnants, well documented in the Slave, include some of the oldest rocks in the world: the Acasta gneisses in the western part of the province, which have been dated at 3.96 Ga (Bowring and Housch, 1995). Metasedimentary and lesser metavolcanic rocks of the Yellowknife Supergroup, deposited mainly between 2.71 Ga and 2.61 Ga, are the most abundant rocks of the supracrustal sequences. At least five swarms of Proterozoic diabase dykes cut the older units in the central Slave Province (Le Cheminant and van Breemen, 1994; Le Cheminant et al., 1996). The Slave Province is a classic setting for diamondiferous kimberlites: a stable Archean craton with a cool mantle root, which is necessary for the development of the diamond stability field (Haggerty, 1986; Janse, 1993). Kimberlite intrudes granites, metasedimentary rocks and, in some cases, diabase dykes (Pell, 1995a). Subsequent to kimberlite emplacement, the area was covered by Laurentide ice during the Late Wisconsinan glaciation.

Kimberlite is an alkali ultramafic igneous rock, formed from the cooling of molten magma that arises from the melt of peridotite in the mantle at depth of 150-200 km. Kimberlite is composed of at least 35% olivine, together with other minerals such as mica, serpentine, and calcite (Kjaarsgard, 1996).

During its upward into the upper mantle and overlying crust, minerals start to crystallize and the volatile gases expand and exert increasingly higher pressures on the surrounding rocks, eventually breaking some of the surrounding rock and incorporating it into the magma.

The kimberlite magma may produce explosive volcanic events. In the Slave Craton and adjacent areas, these eruptions occurred in subaerial to shallow subaqueous environments and consequently many of the resulting vent systems are vertical to steeply dipping carrot-shaped bodies, equidimensional in plan and tapering gradually with depth. Kimberlite intrusions tend to occur in clusters or fields, with the large-scale distribution possibly controlled by deep-seated structural features and local emplacement controlled by shallow

zones of weakness such as faults or the margins of diabase dykes (Power and Hildes, 2007).

The accepted pipe model comprises three different zones from top to bottom, each with distinctive morphology and texture: the crater, diatreme and hypabyssal zones (Scott Smith, 1996).

Kimberlite craters are usually basin shaped excavations formed at the surface by explosive volcanic eruptions.

Crater facies kimberlite is a mixture of tuffaceous kimberlite, surrounding country rock and overlying sediments.

Two main categories of rocks are found in crater facies kimberlite: pyroclastic, deposited by eruptive forces, and epiclastic, which are the same rocks reworked by water.

In much of the Slave Craton, kimberlite crater facies include a significant component of shale and mudstone, sometimes with a significant component of entrained organic material. Large blocks of surrounding country rock (xenoliths) shattered from the volcanic vent margins are present in some pipes. A Crater facies kimberlite is often deeply weathered and serpentinized.

Kimberlite diatremes are cone-shaped bodies with vertical axes and steeply inward dipping margins.

Diatreme facies describes an explosive kimberlite breccia composed of fine-grained kimberlite, mantle nodules and angular fragments of the surrounding country rocks. Diatreme facies rocks are generally confined to a central breccia pipe and are generally less altered than crater facies rocks.

Hypabyssal kimberlite consists of unaltered fine-grained kimberlite with mantle nodules and rare fragments of country rock. Hypabyssal kimberlite bodies include dykes, blind intrusions and the root zones of kimberlite pipes.

In a given kimberlite field all three facies may be present at surface as a result of differential glacial abrasion and quarrying, and because of blind intrusions. The variation in depth of erosion can occur over distances of a few tens of kilometers or less.

In 1991, in the heart of the Archean Slave Province of the Northwest Territories, northern Canada, a significant new kimberlite province, which hosts more than 150 kimberlite pipes was discovered. Middle Jurassic-, Late Ordovician-, and Cambrian-aged kimberlites have been discovered, some of

which have good economic potential. Most of the kimberlites in the Slave Province do not crop out at surface; they have been identified using a combination of heavy mineral sampling, geophysical techniques and drilling. Many of the pipes are characterized by either high or low magnetic anomalies and low resistivity values.

#### **4.4 Geophysical methods for kimberlites detections**

The application of geophysical methods to exploration for kimberlites and their associated diamonds began over 50 years ago with the use of magnetic and gravity measurements. Within a decade, resistivity and later induced polarization were applied to the problem. By the 1970's both ground and airborne methods included magnetic and electromagnetic measurements (Reed and Witherly, 2007).

The capacity of a geophysical method to detect a kimberlite deposit depends on variation in the petrophysics of kimberlites and their host rocks properties. In this section, the discussion is limited to the kimberlites deposits in the Slave Craton and their geophysical responses caused by physical property contrasts between kimberlites and the host rocks of Slave Craton.

Magnetic anomalies are commonly associated with kimberlite intrusions that generally have higher magnetic susceptibility than surrounding gneisses and granites. In addition, they can be affected by remanent magnetism. Diatreme and hypabyssal facies are, in fact, readily detected. For crater facies, the associated magnetic anomalies can be subtle, due to low magnetic contrast with the surrounding rocks, reflecting the proportion of entrained non-susceptible sediments (Power and Hildes, 2007).

The electrical resistivity of kimberlites increases with depth from crater facies through hypabyssal facies. As a consequence, crater facies display the greatest contrast in physical properties with respect to country rocks and is the most readily detectable with EM methods. In fact, during weathering, a highly conductive clay-rich zone forms in the top of the pipe (Macnae, 1979). This part can produce an induced polarization (IP) effect that can be evaluated by measuring the chargeability of the ground, which is related to ability of the material to retain electrical charges.

However, the existence of fine grained glacio-fluvial and lake sediments in the shield regions of northern Canada, with an electrical resistivity and an electrical chargeability comparable to the crater facies, tend to make more complicated the discrimination between these sources. Alternatively, when the discrimination is impossible, a potential crater facies of kimberlite target can be indirectly identified by assessing if the conductor persists at depth below the overburden thickness (Power and Hildes, 2007).

Diatreme and hypabyssal kimberlite have usually low physical property contrast with respect to the country rocks. For this reason, they are almost indistinguishable from granitic or gneissic country rocks on the basis of electrical resistivity or electrical chargeability.

#### **4.5 The Drybones kimberlite in the Northwestern Territories, Canada**

The Drybones kimberlite is located in Drybones bay, situated approximately 45 km SE from the town of Yelloknife, NWT, Canada (figure 4.2a).

The kimberlite was discovered in 1994 with a single drill hole and lies completely underwater (Great Slave lake), at an average depth of 38 m. A thickness of 65-75 m of lake sediments (clay, till and sand), further covers the kimberlite. The morphology of the pipe, in figure 4.2b, shows a spatially elongated intrusion (900 m by 400 m), consisting of crater, pyroclastic and diatreme facies (Kretchmar, 1995).

A geological cross-section (figure 4.2c), along the profile AA', has been drawn basing on drilling information (Kretchmar, 1995).

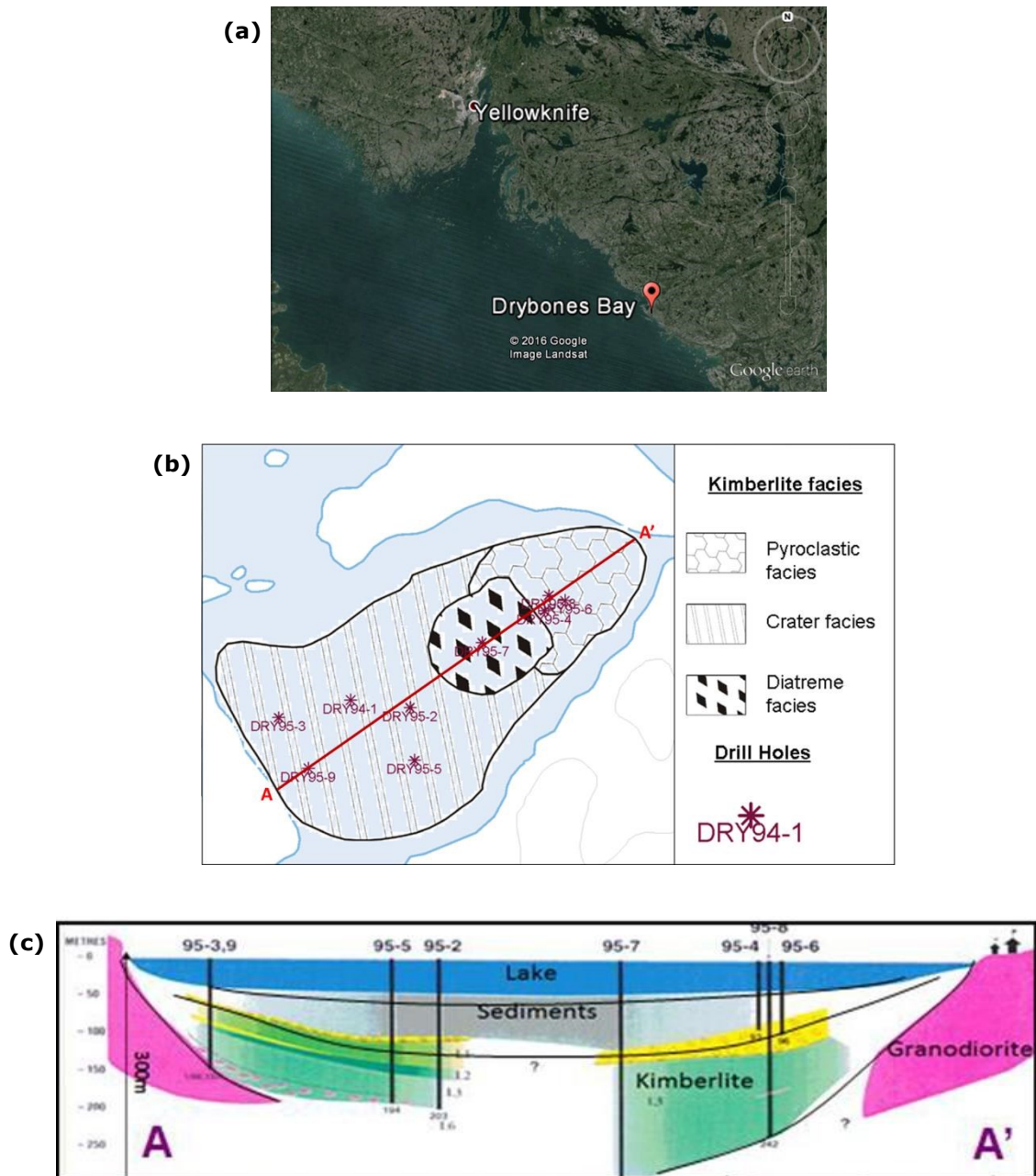


Figure 4.2: (a) Geographic location of Drybones bay (Google Earth); (b) Surface morphology of the Drybones pipe and the locations of 1994-95 drill wells (Kretchmar, 1995); (c) Geological cross-sections along the profile AA' based on drilling (Kretchmar, 1995).

The bedrock geology in Drybones area consists of Archean granite, granodiorite and tonalite (Kretchmar, 1995). Metasediments of Yellowknife supergroup are also present (Dunn et al., 2001). In addition, there are several known tectonic faults present in direct vicinity of the kimberlite area and a diabase dike in the northern part crosses the area from E to W (figure 4.3).

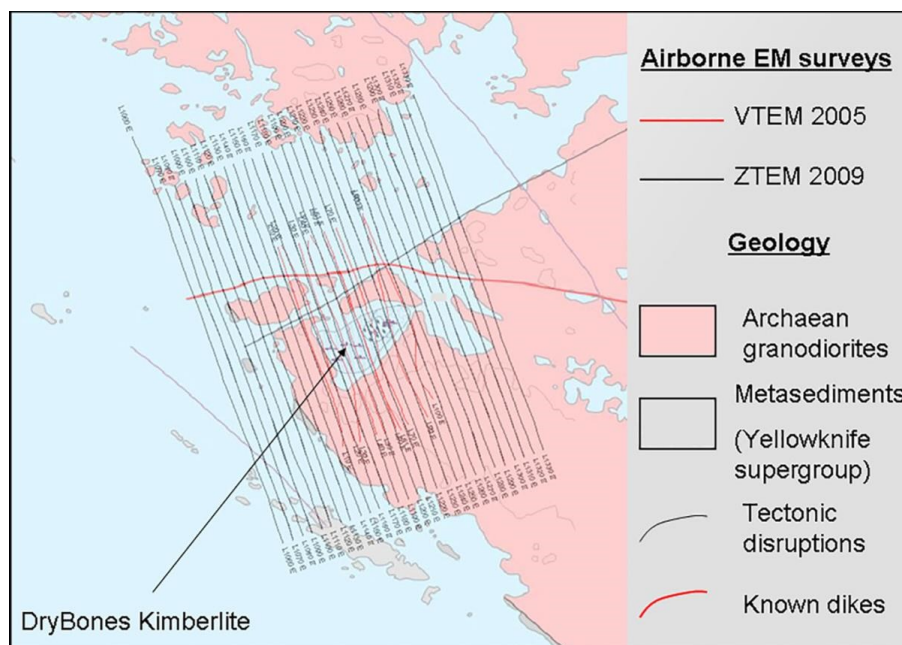


Figure 4.3: Bedrock geology of the area under study and airborne EM survey flight lines over the Drybones kimberlite pipe.

The figure 4.3 includes also the flight lines of two airborne EM surveys that I will describe in detail in the next section.

#### 4.5.1 AEM surveys over Drybones kimberlite

Numerous geophysical surveys have been performed over Drybones kimberlite since 1994. They include electromagnetic, magnetic and gravity surveys (Kaminski et al., 2010). I have focused on two AEM surveys, conducted by Geotech, Ltd. A VTEM survey in 2005 and a larger ZTEM survey in 2009 (figure 4.3). Both included a total magnetic intensity measurement. The ZTEM survey was designed to overlap the flight lines of the VTEM survey.

The airborne Z-Axis Tipper Electromagnetic (ZTEM) system (Lo and Zang, 2008) provides the spatial coverage of an airborne technique with the investigative depth of a natural-source method. Originally conceived as the Audio-Frequency (AFMAG) technique (Ward, 1959), the ZTEM system can resolve resistivity contrasts from the surface to a depth of 2 km based on time variations in the earth's naturally occurring magnetic field.

The VTEM survey carried out in 2005 along 9 flight lines spacing on average of 100 m with orientation approximately N-S.

The geophysical survey consisted of helicopter borne EM using the VTEM system (Witherly et al., 2004) and aeromagnetics using a caesium

magnetometer. The system included also a GPS navigation system and a radar altimeter.

The EM system is concentric and Z-direction oriented. The receiver coils were towed at a mean distance of 45 m below the aircraft

Transmitter and Z-receiver specifications are listed in table 4.1:

| <b>Transmitter</b>         |                        |
|----------------------------|------------------------|
| Coil diameter              | 26 m                   |
| Number of turns            | 4                      |
| Effective transmitter area | 2123.7 m <sup>2</sup>  |
| Base frequency             | 30 Hz                  |
| Peak current               | 180 A                  |
| Pulse width                | 7.4 ms                 |
| Waveform shape             | Trapezoid (figure 4.4) |
| Peak dipole moment         | 382000 nIA             |
| <b>Z-Receiver</b>          |                        |
| Coil diameter              | 1.1 m                  |
| Number of turns            | 100                    |
| Effective receiver area    | 95 m <sup>2</sup>      |

Table 4.1: VTEM system specifications.

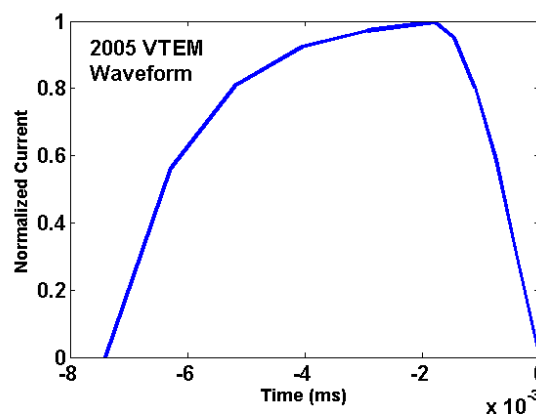


Figure 4.4: VTEM waveform.

The 2005 VTEM decay was sampled using 25 time measurement gates in the range from 0.130 to 6.340 ms after the time-off.

The strength of magnetic field is measured by a magnetic sensor mounted in a separate bird, 20 m below the helicopter. The magnetic data are corrected for diurnal variation using the digitally recorded ground base station magnetic values. The EM and magnetic data are sampled at 0.1 s.

In this work, I have reprocessed and inverted the VTEM data with the combined estimation of the Cole-Cole parameters using the LCI (Auken and Christiansen, 2004) and SCI (Viezzoli et al., 2008) algorithms. I have also performed a Vertical Soundings inversion of magnetic data measured by VTEM system. The inversion results have been compared with 3D inversion results of EM and Magnetic data, presented in Kaminski and Oldenburg (2012).

## **4.6 Processing VTEM data**

The navigation and voltage data collected by 2005 VTEM survey have been imported and processed using the Aarhus Workbench software package (Auken et al., 2009).

The procedures of filtering and averaging of navigation data are automatically performed and their results are manually checked along with other quality control parameters as flight speed, topography, etc. or system parameters as transmitter current, transmitter temperature, etc.

The processing of voltage data affected by IP effects, requires greater attention than ordinary data. In this case, I had to retain the negative data above noise level. Automatic filtering procedures, which have been designed to remove disturbed data (noisy and coupled data), could not be applied. The imported raw data, consisted of transients with time step of 0.1 s, were laterally averaged, by defining a sounding distance of 1.5 s that, considering the helicopter speed (22 m/s), correspond to extract a sounding every 30-35 m.

As explained in Section 3.5.2, this procedure is usually performed using a trapezoidal filter allowing to set a different grade of averaging between the early and late times in order to achieve the best possible resolution for near-surface resistivity structure and the desired depth of penetration.

In the present study, the approach was to not increase the smoothness of voltage data (especially at late times), compromising existing lateral variability. For this reason, no trapezoidal averaging filter was actually applied in this case, but I set an averaging filter with a fixed time window of 1 s for all the gates.

The drawback of setting a constant (and small) time window in the averaging procedure is related to a worsening of data quality at late times. However, in

this case, I was able to obtain an acceptable S/N ratio without losing the desired lateral variability.

After the automatic stacking, the average soundings were displayed in different plots for each flight line. The absolute value of the voltage data is plotted (figure 4.5).

In this phase of manual processing, I assessed, even transient by transient, which negative data of the transient should be retained, as probably explained by IP effects, which part should be removed from the dataset, as contaminated by noise and which part is needed to assign a higher grade of uncertainty in order to improve the data fit of the forward response after the inversion had been run.

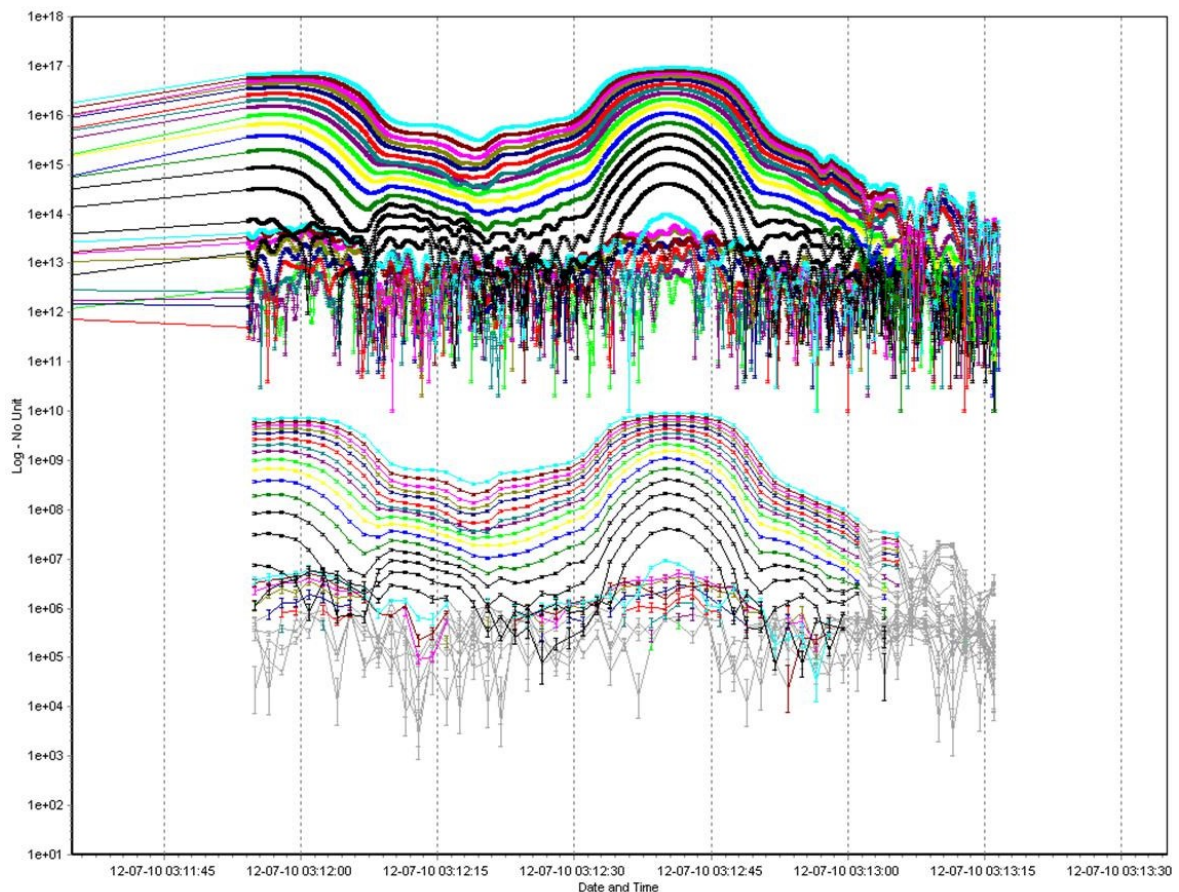


Figure 4.5: Raw (above) and averaged (below) data related to flight line 50.

The voltage data, as shown in figure 4.5, display two evident IP effects.

I noticed, by means of the GIS map, that they occur in correspondence of the northern part of the survey, over the lake (figure 4.6a) and in the center part, where the kimberlite is located (figure 4.6b). These clear IP effects have been identified across all flight lines.

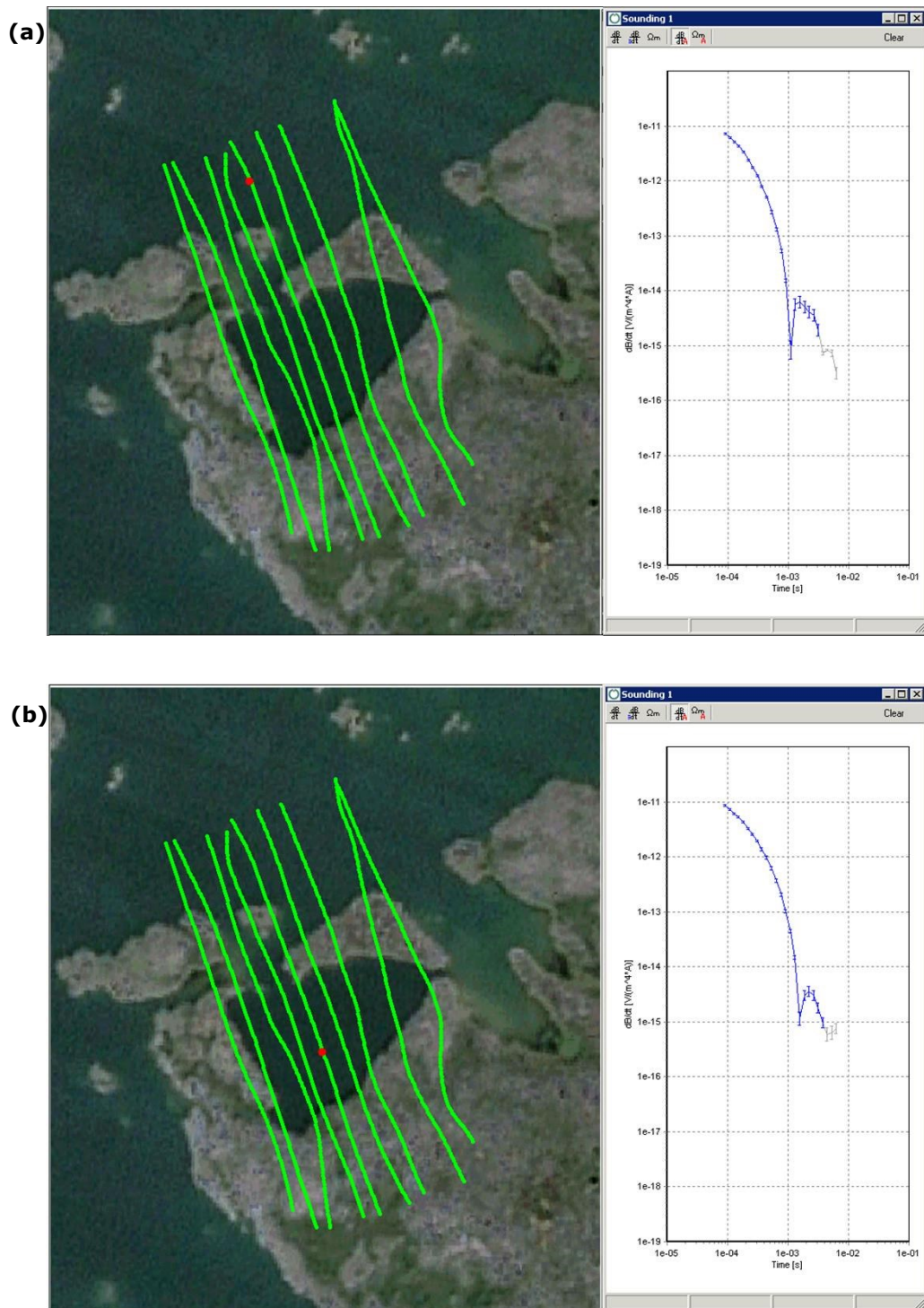


Figure 4.6: The evidences of IP effects in VTEM data, occurring over the lake (a) and over the kimberlite pipe (b).

As I have already said in Section 4.1, the IP effects in the EM transient could not be fitted with layered earth model that does not account for IP. In this case, the negative values should be deleted before the inversion. However,

using the Cole-Cole model, the negative values can be retained and the data can be inverted for much longer decays.

For the estimation of the Cole-Cole parameters, the inversion is performed by applying the LCI and SCI approaches. This means that spatial constraints are applied to all the unknown parameters.

A fast smooth LCI inversion was first applied on EM data of line 50 in order to identify a useful starting model and a set of vertical and lateral constraints that allow to obtain an acceptable data misfit. Based on the results on synthetic tests as in Viezzoli et al. (2013), I set tighter vertical and lateral constraints for  $\tau$  and  $C$ , allowing to  $\rho$  and  $m_0$  to vary more freely.

Following a smooth approach, the model is discretized by 20 layers with fixed thickness. The maximum depth of the model (extending from 0 to 500 m) is chosen according to the penetration capability of the system and the thickness of the layers increases logarithmically with depth, starting from few meters in the shallow part of the model.

In table 4.2, I summarized the values of starting model for the four Cole-Cole parameters and the values of vertical and lateral constraints.

|                            | $\rho$             | $m_0$      | $\tau$   | $C$  |
|----------------------------|--------------------|------------|----------|------|
| <b>Starting Model</b>      | 300 ( $\Omega m$ ) | 100 (mV/V) | 0.001(s) | 0.5  |
| <b>Vertical Constraint</b> | 3                  | 1.3        | 1.1      | 1.01 |
| <b>Lateral Constraint</b>  | 1.5                | 1.5        | 1.1      | 1.01 |

Table 4.2: Starting model, vertical and lateral constraint values of the Cole-Cole parameters.

The inversion results of line 50, using the Cole-Cole model with LCI approach are shown in figure 4.7, where the four vertical cross-sections for the four Cole-Cole parameters are plotted.

The vertical cross-sections for the resistivity and the chargeability show interesting conductive and chargeable structures.

One maximum of conductivity and chargeability is located in the northern part of the survey area, in correspondence of the Great Slave lake. Another maximum of conductivity and chargeability occurs in the center part of the survey area where the kimberlite pipe is placed (figure 4.7).

The cross-sections for  $\tau$  and  $C$  do not show valuable structures as I have set very tight vertical and lateral constraints (10% of allowed variation for  $\tau$  and 1% for  $C$ ). Using these kinds of constraint, I forced these two latter parameters to be rather homogeneous at all depths.

The data misfit, that has a total value of 1.3 (dimensionless), is really acceptable as explained in Section 3.6.

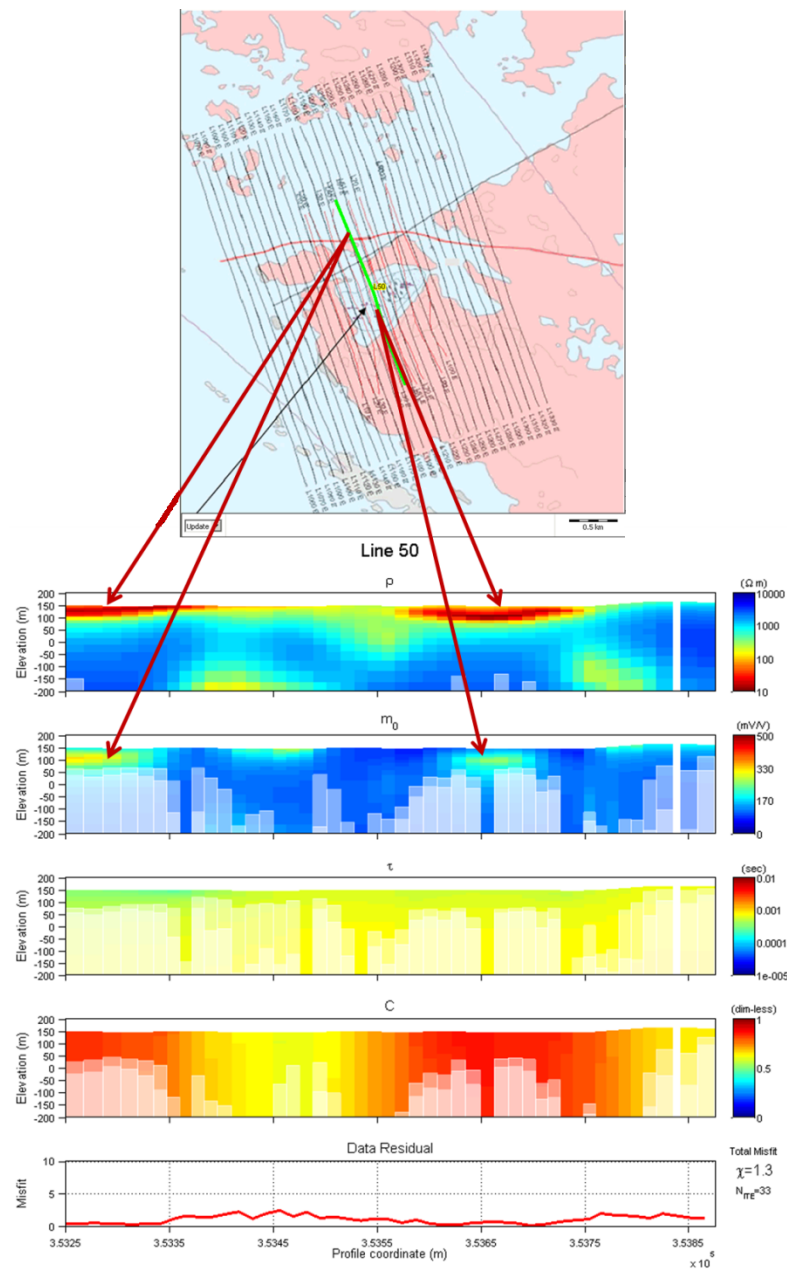


Figure 4.7: LCI inversion results of flight line 50 using Cole-Cole model. The first two cross-sections are related to the resistivity and chargeability and show interesting structures in correspondence of the lake. The third and fourth cross-sections are related to  $\tau$  and  $C$  parameters and are less informative for the role of the applied constraints. The last plot shows the data residual that on average has a value of 1.3 (dimensionless).

## 4.7 SCI of VTEM data modelling IP effects

After the fast LCI inversion, performed to identify a correct combination of the starting model values and of vertical and lateral constraints strengths, all the EM data were inverted using the quasi 3-D Spatially Constrained Inversion

approach (Viezzoli et al. 2008) to solve for complex impedance model. Here the Cole-Cole model represents the forward mapping kernel and its parameters represent the unknowns of the inverse problem (Fiandaca et al., 2012).

Also for this type of inversion, as for the classical resistivity inversion (Section 3.6), the transfer function of the instrumentation is modeled (Tx current, loop area, number of gates, repetition frequency, waveform, repetition frequency, Rx time gates, low pass filters and system altitude).

Using the SCI approach, the model parameters of adjacent soundings, along and across the flight lines, are tied together within an allowed variation to produce a lateral homogeneity.

The inversion was performed using a starting model discretized by 20 layers with thicknesses that increase logarithmically with depth from 0 to 500 m. The strengths of vertical and lateral constraints are those defined in table 4.2.

The inversion has provided a total data residual equal to 1.26 (dimensionless). Figure 4.8 shows the misfit associated to each inverted sounding.

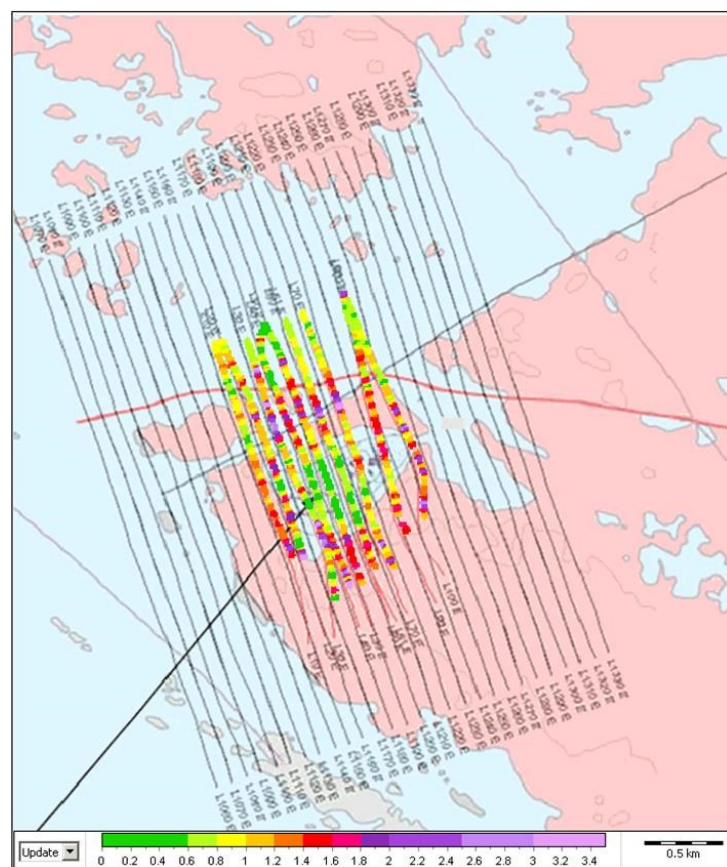


Figure 4.8: Absolute value of the misfit between the forward modeled data and measured data, normalized to the data noise for each time gates.

## **4.8 Interpretation of constrained inversion of IP parameters results**

The interpretations of the inversion results of the VTEM data collected over the Drybones kimberlite was conducted using a number of horizontal geophysical maps at selected depth intervals below the surface.

The maps show an average resistivity (figure 4.9) and chargeability (figure 4.10) and have been superimposed on the bedrock geology.

As already said, the inversion of EM data, using the Cole-Cole model, allows to estimate also the  $\tau$  and  $C$  parameters. However, the approach of using tighter vertical and lateral constraints for these parameters corresponds to force them to be rather homogeneous, and this implies that not easy interpretations may be derived from the analysis of these recovered parameters.

The depth intervals below the ground surface have been chosen from the drilling information over the Drybones kimberlite, where the top of the lake sediments is located at 30-40 m depth and the top of kimberlite at 100 m.

The Great Slave Lake has a shallower depth in the northern part of the survey area (Schertzer et al., 2003) where the top of lake sediments can already be found at 10 m depth. The evidence of the different depth of the lake, and as consequence different depth of the lake sediments, is reflected in both the maps of resistivity and chargeability.

Low values of resistivity ( $< 50 \Omega\text{m}$ ) are associated to the lake and lake sediments, compared with more highly resistive Archean basement (figure 4.9).

High values of chargeability ( $> 300 \text{ mV/V}$ ) are associated to the lake sediments (figure 4.10). These values, occurring at the top depth of the lake sediments in the area where is located the kimberlite, while in the northern part of the survey area, they are valuable at shallower depth, confirming a lower depth of the lake in this area.

The presence of the lake sediments overburden, with low values of resistivity and high values of chargeability, tends to mask the effects of the kimberlite.

Despite the physical properties of the kimberlite, that especially in the crater facies are characterized by lower resistivity and higher chargeability values if compared with a host Archaean granodioritic basement and then should makes it easily recognizable, in this case an obvious detection of its depth is difficult.

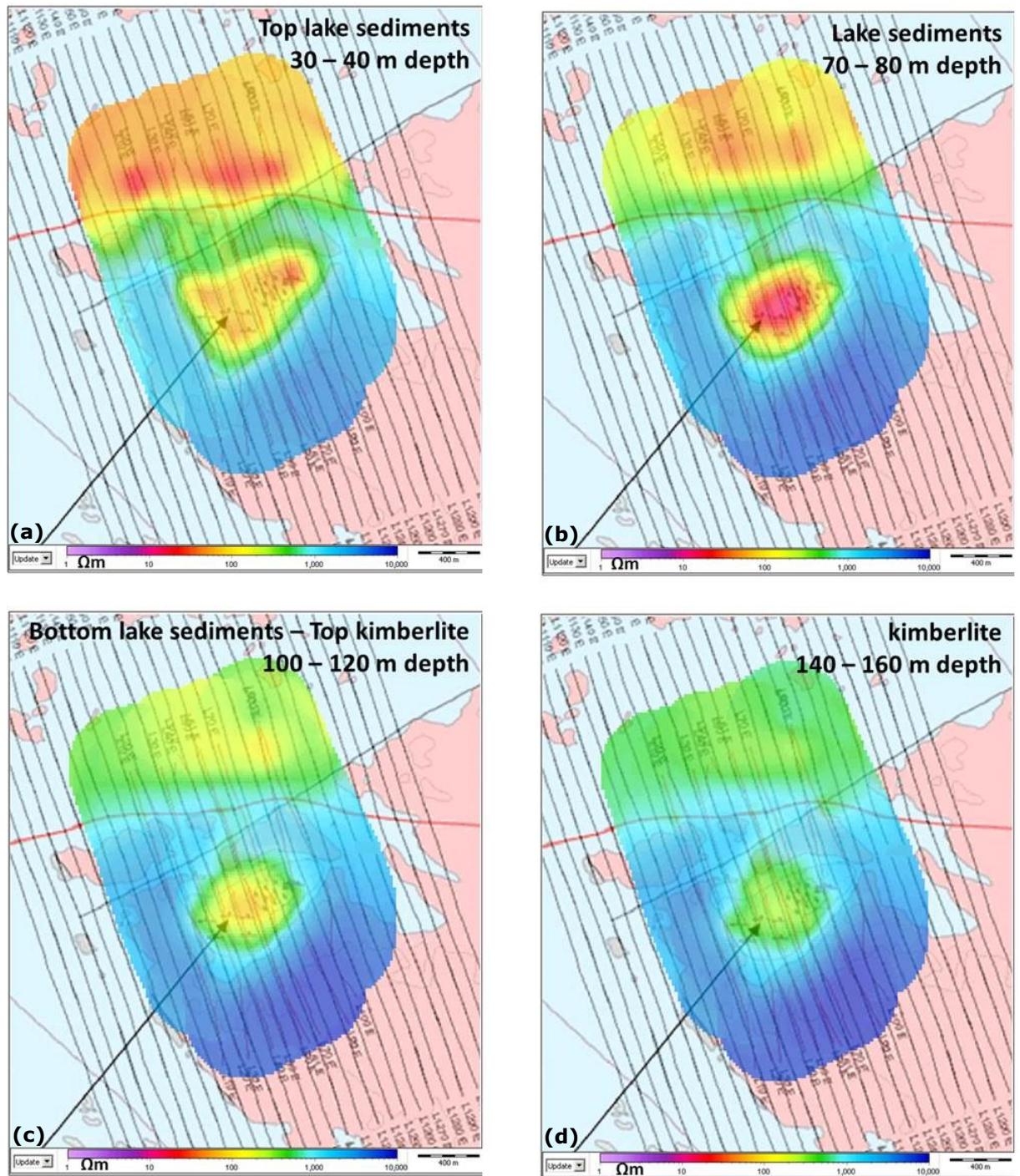


Figure 4.9: SCI inversion result using Cole-Cole model, resistivity maps at: (a) 30-40 m depth; (b) 70-80 m depth; (c) 100-120 m depth; (d) 140-160 m depth.

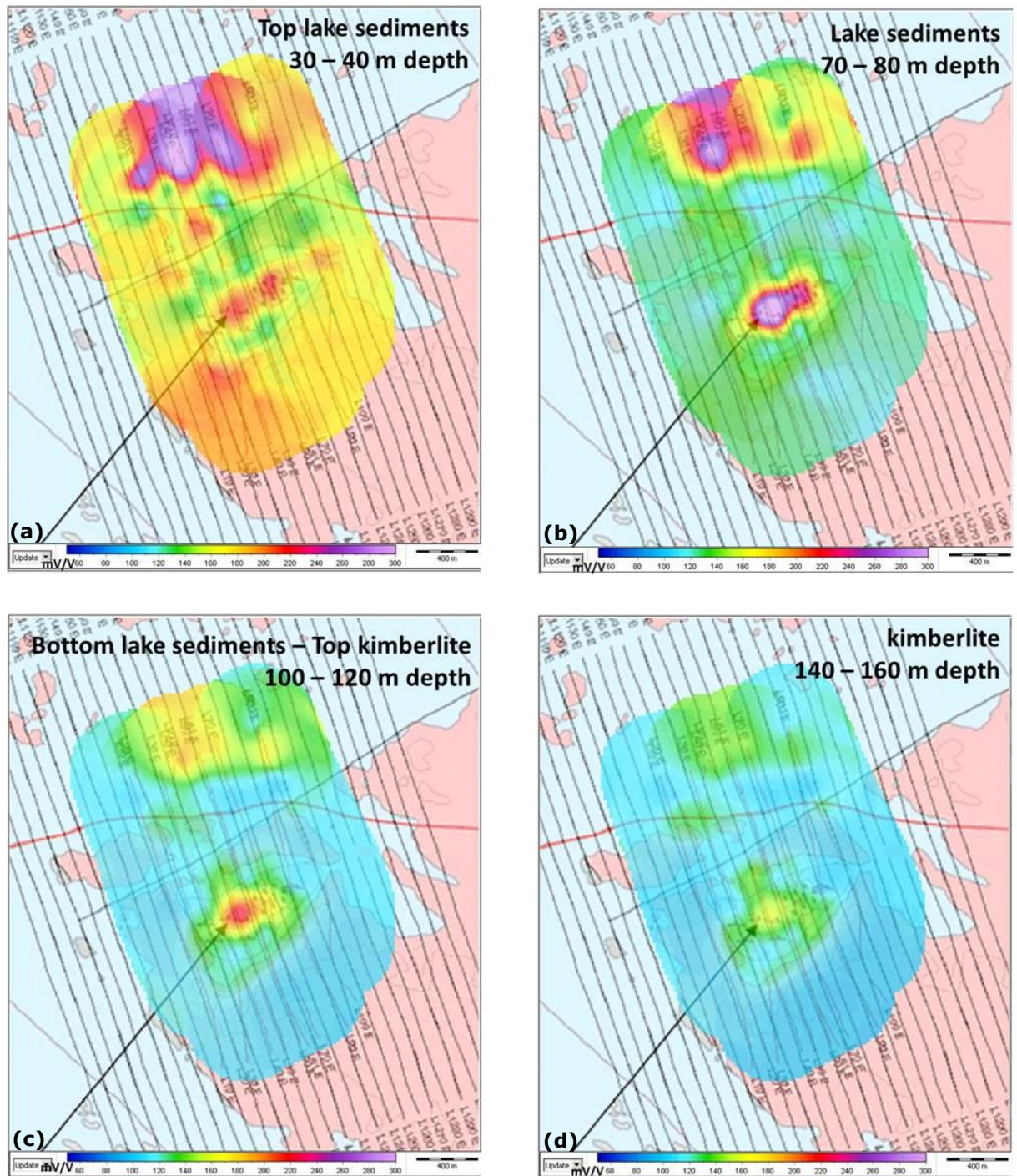


Figure 4.10: SCI inversion result using Cole-Cole model, chargeability maps at: (a) 30-40 m depth; (b) 70-80 m depth; (c) 100-120 m depth; (d) 140-160 m depth.

### 4.8.1 Resistivity and chargeability vertical cross-sections along the profile AA'

The resistivity and the chargeability models, recovered from the 1D constrained inversion, were verified against the known geology along the cross-section AA' (figure 4.11)

The location of the profile AA' is shown in figure 4.2b.

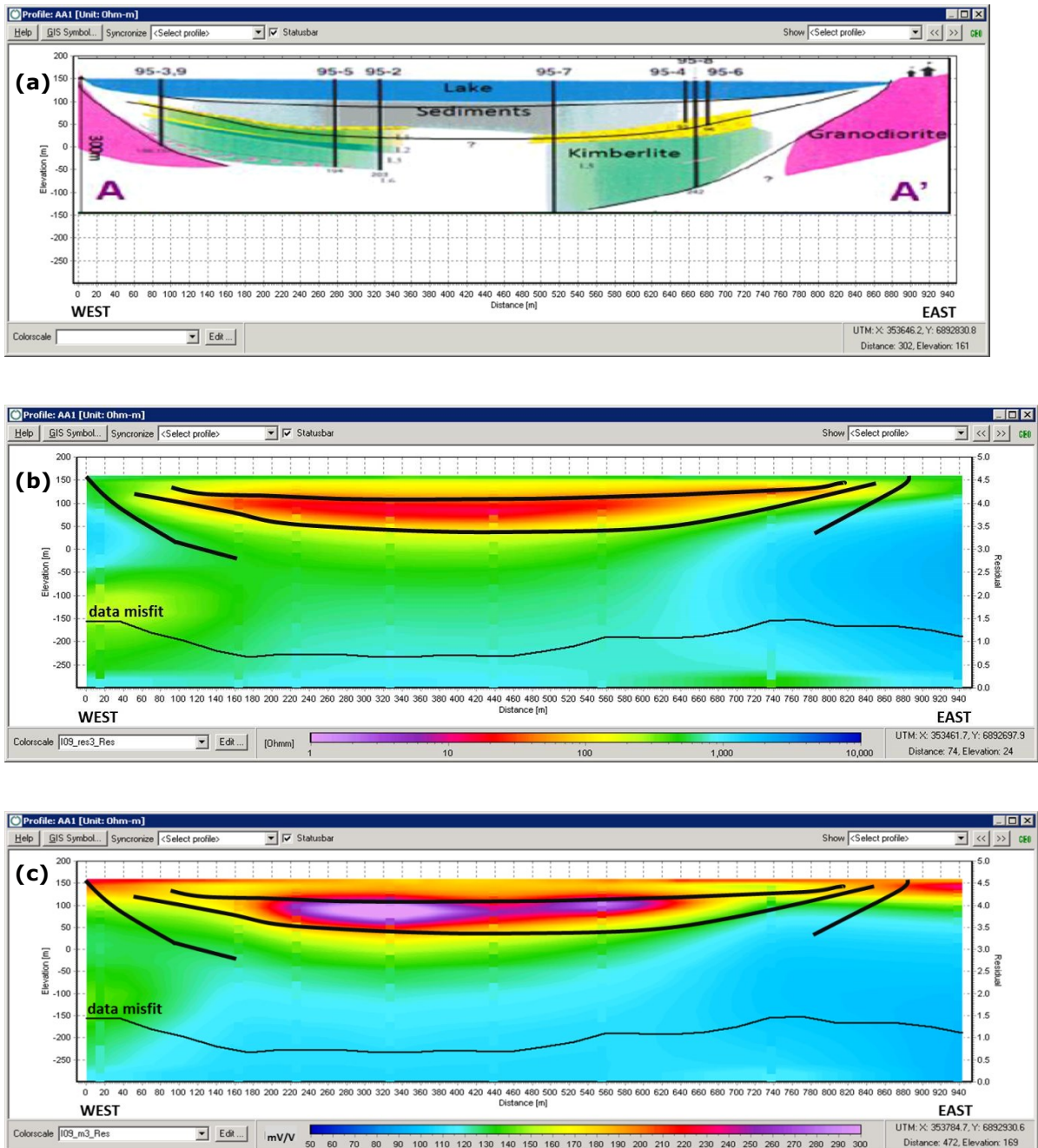


Figure 4.11: Geological cross-section based on drilling (a) compared to the resistivity (b) and chargeability (c) models recovered by SCI inversion using Cole-Cole model.

The resistivity section appears rather consistent with the outline of the different layers as determined by wells information (figure 4.11a). The yellow-red zone reflects the presence of water-saturated fine-grained sediments at the bottom of the bay and lake water, with low values of resistivity ( $< 100 \Omega\text{m}$ ). Below these formations, a lateral contact is marked between the kimberlite (yellow-green zone below the sediments, with resistivity values in the interval between 100 and 500  $\Omega\text{m}$ ) and granodiorite (high values of resistivity,  $> 500 \Omega\text{m}$ ).

Thus, the resistivity section, obtained by modelling airborne IP produces results that fit the measured data and are consistent with the available geological information. A good correlation with the shallowest part of the geological model is found, especially considering that the first gate of the system has a center time of 130  $\mu\text{s}$  after the end of ramp, and therefore the near-surface resolution was expected to be limited.

The chargeability section shows a high chargeable layer in correspondence to the lake sediments that were expected to be very chargeable for the presence of fine-grained products (clay). The effect of these sediments does not allow an easy detection of the crater facies of the kimberlite that, usually, as a result of weathering, can produce an IP effect. Even if a clear separation between the sediments and the crater facies is hard to recognize, it is equally clear that the chargeable structure extends well beyond the thickness of the sediments as identified by the geological information. However, it is still confined in the upper part of the cross-section, coinciding with the crater facies of the kimberlite.

#### **4.8.2 Comparison of three resistivity models cross-sectioned at line 1210 (ZTEM) and line 70 (VTEM)**

The 1D inversion results, obtained modelling the IP effects in VTEM data, were compared with the resistivity models recovered using 3D inversion algorithm on ZTEM and VTEM data. These results of 3D inversion were presented in Kaminski and Oldenburg (2012). The comparison was carried out considering the cross-sections along the line 1210 of ZTEM survey and the line 70 of VTEM survey (figure 4.12).



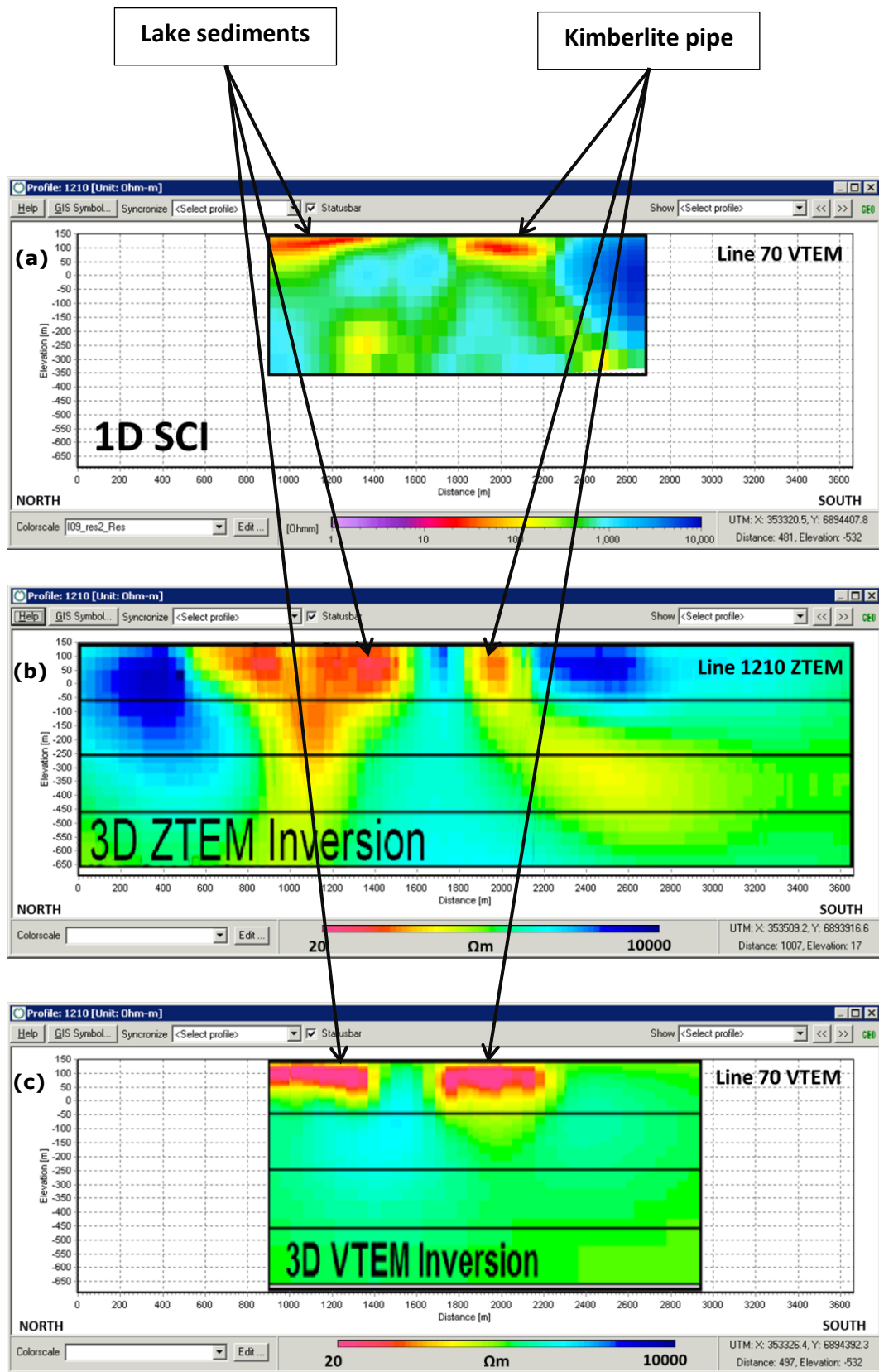


Figure 4.13: Comparison of three conductivity models cross-sectioned at ZTEM line 1210 and at VTEM line 70. (a) 1D SCI VTEM inversion using Cole-Cole model; (b) 3D ZTEM inversion (UBC-GIF); (c) 3D VTEM inversion (UBC-GIF).

For the deeper structures, the 1D SCI section shows more similarities with 3D ZTEM section compared to 3D VTEM section. The capability of recovering deeper structures for ZTEM system is quite obvious (being a natural plane wave source EM system, it ensures a greater penetration depth).

The fact the no deeper response is resolved in 3D VTEM section is partially due to the lower penetration capability of this system along with the strong attenuation of the EM signal in the conductive lake sediments. However, the 3D inversion code, used to invert the VTEM data, without modeling the IP effects, does not consider negative voltage data. These data have been removed before the inversion and this operation has caused a loss of resolution at depth with a reduction of the investigation depth.

Conversely, as shown in the 1D cross-section, where I have modelled the IP effects, retaining the negative voltage data, a significative increase of the recoverability at depth is now achieved. This confirms the importance of modelling the IP effects in the AEM data.

#### **4.9 Vertical Soundings Inversion of magnetic data over Drybones kimberlite**

The VTEM system, used in 2005, is equipped with a caesium magnetometer that allows measuring the total magnetic field at sampling rate of 0.1 s.

This magnetometer was carried out on a separate bird, 20 m below the helicopter. Its position is calculated indirectly from the position of the helicopter, using the nominal distance of the magnetic bird.

The magnetic data were corrected for diurnal variation using the digitally recorded ground base station magnetic values after the acquisition.

In this phase were performed also the IGRF removal and a leveling process between adjacent lines.

In this work I have performed the inversion of vertical soundings along SW-NE profile corresponding to the known geological cross-section AA' (figure 4.2c), located over the kimberlite (figure 4.2b).

Before calculating the vertical magnetic soundings, I applied the reduction to pole (Baranov and Naudy, 1964) to the magnetic data. This transformation is necessary, as stated in Chapter 2, to obtain a correct estimation of the horizontal dimensions of the anomaly source.

The total magnetic field map after the reduction to pole is shown in figure 4.14. The map shows two magnetic anomalies: the first and the strongest one, in the northern part of the survey, crossing the area from E to W is related to the known diabase dike; the second one in the center of the survey, related to the presence of the kimberlite. I have performed the Vertical Soundings inversion for the magnetic data along the AA' profile shown in Figure 4.14.

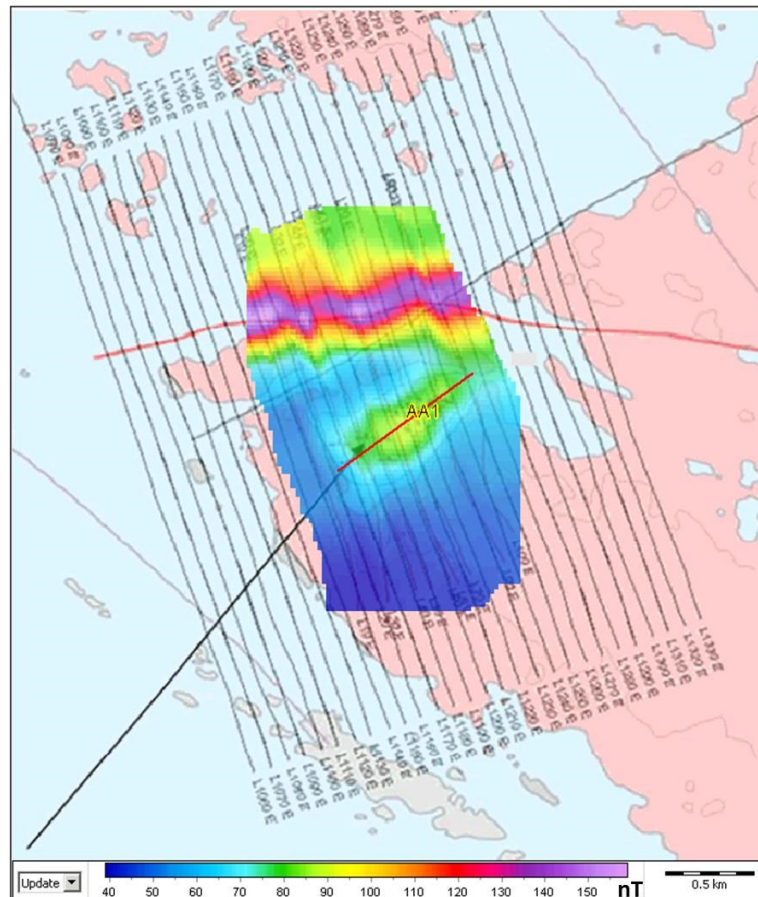


Figure 4.14: Total magnetic field after the reduction to pole over bedrock geology of the area under study. The AA' profile is shown on the map (red line).

The first step of the inversion process is the calculation of the vertical soundings.

In this case, each vertical sounding consists of magnetic data upward continued to 15 different altitudes, from the first level at 170 m above the ground up to the highest level at 240 m above the ground, with a 5 m constant step.

The magnetic anomaly along the profile AA', and at different altitudes, is shown in figure 4.15.

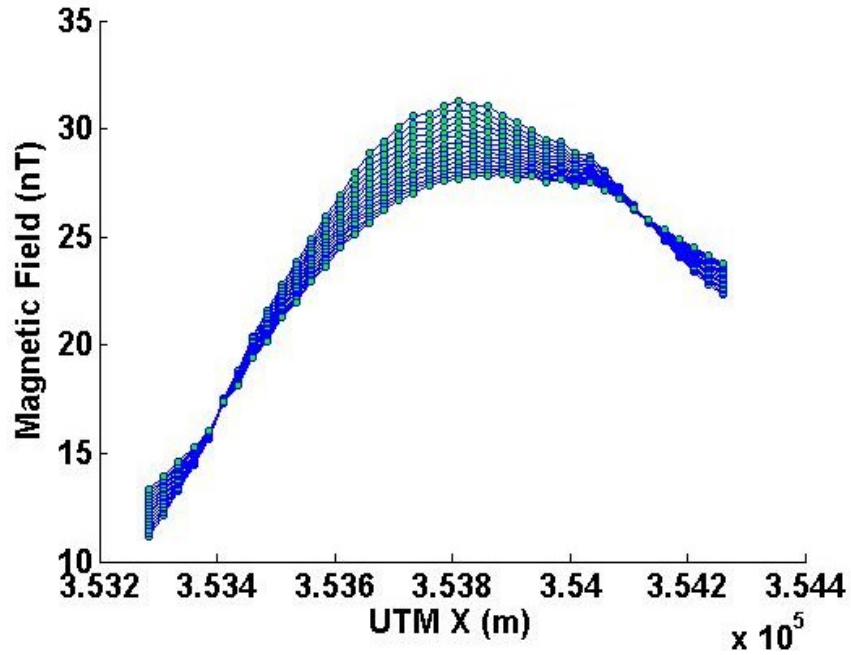


Figure 4.15: Behavior of the magnetic data at different altitudes, along the AA' profile. The green dots represent, for each altitude, the horizontal positions of the measuring stations and then the individual vertical soundings.

In order to calculate the kernel, I need to estimate the horizontal dimensions of the anomaly source. This estimate was performed using the total horizontal derivative method applied to the magnetic field reduced to the pole (figure 4.16).

In this case, I didn't use any vertical derivatives of the magnetic field since they caused only the enhancement of the noise, without improving the resolution.

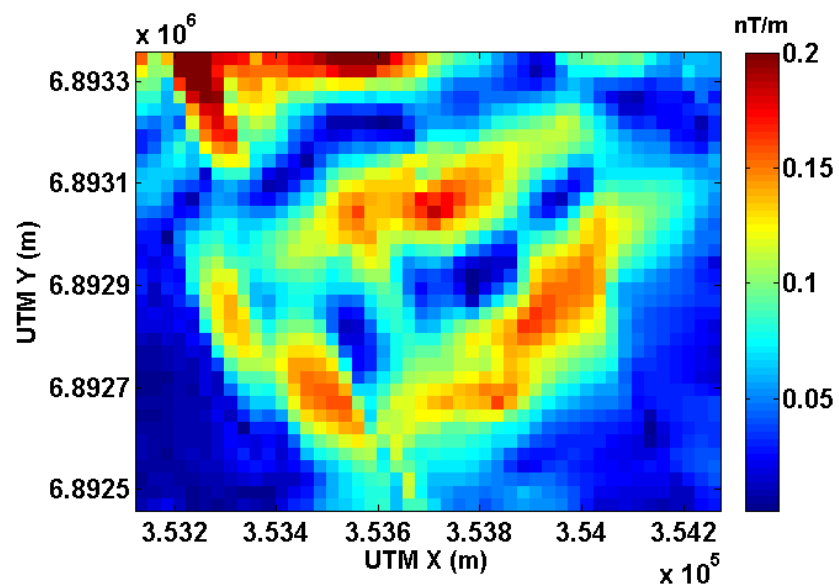


Figure 4.16: Total horizontal derivative of magnetic data above the kimberlite.

The total horizontal derivative method applied on the magnetic data shows complex edges for the magnetic source. The maximum NW and SE estimated dimensions are in agreement with Kretchmar (1995), which described and elongated intrusion of 900 m by 400 m.

Accepting these dimensions, I built an irregular prismatic source that I used in the kernel calculation.

I discretized the vertical dimension of the source volume with 100 layers each one of 10 m thick. In addition, to try to approximate the continuation error, I added to these 100 unknown parameters the coefficients of a first-order polynomial, following the approach described in Section 2.7. For the values of the constraints on the model parameters, i.e. the susceptibility, I did not have any a-priori information, so I set the upper limit to a very large value, equal to  $10^{-2}$ . The experimental error on the measured data has been set to a value of  $5 \times 10^{-1}$  nT.

The Vertical Soundings inversion of the magnetic data along the AA' profile allows recovering a model showing high susceptibility material possibly associated with the kimberlite body (figure 4.17).

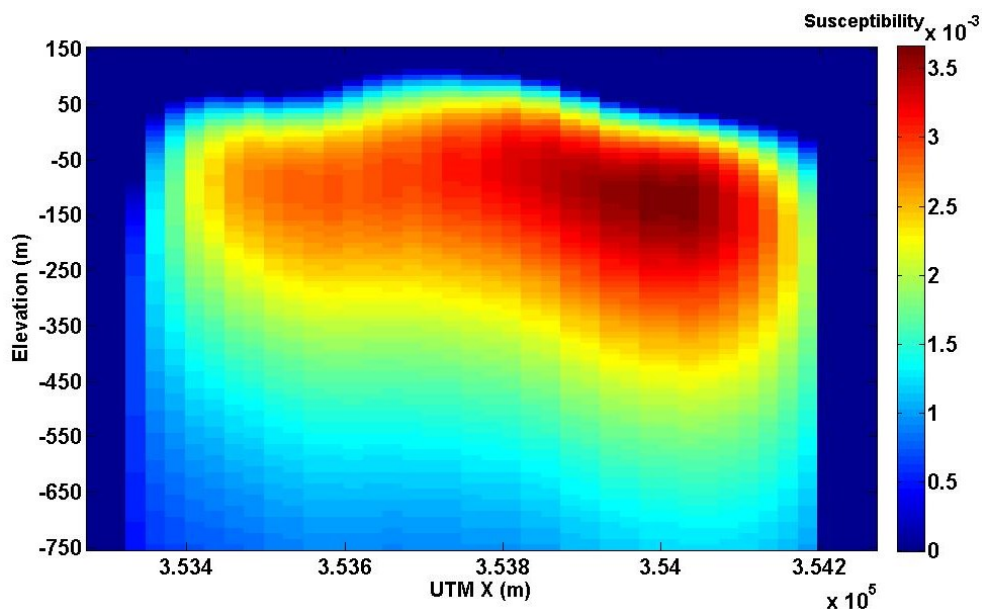


Figure 4.17: Vertical Soundings inversion of the magnetic data along the AA' profile.

In fact, the estimated depths (top of the kimberlite at about 50 m above sea level) are consistent with the geological information derived by the available drill holes, from which the top of the kimberlite was detected at depth of 100-110 m from the surface. The magnetization model (Figure 4.17) shows that

magnetized body is clearly separated from the overlying non-magnetic sediments and lake water.

The most magnetically susceptible material should mark the shallowest portion of the kimberlite that is subject to geochemical alteration (Kaminski and Oldenburg, 2012). In fact, the mineralogical analysis of the Drybones kimberlite samples revealed signs of alteration due to elevated contents of Cr and Nb, as well as due to low totals of TiO<sub>2</sub> in ilmenites (Dunn et al, 2001). This geochemical alteration may have a strong influence on the magnetic properties of the kimberlite, causing an increase of the magnetization (Dunn et al, 2001).

The inverse model along the AA' profile at different depths below the surface and plotted over the known outcropping lithology of the Drybones kimberlite (Kretchmar, 1995) is shown in figure 4.18.

The shallowest parts of the inverse model (up to 200 m) are in good agreement with the outcropping geological facies of the kimberlite obtained from the drill holes information. In fact, the values of the recovered magnetic susceptibility are higher in correspondence of the diatreme facies that usually is more magnetized than the crater facies (Power and Hildes, 2007).

At depth of 300 meters, the most magnetized part migrates to North-East (figure 4.18), outlining a non-vertical shape of the kimberlitic pipe. Unfortunately, this evidence, derived from the inversion of the magnetic data, cannot be confirmed by the drill holes (95-4, 95-6, 95-8), which in the north-eastern part of the kimberlite body reach a maximum depth of only 240 m.

In this case the magnetic method has been an effective technique for kimberlite exploration. The vertical sounding inversion of the magnetic data confirmed the geological information deduced from the drill holes and in addition provided more details about the shape of the kimberlitic body at depth that could be very important for the mineral exploration of the area.

Chapter 4 – Spatially Constrained Inversion of IP parameters from airborne EM data and inversion of Vertical Magnetic Soundings from aeromagnetic data: the case study of Drybones kimberlite, Northwest Territories (CANADA)

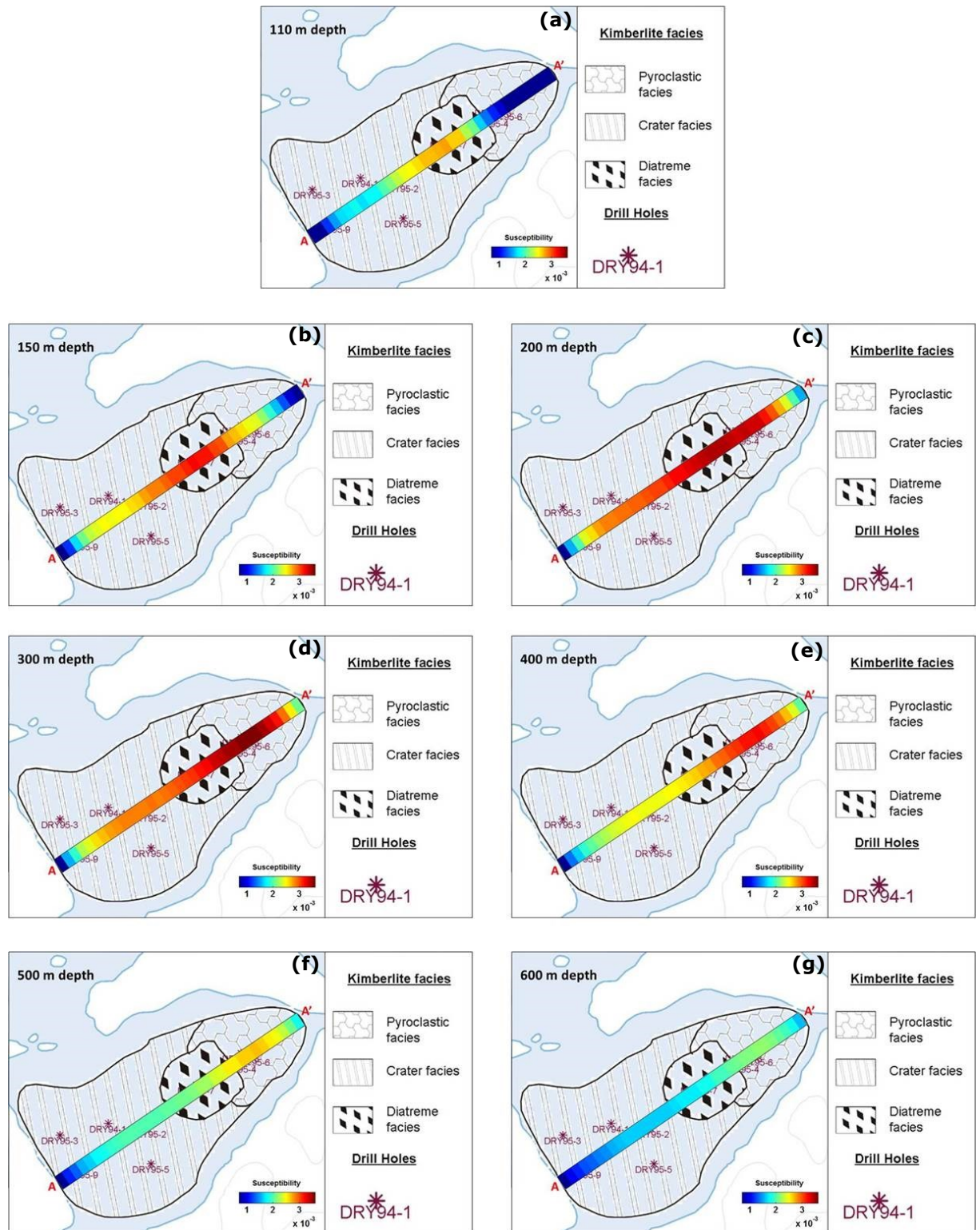


Figure 4.18: Vertical Sounding inversion of magnetic data at: (a) 110 m depth; (b) 150 m depth; (c) 200 m depth; (d) 300 m depth; (e) 400 m depth; (f) 500 m depth; (g) 600 m depth.

From the recovered susceptibilities, I calculated the estimated data along the AA' profile (in this case at the first continuation altitude, i.e. 170 m above the ground), and I compared them with the measured data related to the same profile and at the same altitude (figure 4.19)

The fitting is good, with a RMSD value of just 0.4 nT.

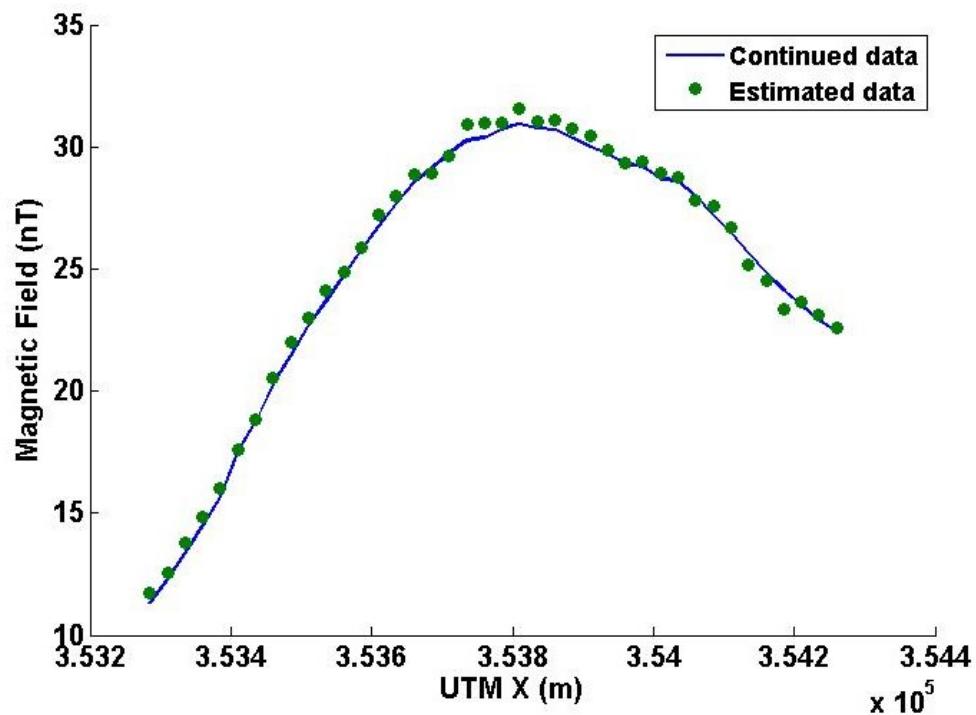


Figure 4.19: Comparison between the continued and the estimated data along the AA' profile at 170 m height above the ground.

#### 4.9.1 Comparison of Vertical Magnetic Soundings inversion and 3D magnetic inversion along the AA' profile

A 3D magnetic inversion of the data acquired over Drybone kimberlite was carried out and presented in Kaminski and Oldenburg (2012), using the inversion strategy proposed by Li and Oldenburg (1996).

The characteristic of this algorithm has been already discussed in Section 3.8.3. Dealing with magnetic data, the exponent of the depth weighting function was set to 3.

The inverse model recovered by the Vertical Soundings inversion applied to the magnetic data along the AA' profile and presented in Section 4.9 was compared to the inverse model along the same profile obtained from 3D inversion (Kaminski and Oldenburg, 2012); figure 4.20).

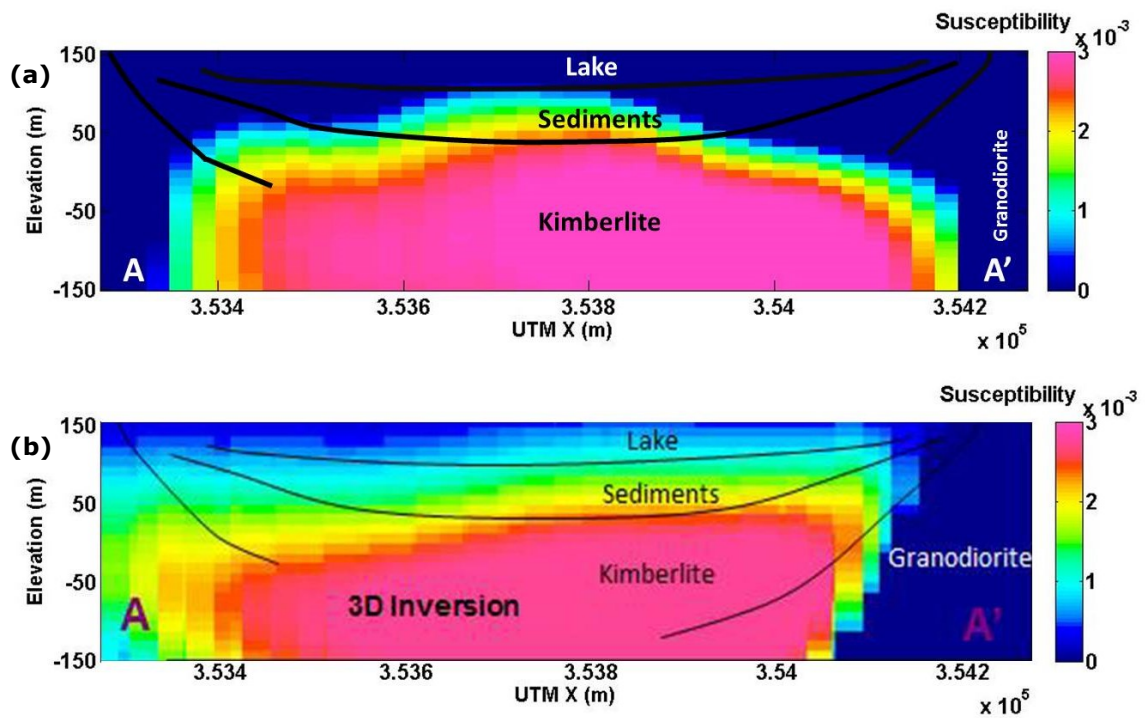


Figure 4.20: Vertical Soundings inversion (a) and Mag3D inversion (b) of the magnetic data along the AA' profile.

The two inverse models are consistent each other for the range of the recovered susceptibility values. The most magnetized part of the models is associated to the kimberlite, with the depth to the top in agreement with the geological information derived from drill holes. This most magnetized region of the model is clearly at depths greater than the non-magnetic sediments and lake water. As already shown in Chapter 2 and in Section 3.8.3, also in this case the Vertical Soundings inversion (figure 4.20a) seems to be more accurate in the definition of the depth to the top of the magnetized structure than the model recovered by 3D inversion (figure 4.20b). In fact, above the kimberlite, the model obtained by inversion of the vertical soundings (figure 4.20a) presents no significant magnetizations, except in the central part of the profile, where some magnetization is assigned to cells pertaining to shallow sediments. The 3D model, on the contrary, presents magnetized cells in all the volume above the kimberlite, up to the surface (figure 4.20b).

## **4.10 Comparison of magnetic inversion and EM inversion along the AA' profile**

I compare now the inverse models recovered by inverting the magnetic data and the EM data, modeling the IP effects. The figure 4.21 shows the susceptibility, resistivity and chargeability vertical sections along the AA' profile.

The susceptibility section (figure 4.21a) shows a high magnetized structure in correspondence of the shallowest part of the kimberlite at depth of 100-110 m. This structure is well distinguished from the non-magnetic overlying horizons. The resistivity section (figure 4.21b) is instead dominated by the presence of the water lake and of water-saturated fine-grained sediments at the bottom of the bay, imaged as highly conductive horizons. These two highly conductive horizons mask the presence of the kimberlite that is characterized by resistivity values lower than the granodioritic basement but higher than the lake water and sediments.

Also the chargeability section (figure 4.21c) shows the most chargeable structure in correspondence to the lake sediments, which were expected to be very chargeable for the presence of fine-grained products (clay). The effects of this layer, highly chargeable, are well differentiated from the lake water that does not show any chargeable properties but at same time it does not allow an easy detection of the crater facies of the kimberlite that usually, as a result of weathering, can produce IP effects (Macnae, 1979).

The presence of a highly conductive/chargeable horizon in the TEM models, very well correlated in depth and thickness to the fine-grained lake sediments, confirms the available scattered well data, extending their information all along the analyzed section. In this sense, the TEM and magnetic models complements each other in the definition of the buried geological structures.

As shown, a joint interpretation of different datasets, acquired over the same area, can help to improve the knowledge of the study area and can lead to a better understanding of the structures at depth.

A joint interpretation represents, usually, the first stage of the integration between different geophysical methodologies where, as shown in this section, the inversion results obtained by using two different algorithms, used separately, have been compared.

The comparison revealed, in this case, the different sensitivity of the magnetic and electromagnetic methods with respect to the investigated geological structures. This allowed a complete characterization of the studied area at Drybones kimberlite but at same time it could imply greater difficulty in setting up a true joint inversion, where the physical properties need to be linked in some way by means petrophysical relationship or, as stated in Section 3.9, by an empirical relationship.

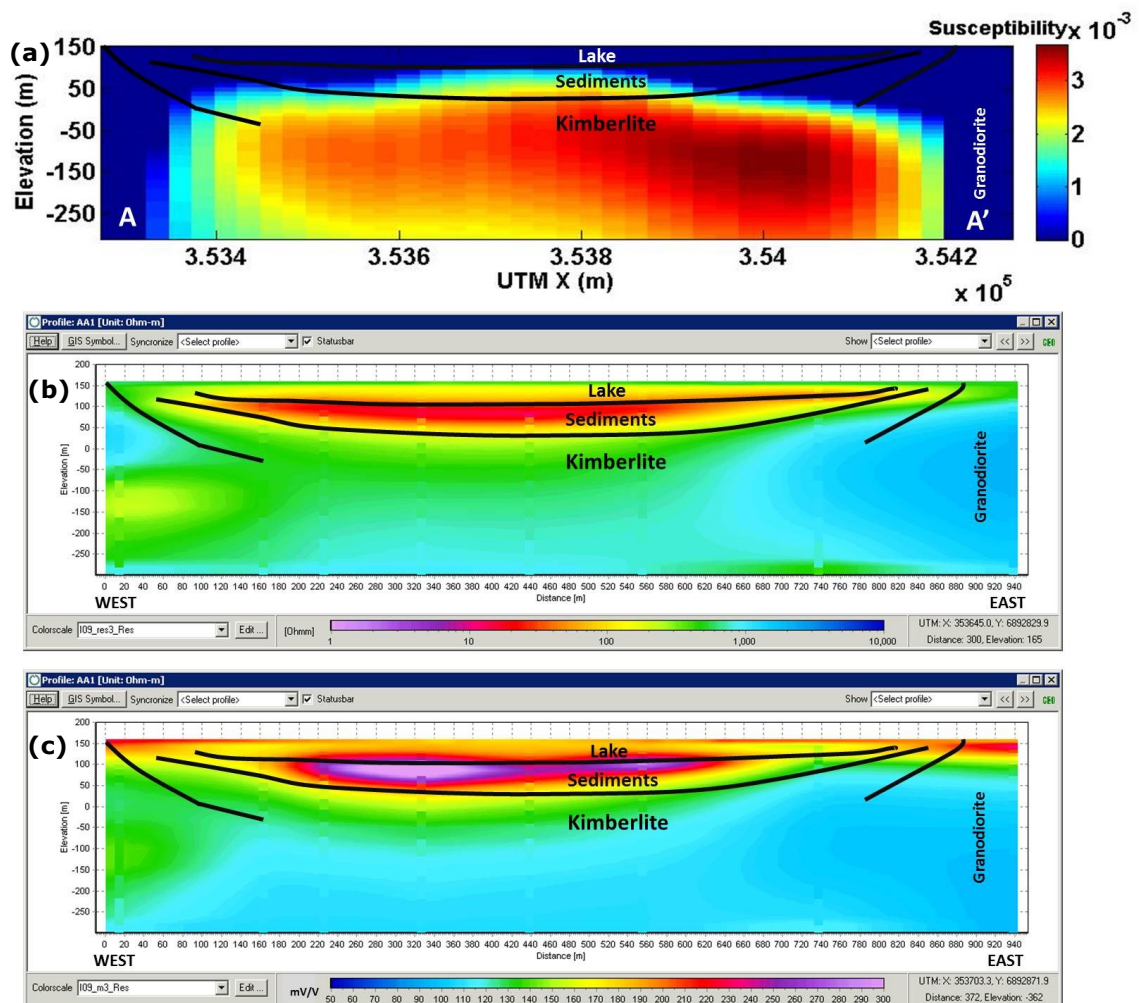


Figure 4.21: Susceptibility section (a) recovered by Vertical Soundings inversion, resistivity (b) and chargeability (c) sections recovered by SCI inversion using Cole-Cole model along the AA' profile.

## CONCLUSIONS

My research dealt with the processing and the modeling of TDEM and aeromagnetic data. These data are often collected simultaneously during the same survey, providing the possibility of studying the buried geological structures by using two different geophysical methods, investigating the distributions in the subsurface of different physical properties.

The use of two different datasets allows carrying out an integrated study that may lead to a remarkable improvement of the interpretation models and a better understanding of the studied geological problems.

In particular, I worked on two different surveys both conducted in Canada over two areas of interest for mining exploration.

The integrated study of the results obtained by inverting the EM and the magnetic data separately showed that not always the two methods have the same sensitivity with respect to the geological structures.

In the case of the Broken Evil prospect (Ontario) both methods are sensitive to the same sources, with a positive correlation between the susceptibility and the conductivity models; also the estimated depths are very similar. The inversion models are also in agreement with the information derived from a drill hole which confirms that the magnetic and the electromagnetic anomaly are caused by graphitic sediments with seams and heavy disseminations of pyrrhotite. Thus, in this case, the use of the two methods help in increasing the confidence in the geophysical models.

In the case of the Drybones kimberlite (Northwest Territories), the EM and the magnetic method revealed instead a different sensitivity to the geological structures. In fact, while the most conductive/chargeable structures are found in correspondence of the water lake and the lake sediments, the most magnetized structure coincides with the depths of top of the kimberlite and is well distinguished from the non-magnetic overlying structures. In this case the integration of the inverse models improved the interpretation model. All the geological structures at Drybones bay are well retrieved by the inversion processes and are in very good agreement with the drill hole information available for this area.

The different behavior in terms of sensitivity of the TEM and magnetic methods, combined with the fact that in literature a simple and general petrophysical relationship between the magnetic susceptibility and the electrical conductivity is not known, poses some limitations in setting up a joint inversion algorithm which keeps its validity in all the studied cases. However, as for the case study over Broken Evil prospect, where the two physical properties have displayed a certain degree of correlation, an empirical relationship between them could be derived from some direct measurements of susceptibility and conductivity. This empirical relationship, at local level, could allow the inversion of the different geophysical data simultaneously.

In the other case, when the physical properties show different sensitivity with respect to the geological structures, as in the case of Drybones kimberlite, a quantitative integration of the models obtained by the single inversions could be performed by a statistical multivariate analysis with the aim of defining a single joint multiparameter model (Lanne, 1986).

For the magnetic data I worked on an inversion algorithm that allows the inversion of vertical soundings of magnetic data. The vertical soundings consisted of magnetic data at different altitudes while the forward problem consisted in assuming a volume of layers of different magnetizations. The volume is finite vertically and horizontally. The vertical dimension is such as to completely contain the anomaly source while the horizontal dimensions are those of the anomaly source itself. This last condition is necessary to avoid the "Bouguer-slab effect". The inversion of the vertical soundings was performed by adding some set of inequality constraints on the model parameters, reflecting the a-priori knowledge on the studied area, and on the experimental data error. These constraints help to regularize the inversion process and allow avoiding unrealistic model estimates.

Numerous tests performed on synthetic cases both for perfect measured data and for more realistic upward continued data at different altitudes showed that good results can be retrieved if a correct estimation of the horizontal dimensions of the anomaly source is provided for the kernel calculation. Accurate estimations of the depth to the top and to the bottom as well as correct magnetization contrast are obtained using perfect measured data. For the continued data, I needed to slightly modify the equations system in the

inversion process, by adding to the equations a first-order polynomial. The estimation of the coefficients of this polynomial compensates the errors in the model caused by the upward continuation process.

The use of this polynomial results in a less accurate estimate of the depth to the bottom while the top and the magnetization contrast of the anomaly source are still correctly estimated.

For all the synthetic cases I considered a positive magnetic contrast between the anomaly source and the host rocks. This implied that the constraints on model parameters should vary between zero, representing the minimum magnetization contrast, and the maximum magnetization contrast. I observed that even using an upper bound much larger than the real magnetization, the estimated magnetizations are very close to the true values. This demonstrates that it is not crucial to know in advance an accurate maximum magnetization contrast.

For the estimation of the horizontal dimensions, I used the total horizontal derivative method. However, depending on the real dimensions and the depth of the anomaly source, the horizontal derivative method may lead to an overestimation of the horizontal dimensions. In these cases it may be advantageous to try to increase the resolution by applying this method on the vertically derived (Fedi and Florio, 2002) or downward continued data. In real cases, these procedures must be used carefully as enhancing the signal at high frequencies may prevent the desired increase of resolution. For the estimation of the horizontal dimensions in both the real cases studied I used the first order vertical derivative.

For TDEM data, the inversion process was conducted by using the Spatially Constrained Inversion algorithm that is a 1D inversion method where the parameters of the earth model for each sounding are connected spatially by means of lateral constraints, defining a specified variance of the model parameters.

For the EM data over Broken Evil prospect, where two different EM surveys were conducted with two different airborne systems, the data inversion was carried out with a joint approach. This approach provided a unique resistivity model fitting both data sets to an acceptable misfit, while the closer line spacing granted a greater spatial resolution with respect to the models

obtainable from a single EM dataset. The advantage of obtaining one single model fitting all data at once is obvious, in terms of overall robustness of the geophysical results and of any subsequent modeling. In order to increase the spatial coherence in the model space I applied a calibration factor to the voltage data of one of the data sets.

The most interesting conductivity anomalies (values greater than 500 mS/m) visible in the inverse model are associated to geological facies that can host massive sulfide mineralizations. In particular, two areas have been identified that are subject to current mineral exploration and are classified as priority drill targets. As the exploration targets, characterized by pronounced 3D features, have been modeled using 1D inversion algorithm, the obtained inverse model is influenced by artifacts which do not prevent, however, meaningful geological interpretations.

For the EM data over Drybones kimberlite, the clear presence of IP effects in the measured data, that result mainly in negative values of the voltage data, led to use a 1D algorithm able to model these effects by using the Cole-Cole model. Even in this case, the estimation of the Cole-Cole parameters was performed following the spatially constrained approach by using a set of lateral constraints that tie together the parameters of the neighboring soundings. The obtained inversion results, both for resistivity and chargeability parameters, are in good agreement with available the drill hole information.

In addition, the comparison between the inversion results and previous inverse models, recovered without taking into account the IP effects in TDEM data, confirmed the importance of modelling the IP effects. In fact, retaining the negative voltage data produced a significative increase of the recoverability of the geological structures at depth.

With regard to TDEM method, I presented a new approach for defining a gating scheme for the sampling of the AEM data obtained from modern airborne EM systems.

The method is based on sampling the EM transient decay in a more detailed way in correspondence of the maxima of the curvature of the data, marking the transition from a resistive layer to a conductive one. The adaptive-gating scheme consists in reducing the width of the gate in correspondence of the

maxima of the curvature and increasing the width of the adjacent gates at its sides in a progressive way.

However, the computation of the second derivative of the EM transient enhances excessively the noise contained in the signal, so this method necessarily involves a preliminary low-pass filter.

I chose to use a technique based on Discrete Wavelet Transform that allows performing a localized denoising. The study of synthetic data allowed me to verify that the DWT is a suitable filtering technique for this type of signal. This leads to consider the possibility of using DWT during processing of AEM data.

The improvements, in both the accuracy and precision of the inverse model estimated parameter obtained with the adaptive-gating scheme, confirm the validity of the idea of adapting the sampling of the EM transient to the specific characteristics of the data.

Instead of defining a priori the type of gating (such as log-gating) and the characteristics of the gating of the different channels (center times, width), I have shown that it may be advantageous to define a priori only the maximum number of channels to use, and place them adaptively across the transient.

Although this study was conducted on synthetic data, the results have been very encouraging and have demonstrated that an adaptive sampling of the EM transient can produce more correct inverse resistivity models, and subsequent interpretations.

In this work I didn't investigate a way to automate this procedure. However, I think that some ideas to automate the denoising of the second derivative and the selection of its maxima could be implemented.

1. To denoise the data with DWT, I could choose to filter a fixed number of scales for all the survey. The scales to be filtered could be checked by a preliminary analysis of a selection of soundings from different areas of the survey.
2. As about the identification of the maxima, I think that some criteria involving an amplitude threshold of the maxima and excluding the late times, when the S/N ratio is evidently low, may be applied with success or even a combined study of the first and the second derivative of the EM transient.

## *Conclusions*

I demonstrated the validity of this technique when applied to 1D cases and I plan to investigate under which conditions this approach can be applied successfully in more complex synthetic 2D or 3D and real cases.

## REFERENCES

- Aarhus Geophysics, 2009, Aarhus Workbench. Available online at <http://www.aarhusgeo.com/products/workbench.html> (accessed 9 May, 2009).
- Allard, M., 2007, On the origin of the HTEM species, In Proceedings of Exploration 07: Fifth Decennial International Conference on Mineral Exploration, Toronto, Canada.
- Annan, A.P., 1983, Effect of differential transmitter/receiver motion on airborne transient EM interpretation, 53rd Annu. Int. Mgt. Soc. Expl. Geophys. Expanded Abstracts, SEG, Soc. Expl. Geophys., 622-623.
- Árnason, K., 1995, A consistent discretization of the electromagnetic field in conducting media and application to the TEM Problem, In Proceeding at International Symposium on Three- Dimensional Electromagnetics, 167–180.
- Aster, R.C., Thurber, C.H., Borchers, B., 2005, Parameter estimation and inverse problems, Elsevier Academic Press, 301.
- Auken, E., 1995, 1D time domain electromagnetic interpretations over 2D and 3D structures, In Proceedings of the Symposium on the Application of Geophysics to Engineering and Environmental Problems, Orlando, USA, 329–338.
- Auken, E., Jørgensen F., Sørensen K.I., 2003, Large-scale TEM investigation for groundwater, Expl. Geoph., 33, 188–194.
- Auken, E. and Christiansen, A.V., 2004, Layered and laterally constrained 2D inversion of resistivity data, Geoph., 69, 752-761.
- Auken, E., Christiansen, A.V., Jacobsen, B.H., Foged, N., Sørensen, K.I., 2005a, Piecewise 1D laterally constrained inversion of resistivity data, Geoph. Prosp., 53, 497–506.
- Auken, E., Christiansen, A.V., Westergaard, J.H., Kirkegaard, C., Foged, N., Viezzoli, A., 2009, An integrated processing scheme for high-resolution airborne electromagnetic surveys, the SkyTEM system, Explor. Geophys., 2009, 40, 184–192.

- Auken, E., Viezzoli, A., Christiansen, A.V., 2009, A single software for processing, inverting, and presentation of AEM data of different system: The Aarhus Workbench. Australian Society of Exploration Geophysics Geophysicist (ASEG) 2009, Sydney, Australia, Expanded Abstract, 1-5.
- Auken, E., Christiansen A.V., Kirkegaard C., Fiandaca G., Schamper C., Behroozmand A.A., Binley A., Nielsen E., Effersø F., Christensen N.B., Sørensen K.I., Foged N., Vignoli G., 2014, An overview of a highly versatile forward and stable inverse algorithm for airborne, ground-based and borehole electromagnetic and electric data, *Exploration Geophysics*, 1–13.
- Aurenhammer, F., 1991, Voronoi diagrams - A survey of a fundamental geometric data structure, *ACM Comp. Surv.*, 23, 345–405.
- Balch, S., Boyko, W., Paterson, N., 2003, The AeroTEM airborne electromagnetic system, *The Leading Edge*, 22, 562-566.
- Banerjee, B., and Pal, B.P., 1986, A simple method for determination of depth of investigation characteristics in resistivity prospecting, *Exploration Geophysics (USSR)*, 17, no. 2, 93–95.
- Baranov, V. and Naudy, H., 1964, Numerical calculation of the formula of reduction to the magnetic pole, *Geophysics*, 29, 67-79.
- Baranov, W., 1976, *Potential Fields and Their Transformations in Applied Geophysics*, Gebruder-Borntraeger, Berlin.
- Barber, B., Dobkin, D., Huhdanpaa, H., 1996, The Quickhull algorithm for convex hulls, *ACM Trans. on Math. Software*, 22, 469–483.
- Barbosa, V.C.F. and Silva, J.B.C., 1994, Generalized compact gravity inversion, *Geophysics*, 59, 57–68.
- Barbosa, V.C.F. and Silva, J.B.C., 2006, Interactive 2D magnetic inversion: a tool for aiding forward modeling and testing geological hypotheses, *Geophysics*, 71 (5), 43–50.
- Barnes, G. and Barraud, J., 2012, Imaging geologic surfaces by inverting gravity gradient data with depth horizons, *Geophysics*, 77, G1–G11.
- Barringer, A.R., 1962, A new approach to exploration – the INPUT airborne-electrical pulse prospecting system, *Min. Con. Jour.*, 48, 49-52.

- Best, M.E., Duncan, P., Jacobs, F.J., Scheen, W.L., 1995, Numerical modeling of the electromagnetic response of three-dimensional conductors in a layered earth, *Geoph.*, 50, 665–676.
- Bishop, J.R. and Emerson, D.W., 1999, Geophysical properties of zinc-bearing minerals, *Australian Journal of Earth Sciences*, v. 46, p. 311–328.
- Blakely, R.J. and Simpson, R.W., 1986, Approximating edges of source bodies from magnetic or gravity anomalies, *Geophysics*, 51, 1494-1498.
- Blakely, R.J., 1996, *Potential theory in gravity and magnetic applications*, Cambridge University Press, Cambridge.
- Bleeker, W. and Parrish, R.R., 1996, Stratigraphy and U-Pb geochronology of Kidd Creek: Implications for the formation of giant massive sulfide deposits and the tectonic history of the Abitibi greenstone belt, *Canadian Journal of Earth Sciences*, v. 33, p. 1213-1231.
- Bodger, T., Grand, T., Hearst, R., 2005, THEM-A helicopter-borne time domain electromagnetic system, KEGS Airborne Symposium, Toronto.
- Boivin, M., 2007, Advances in geophysical technology for VMS exploration, in B. Milkereit, ed., *Proceedings of Exploration 07: Fifth Decennial International Conference on Mineral Exploration*, Decennial Mineral Exploration Conferences, 731–739.
- Boyd, G., 2001, Normandy heli-borne time domain EM system, ASEG 15th Geophysical Conference and Exhibition, Brisbane.
- Boyd, G.W., 2004, HoisTEM – a new airborne electromagnetic system, PACRIM Proceedings, Adelaide.
- Boyko, W., Paterson, N., Kwan, K., 2001, AeroTEM: System characteristics and field results, *The Leading Edge*, 20, 1130-1138.
- Breaks, F.W., 1991, English River subprovince, in Thurston, P.C., Williams, H.R., Sutcliffe, R.H., and Stott, G.M., eds., *Geology of Ontario: Ontario Geological Survey, Special Volume 4, Part 1*, p. 239-277.
- Brodie, R. S. and Sambridge, M., 2006, A holistic approach to inversion of frequency domain airborne EM data, *Geoph.*, 71, 301–312.
- Brodie, R., 2010, *Holistic Inversion of Airborne Electromagnetic Data*, PhD thesis, The Australian National University, Canberra, Australia.

- Bowring, S. A. and Housch, T., 1995, The Earth's early evolution, *Science*, v. 269, pp. 1535–1540.
- Buchan, K.L. and Ernst, R.E., 2004, Diabase dyke swarms and related units in Canada and adjacent regions, Geological Survey of Canada, Map 2022A, scale 1:5,000,000.
- Card, K.D. and Ciesielski, A., 1986, Subdivisions of the Superior Province of the Canadian Shield: *Geoscience Canada*, v. 13, p. 5-13.
- Castaldo, R., Fedi M., Florio G., 2014, Multiscale estimation of excess mass from gravity data, *Geophys. J. Int.*, 197, 1387–1398.
- Cella, F. and Fedi, M., 2012, Inversion of potential field data using the structural index as weighting function rate decay: *Geophysical Prospecting*, 60, 313–336.
- Chown, E.H., Daigneault, R., Mueller, W., Mortensen, J.K., 1992, Tectonic evolution of the northern volcanic zone, Abitibi belt, Quebec, *Canadian Journal of Earth Sciences*, v. 29, p. 2211-2225.
- Christiansen, A.V., Auken, E., Sørensen, K., 2009, The transient electromagnetic method, In *Groundwater geophysics*, Springer Berlin Heidelberg, 179-226.
- Christensen, N.B. and Tølbøll, R.J., 2009, A lateral model parameter correlation procedure for one-dimensional inverse modeling, *Geoph. Prosp.*, 57, 919-929.
- Christiansen, A.V., Auken, E., Viezzoli, A., 2011, Quantification of modeling errors in airborne TEM caused by inaccurate system description, *Geoph.*, 76, 43-52.
- Christiansen, A.V. and Auken, E., 2012, A global measure for depth of investigation, *Geoph.*, 77, 171-177.
- Cole, K.S. and Cole, R.H., 1942, Dispersion and absorption in dielectrics, *Journal of Chemical Physics*, 9-4, 341–351.
- Constable, S.C., Parker, R.L., Constable, C.G., 1987, Occam's inversion: a practical algorithm for generating smooth models from electromagnetic sounding data, *Geophysics*, 52, 289-300.

- Cordell, L. and Grauch, V.J.S., 1985, Mapping basement magnetization zones from aeromagnetic data in the San Juan basin, New Mexico. In: *The Utility of Regional Gravity and Magnetic Anomaly Maps* (ed. W.J. Hinze), pp. 181-197, Society of Exploration Geophysicists.
- Cox, L.H., Wilson, G.A., Zhdanov, M.S., 2010, 3D inversion of airborne electromagnetic data using a moving footprint, *Exploration Geophysics*, 41, 250–259.
- Daigneault, R., Mueller, W.U., Chown, E.H., 2002, Oblique Archean subduction: accretion and exhumation of an oceanic arc during dextral transpression, Southern Volcanic Zone, Abitibi Subprovince Canada, *Precambrian Research*, v. 115, p. 261-290.
- Danielsen, J.E., Auken, E., Jørgensen, F., Søndergaard, V.H., Sørensen, K.I., 2003, The application of the transient electromagnetic method in hydrogeophysical surveys, *J. of Appl. Geoph.*, 53, 181–198.
- Davis, D.W., 2002, U-Pb geochronology of Archean metasedimentary rocks in the Pontiac and Abitibi subprovinces, Quebec, constraints on timing, provenance and regional tectonics, *Precambrian Research*, v. 115, p. 97-117.
- Dell'Aversana, P., 2014, *Integrated Geophysical Models*, EAGE Publications bv, HOUTEN The Netherlands.
- Dimroth, E., Rocheleau, M., Mueller, W., 1984, Paleogeography, isostasy, and crustal evolution of the Archean Abitibi Belt: Comparison between the Rouyn-Noranda and Chibougamau-Chapais areas, in Guha, J., and Chown, E.H., eds., *Chibougamau-Stratigraphy and Mineralization: Canadian Institute of Mining and Metallurgy, Special Volume 34*, p. 73-91.
- Di Massa, D., Florio, G., Viezzoli, A., 2016, Adaptive sampling of AEM transients, *Journal of Applied Geophysics*, 125, 45-55.
- Di Massa, D., Kaminski, V., Viezzoli, A., Prikhodko, A., 2015, Joint inversions of two VTEM surveys using quasi 3D TDEM and 3D magnetic inversion algorithms, *SAGA Expanded abstracts*, Drakensberg, South Africa.
- Dolan, W.M., 1970, Geophysical detection of deeply buried sulfide body in weathered region. In *Mining and Groundwater Geophysics*, Econ. Geol. Report 26, L.W. Morley, ed. Geol. Surv. Canada, pp. 336-44.

- Dubé, B., Gosselin, P., Mercier-Langevin, P., Hannington, M., Galley, A., 2007, Gold-rich volcanogenic massive sulphide deposits, in Goodfellow, W.D., ed., Mineral deposits of Canada—A synthesis of major deposit-types, district metallogeny, the evolution of geological provinces, and exploration methods: Geological Association of Canada, Mineral Deposits Division, Special Publication 5, p. 75–94.
- Dunn, C.E., Smith, D., Kerr, D.E., 2001, Biogeochemical survey of the Drybones Bay area, NWT using outer bark of black spruce. Geological Survey of Canada, Open File 3919.
- Eaton, P., Anderson, B., Nilsson, B., Lauritsen, E., Queen, S., Barnett, C., 2002, NEWTEM — A novelttime-domain helicopter electromagnetic system for resistivity mapping: 72th Ann. Internat. Mtg.: Soc. of Expl. Geophys., Expanded Abstract,, 1-4.
- Eaton, P., Anderson, B., Lubbe, B., 2004, NEWTEM — Adventures in thin air, 74th Ann. Internat. Mtg.: Soc. of Expl. Geophys., Expanded Abstract, 1213-1216.
- Effersø, F., Auken, E., Sørensen, K.I., 1999, Inversion of band-limited TEM responses, *Geoph. Prosp.*, 47, 551–564.
- Fedi, M., 2007, DEXP: A fast method to determine the depth and the structural index of potential fields sources: *Geophysics*, 72, I1–I11.
- Fedi, M. and Rapolla, A., 1995, Vertical Gravity an Magnetic Soundings: forward problem formulation and data inversion, *Bollettino di Geofisica Teorica ed Applicata*, Vol. XXXVII, N.147.
- Fedi, M. and Quarta, T., 1998, Wavelet analysis for the regional-residual and local separation of potential field anomalies, *Geophysical Prospecting*, 46, 507 – 525.
- Fedi, M. and Florio, G., 2001, Detection of potential fields source boundaries by enhanced horizontal derivative method, *Geophysical Prospecting*, 49, 40–58.
- Fedi, M., Florio, G., Cascone, L., 2012, Multiscale analysis of potential fields by a ridge consistency criterion: the reconstruction of the Bishop basement, *Geophys. J. Int.*, 188, 103–114.

- Fiacco, A.V. and McCormick, G.P., 1968, *Nonlinear Programming: Sequential Unconstrained Minimization Techniques*, John Wiley & Sons, New York.
- Fiandaca, G., Auken, E., Christiansen, A.V. Gazoty, A., 2012, Time-domain induced polarization: Full-decay forward modelling and 1D laterally constrained inversion of Cole-Cole parameters, *Geophysics*, 77, E213-E225.
- Fisher, N.J. and Howard, L.E., 1980, Gravity interpretation with the aid of quadratic programming, *Geophysics*, 45, 403-419.
- Fitterman, D.V. and Stewart, M.T., 1986, Transient electromagnetic sounding for groundwater, *Geoph.*, 51, 995-1005.
- Fitterman, D.V., 1987, Examples of transient sounding for groundwater exploration in sedimentary aquifers, *Ground Water*, 25, 684-693.
- Fitterman, D.V., Anderson, W.L., 1987, Effect of transmitter turn-off time on transient soundings. *Geoexpl.*, 24, 131-146.
- Flis, M.F., Newman, G.A., Hohmann, G.W., 1989, Induced-polarization effects in time-domain electromagnetic measurements, *Geophysics*, 54, 514-523.
- Florio, G., Fedi M., Rapolla A., 2009, Interpretation of regional aeromagnetic data by the scaling function method: the case of Southern Apennines (Italy): *Geophysical Prospecting*, 57, 4, 479-489.
- Foged, N., Auken, E., Christiansen, A.V., Sørensen, K.I., 2013, Test site calibration and validation of airborne and ground based TEM-systems, *Geophysics*, 78, 95-106.
- Ford, K., Keating, P., Thomas, M.D., 2007, Overview of geophysical signatures associated with Canadian ore deposits, in Goodfellow, W.D., ed., *Mineral deposits of Canada – A synthesis of major deposit-types, district metallogeny, the evolution of geological provinces, and exploration methods: Geological Association of Canada, Mineral Deposits Division, Special Publication 5*, p. 939-970.
- Fountain, D.K., 1998, Airborne Electromagnetic systems – 50 years of development, *Expl. Geoph.*, 29, 1-11.
- Fountain, D.K. and Smith, R.S., 2003, 55 years of AEM, 50 years of KEGS. KEGS 50th Anniversary Symposium, Toronto, Canada.

- Fountain, D., Smith, R., Payne, T., Lemieux, J., 2005, A helicopter time-domain EM system applied to mineral exploration: system and data. *First Break*, 23, 73-80.
- Galkine, V., 2012, Technical report on the 2010-2011 field program in the Cochrane area, Ontario.
- Galley, A.G., Hannington, M., and Jonasson, I., 2007, Volcanogenic massive sulphide deposits, in Goodfellow, W.D., ed., *Mineral deposits of Canada – A synthesis of major deposit-types, district metallogeny, the evolution of geological provinces, and exploration methods*: Geological Association of Canada, Mineral Deposits Division, Special Publication 5, p. 141–161.
- Goldman, M.M. and Stoyer, C.H., 1983, Finite-difference calculations of the transient field of an axially symmetric earth for vertical magnetic dipole excitation. *Geophysics*, 48, 953-963.
- Goldman, M., Tabarovsky, L., Rabinovich, M., 1994, On the influence of 3-D structures in the interpretation of transient electromagnetic sounding data. *Geophysics*, 59, 889-901.
- Grant, F. and West, G., 1965, *Interpretation Theory in Applied Geophysics*, Mc Graw-Hill.
- Green, W.R., 1975, Inversion of gravity profiles by use of a Backus-Gilbert approach, *Geophysics*, 40, 763-772.
- Guillemoteau, J., Sailhac, P., Behaegel, M., 2012, Fast approximate 2D inversion of airborne TEM data: Born approximation and empirical approach, *Geophs.*, 77, 89-97.
- Guillen, A. and Menichetti, V., 1984, Gravity and magnetic inversion with minimization of a specific functional, *Geophysics*, 49, 1354–1360.
- Hannington, M.D., Barrie, C.T., Bleeker, W., 1999a, The giant Kidd Creek volcanogenic massive sulfide deposit, western Abitibi Subprovince, Canada, in Hannington, M.D., and Barrie, C.T., eds., *The Giant Kidd Creek Volcanogenic Massive Sulfide Deposit, Western Abitibi Subprovince, Canada: Economic Geology Monograph*, 10, p. 1-30.
- Haggerty, S.E., 1986, Diamond genesis in a multiply-constrained model, *Nature*, Volume 320, Page 34-38.

- Hördt, A. and Scholl, C., 2004, The effect of local distortions on time-domain electromagnetic measurements, *Geophys.*, 68, 87–96.
- Huang, H. and Fraser, D.C., 2003, Inversion of helicopter electromagnetic data to a magnetic conductive layered earth, *Geoph.*, 68, 1211–1223.
- Huang, H., 2005, Depth of investigation for small broadband electromagnetic Sensors, *Geophysics*, 70, no. 6, G135–G142.
- Jackson, D.D., 1972, Interpretation of inaccurate, insufficient, and inconsistent data, *Geophysical Journal of the Royal Astronomical Society*, 28, 97-109.
- Jackson, D.D., 1979, The use of a priori information to resolve non-uniqueness in linear inversion. *Geophysical Journal of the Royal Astronomical Society*, 57, 137-157.
- Janse, A.J.A., 1993, The aims and economic parameters of diamond exploration, *Diamonds: Exploration, Sampling and Evaluation*, Prospectors and Developers Association of Canada, pp. 173-184.
- Kaminski, V., Legault, J.M, Kumar, H., 2010, The Drybones kimberlite: a case study of VTEM and ZTEM airborne EM results, 21ST ASEG International Geophysical Conference and Exhibition, Extended Abstract. Sydney, Australia, 22-25 August 2010, 4 pp.
- Kaminski, V., Prikhodko, A., Oldenburg, D., 2011, Using ERA low frequency E-field profiling and UBC 3D frequency-domain inversion to delineate and discover a mineralized zone in Porcupine district, Ontario, Canada., SEG Annual Meeting Expanded abstracts, San Antonio, US.
- Kaminski, V. and Oldenburg, D., 2012, The geophysical study of drybones kimberlite using 3D time domain EM inversion and 3D ZTEM inversion algorithms. *Aust Soc Explor Geophys Ext Abstr*.
- Kearey, P., Brooks, M., Hill, I., 2002, *An Introduction to Geophysical Exploration*, Blackwell Publishing, Oxford.
- Kirkegaard, C. and Auken, E., 2015, A parallel, scalable and memory efficient inversion code for very large-scale airborne EM surveys, *Geophysical Prospecting*, 63, 495 – 507.
- Kjarsgaard, B.A., 1996, Kimberlites. In *Searching for Diamonds in Canada*. Edited by A.N. LeCheminant, D.G. Richardson, R.N.W. DiLabio, K.A. Richardson. Geological Survey of Canada, Open File 3228, p. 29-37.

- Kratzer, T. and Macnae, J., 2012, Induced polarization in airborne EM, *Geophysics*, 77(5), E317–E327.
- Kretschmar, U., 1995, Drill Report on the Drybones Bay Kimberlite Property, Drybones Bay, Great Slave Lake, District of MacKenzie, Northwest Territories, Canada.
- Lanne, E., 1986, Statistical multivariate analysis of airborne geophysical data on the SE border of the Central Lapland Greenstone complex, *Geophysical Prospecting*, 34, 1111-1128.
- Last, B.J. and Kubik, K., 1983, Compact gravity inversion, *Geophysics*, 48, 713–721.
- Legault, J.M., Prikhodko, A., Dodds, D.J., Macnae, J.C., Oldenborger, G.A., 2012, Results of recent VTEM helicopter system development testing over the Spiritwood Valley aquifer, Manitoba, in *Expanded Abstracts: 25th SAGEEP Symposium on the Application of Geophysics to Engineering and Environmental Problems*, Tucson, Arizona (USA).
- Legault, M., Gauthier, M., Jebrak, M., Davis, D.W., and Baillargeon, F., 2002, Evolution of the subaqueous to near-emergent Joutel volcanic complex, Northern Volcanic Zone, Abitibi Subprovince, Quebec, Canada, *Precambrian Research*, v. 115, p. 187-221.
- Lee, T.J., 1981, Transient electromagnetic response of a polarizable ground, *Geophysics*, 46, 1037-1041.
- Lewis, J.G. and Lee, T.J., 1984, The detection of induced polarization with a transient electromagnetic system, *Inst. Elect. Electron. Eng., Trans. Geosci. Remote Sensing*, GE-22, 69-80.
- Le Cheminant, A.N. and van Breemen, O., 1994, U-Pb ages of Proterozoic dyke swarms, Lac de Gras area, N.W.T.: Evidence for progressive break-up of an Archean supercontinent. *GAC Programs with Abstracts* 19, 62.
- Le Cheminant, A.N., Heaman, L.M., van Breemen, O., Ernst, R.E., Baragar, W.R.A., Buchan, K.L., 1996, Mafic magmatism, mantle roots, and kimberlites in the Slave Craton. In *Searching for Diamonds in Canada*. Edited by A.N. Le Cheminant, D.G. Richardson, R.N.W. DiLabio, K.A. Richardson. Geological Survey of Canada, Open File 3228, p. 161-169.
- Li, Y. and Oldenburg, D., 1996, 3D inversion of magnetic data, *Geophysics*, 61, 394-408.

- Li, Y. and Oldenburg, D., 1998, 3D inversion of gravity data, *Geophysics*, 63, 109–119.
- Li, Y. and Oldenburg D., 2003, Fast inversion of large-scale magnetic data using wavelet transform and logarithmic barrier method, *Geophysical Journal International*, 152, 251-265.
- Liu, G., 1998, Effect of transmitter current waveform on airborne TEM response, *Expl. Geophys.*, 29, 35–41.
- Lo, B., and Zang, M., 2008, Numerical modeling of Z-TEM (airborne AFMAG) responses to guide exploration strategies, *SEG Expanded Abstracts*, 27, 1098-1101.
- Ludden, J.N., Hubert, C., Gariépy, C., 1986, The tectonic evolution of the Abitibi greenstone belt of Canada, *Geological Magazine*, v. 123, p. 153-166.
- Macnae, J.C., 1979, Kimberlites and exploration geophysics, *Geophysics*, 44, No. 8, p. 1395 – 1416.
- Macnae, J.C., Lamontagne, Y., West, G.F., 1984, Noise processing techniques for time-domain EM systems, *Geophys.*, 49, 934-948.
- Macnae, J. and Lamontagne, Y., 1987, Imaging quasi-layered conductive structures by simple processing of transient electromagnetic data, *Geoph.*, 52, 545–554.
- Macnae, J., 2008, Airborne EM systems compared, *Preview*, 133, April Issue, 24–29.
- Macnae, J. and Baron-Hay, S., 2010, Reprocessing strategy to obtain quantitative early-time data from historic VTEM surveys, In *Expanded Abstract at 21st International Geophysical Conference & Exhibition, ASEG, Sydney, Australia.*
- McCracken, K.G, Oristallo, Hohmann, G.W., 1986, Minimization of noise in electromagnetic exploration systems, *Geophys.*, 51, 819-832.
- Menke, W., 1984, *Geophysical data analysis, discrete inverse theory*, Academic Press, 260.

- Meju, M.A., 1994a, Biased estimation: a simple framework for parameter estimation and uncertainty analysis with prior data, *Geophysical Journal International*, 119, 521-528.
- Meju, M.A., 1994b, *Geophysical data analysis, understanding inverse problem theory and practice*, Society of Exploration Geophysicists Course Notes Series 6, SEG Publishers, Tulsa, Oklahoma, 296.
- Morrison, H.F., Phillips, R.J., O'Brien, D.P., 1969, Quantitative interpretation of transient electromagnetic fields over a layered halfspace, *Geophys. Prosp.*, 17, 82-101.
- Munkholm, M.S. and Auken, E., 1996, Electromagnetic Noise Contamination on Transient Electromagnetic Soundings in Culturally Disturbed Environments, *J. Env. Eng. Geophs.*, 1, 119 – 127.
- Nabighian, M.N., 1979, Quasi-static transient response of a conducting half-space. An approximation representation, *Geophys.*, 44, 1700-1705.
- Nabighian, M.N. and Macnae, J.C., 1991, Appendix A: TEM systems, In *Electromagnetic methods in applied geophysics – Application*, (ed. M.N. Nabighian): 479 – 483, SEG publication.
- Nabighian, M. and Macnae, J., 2005, *Electrical and EM methods 1980-2005, The Leading Edge*, 24, 42-45.
- Nekut, A.G. and Eaton, P.A., 1990, Effects of pipelines on EM soundings, 60th SEG meeting, 1990, Expanded Abstracts, 491-494.
- Newman, G.A., Anderson W.L., Hohmann G.W., 1987, Interpretation of transient electromagnetic soundings over three-dimensional structures for the central-loop configuration, *Geoph. J. Roy. Astr. Soc.*, 89, 889-914.
- Newman, G.A. and Alumbaugh, D.L., 1997, Three-dimensional massively parallel electromagnetic inversion 1, Theory, *Geophysical Journal Interiors*. 128, 345-354.
- Nyboe, N.S., Sørensen, K.I., 2012, Noise reduction in TEM: Presenting a bandwidth- and sensitivity-optimized parallel recording setup and methods for adaptive synchronous detection, *Geophysics*, 77, no. 3, E203– E212.
- Oldenburg, D.W. and Li, Y., 1999, Estimating depth of investigation in DC resistivity and IP surveys, *Geophys.*, 64, 403–416.

- Oldenburg, D., Haber, E., Shekhtman, R., 2013, Three dimensional inversion of multisource time domain electromagnetic data, *Geophysics*, 78, E47-E57.
- Oppenheim, A.V. and Schaffer, R.W., 1975, *Digital Signal Processing*, Prentice-Hall.
- Palacky, G.J. and West, G.F., 1991, Airborne Electromagnetic methods: in Nabighian, M.N., Ed., *Electromagnetic methods in applied geophysics-applications Part A and B: Soc. Expl. Geophys., Inv.in Geophys.* 3, 811-879.
- Parker, R.L., 1994, *Geophysical inverse theory*, Princeton University Press, 400.
- Pell, J.A., 1995, Kimberlites in the Slave Structural Province, Northwest Territories: A preliminary review. EGS 1995-12, Indian and Northern Affairs Canada, NWT Geological Mapping, 20 pages
- Percival, J.A., 2007, Geology and metallogeny of the Superior Province, Canada, in Goodfellow, W.D., ed., *Mineral Deposits of Canada: A Synthesis of Major Deposit-Types, District Metallogeny, the Evolution of Geological Provinces, and Exploration Methods: Geological Association of Canada, Mineral Deposits Division, Special Publication No. 5*, p. 903-928.
- Peter, J.M., Kjarsgaard, I.M., and Goodfellow, W.D., 2003, Hydrothermal sedimentary rocks of the Heath Steele Belt, Bathurst mining camp, New Brunswick-Part 1. Mineralogy and mineral chemistry, in Goodfellow, W.D., McCutcheon, S.R., and Peter, J.M., eds., *Massive sulfide deposits of the Bathurst mining camp, New Brunswick, and northern Maine: Economic Geology Monograph 11*, p. 361-390.
- Pilkington, M., 1997, 3-D magnetic imaging using conjugate gradients, *Geophysics* 62, 1132-1142.
- Pilkington, M., 2009, 3D magnetic data-space inversion with sparseness constraints, *Geophysics* 74, L7-L15.
- Podgorski, J.E., Auken, E., Schamper, C., Christiansen, A.V., Kalscheuer, T., Green, A.G., 2013, Processing and inverting commercial helicopter time-domain electromagnetic data for environmental assessments and geological and hydrological mapping, *Geophysics*, v. 78, E149-E159.

- Portniaguine, O. and Zhdanov, M.S., 1999, Focusing geophysical inversion images, *Geophysics* 48, 713-721.
- Portniaguine, O. and Zhdanov, M.S., 2002, Magnetic inversion and compression, *Geophysics* 67, 1532-1541.
- Power, M. and Hildes, D., 2007, Geophysical strategies for kimberlite exploration in northern Canada. *Geophysical Case Histories. Paper 89. Proceedings of Exploration 07: Fifth Decennial International Conference on Mineral Exploration*, edited by Milkereit, B. pp. 1025-1031.
- Raiche, A.P., 1983, Negative transient voltage and magnetic field responses for a half-space with Cole-Cole impedance, *Geophysics*, 48. 790-791.
- Raiche, A.P., Bennett, L.A., Clark, P.J., Smith, R.J., 1985, The use of Cole-Cole impedances to interpret the TEM response of layered earths, *Exp. Geophys.*, 16, 271-272.
- Reed, L.E. and Witherly, K.E., 2007, 50 years of kimberlite geophysics, a review, in *Proceedings of Exploration 07: Fifth Decennial International Conference on Mineral Exploration*, Milkereit, B. (ed.), p679-689.
- Reid, J.E. and Viezzoli, A., 2007, High-Resolution Near Surface Airborne Electromagnetics–SkyTEM Survey for Uranium Exploration at Pells Range, WA. 19th Geophysical Conference and Exhibition, Australian Society of Exploration Geophysicists, Extended Abstracts.
- Reynolds, J.M., 1997, *An introduction to applied and environmental geophysics*, John Wiley & Sons Ltd, Chichester, West Sussex.
- Robert, F. and Poulsen, K.H., 1997, World-class Archaean gold deposits in Canada: An overview: *Australian Journal of Earth Sciences*, v. 44, p. 329-351.
- Safon, C., Vasseur, G., and Cuer, M., 1977, Some applications of linear programming to the inverse gravity problem, *Geophysics*, 42, 1215-1229.
- Sattel, D., 2006, A brief discussion of helicopter time-domain EM system, In *Extended Abstracts: 20th Geophysical Conference ASEG, Australia*.
- Sattel, D., 2009, An overview of helicopter time-domain EM systems, In *Extended Abstracts: 22th Geophysical Conference ASEG, Sidney, Australia*.

- Scales, J.A., Smith, M.L., Treitel, S., 2001, *Introductory Geophysical Inverse Theory*, Samizdat Press, Colorado School of Mines, 193.
- Schertzer, W.M., Rouse, W.R., Blanken, P.D., Walker, A.E., 2003, Over-lake meteorology and estimated bulk heat exchange of Great Slave Lake in 1998 and 1999, *J. Hydrometeor.*, 4, 649- 659.
- Scott Smith, B.H., 1996, Kimberlites. In Mitchell, R.H. (Ed.), *Undersaturated Alkaline Rocks: Mineralogy, Petrogenesis and Economic Potential*. Mineralogical Association of Canada, Short Course Volume 24, p. 217-244.
- Sengpiel, K.P. and Siemon, B., 2000, Advanced inversion methods for airborne electromagnetic exploration, *Geoph.*, 65, 1983-1992.
- Smith, R. and Annan, P., 1998, The use of B-field measurements in an airborne time-domain system: Part I. Benefits of B-field vs dB/dt data: *Exploration Geophysics*, 29, 24-29.
- Smith, R.S., and J. Klein, 1996, A special circumstance of airborne induced polarization measurements, *Geophysics*, 61, 66-73.
- Sørensen, K.I., Auken, E., Thomsen, P., 2000, TDEM in groundwater mapping – a continuous approach, In *Proceedings of the Symposium on the Application of Geophysics to Engineering and Environmental Problems*, Arlington, Virginia, 485-491.
- Sørensen, K.I. and Auken, E., 2004, SkyTEM – a new high-resolution helicopter transient electromagnetic system, *Exp. Geoph.*, 35, 191-199.
- Spies, B.R., 1980a, A field occurrence of sign reversals with the transient EM method, *Geophys. Prosp.*, 28, 620-632.
- Spies, B.R. and Eggers, D.E., 1986, The use and misuse of apparent resistivity in electromagnetic methods, *Geophysics*, 51, 1462-1479.
- Spies, B.R. and Frischknecht, F.C., 1991, Electromagnetic sounding, In *Electromagnetic methods in applied geophysics*, Nabighian, M.N., Ed., II, 285-426.
- Stolz, E.M. and Macnae, J.C., 1998, Evaluating EM waveforms by singular value decomposition of exponential basis functions, *Geophysics*, 63, 64-74.

- Sugeng, F., 1998, Modelling the 3D TDEM response using the 3D full-domain finite element method based on the hexahedral edge-element technique, *Expl. Geoph.*, 615–619.
- Szalai, S., Novak, A., Szarka, L., 2009, Depth of investigation and vertical resolution of surface geoelectric arrays, *Journal of Environmental and Engineering Geophysics*, 14, no. 1, 15–23.
- Tarantola, A. and Valette, B., 1982, Generalized nonlinear inverse problems solved using least squares criterion. *Reviews of Geophysics & Space Physics*. 20, 219-232.
- Tarantola, A., 1987, *Inverse Problem Theory*: Elsevier, Amsterdam, Oxford, New York, Tokyo, pp. 613.
- Tarantola, A., 2005, *Inverse problem theory and methods for model parameter estimation*. Society for Industrial and Applied Mathematics. Philadelphia, 342.
- Telford, W.M., Geldart, L.P., Sheriff, R.A., 1990, *Applied geophysics*, 2nd edition: Cambridge Univ. Press.
- Thomas, M.D., Walker, J.A., Keating, P., Shives, R., Kiss, F., Goodfellow, W.D., 2000, *Geophysical atlas of massive sulphide signatures*, Bathurst mining camp, New Brunswick, Geological Survey of Canada Open File 3887, 105 p.
- Thomson, S., Fountain D., Watts T., 2007, Airborne geophysics - Evolution and revolution. In *Proceedings of Exploration 07: Fifth Decennial International Conference on Mineral Exploration*, Toronto, Canada, 19-37.
- Thurston, P.C., 1994, Archean volcanic patterns, in *Condie, K.C., ed., Archean Crustal Evolution: Developments in Precambrian Geology*, 11, Elsevier, Amsterdam, p. 45-84.
- Tikhonov, A.N. and V.Y. Arsenin, 1977, *Solution of ill-posed problems*: V. H. Winston and Sons, pp. 258.
- Tivey, M.A., Rona, P.A., Schouten, H., 1993, Reduced crustal magnetization beneath the active sulfide mound, TAG hydrothermal field, Mid-Atlantic Ridge at 26°N, *Earth and Planetary Science Letters*, v. 115, p. 101–115.
- Tivey, M.A., Rona, P.A., and Kleinrock, M.C., 1996, Reduced crustal magnetization beneath relict hydrothermal mounds TAG hydrothermal

- field, Mid-Atlantic Ridge, 26°N: *Geophysical Research Letters*, v. 23, p. 3511–3514.
- Vallée, M.A. and Smith R.S., 2009, Inversion of airborne time-domain electromagnetic data to a 1D structure using lateral constraints, *Near Surf. Geoph.*, 7, 63-71.
- Viezzoli, A., Christiansen, A.V., Auken, E., and Sørensen, K., 2008, Quasi-3D modeling of airborne TEM data by spatially constrained inversion, *Geoph.*, 73, 105-113.
- Viezzoli, A., Munday T., Auken E., and Christiansen A.V., 2010, Accurate quasi 3D versus practical full 3D inversion of AEM data - the Bookpurnong case study, *Preview*, 149, 23-31.
- Viezzoli, A., Tosi, L., Teatini, P., Silvestri, S., 2010, Surface water-groundwater exchange in transitional coastal environments by airborne electromagnetics: the Venice Lagoon example, *Geophys. Res. Lett.*, 37, L01402, 6 pp.
- Viezzoli, A., Fiandaca, G., Segio, S., Auken., E., 2013, Constrained inversion of IP parameters from Airborne EM data, ASEG-PESA Expanded abstracts, Melbourne, Australia.
- Viezzoli, A., Kaminski, V., Cooper, Y.L., Hardy, L., Fiandaca, G., 2015, Improving modelling of AEM data affected by IP, two case studies, ASEG-PESA Expanded abstracts, Perth, Australia.
- Viezzoli, A., Kaminski, V., Goncharov, E., 2015, Airborne IP: examples from gold and kimberlite exploration, SAGA Expanded abstracts, Drakensberg, South Africa.
- Wait, J.R. and Debroux, P., 1984, Induced polarization in electromagnetic inductive schemes, *Geophys. Prosp.*, 32, 1147-1154.
- Walker, S. and Rudd, J., 2008, Airborne resistivity mapping with helicopter TEM: An oil sands case study. In *Proceedings of the 5th International Conference on Airborne Electromagnetics*, Helsinki, Finland, 03-06.
- Ward, S.H., 1959, AFMAG - Airborne and Ground: *Geophysics*, 24, 761-787.
- Ward, S.H. and Hohmann, G.W., 1988, Electromagnetic theory for geophysical applications, in M. N. Nabighian, ed., *Electromagnetic methods in applied geophysics*: SEG, 131–311.

- Weidelt, P., 1982, Response characteristics of coincident-loop transient electromagnetic systems, *Geophysics*, 47. 1325-1330.
- West, G.F. and Macnae, J.C., 1991, Physics of the electromagnetic induction exploration method. In: *Electromagnetic methods in applied geophysics*, Nabighian M.N. and Corbett J.D. (eds.) Society of Exploration Geophysicists.
- Wijns, C. and Kowalczyk, P., 2007, Interactive geophysical inversion using qualitative geological constraints, *Exploration Geophysics*, 38, 208–212.
- Williams, H.R., 1991, Quetico subprovince, in Thurston, P.C., Williams, H.R., Sutcliffe, R.H., and Stott, G.M., eds., *Geology of Ontario: Ontario Geological Survey, Special Volume 4, Part 1*, p. 383-403.
- Witherly, K., 2000, The Quest for the Holy Grail in Mining Geophysics, *The Leading Edge*, 19, 270-274.
- Witherly, K., Irvine, R., Morrison, E., 2004, The Geotech VTEM Time Domain helicopter EM System, In *Expanded Abstract of 74th Ann. International meeting SEG, Denver, Colorado (USA)*, 1217-1220.
- Witherly, K., Irvine R., Morrison E., 2005, Update on the Geotech VTEM System; improvements to the technology and recent applications, *KEGS Airborne Geophysics Workshop*. Toronto, March 2005.
- Zhang, Z., 2003, 3D resistivity mapping of airborne EM data, *Geophysics*, 68,1896–1905.
- Zhdanov, M.S., 2002, Geophysical Inverse Theory and Regularization Problems, *Methods in Geochemistry and Geophysics*, 36, Elsevier, 628 pages.
- Zhdanov, M.S. and Tartaras, E., 2002, Three-dimensional inversion of multitransmitter electromagnetic data based on the localized quasi-linear approximation, *Geophysical Journal International*, V. 148, No. 3, 506-519.

## **ACKNOWLEDGEMENTS**

I would like to express my heartily thanks to the people who have helped me to achieve this important aim of my life.

First of all my sincere gratitude goes to my tutor, Prof. Giovanni Florio, who gave me the chance to work under his supervision, overseeing my research and leading it in the right direction and my co-tutor, Dr. Andrea Viezzoli, for all that he taught me, for the time he dedicated to my research, and for the friendship that he has shown me.

I am very grateful to Prof. Maurizio Fedi and Dr. Vlad Kaminski for their valuable comments and inputs during discussions throughout all these years.

I am also grateful to the referee of my thesis, Prof. Agata Siniscalchi, for her critical suggestions and comments.

I am highly thankful to Promiseland Exploration, Ltd. and Geotech, Ltd for providing the VTEM data for research purposes of my work.

My special thanks go to Prof. Federico Cella, to Prof. Valeria Paoletti, to Dr. Mauro La Manna and to all my friends/colleagues Mahmoud, Mahak Singh, Maurizio, Davide, Andrea, Mouna, Payal, Paola, Roberta, Monica, Silvia, Cecilia, Gabriella, Stefania, Daniela, Tina, Fabio who have been constant source of encouragement and enrichment throughout the last three years.

My lovely thanks go to the important people, to my lifetime friends: Alfonso, Ciro, Antonella, Carmen, Anna, Mariano, Luca, Monica, Valentina and Vincenzo for continuously supporting me whenever I needed their help.

Last but not the least, my gratitude to my parents, my sister, my brother, my nephews and my relatives for tolerating me all these years and for their complete support and love that makes my life really lucky.